INTEGRATED HYDROLOGIC AND HYDROGEOLOGIC MODELLING FOR BASIN SCALE SUBSIDENCE ANALYSIS

Dissertation

submitted to and approved by the

Faculty of Architecture, Civil Engineering and Environmental Sciences
Technische Universität Braunschweig

and the

Department of Civil and Environmental Engineering
University of Florence

in candidacy for the degree of a
Doktor-Ingenieur (Dr.-Ing.) /
Dottore di Ricerca in Civil and Environmental Engineering*)

by
Mattia Ceccatelli
born 10/05/1991
from Bagno a Ripoli (FI), Italy

Submitted on	16 January 2020
Oral examination on	22 April 2020
Professorial advisors	Prof. Matthias Schöniger
	Prof. Fabio Castelli

2020

*) Either the German or the Italian form of the title may be used.

Table of contents

1 Abstract

Land subsidence, together with landslides and floods, represents one of the main natural hazards that affect several countries all over the world, potentially causing significant damages to buildings and infrastructures. In particular, Firenze-Prato-Pistoia basin has a long experience of ground deformation related to groundwater withdrawal. InSAR satellite data collected since 1992 have revealed the presence of several subsiding areas in the basin, such as the south-eastern portion of Pistoia city. Sentinel-1 persistent scatterer interferometry measurements for 2015–2018 confirmed the long-term subsidence of this area, associated with intense horticulture (plant nurseries). At the same time, Sentinel-1 data revealed the unexpected movement of Pistoia historic center, which has always been considered stable in the past. To identify the complex relationship between aquifer conditions and ground displacement, a hydrogeologic model of the Pistoia aquifers was developed, applying an integrated modelling procedure. This approach was firstly tested in a small pilot basin, to confirm the reliability of the numerical procedure, obtaining promising results. Hydrodynamic-parameter distributions, calibrated and validated by means of Sentinel-1 PSI measurements, suggest that subsidence in Pistoia area is probably related with the combined impacts of groundwater extraction and highly compressible aquitards. To evaluate the potential evolution of ground displacement, numerical simulations were extended until 2050, using regional and global climate model data, analyzing three different pumping-rate scenarios. This, together with damage information of buildings collected on the field, led to the development of several subsidence hazard maps of Pistoia city that display the influence of groundwater extraction in controlling land subsidence in the area. The present study enhances the importance of developing proper groundwater management policies, especially in alluvial aquifers made of fine compressible sediments, in order to sustainably utilize underground freshwater resources and to avoid related side effects. It also emphasizes the role of integrated numerical simulations and the necessity to consider surficial network and groundwater as a unique interacting system, when developing basin scale hydrogeologic analysis.

2 Introduction

Groundwater is a fundamental resource for fresh water supplies in many urban and rural areas all over the World, as it guarantees support for agricultural economy and the availability of large amount of drinkable water. Even if groundwater represents only the 1.7% of all water on the Earth, it supplies a large percentage of total freshwater for World population. It has been estimated that about 30.1% of water supply occurs as groundwater (Winter et al., 1998). In Italy these percentages rise, with the population water demand that is managed for more than 85% with water from the underground (48% from wells and 37% from springs). Advantages in groundwater use come from its usual good status in terms of supplied water quality and quantity and its spreading occurrence all over the places of the World (Cao et al. 2013). During dry seasons, when water from surface sources is limited, groundwater offers a vital buffer for water supply, providing a high volume of water even in critical situations. Despite the quality of groundwater is changing as a result of human activities, it is still less susceptible to chemical and biological pollution than surface water, because of the protective action of soil and rocks in which the resource is contained.

Nowadays, with the growing of water demands related with World population increase, the development of water management policies, in order to guarantee the water resource safety, it is becoming always more important. Uncontrolled human activities and bad natural conditions may lead to the emergence of a high number of specific issues that should always be considered. To adopt better strategies in water assessment and management plans should be one of the first step for improving performance and efficiency of water uses and for preserving the natural state of the environment (Tahiri et al., 2018). In this field, the Common Implementation Strategy (CIS) for the European Water Framework Directive (Directive 2000/60/EC) attributes an important role to numerical models for water resource management practices, in order to preserve its good chemical and quantitative status.

The evaluation of the effects of medium and long-term disturbances like changes in land-use, storage systems or variations in pumping rates on natural systems is very hard to perform, especially with the continuous changing climate conditions that are affecting the entire planet in the last century. Therefore, efficient groundwater management policies require the development of integrated modelling tools that can properly simulate hydrogeological processes, by also considering the influence and the contribution of the evolving surrounding systems affecting the water cycle.

Historically, groundwater has been exploited in many areas of the world as required, often with little regard for the effects of over pumping on natural aquifer systems. Over exploitation of groundwater is not sustainable for the environment and can induce many consequences in the long term, as water quality worsening, increasing costs for groundwater pumping or wells replacement and drainage of nearby rivers. One of the main consequences caused by groundwater over pumping, especially in areas characterized by the presence of unconsolidated alluvial deposits, is the development of land subsidence.

When groundwater pumping exceeds aquifer recharge for long term periods, a decline of water levels usually occurs, with a relative decrease in pore water pressure and the increase in effective stress of unconsolidated sediments. This phenomenon leads to the compression of aquifers and confining aquitards and to a gradual land surface lowering. Some of the more costly consequences of land subsidence include damages to building and structures, as well as the extension of coastal and inland flooding areas. Buildings and underground facilities are under higher risks of damage if they are placed in locations characterized by important differential ground deformation.

In China, for example, land subsidence has become one of the most impactful natural hazards in last decades, especially considering the economical aspect of the phenomenon. In Shanghai, ground lowering caused damages for more than 13 billion dollars during the last two decades of 20th century and up to 3.3 billion in the first years of 2000' (China Daily, Feb. 14, 2007). In the United States, the annual cost deriving from flooding and structural damages exceeded 125 million dollars, as estimated by the National Research Council in 1991, but the assessment of the effects of land subsidence are hard to evaluate and the estimation probably under evaluate the real cost of the issue (Galloway et al., 1999).

In the same way, many European country are facing an increase in structures damages due to soil subsidence, and a 2011 model developed by Swiss Re and the Swiss Federal Institute of Technology (ETH Zurich) suggests that this trend is going to worsen and spread in the future (Swiss Re, 2011). Estimations from the Association of British Insurers (ABI) indicate that building damages as a result of subsidence cost about £500 million over the dry summers of 1975–1976, and about £400 million in 2003. Other previsions from the ABI (Dlugolecki, 2004) suggest that with the effects of climate change, within 2050 the costs could increase up to £600 million in a normal year and £1.2 billion in a particular dry year (at nowadays prices).

Land subsidence, especially if induced by anthropic causes, is widespread all over the world and can be very dangerous for buildings and human activities. Because of this, many case studies related with this phenomenon are available in literature, enhancing the importance of the research on it.

From more than one century, Mexico City has been characterized by important subsidence phenomena due to groundwater withdrawal (Figure 1). Mexico City valley is situated at the South end of the highest part of the Mexican Plateau, in a lacustrine area. During the late Pleistocene, a large lake occupied the entire extent of the basin, and the deepest part of it was filled with lacustrine fine materials. The hydrogeological conditions of the Mexico Valley are represented by a main hydrogeological quaternary alluvial unit. This layer has a maximum thickness of about 800 m and is covered by 30 to 300 m thick quaternary lacustrine deposits, forming the aquitard (Carrera-Hernández and Gaskin, 2007). Since the middle of the XIX century, a large number of wells have been drilled between 50 and 300 m deep, for the extraction of large quantities of water from the subsoil. At present, groundwater provides about 70% of Mexico City population freshwater consumption (Tortajada, 2006) and its over exploitation caused a lowering in water levels of about 70 m between 1975 and 2002 (Carrera-Hernández and Gaskin, 2007). The result was the formation of large depressions around these water wells, producing damage and tilting of the nearby constructions, which in some cases they had to be abandoned and/or demolished. It has been observed that, between 2005 and 2013, a great part of the urban area of the city lowered down of 1.5 to 3.2 meters (Albano et al., 2016). Subsidence is damaging urban structures of the city such as domestic and historical buildings, water supply facilities, drainage pipes, gas, electricity and telephone installations (Santoyo et al., 2005). Studies on Mexico City subsidence found that the high compressibility of the clay and silt lacustrine sediments of the aquitard, represents the main cause of this anomalous subsidence rate (Zeevaert, 1983).

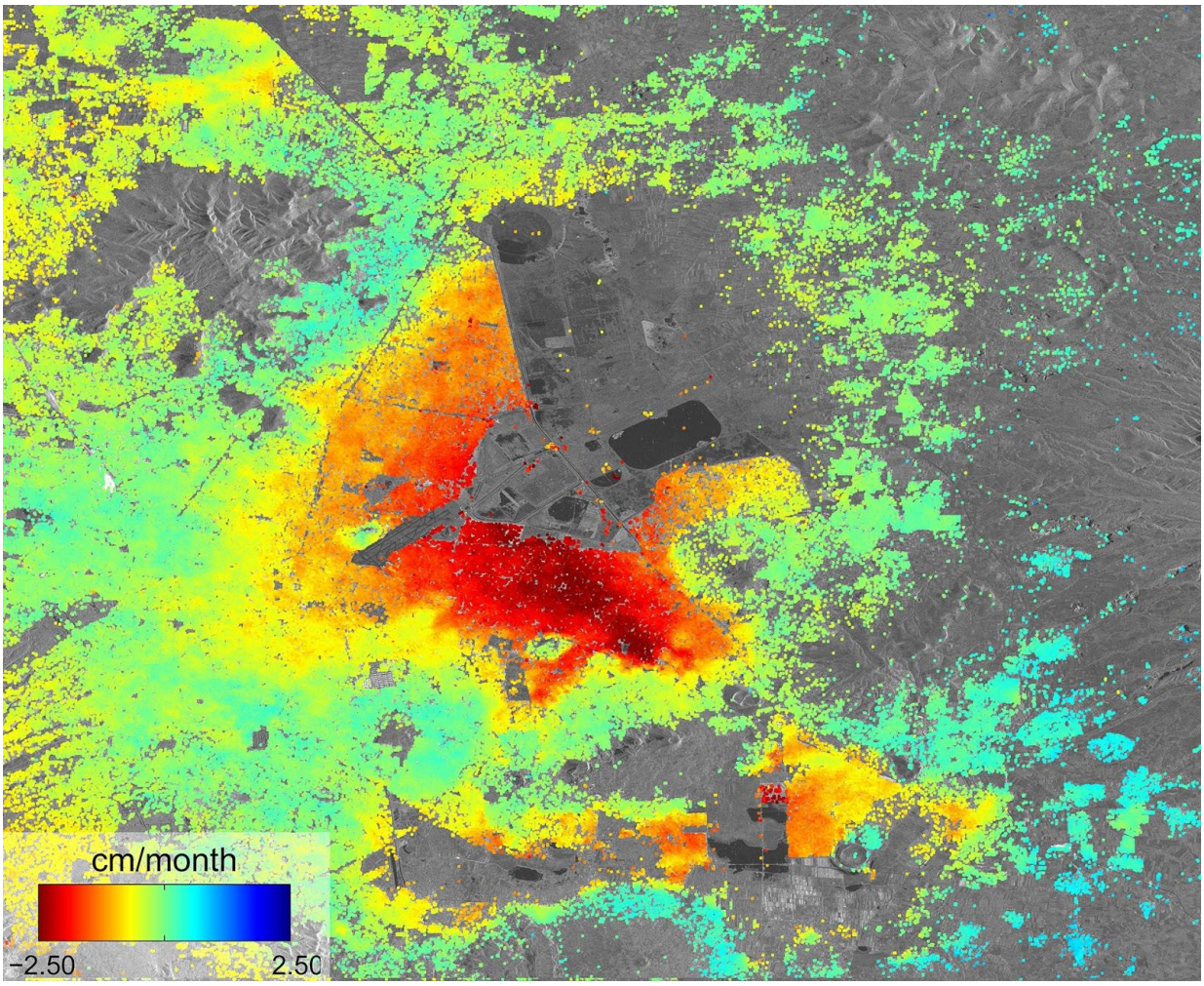

Figure 1 – Mexico City subsidence between October and December 2014 (European Space Agency, 2014)

In San Joaquin valley, California, groundwater withdrawal for agriculture has enabled it to become one of the most productive agricultural regions in the World. Subsidence in the valley began in the mid-1920s and increased as agricultural development intensified after 1940s, with displacement rates that exceeded 30 cm per year in some places. Despite the early recognition of ground lowering, in San Joaquin Valley subsidence was not directly investigated until first years of the 1950s, when became necessary to study its effects on the Delta Mendota Canal, that was under construction. Subsidence occurred uniformly over such a wide area, that people and authorities struggled to even recognized it, justifying the delay in the reactions to the phenomenon. In 1970, when the last complete surveys of land subsidence were made, subsidence in excess of 30 cm had affected more than 13.000 square meters of irrigable land, with a maximum measured subsidence of more than 8.5 meters (Poland et al., 1977). Most of subsidence measured in the valley has been correlated with the distribution of groundwater withdrawal and the reduction of water levels in the deep confined aquifer systems. Groundwater levels in the west side of the valley showed a decline of more than 120 meters in some observation wells. By the late 1960s, groundwater extraction was largely reduced, and subsidence slowed down, with the related recover of water levels in the deep aquifer over a large part of the area. During the 1968 to 1974 period, water levels recover reached up to 60m in some observation wells, while 10 cm/year of subsidence still continued (Ireland et al., 1984). This apparent contradiction is the result of the time delay in the compaction of the aquifers, since the time needed for pressure to equilibrate depends on aquifers thickness and permeability. In 2015, several spots of San Joaquin Valley have been identified that are continuing to subside at rates as high as 0.6 meters per year.

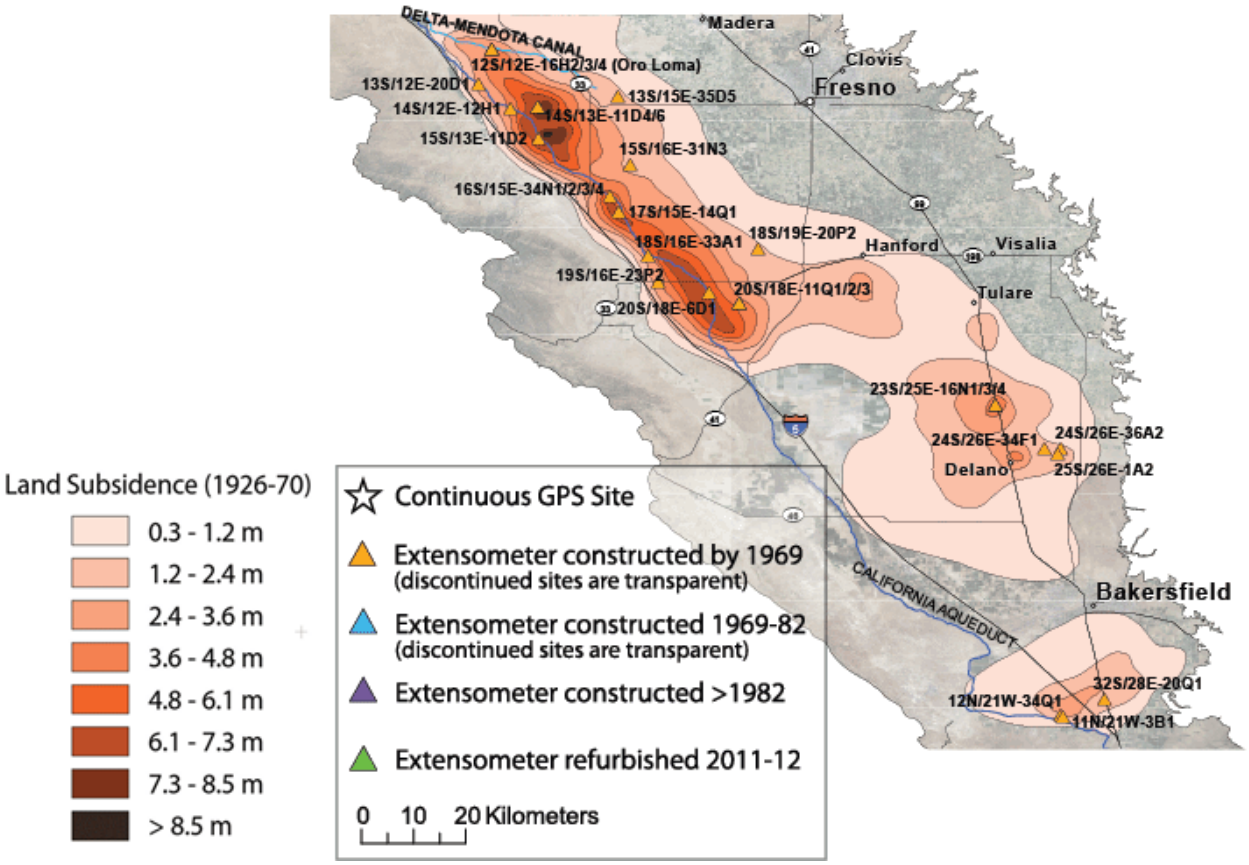

Figure 2 – Measured land subsidence in San Joaquin Valley between 1926 and 1970 (USGS, 2011)

In Beijing, land subsidence was recorded for the first time in the 1950s, mainly caused by the high groundwater extraction rate from the main aquifer system of the region (Chen et al., 2016). Between 1998 and 2005, a decrease of 15-20 m in groundwater levels has been identified, related with the occurrence of many centimeters of ground displacement. Satellite InSAR data over Beijing area identified a maximum subsidence rate of 115 mm per year during 2003-2009 (Ng et al., 2012).

By the end of 2005 land subsidence has been recorded over 50 cities in China, mainly located in the Yangtze river delta region, the north China plain and some inland basins, with a maximum accumulated subsidence of 3.187 m found in Tianjin.

In Italy, economical evaluation studies on subsidence effects still do not exist, however, in 2006 the Istituto Superiore per la Protezione e la Ricerca Ambientale (ISPRA, 2006) demonstrated that about 10% of Italian municipalities are affected by this phenomenon (Figure 3). Over the last century Po Valley has been affected by widespread land subsidence phenomena, with both natural and anthropogenic origins, becoming a matter of increasingly great concern (Fabris et al., 2014). Land settlement, initially of the order of few mm/year, increased up to 100 mm/year in some area during 1950s, primarily due to groundwater pumping and, subordinately, gas production from several deep reservoirs above the whole valley. Subsidence increase moving from the West side of the valley to the East side. Zero subsidence values have been registered at Genova, on the Tyrrhenian coast, and in correspondence of Brescia city, while 25 cm displacement occurred during the last 50 years at Venice and Ravenna, on the Adriatic coast. The northern Adriatic coast is the most extent subsidence area in Italy, with some sectors that lowered up to 5 m below the mean sea level. Venice and Ravenna are the two cities where the effect of the relative sea level rise has been always tangible, making necessary the realization of many direct actions to counteract the effect of the sea level rise (Bitelli et al., 2010).

In the inland, Bologna city experimented a long history of land subsidence since the first years of the 1950s (Pieri and Russo, 1984). It has been estimated that, between 1950 and 2000, most subsiding areas of the city showed a displacement of more than 2.5 m. Enviset satellite InSAR data revealed that this lowering pattern did not stop in the recent years, showing a settlement rate of more than 9 mm/year between 2003-2010. The principal cause of land subsidence in Bologna City has been found in the overexploitation of aquifers for potable and agricultural purposes (Stramondo et al., 2006).

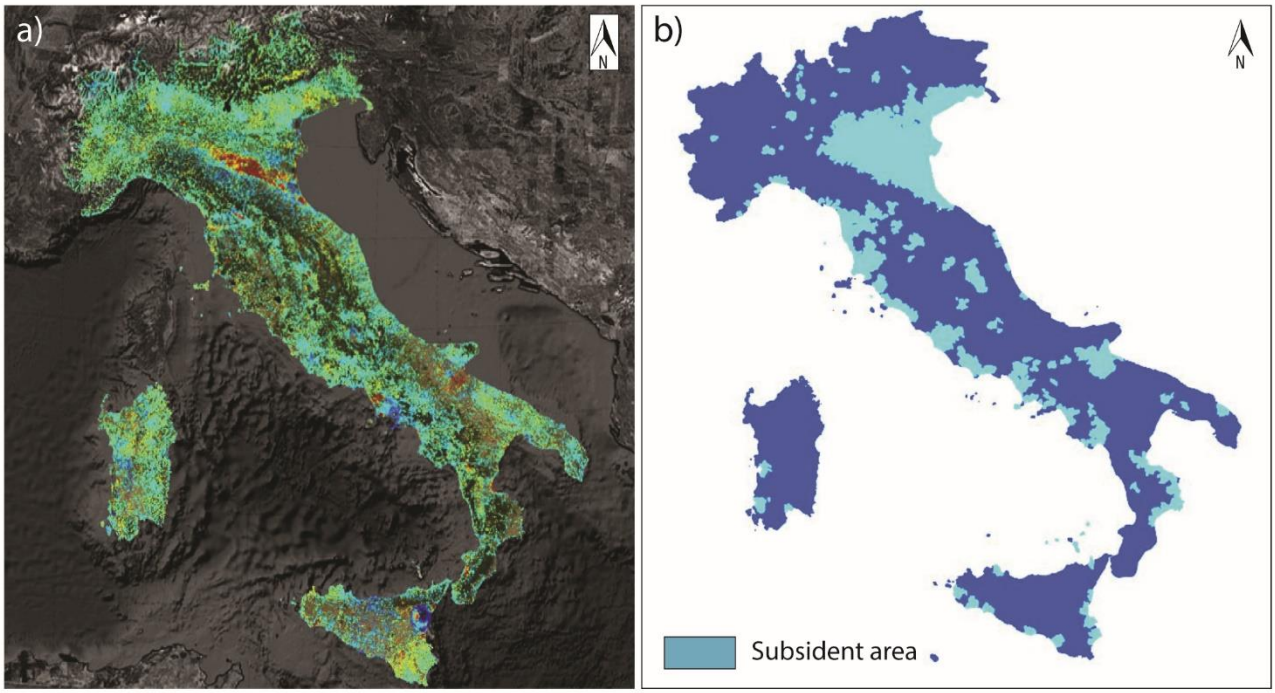

Figure 3 – a) Subsidence in Italy identified by ESA's ERS missions between 1992-2001 (European Space Agency, 2001) and b) Map of subsident area (ISPRA, 2006).

In Tuscany region, several subsidence areas have been recognized in the last 25 years, thanks to the numerous satellite data available for the whole country. Rosi et al. (2016) identified 3 main subsidence bowl in the region: in the Firenze – Prato – Pistoia basin, in the Valdarno Inferiore plain close to Pisa city and in Larderello geothermal area (Figure 4). Ascending and descending datasets of the Envisat satellite between 2002 to 2010 were used to perform the investigation.

The area at the East of Pisa City (Valdarno Inferiore Plain) is an alluvial plain characterized by the presence of high compressive fluvial and marine sediments. Land subsidence has been recorded in the plain during the analyzed period, with an average velocity of about 8 mm per year with peaks of more than 20 mm per year in the southern part of it. Cause of ground lowering can be related to both natural and anthropic reasons.

Subsidence in Larderello geothermal district, due to gas extraction, has been observed for the first time in 1923 by means of topographic surveys. Many authors kept studying subsidence patterns in the area during last 40 years, identifying different displacement rate ranging between 10 to 25 mm/year (Ciulli et al., 2005; Batini et al., 2006).

Firenze – Prato – Pistoia plain is an alluvial tectonic basin that consists of up to 400 m of fluvial and lacustrine sediments set up on a substrate made of flysch formations. Rosi et al. (2016) identified a high subsidence rate of 15-20 mm/year near to Pistoia city and uplift close to Prato city.

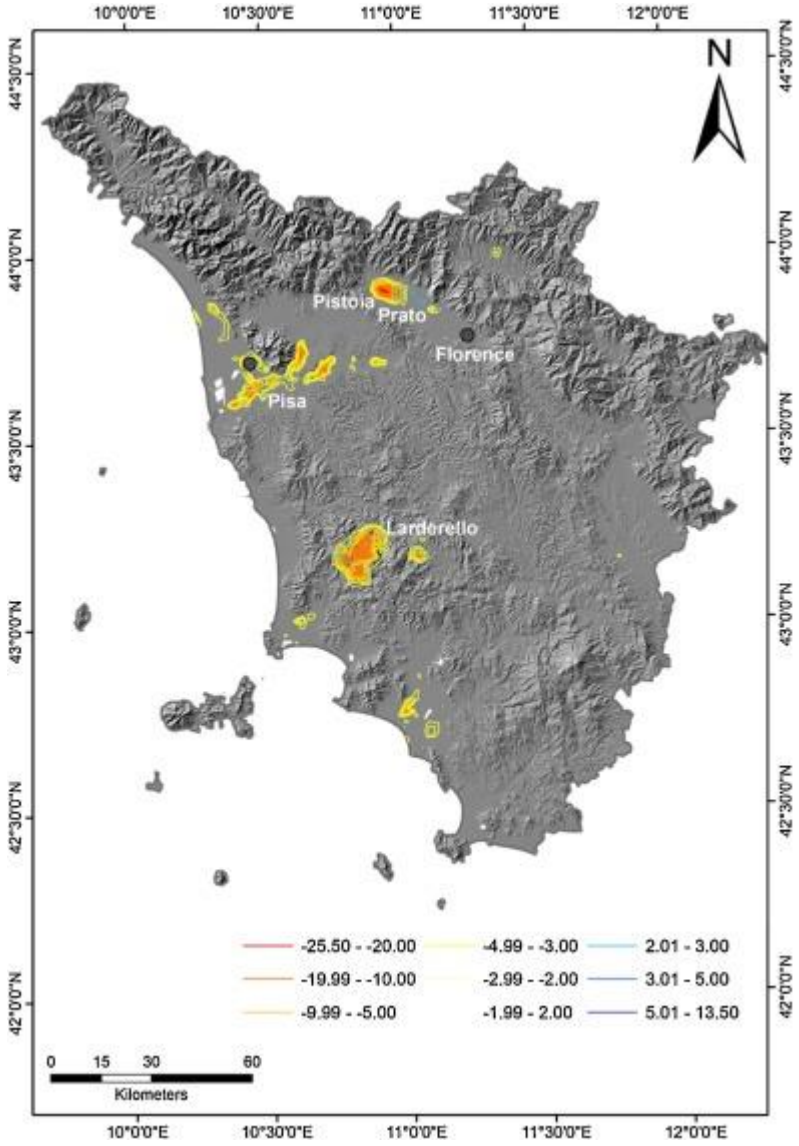

Figure 4 – Tuscany region subsidence rate for the 2003-2010 period (Rosi et al., 2016)

Canuti et al. (2006) shows, for the 1992-2000 period, similar ground lowering rate for Pistoia area (about 10 mm/year) while Prato city was characterized by a subsidence rate of 15-20 mm/year. Many studies related this inversion in ground displacements pattern (subsidence for the 1992-2000 period and uplift for the 2003-2010) to the lower groundwater exploitation occurred in the first 2000s, linked to the textile industry regression. Del Soldato et al. (2018), analyzing Sentinel-1 PS-InSAR data (between 2014-2017) found two main subsidence bowls close to Pistoia city (Figure 5). The first one, located in the plant nursery area at South-East of the city, shows a mean displacement rate of 10-15 mm per year, slightly lower than the previous 2003-2010 period. The second bowl is located in the historical center of the city and it is characterized by a higher velocity, of about 20 mm/year.

Combining ENVISAT (2003–2010) and Sentinel-1 (2014–2017) information, Del Soldato et al. (2018) realized two time series of the subsiding areas, representing the temporal evolution of ground displacement in correspondence of the two identified subsidence bowls (Figure 6). ERS/ENVISAT and Sentinel-1 time series were connected to each other, considering a constant trend of deformation, to estimate the cumulative value of the displacement for the first Sentinel-1 acquisition.

Subsidence pattern analysis identified different evolutions for the two sites. ENVISAT data in the historical center of Pistoia show a stable trend until December 2007 and then, until July 2010, the area slowly subsided (Figure 6a).

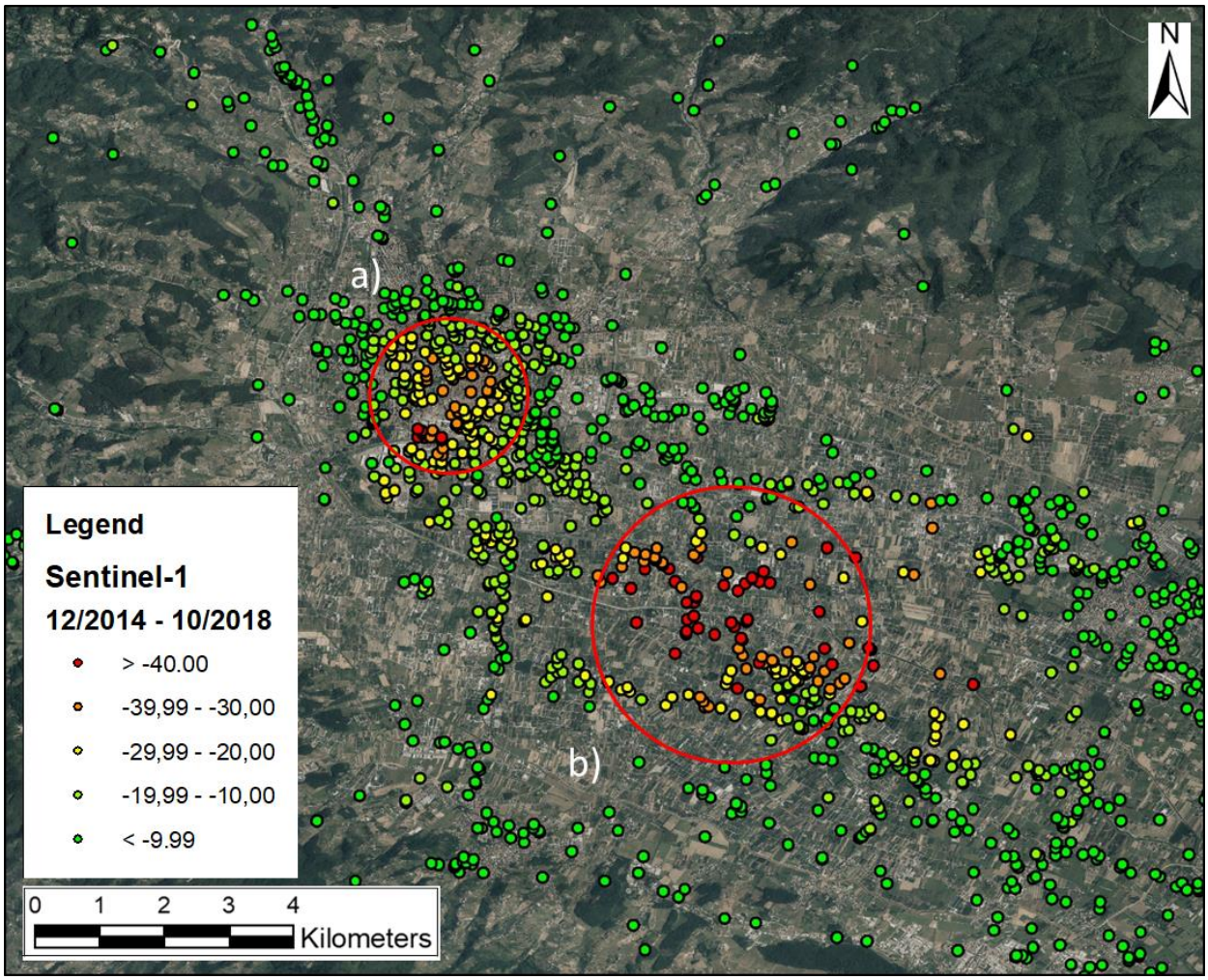

Figure 5 – PS-INSAR data of Pistoia area for 12/2014 – 10/2018 period with the identification of the two characteristic subsidence bowls: a) Pistoia historic center and b) Plant nursery area.

Starting from the end of 2014, Sentinel-1 data evidence an important increase in subsidence rate, characterized by an anomalous displacement rate of about 20 mm/year.

In plant nursery area, subsidence pattern shows a slightly different behavior. During the 2003-2010 period, ENVISAT sensors recognize an important and constant trend of subsidence, with a mean displacement rate of more than 20 mm/year. Sentinel-1 data, available starting from December 2014, show a lower subsidence rate in plant nursery area, with a constant displacement velocity of about 10-15 mm/year (Figure 6b).

Del Soldato et al. (2018) ascribe subsidence phenomena identified in plant nursery area of Pistoia to the overexploitation of groundwater, that caused a reduction in groundwater levels with the consequent compaction of the sedimentary deposits. Unfortunately, continuous time series of groundwater level variation were not available in Pistoia area, and a direct comparison between ground displacement rate and hydraulic head changes in the aquifer was not possible. In Pistoia downtown, water extraction from the aquifer is very low, but it is still possible to speculate that subsidence is driven by groundwater states variation as well. Similar instability phenomena, in fact, were recorded in Pistoia historical center during the last years of 1960' (1964-1967, Fancelli et al., 1980). These phenomena, named "dissesti statici - static

instability", caused several damages to many buildings until they suddenly stopped with no apparent reason in 1967. The hypothesis concerning the causes of the static instability were about the increasing of horizontal stresses in the damaged area, due to the growth of the water pore pressure in the soil, related with the rising of groundwater levels.

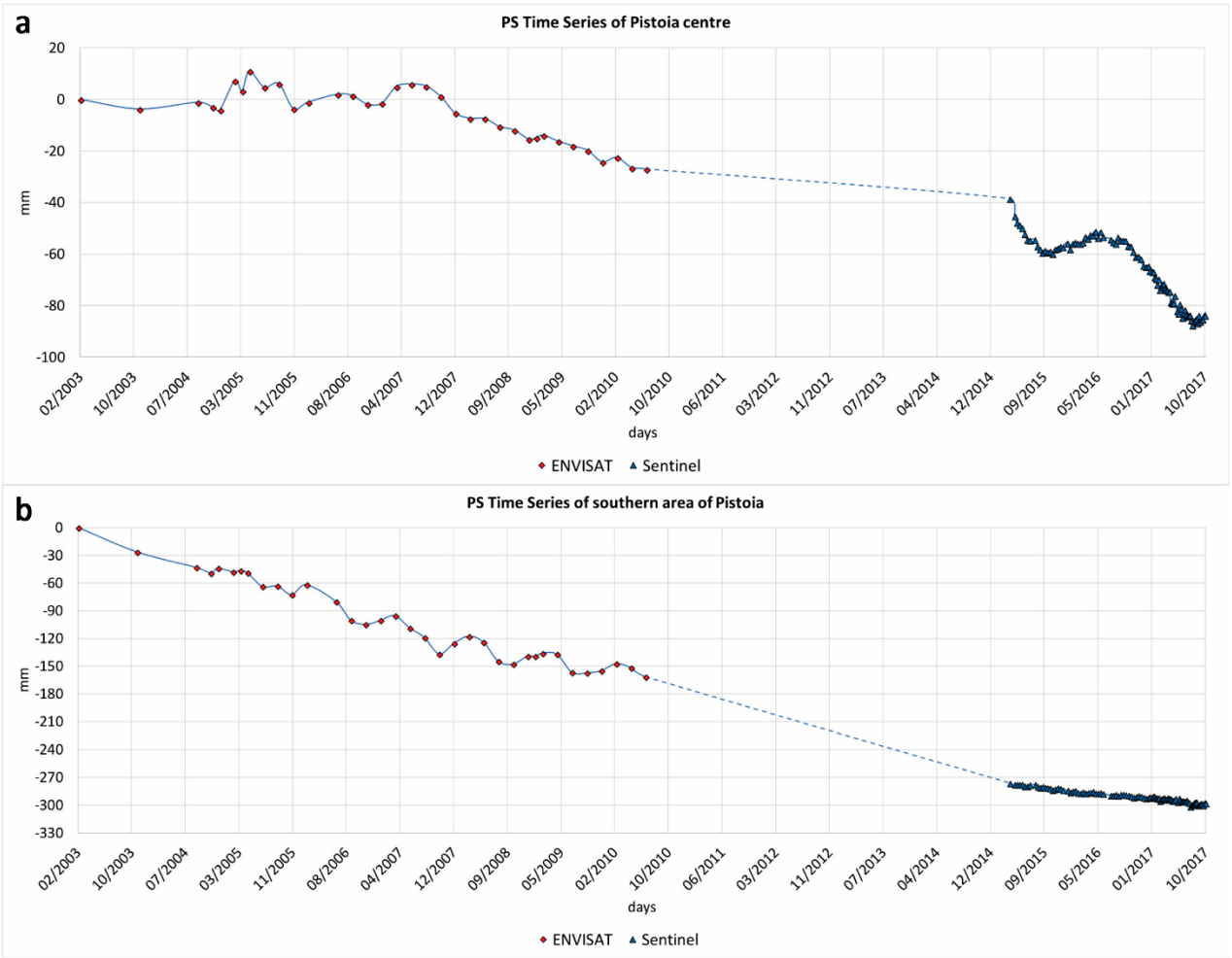

Figure 6 – Time series of the two subsidence bowls in Pistoia area: a) historic center of Pistoia and b) nursery area from Del Soldato et al., 2018.

Obviously, this is just a theory based on 50 years old observations, but it seems reasonable to state that the effects of the groundwater fluxes and their relation with surficial processes play an important role in the control of ground instability phenomena in Pistoia area.

Existing studies and proposed hypothesis have not yet been able to identify the effective causes of the instability phenomena and many doubts on the subsidence dynamics in Pistoia area still persist. Because of this, there is a growing need to deeply analyze the interaction between hydrogeologic systems and land surface dynamics processes, in order to improve the knowledge of the phenomenon and to find the best strategy to reduce the risk associate with it.

Simulation tools for characterizing, understanding, and predicting response of aquifer systems to stresses imposed by groundwater use can be very useful in this regard.

The use of numerical groundwater models to simulate changes in piezometric levels and related ground deformation, together with satellite interferometry that detects surface movements, represent a global

approach to assess main aquifer issues. These techniques have been used to identify subsidence related to groundwater withdrawal and calibrate hydrogeological parameters (Bozzano et al., 2015; Burbey and Zhang, 2015). Ezquerro et al. (2017) presented a hydrogeologic model to reproduce groundwater evolution of the Alto Guadalent´ın basin (Spain). Then, they compared model results with ENVISAT satellite data, detecting a direct relationship between groundwater changes and surface deformation. Arjomandi et al. (2018) developed a MODFLOW model of Tehran plain (Iran) to estimate and predict the rate of land subsidence in the area, calibrating its results by means of synthetic aperture radar method.

The assessment of the effects of climate, natural processes and human activities on freshwater availability requires the development and the implementation of a numerical model that considers all the components of the hydrologic cycle with a holistic approach. The hydrologic cycle in terrestrial environment includes the entire system of processes that occur within atmosphere, land surface and subsurface. Traditional modelling approaches used to represent only one hydrological reservoir in detail, without explicitly consider links and interactions between the others (Mugunthan et al., 2017). In some cases, where large dynamic fluxes between the two systems occur, natural systems cannot be adequately modelled using an uncoupled approach, that can lead to evident discrepancies and mismatches in terms of water budget definition. Nowadays, the interaction between groundwater and surface water is one of the major concerns in water resources management field, as almost all surface water bodies interact with groundwater. Even in systems where exchanges between river network and groundwater surface are very limited, aquifers are affected by infiltration from irrigation and river discharge, in long term steady state condition. Therefore, surficial and groundwater reservoirs need to be treated as a single coupled system when looking at water quantity and water quality issues.

The integration of groundwater and surface processes in a single coupled model is still an active field of research. Early work focused on integrating surficial streamflow models with underground fluxes models had the primary focus on water exchanges (Swain and Wexler, 1996). However, to more accurately simulate the complete system of interaction occurring between these two systems, the entire set of natural processes occurring in the hydrologic cycle need to be considered. Several existing models with groundwater - surface water interactions simulation capability have been proposed in literature during the last three decades, with different nature and structures (Furman et al., 2008).

Generally, three main approaches can be used in designing integrated models: iterative, simultaneous and time lagged solutions (Huang and Yeh, 2009). In the simultaneous solutions approach, known also as fully coupled approach, surface and subsurface fluxes are linked each other by solving the governing equations of the two systems at the same time (Panday and Huyakorn, 2004). The iterative or coupled regions approach, divides groundwater and surface water systems into separate reservoirs and solves the governing equations in each region by means of iterative numerical methods (Sophocleous and Perkins, 2000). Time lagged solutions concern the use of a loosely coupled modelling approach, combining two different existing models (one for surface water and one for groundwater) that are connected in order to simulate the entire system of hydrological processes within the studied watershed (Langevin et al. 2005, Yuanyuan et al, 2013). With this procedure, models are linked unidirectionally by using output information of the surface water model as input for the groundwater model, or vice versa. Although iterative and simultaneous approach-based models can better capture flow dynamics and local variations of surface and subsurface water fluxes, these models experience many limitations, especially in terms of increased complexity of the model domain, computer code, data requirements, and computational time. Moreover, even if they can provide important information about water resources, construction of input data sets for fully and coupled modelling approaches are not well formalized or automated, making their reproducibility very difficult (Gardner et al., 2018). Time lagged

solution models, on the other side, even if they do not guarantee the accuracy of the coupled solutions, represent a simpler practical tool in the integrated hydrological modelling field, providing an inexpensive way to combine the advantages of both models without the need of excesses simplifications.

An integrated hydrologic model called GSFLOW (Groundwater and Surface water FLOW), was developed by USGS to simulate coupled groundwater and surface water systems (Markstrom et al., 2008). The model is based on the integration between the U.S. Geological Survey Precipitation-Runoff Modeling System (PRMS) and the U.S. Geological Survey Modular Ground-Water Flow Model (MODFLOW, Mcdonald and Harbaugh, 1984). The Precipitation-Runoff Modeling System (PRMS) is a semi-distributed hydrologic model in which the watershed domain is discretized into many hydrologic response units (HRUs). The discretization may be based both on hydrologic and geomorphologic properties of the watershed (such as land use, slope, soil type, etc.). HRUs are normally defined by lumping hydrological and physical characteristics of the studied basin, that are considered to be homogeneous within each HRU. Water and energy balances are computed for each HRU.

Most of the newest works concerning the use of coupled groundwater – surface water models usually refer to the SWAT-MODFLOW code, an open source model that links SWAT (Soil and Water Assessment Tool, Arnold et al., 1998) with the newest versions of MODFLOW. SWAT code alone has no mechanism to solve the groundwater flow equations in porous media, and its integration with MODFLOW make it able to simulate the dynamic behavior of underground fluxes with good precision and accuracy. In literature, there are many works in which SWAT and MODFLOW are coupled together, in order to simulate the interaction between groundwater and surface water with a fully combined approach.

Kim et al., 2008 developed an integrated SWAT-MODFLOW model for estimating groundwater recharge, based on water-balance components, to the Musimcheon Basin in Korea. Their application demonstrates that integrated modelling procedures are capable of simulating the distribution of groundwater recharge rates, aquifer evapotranspiration and groundwater levels both in time and space domain. Velazquez et al. (2015), by means of an integrated modeling framework of SWAT-MODFLOW-MT3DMS, studied the potential impacts of climate change and land use variation in an irrigated surface water-groundwater system that consider groundwater quality and quantity. Bailey et al. (2016) apply SWAT-MODFLOW code to explore the spatial-temporal patterns of groundwater discharge to a river system in a semi-arid region in Oregon, USA. Ehtiat et al., 2018 use the model to analyze the status of groundwater system, depending on the conditions of land and surface water, in Dehloran Plain (Iran), where a confined alluvial aquifer represents the only source of freshwater for potable water supply and agricultural activities.

SWAT model guarantees an arbitrary temporal discretization, giving the possibility to choose sub-daily to yearly time steps for hydrological simulations but, as well as PRMS for GSFLOW, it computes water and energy balance equations using a semi-distributed approach by means of Hydrologic Response Units (HRUs). Lumped nature of the code represents a huge limitation for semi-distributed models. This kind of approach, compared to a fully distributed model, it is easier to setup and require shorter time and computational burden, but considers the spatial variability only partly, with all the hydrological variables represented by a unique value for each HRU. The implementation of HRUs, in fact, do not guarantees a homogeneous distribution of hydrological and geomorphological properties all over the simulated domain, leading to the need of great simplifications in terms of watershed geo-hydrologic characteristics.

Most coupled models, included those not treated previously, use as basic code for groundwater system simulation, the USGS's Modular Ground-Water Flow Model MODFLOW. MODFLOW is one of the most widely used and tested groundwater flow code, for its capabilities in solving the three-dimensional groundwater flow equation in the saturated medium and in estimating the groundwater interaction with surface water.

Although MODFLOW was originally developed to only simulate groundwater flows, its modular structure allowed the implementation of additional simulation capabilities. The program has been widely improved in the last 25 years and currently can be also used to simulate solute transport, flows in the unsaturated zone, parameter estimation and aquifer system compaction.

It is quite hard to say in absolute which kind of model performs better, since both semi-distributed and fully distributed could give good results, depending on the modelling purpose and on the characteristics of the simulated area. Reed et al. (2004) state that very often lumped models are more suitable than distributed models in the hydrologic field, while Carpenter and Georgakakos (2006) attribute better modelling performances to fully distributed models in surface water processes analysis. El-Nasr et al. (2005), according to Refsgaard and Knudsen (1996), reports that after a good calibration phase both semi-distributed and fully distributed give acceptable results in simulating watersheds hydrology.

Fully distributed models require greater simulation and calibration time than semi-distributed models and need higher quality input data, making them harder to configure, especially in region with lack of widespread detailed information. However, fully distributed models are capable to better capture the spatial distribution of input variables, including meteorological conditions and physical parameters of the modelled domain, enabling to perform deeper analysis of involved hydrologic processes.

2.1 Motivation of the research

Groundwater overexploitation and depletion of aquifers represent a challenging issue that impacts many areas of the World, especially during dry seasons and in arid regions. Water obtained from aquifers is considered one of the main sources of freshwater for drinkable and agricultural purposes and its uncontrolled usage can lead to many long-term consequences. Ground subsidence related to water levels decreasing is a common hazard especially occurring in large alluvial basins filled up with hundreds of meters of fine and compressible sediments, that can lead to several social and economic repercussions. Therefore, groundwater management policies for the sustainable use of the resource are needed, in order to reduce the effect of the phenomena associated with its over exploitation.

Firenze – Prato – Pistoia basin (Tuscany region, central Italy) has a long experience of land subsidence and ground deformation, that has been observed in the area since the early 1960s. During the last three decades, with the development of InSAR technique, it has been possible to better analyze and identify ground displacement patterns occurring in Firenze-Prato-Pistoia basin, to characterize the effect of subsidence on structures and environment. Many studies ascribe Firenze – Prato – Pistoia basin subsidence to the over exploitation of groundwater resources, but neither quantitative analysis nor numerical modelling has been carried out so far to deeply investigate their relation. In last 20 years, PS-InSAR data identified a substantial decreasing of ground deformation patterns all over the basin. However, Pistoia area keeps showing alarming subsidence rates, enhancing the importance of clearly identify the causes of the phenomenon, to reduce the risk associated with it. In recent times, Ezquerro et al. (2020) performed two damage assessment surveys in the city of Pistoia, in order to detect the extent of damage of edifices that could be potentially ascribed to the ground displacement detected by Sentinel-1 PSI in last years. The study resulted in the identification of more than 200 buildings with different level of damage, demonstrating that the effect of subsidence in Pistoia city is active and cannot be neglected. However, the trigger mechanism of observed ground displacement was not completely investigated.

To prevent the occurrence of major problems, the development of adequate groundwater management strategies should be one of the main priorities for local authorities and policy makers. The use of numerical

groundwater models to identify the hydrogeological condition of an area, together with interferometric synthetic aperture radar (InSAR) data that detect ground surface displacement, provides a powerful tool to analyze aquifers threads and it was largely covered in literature in recent years (Ezquerro et al., 2018; Arjomandi et al., 2018). However, one of the biggest uncertainty found in the proposed methodologies is represented by the traditional approach of water resource modelling, that used to represent in detail the groundwater reservoir, simplifying the surface hydrology contribution only as boundary conditions of lower importance. Even in aquifers where fluxes between surface and groundwater are limited, in long term condition is essential to consider the entire hydrologic cycle as a single system, in order to quantify the water exchanges between different reservoirs (Mugunthan et al., 2017).

Many coupled surface water – groundwater models can be found in literature, but many of them use a semi-distributed approach to describe the hydrological and geographical features of the simulated watershed. Fully distributed models are harder to set up and to configurate, but they guarantee a more realistic representation of the spatial distribution of the input variables all over the model domain.

In the present study, in order to identify the causes of subsidence phenomena that are still affecting Pistoia area and to reduce the risk associated with their potential consequences, a numerical model of the Pistoia aquifer was developed. The model is based on an integrated simulation developed combining the USGS's finite difference groundwater model MODFLOW (McDonald and Harbaugh 1984; Harbaugh et al. 2000) with MOBIDIC hydrologic model (Castelli et al., 2009; Campo et al., 2006).

The integrated methodology has been developed and firstly tested in the alluvial basin of Pesa river (central Tuscany) to prove its validity, and then it has been applied to simulate the water processes dynamic in Pistoia basin. Once the hydrologic model has been calibrated and validated, subsidence affecting the area has been modelled, by means of MODFLOW capabilities in simulating aquifer compaction. Finally, high spatial and temporal resolution subsidence observations from satellite InSAR and available hydraulic head have been used to inversely calibrate transmissivities (T), elastic and inelastic skeletal storage coefficients (Ske and Skv) of the Pistoia aquifer. The comparison between model results and field data demonstrated the benefits of using direct subsidence measurement in the characterization of aquifer properties values when detailed and complete hydraulic head measurements are poorly available. Moreover, the calibration procedure provides important information about the identification of reliable storage coefficients values, that can be used to evaluate how the anomalous ground displacement rate of Pistoia area is affected by the combined effect of groundwater extraction and the presence of compressible fine sediments.

The understanding of how global change affects water resources around the world is limited. Potential impacts of climate variation on surface water have been studied in detail by some authors (Green, 2016; Shrestha et al., 2016). However, studies of how subsurface waters will respond to the combined effect of climate change and human activities have started only in last decade (Green et al. 2011; Taylor et al. 2013; Burbey et al., 2015). Our present knowledge provides abundant evidences about the vulnerability of both surface and subsurface water resources to climate changes, including all the potential consequences for society and ecosystems (Bates et al. 2008). The assessment of climate change effects on groundwater conditions, even if essential in a long term hydrogeological analysis, can be very challenging, because climate variability may lead to direct and indirect repercussions on hydrogeological processes that can be difficult to quantify (Dettinger and Earman 2007). Increased variability in precipitation patterns and more extreme weather events caused by climate change can lead to longer periods of droughts and floods, which directly affects availability of groundwater. In long periods of droughts there is a higher risk of groundwater depletion, especially in locations that strictly depend on subsurface water for freshwater supplying. At the same time, indirect climate change impacts such as the intensification of human activities and/or

modifications in land use may result in the increase of groundwater demand. This can be very impactful for highly stressed aquifers, where a further increasing of external loads can lead to a worsening of their current conditions and of related problematics.

Global Climate Models (GCMs) and Regional Climate Models (RCMs) are the most powerful tool for simulating future climate scenarios, providing all the basic information needed for climate change impact assessment. GCMs and RCMs output have been used in this study as input data to perform hydrologic forecasting with MOBIDIC model for the next decades. Then, applying the presented integrated modelling approach and by means of the calibrated subsidence model built with MODFLOW code, future predictions of land subsidence affecting Pistoia area in the years to come have been performed, based on different pumping rate and water dynamics scenarios.

In order to detect the level of damage affecting buildings in Pistoia city caused by subsidence effects, two surveys campaigns were carried out. By means of the combination between damage information and ground displacement rate detected by means of PS-InSAR data, fragility curves of the surveyed buildings have been developed. Damage fragility curves were used to generate the subsidence vulnerability map of Pistoia city, in order to identify the damage probability distribution of building and structures as a function of ground displacement patterns.

Finally, using the forecasted subsidence rate obtained by GCMS and RCMs simulations and the developed fragility curves for the area of interest, it has been possible to define the potential damage probability distribution that could affect Pistoia city in the future (Figure 7).

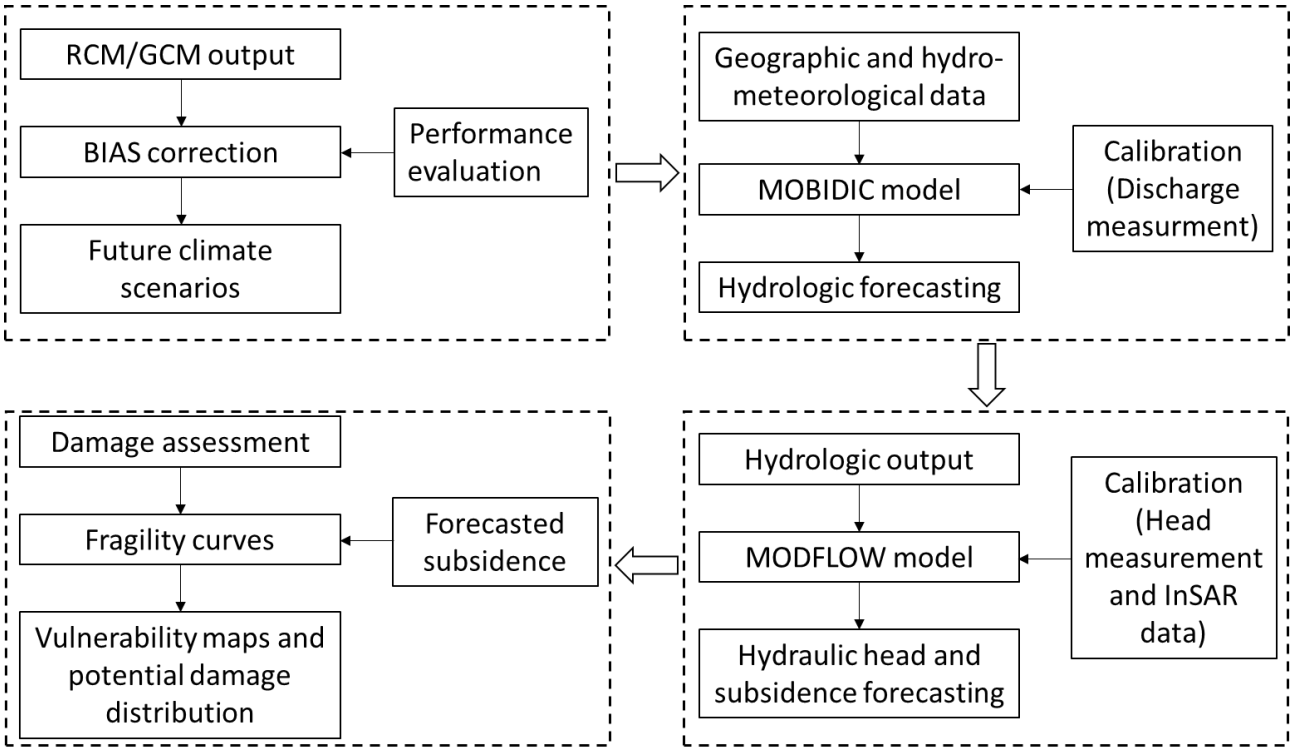

Figure 7 – Workflow of the research project

Land subsidence in Pistoia area is still an active and evolving phenomenon, and the analysis of potential ground displacement patterns that could affect the area in the future, as a result of the combined effect of climate variations and changing in groundwater withdrawal patterns, may represent a valuable tool for urban planners and policy makers. This research represents one of the first attempt to investigate the spatial and

temporal evolution of subsidence induced by groundwater levels variations considering the combined effect of hydrogeology, surface hydrology processes and climate changing effects at basin scale. Such effects are commonly neglected by many authors in literature, but they can represent an impactful variable in long term hydrogeologic simulations. Furthermore, subsidence modelling performed along the study can represent a valuable tool for urban planners and authorities for the identification of the most susceptible areas within the basin and for risk assessment analysis.

3 Materials and methodologies

3.1 Groundwater models

Mathematical groundwater models are the most powerful tools to simulate and predict aquifers condition and groundwater flows, modelling the behavior of the natural system by means of a governing equation and a set of boundary and initial conditions.

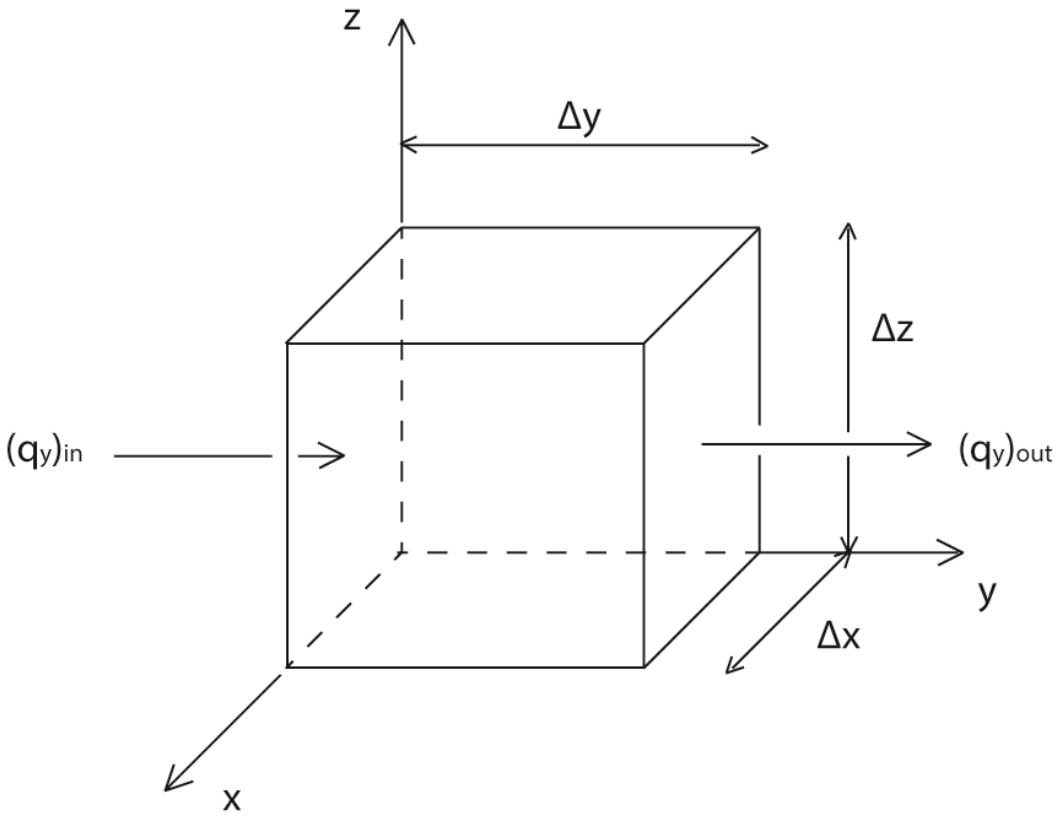

Figure 8 – Representative elementary volume (REV)used in the derivation of groundwater models governing equation

The mathematical equation that describe groundwater flow has been developed starting from the fundamental principle of conservation of mass of fluid. Given a representative elementary volume (REV, Figure 8) of a cube of porous material, a general equation for conservation of mass for that volume is expressed as:

$$\text{Rate of inflow - Rate of outflow = Rate of change} \quad (1)$$

Flow along the y-axis of the REV occurs through the face $\Delta x \Delta z$ and is equal to $q_{yIN} - q_{yOUT}$:

$$(q_{yIN} - q_{yOUT})\Delta x \Delta z = change\ in\ storage \quad (2)$$

That can also be wrote, dividing by Δy, as:

$$\frac{\left((q_{yIN}-q_{yOUT})\right)}{\Delta y}\Delta x\Delta y\Delta z = change\ in\ storage \tag{3}$$

So, the flow rate through the REV along the y-axis is:

$$\frac{\partial qy}{\partial y}(\Delta x\Delta y\Delta z) \tag{4}$$

The total change in flow rate along the 3 directions of the REV can be expressed as:

$$\left(\frac{\partial qx}{\partial x}+\frac{\partial qy}{\partial y}+\frac{\partial qz}{\partial z}\right)\Delta x\Delta y\Delta z = change\ in\ storage \tag{5}$$

Inside the REV it might be possible the presence of a sink or a source of water, represented by R $\Delta x\Delta y\Delta z$. R is considered to be positive when water is added to the REV and negative when water is removed:

$$\left(\frac{\partial qx}{\partial x}+\frac{\partial qy}{\partial y}+\frac{\partial qz}{\partial z}-R\right)\Delta x\Delta y\Delta z = change\ in\ storage \tag{6}$$

Considering the right side of the equation, change in storage is represented by Specific Storage Ss, which is defined as the volume of water removed from a unit volume of aquifer for a unit drop in hydraulic head:

$$Change\ in\ storage = S_s = -\frac{\Delta V}{\Delta h\Delta x\Delta y\Delta z} \tag{7}$$

The rate of change in storage is:

$$\frac{\Delta V}{\Delta t} = -S_s\frac{\Delta h}{\Delta t}\Delta x\Delta y\Delta z \tag{8}$$

Combining this term with the left side of the previous equation and dividing by $\Delta x\Delta y\Delta z$, the final form of the water balance equation is obtained:

$$\frac{\partial qx}{\partial x}+\frac{\partial qy}{\partial y}+\frac{\partial qz}{\partial z} = -S_s\frac{\partial h}{\partial t}+R \tag{9}$$

This equation is not very handy, because flow discharge in the aquifer q is very hard to measure. Thus, Darcy's Law is used in order to relate flow discharge with hydraulic heads, *h*, by means of:

$$q_x = -K_x\frac{\partial h}{\partial x} \tag{10}$$

Finally, the general groundwater flow equation can be written as:

$$\frac{\partial}{\partial x}\left(K_x \frac{\partial h}{\partial x}\right) + \frac{\partial}{\partial y}\left(K_y \frac{\partial h}{\partial y}\right) + \frac{\partial}{\partial z}\left(K_z \frac{\partial h}{\partial z}\right) = S_s \frac{\partial h}{\partial t} - R \tag{11}$$

Where K is the hydraulic conductivity, *R* are input and/or output fluxes and S_s is the specific storage.

The groundwater flow equation is a second order differential equation that can be solved analytically when particular condition occurs, or it can be approximated by means of numerical methods. In groundwater modelling, finite elements and finite difference methods represent the most used and widespread numerical methods for second order differential equations solving. Both methods discretize the spatial domain in grid of cells of various shape but differ for a fundamental difference. Finite difference method computes a value for the head at the center of each cell which also is the average head of the entire cell. Finite elements, on the other hand, calculates hydraulic head at the nodes of the elements and then define it everywhere by means of interpolation functions.

Every model requires an appropriate set of boundary conditions to represent the simulated system's relationship with the surrounding environment. In case of a groundwater flow model, boundary conditions will describe the exchange of flow between the model and the external system. Boundary conditions fall into one of the three following categories: specified head or Dirichlet, specified flux or Neumann and mixed or Cauchy boundary conditions.

Type 1 – Specified head boundary conditions: for which head is given and constant in time;

Type 2 – Specified flux boundary conditions: for which the derivative of head across the boundary is given;

Type 3 – Head-dependent flow boundary conditions: for which flux across boundary is calculated, given a boundary head value.

3.1.1 MODFLOW code

MODFLOW is the USGS's three-dimensional finite-difference modular groundwater model. In MODFLOW the groundwater flow equation is solved using a block-centered finite-difference approach, dividing the horizontal modelled domain into a grid constituted of an arbitrary number of rectangular cells. Each cell position in the grid is defined by three number, representing its position in the j-row, k-column and n-layer (Figure 9). Geological variability of the modelled system is represented by dividing its vertical domain into different layers, that can be simulated as confined or unconfined. The modular structure of the MODFLOW code consists of a main program and a series of independent subroutines. The subroutines are grouped into "packages." Each package deals with a specific feature of the hydrologic system that can be simulated, such as flow from rivers or flow into drains, or with a specific method of solving the set of simultaneous equations resulting from the finite-difference method.

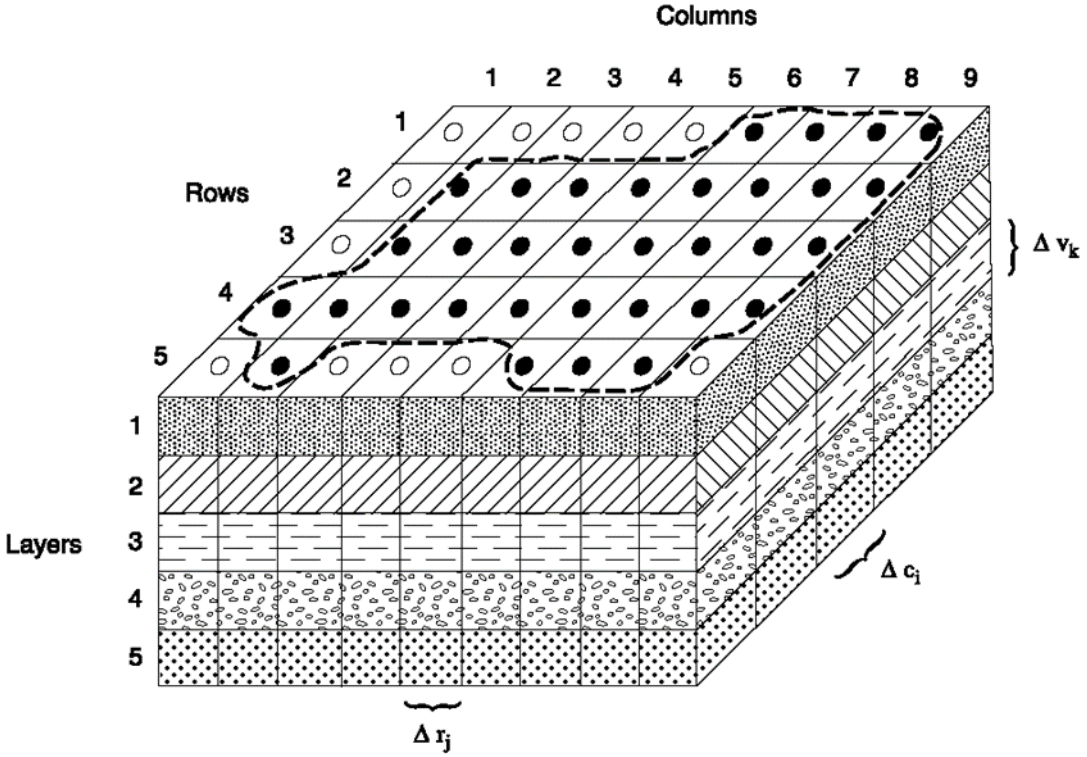

Figure 9 – Horizontal and vertical discretization of model domain in MODFLOW

3.1.2 MODFLOW boundary conditions

Rivers (RIV package)

The river boundary condition (defined in MODFLOW by the RIV package) is a third type head-dependent boundary condition. In a river cell, the flow of water into or out of the aquifer is dependent on the head assigned to the river and the conductance term. The head, corresponding to the water stage of the river, is compared to the computed head in the aquifer for the cell in which the river condition is contained. If the aquifer head is higher than the river head, then the river removes water from the aquifer and viceversa.

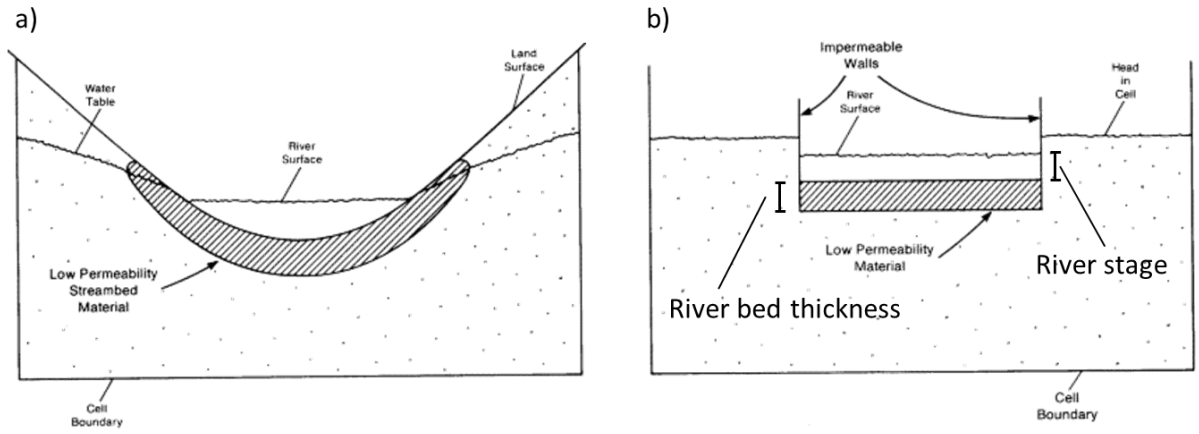

Figure 10 – a) Real configuration of a river section and b) MODFLOW RIVER package discretization (modified from http://inside.mines.edu)

The amount of water exchanged is based on the conductance term, computed by the RIV package as follows:

$$C = \frac{KLW}{D} \tag{12}$$

Where K is the hydraulic conductivity of the river bed material, L and W are respectively the length and the width of the river in the selected cell and D is the thickness of the river bed material (Figure 10).

Wells (WEL package)

The WEL package represents a second type boundary condition and it is used in MODFLOW to simulate pumping and injection wells. Wells are simulated as specified flux boundary conditions, in which only the amount of water extracted from or injected into the model need to be specified.

Recharge (RCH package)

Recharge represents the infiltration of water from precipitation into the aquifer and it is simulated in MODFLOW with the RCH package. In models that do not simulate explicitly the evapotranspiration, recharge represents the net amount of water that reaches the aquifer (percolation). On the other hand, when evapotranspiration is computed in MODFLOW, the recharge should represent total amount of water that infiltrates from the land surface.

General Head Boundary (GHB package)

The GHB (General Head Boundary) boundary condition is a head-dependent boundary condition usually set at the edges of the model domain where there are no natural groundwater or known hydraulic boundaries.

As for the RIV package, GHB allows groundwater to move either into or out from the model domain, depending on groundwater elevation changes along the boundary and it can approximate the hydraulic response of model boundaries to the groundwater condition variations.

The amount of water removed is based on the conductance term, calculated similarly to the RIV boundary condition conductance, by the following equation:

$$C = \frac{K\ Thick\ W}{D} \tag{13}$$

The only difference is represented by the variable Thick, which represents the saturated thickness of the aquifer in the considered cell, and by the variable D, which is the distance of the GHB head (considered external to the modell domain) from the model boundary.

No flow boundary (NO FLOW)

No-flow boundaries are used in MODFLOW to model inactive cells, that are cells not considered during the numerical resolution of the groundwater flow equation. These cells are used to represent irregular shaped borders of model domains in a regular grid environment.

3.1.3 Subsidence (SUB package)

Land subsidence related to the compaction of aquifer systems is a common hazard in many areas of the world subjected to groundwater extraction. Whenever a groundwater pumping system is set up in a natural aquifer, most of the water comes initially from the more permeable layers of aquifers. Then, when hydraulic heads in the aquifers are lowered, vertical fluxes from confining units and interbeds start to establish, with water flowing from these lower permeability layers to the aquifers. Interbeds are low permeability clayey or silty layers of an aquifer characterized by high compressibility and an insufficient lateral extent to be considered as confining unit, but large enough to assume their thickness negligible. Interbeds hydraulic conductivity is much lower than hydraulic conductivity of surrounding sediments, but it is high enough to allow vertical water fluxes in response of a hydraulic head variation (Figure 11).

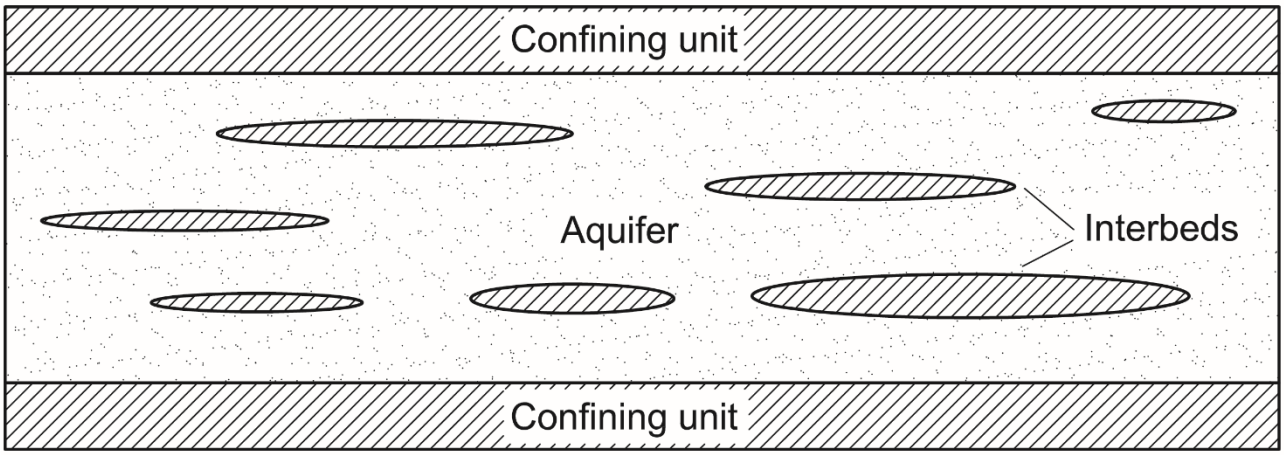

Figure 11 – Low permeability interbeds inside a coarse-grained aquifer confined at its top and bottom

When groundwater exploitation becomes large in magnitude and in extent, a significant percentage of pumped water can become from interbeds and confining units storage (Poland et al., 1975). Removing water

from fine layers can result in a compaction of silty and clayey sediments, leading to land subsidence phenomena. Depending on the stress history of the sediments, compaction can occur elastically or inelastically, with relative recoverable or not recoverable subsidence.

Simulation tool for predicting groundwater system behavior in response to stress variation are needed to improve the understanding of these complex phenomena and to improve the sustainable management of groundwater resources. With the development of computer sciences, many numerical models have been developed in last decades in order to simulated aquifer systems compaction. First studies presented by Gambolati (1970), Helm (1975), Narasimhan and Witherspoon (1977), and Neuman et al. (1982) introduced one-dimensional compaction models to analyze aquifers thickness variation at borehole extensometers, where many information of compaction and hydraulic head changes were available. One of the first three-dimensional subsidence simulation tool, known as Interbed Storage Package, version 1 (IBS1), was developed by Leake and Prudic (1991) and implemented in the USGS' groundwater model MODFLOW. IBS1 assumes that hydraulic heads in interbeds equilibrate instantaneously with head changes in aquifers or with a short time if compared with the model time step. To eliminate this assumption, Hoffmann et al. (2003) developed an additional package for MODFLOW-2000 (Harbaugh et al., 2000), known as the Subsidence and Aquifer-System Compaction Package (SUB package), that allows to directly simulate the interbeds hydraulic heads dissipation process.

Effective stress and stress changes

Sediments compaction and groundwater flow equations are coupled together by means of the Terzaghi principle of consolidation, stating that all changes in soil total stress are directly related to changes in effective stress or changes in pore pressure (Terzaghi, 1925):

$$\sigma = \sigma' + p \tag{14}$$

Where σ' is the effective stress, p is the pore water pressure and σ is the total stress. The latter, is the result of the geostatic load caused by overlying sediments and tectonic stress.

MODFLOW SUB package works with the assumption that the total stress remains constant in time, considering only confined aquifers with a constant geostatic load ($\Delta\sigma = 0$). Moreover, since changes in pore water pressure gradient within the interbeds and resulting strains are mainly vertical, σ and σ' are both considered one dimensional.

In groundwater systems analysis, hydraulic head is the most common used variable rather than pore water pressure. Hydraulic head is given by the sum of pore pressure and the elevation head, as following:

$$h = \frac{p}{\rho_w g} + h_e \tag{15}$$

Where h is the total hydraulic head, ρ_w is the density of water, g is the gravitational acceleration and h_e is the elevation head from a reference datum.

In an unconfined aquifer, a variation in hydraulic head correspond to a change of the position of water table, with the resulting variation in the geostatic load and in the pore water pressure. This represents a change in the total stress of all underlying sediments.

Effective stress change, as a result of hydraulic head variation in an unconfined aquifer, can be described by Poland and Davis (1969) equation:

$$\Delta\sigma' = -\rho_w g(1 - n + n_w)\Delta h \tag{16}$$

Where $\Delta\sigma'$ is the change in effective stress (vertical), n is the aquifer porosity, n_w is the water content in the part of aquifer above the water table, as a fraction of total volume, and Δh is the change in hydraulic head.

The SUB package was developed to simulate sediments compaction in confined aquifers. For unconfined aquifers, where total stress variation as a result of change in the position of water table occurs, this package overestimate effective stress change by the $(1 - n + n_w)^{-1}$ factor.

In a confined aquifer, water is released from or is taken into storage as a result of compression or expansion of the porous sediments constituting the aquifers and of the water, with negligible change in total stress. Water density change as a result of water compression or expansion is negligible as well. Thus, effective stress variation in a confined aquifer for a certain hydraulic head change is given by:

$$\Delta\sigma' = -\rho_w g\Delta h \tag{17}$$

Sediments compressibility

The amount of expansion or compaction of aquifers sediments in response of effective stress changes depends of sediment compressibility, as defined by:

$$\alpha = \frac{-\frac{\Delta V}{V}}{\Delta\sigma'} \tag{18}$$

Where α is sediments compressibility and $\frac{\Delta V}{V}$ is the change in volume with respect of initial volume V.

Considering only one-dimensional compressibility, change in volume can be represented as change in interbeds thickness *b*, obtaining:

$$\alpha = \frac{-\frac{\Delta b}{b}}{\Delta\sigma'} \tag{19}$$

Combining (4) and (6) and considering that change in effective stress is only related with change in pore water pressure, equation (7) is given by:

$$\rho_w g\alpha b = S_{sk} b = S_k = \frac{\Delta b}{\Delta h} \tag{20}$$

Where S_{sk} is the skeletal specific storage, defined as $\rho_w g\alpha$ and S_k is the skeletal storage coefficient defined by $S_{sk}b$.

Compressibility, and skeletal specific storage as well, can assume a wide range of values depending on the amount of effective stress to whom aquifers sediments are subjected, compared with the previous maximum effective stress (known as the preconsolidation stress, Casagrande (1936).

If the new effective stress remains lower than the preconsolidation stress, a variation in hydraulic head (and in effective stress) causes small elastic compaction. These deformations are completely recoverable if the effective stress return to its previous value.

If the effective stress becomes bigger than the preconsolidation stress, inelastic compaction occurs, with a rearrangement of sediments structure and permanent deformations. In order to take into account the big differences between values that skeletal coefficient can assume as a consequence of exceedance, or not, of the preconosolidation stress, two different values of S_{sk} are commonly used:

$$S_{sk} = \begin{cases} S_{ske} \; for \; \sigma' < \sigma_{max} \\ S_{skv} \; for \; \sigma' > \sigma_{max} \end{cases} \tag{21}$$

Where S_{ske} is the elastic skeletal specific storage, S_{skv} is the inelastic skeletal specific storage and σ_{max} is the preconsolidation stress.

Time Delays

Since fine sediments constituting the interbeds are characterized by a very low vertical hydraulic conductivity, the equilibration of hydraulic heads within the interbeds is usually delayed compared with head changes in the aquifers. Because thickness of interbeds is much smaller than their lateral extension, water fluxes through them can be considered vertical and heads equilibration time lags can by simulated by the following one-dimensional equation:

$$\frac{\partial^2 h}{\partial z^2} = \frac{S_S'}{K_v'} \frac{\partial h}{\partial t} \tag{22}$$

Where *z* is the vertical spatial coordinate, S_S' is the specific storage of the interbed, K_v' is the vertical hydraulic conductivity and *t* is time. The $\frac{S_S'}{K_v'}$ ratio represents the vertical hydraulic diffusivity of the interbed, D'. The time delay necessary to equilibrate the hydraulic heads inside interbeds τ_0, at which 93% of total compaction has occurred (Riley, 1969), is given by:

$$\tau_0 = \frac{\left(\frac{b_0}{2}\right)^2 S_S'}{K_v'} = \frac{\left(\frac{b_0}{2}\right)^2}{D'} \tag{23}$$

No-Delay Interbeds

No-delay interbeds represent interbeds in which time delay τ_0 is very short, compared with the simulation time step. In such a case, hydraulic head dissipation time is not considered and the assumption that heads within interbeds equilibrate instantaneously with aquifers heads is made. This was the theory at the base of the old IBS1 package, that calculates flow per unit volume through interbeds as:

$$q = \gamma S_{sk}' \frac{\partial h}{\partial t} \quad with \quad S'_{sk} = \begin{cases} S'_{ske} \; for \; h > h_{min} \\ S'_{skv} \; for \; h < h_{min} \end{cases} \tag{24}$$

Where h_{min} is the lowest previous hydraulic head and γ is the volume fraction of compressible interbeds inside aquifers.

Delay Interbeds

Delay interbeds indicate interbeds in which time delay τ_0 is grater than simulation time step and that need for the heads dissipation in the interbeds to be calculated. This is made by solving the equation (22) by means

of numerical methods for each time step of the simulation. Since the modelled aquifers can be characterized by the presence of several interbeds of different thickness, solving equation (22) for every single interbed can be computationally prohibitive. In order to reduce the computational burden, delay interbeds with the same hydraulic conductivity and elastic and inelastic skeletal storage coefficients can be joined and simulated together. Thus, every interbed group is characterized by a single hydraulic conductivity, two values of elastic and inelastic skeletal storage coefficients and an equivalent thickness calculated by Helm (1975) equation:

$$b_{equiv} = \sqrt{\frac{1}{N}\sum_{i=1}^{N} b_i^2} \tag{25}$$

Where N is the number of delay interbeds with thickness bi in the considered group.

To simulate the same amount of interbeds and the correct magnitude of compaction for each group of delay interbeds, the SUB package multiplies the calculated compaction and the exchanged water with surrounding aquifers by:

$$n_{equiv} = \frac{\sum_{i=1}^{N} b_i}{b_{equiv}} \tag{26}$$

Model assumption and limitations

The described MODFLOW SUB package is a very important tool to simulate aquifers sediments compaction due to groundwater withdrawal in subsidence susceptible area. Of course, since the SUB package is a computer code that models a quite complex phenomenon, some assumption and simplifications have to be made.

Since geostatic load variations are not considered by the SUB Package, only changes in effective stress caused by changes in fluid pore pressure can be simulated. On short time scales (years to decades), geostatic load changes may occur for the presence of new buildings or engineered structures and/or by changes in water levels in overlying unconfined aquifers. On longer time scales (centuries), changes in geostatic stress due to erosion or sedimentation may also become important.

The SUB Package assumes that elastic and inelastic skeletal storage coefficients and vertical hydraulic conductivity do not vary with stress for the temporal range of the simulation. In reality, the dependence of these parameters on stress may be important, particularly for shallow aquifer systems where the total stresses are small.

Since neither interbeds nor model layers thickness are adjusted to account their compaction during the simulation, the SUB package also assumes that compaction of individual interbeds is small if compared with their total original thickness. Layers thickness is fixed during the development of the groundwater model and it does not change even if subsidence occurs.

Another assumption concerns the geometry of interbeds, that are considered to be laterally extensive compared to their thickness, resulting that hydraulic gradients within the interbeds, as well as strains and displacements (compaction and expansion), are vertical only. However, especially in elastic media, even purely vertical gradients in hydraulic head may cause horizontal strains. Because horizontal strains are ignored in SUB package, the model could overestimate compaction in areas subject to horizontal compression.

3.2 MOBIDIC code

MOBIDIC (MOdello di Bilancio Idrologico DIstribuito e Continuo; Castelli et al., 2009; Campo et al., 2006) is a fully distributed and raster-based hydrological model for water balance calculation, qualitative and quantitative water resource assessment and flood risk management. MOBIDIC discretizes the horizontal domain by means of a square cells grid with arbitrary dimensions and the vertical domain into five different layers: (1) Surface canopy storage, (2) River system, (3) Gravitational and (4) Capillary storage and (5) Groundwater storage.

Figure 12 shows a schematic representation of MOBIDIC.

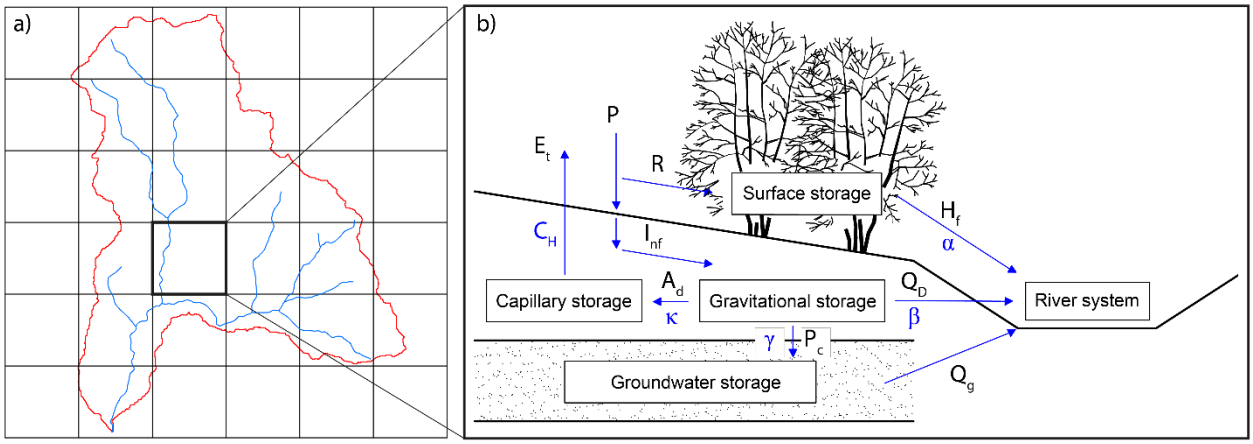

Figure 12 - Schematization of MOBIDIC model. a) Horizontal and b) vertical discretization of the domain, modified after Yang et al. (2014), where: P, precipitation; Et, evapotranspiration; R, surface runoff; Hf, hillslope flow; Inf, infiltration; Pc, percolation; QD, interflow; Qg, groundwater discharge; Ad, adsorption. Blue symbols represent some model parameters, where: α, hillslope flow coefficient; β, hypodermic flow coefficient; κ, adsorption flow coefficient; γ, percolation coefficient; CH, heat turbulent exchange coefficient. Rectangles represent the five model layers.

MOBIDIC approaches the energy balance by solving the heat diffusion equations in the soil–vegetation system, as following:

$$\rho_d C_d \frac{dT_0}{dt} = 2K_d \frac{T_d T_0 \frac{z_d G_{atm}}{K_d}}{z_d^2} \tag{27}$$

$$\rho_d C_d \frac{dT_d}{dt} = 2K_d \frac{(z_y - z_d)T_0 + z_d T_y - z_y T_d}{(z_y - z_d) z_y z_d} \tag{28}$$

Where: z_d and z_y are the thickness of the two layers in which the soil is subdivided (an upper part influenced by daily temperature variation, T_0 and a deeper part with constant temperature, T_y); T_d is the intermediate temperature between T_0 and T_y; C_d, K_d and ρ_d represent respectively soil specific heat, soil thermal diffusivity and soil density.

The ground heat flux G_{atm}, representing the loss of energy by heat conduction through the lower boundary, can be calculated as follows:

$$G_{atm} = R_{in} - R_{out} - H - LE \quad (29)$$

$R_{in} - R_{out}$ is the net surface irradiance, that represents the gain of energy by the surface from radiation and that is composed of an input and an output parameter, defined by:

$$R_{in} = (1 - A)R_s + \xi_a e_a \sigma T_a^4 \quad (30)$$

The left part of the equation represents the shortwave term, where A is surface albedo and R_s is the incident solar radiation; the right part of the equation represents the longwave term, estimated by the grey body law, where T_a, ξ_a and e_a are respectively air temperature, air emissivity and air humidity.

The output radiation is calculated considering only the longwave term of the previous equation:

$$R_{out} = \xi_s \sigma T_0^4 \quad (31)$$

Where T_0 is the surface temperature, as defined by the balance energy equation, and σ is the Stefan–Boltzmann constant.

Heat fluxes from the earth surface (soil and vegetation) are computed following a "bulk" heat transfer formulation in terms of temperature and humidity gradients between land surface and atmosphere:

$$H = \rho c_p C_H U(T_s - T_a) \quad (32)$$

$$L\,E = \rho L C_H U(q_s - q_a) \quad (33)$$

where H is the total heat flux, E is the evapotranspiration, U is windspeed, c_p is the air specific heat, L is the latent heat of vaporization and T_s/T_a and q_s/q_a are respectively temperature and humidity of soil and air.

C_H is the bulk transfer dimensionless coefficient for heat and includes the effects of both land surface characteristics (roughness and surface geometry) and atmospheric conditions (Van Den Hurk & Holstlag, 1997).

The water balance in the soil is carried out by dividing it into two different reservoirs, characterized by a capillary or a gravitational behavior. Water content of each reservoirs has an upper limit, defined respectively by their maximum water capacity W_{cmax} and W_{gmax}, and it varies in time with the following equations:

$$\frac{dW_g}{d_t} = I_{nf} - S_{per} - Q_d - S_{as} \quad (34)$$

$$\frac{dW_c}{d_t} = S_{as} - E_t \quad (35)$$

Where W_g and W_c are respectively the water contents in soil gravitational and capillary storage, I_{nf} is water infiltration, Q_d is the interflow, S_{per} is percolation through the aquifers and E_t is the evapotranspiration, considered to be driven only by capillary reservoir. The adsorption from gravitational to capillary storage S_{as} is an irreversible flux linked, by means of Ƙ parameter, to the capillary storage residual relative capacity:

$$S_{as} = \kappa \left(1 - \frac{W_c}{W_{cmax}}\right) \tag{36}$$

Percolation S_{per} and interflow Q_d fluxes are considered to be proportional to the gravitational storage, by means of γ and β parameters. γ and β depend on the saturated hydraulic conductivity K_s and on the grid cells dimension Δx, with the introduction of the global land calibration parameters γ*, β* and C*:

$$S_{per} = \gamma W_g \tag{37}$$

$$Q_d = \beta W_g \tag{38}$$

$$\beta = \beta^* \frac{K_s}{\Delta x} \tag{39}$$

$$\gamma = \gamma^* \left(\frac{K_s}{\Delta x} + C^*\right) \tag{40}$$

Where γ, β and κ are the percolation coefficient, the interflow coefficient and the soil adsorption coefficient, respectively. Finally, water infiltration through the soil is calculated as follow:

$$I_{nf} = \begin{cases} \left[P + (Q_d + Q_h + R_d)_{up}\right]\left[1 - exp\left(\frac{-K_s}{P+(Q_d+Q_h+R_d)_{up}}\right)\right] & \text{if } W_g < W_{gmax} \\ 0 & \text{if } W_g = W_{gmax} \end{cases} \tag{41}$$

Where P is precipitation, Q_h and R_d are Horton and Dunne runoff, K_s is the soil hydraulic conductivity and W_{gmax} and W_{cmax} are the gravitational and capillary storage maximum capacities.

Considering q_{up} as the surficial runoff flowing to the considered cell from the upstream cells, the surficial runoff is represented by the linear reservoir W_s, with unlimited capacity:

$$\frac{dW_s}{dt} = -\alpha_s W_s + R_H + R_D + q_{up} \tag{42}$$

α_s is the propagation coefficient, estimated for each grid cell as a function of the contributing upstream area and of the local slope:

$$\alpha_s = \frac{\alpha_0}{\Delta x}\sqrt{Ai} \tag{43}$$

With α_0 representing the hillslope flow calibration coefficient.

River network is represented in MOBIDIC as cylindrical vectors with fluvial discharge, simulated by means of the general Saint-Venant equation:

$$\frac{\partial Q}{\partial t} + c\frac{\partial Q}{\partial x} = \mu\frac{\partial^2 Q}{\partial x^2} + c(q_L + q_D + q_w) \tag{44}$$

Where q_L represents lateral affluxes (surficial runoff and subsurface flow), q_D is the interflow from the aquifers and q_w are output or input flows from withdrawal and/or water release.

3.3 InSAR technique

3.3.1 Radar

RADAR, Radio Detection And Ranging, is a tecnique that uses electromagnetic waves to determine the position and the velocity of fix or moving targets with high precision. A radar system is composed by a transmitter that produces radio waves, and a receiving antenna, able to capture echo waves reflected by the investigated object and to determine its position in time and space. The technology was originally developed for military uses, especially in combination with airborne systems, but in last decades it has been applied successfully also for civil and scientific purposes. Radar is an active remote sensing tecnique that can work both during day and night and independently by weather condition and illumination. Since it has the capability to investigate large regions of the Earth surface with few acquisitions, when combined with satellite constellation, RADAR tecnique obtained great success and wide application in geosciences for surficial processes monitoring. A radar system is capable to identify and distinguish targets only based on their reflected signal returning time, using a side-looking position of the investigated object in order to enlight only one side of ground range (Figure 13a). Radar can work with different bands of the electromagnetic spectrum and, depending on the needed penetration degree, several different wavelengths can be selected (Figure 13b).

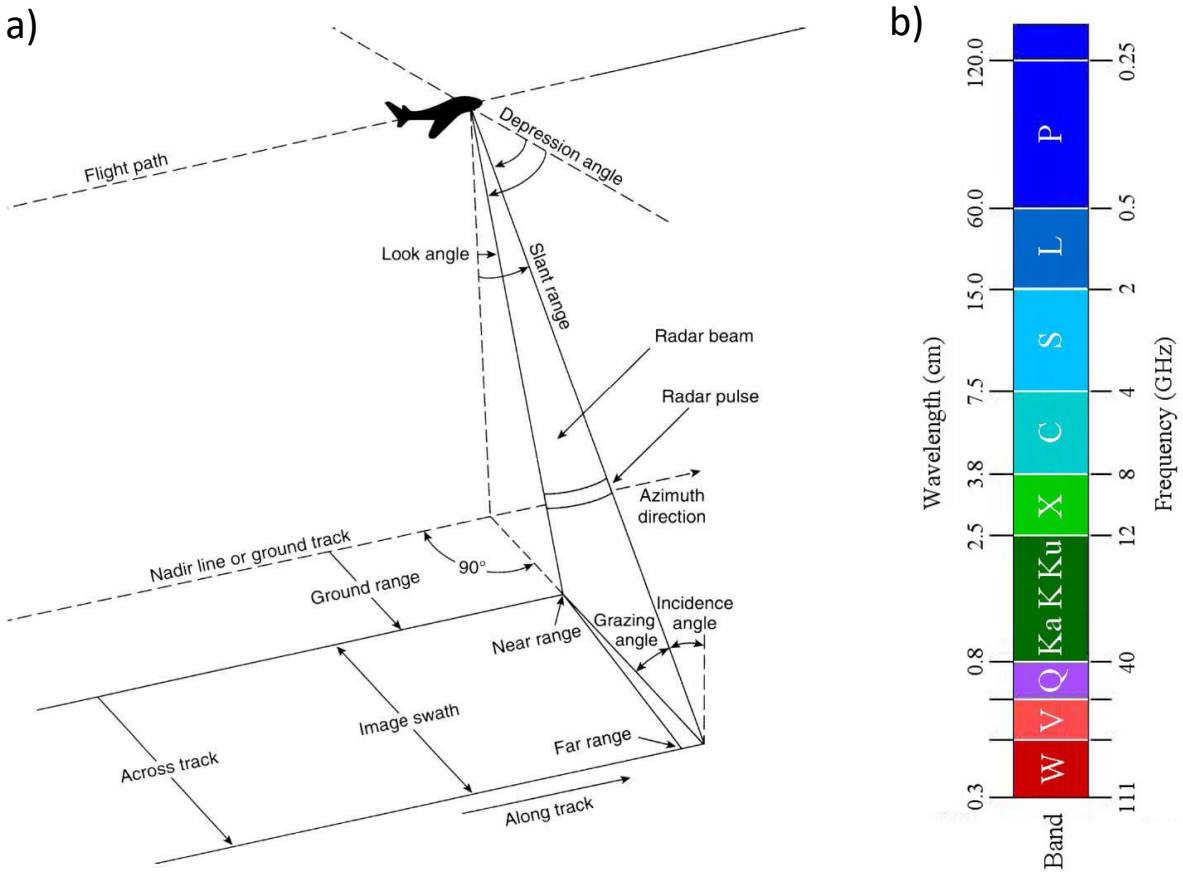

Figure 13 – a) Satellite radar geometry and b) radar microwave spectrum (Ouchi et al., 2013)

In radar geometry, *swath* is the monitored part of the Earth surface hit by the radar waves beam, characterized by a longitudinal extent depending on the transportation system motion and a width depending on the radar sensor characteristics. The *azimuth range* or *along track* is the direction along the trajectory of the moving system, while the *ground range* or *across track* is the perpendicular way. The

distance between radar antenna and monitored target, along the *Line of Sight* (LOS), is called *Slant range.* Since the radar has a *side-looking* geometry, when the microwaves beam hit the ground surface, two different incident angles can be distinguished (Figure 14). The *angle of incidence ss* is the angle between the radar waves direction and the vertical (depending only by the radar system), whereas the *local incidence angle* is the one between the radar waves and the surface normal, also depending on the local geometry of the Earth surface.

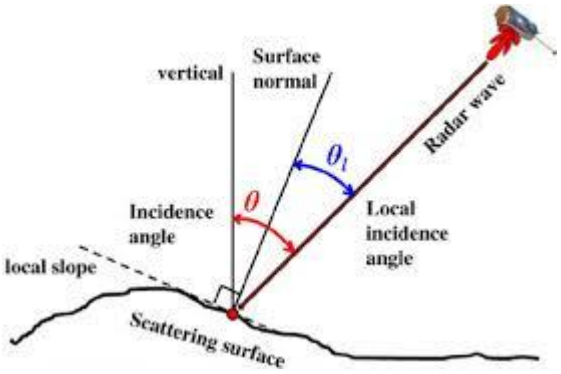

Figure 14 – Interaction between the LOS and the Earth surface geometry (Rizzoli and Brautigam, 2014).

3.3.2 Synthetic aperture radar

A Synthetic Aperture Radar, or SAR, is a remote sensing tecnique system which utilizes the flight path of the platform to simulate an extremely large antenna, in order to maintain a physical antenna with reasonable dimension while generating high-resolution remote sensing imagery (Figure 15).

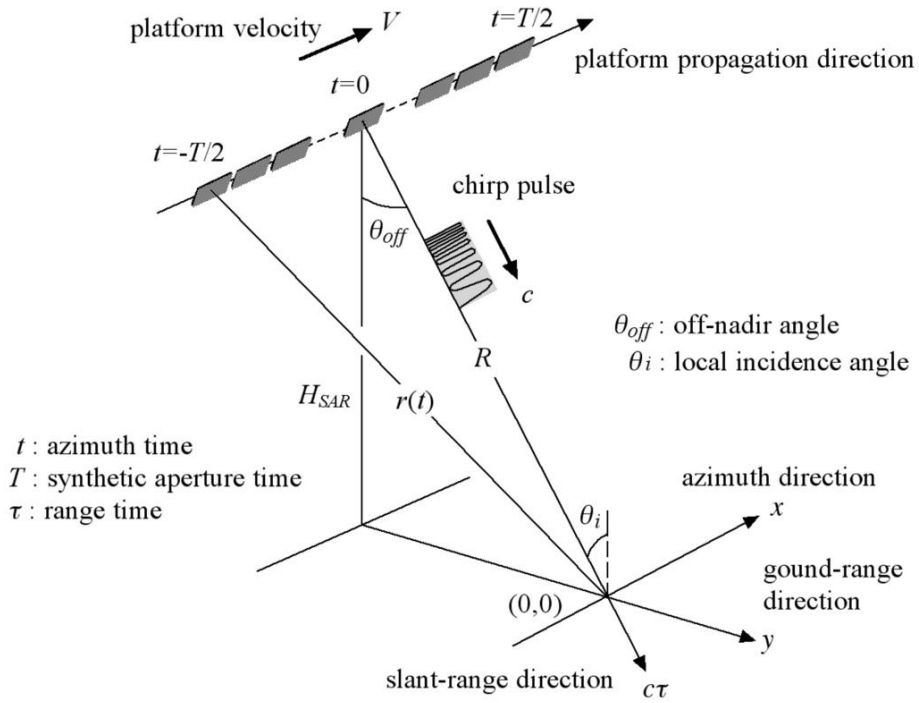

Figure 15 – Synthetic aperture radar technique (Ouchi et al., 2013); HSAR is the height of the SAR platform, c is the velocity of the microwave, and r(t) and R are respectively the slant-range distances at the azimuth time t and when the antenna is nearest to the target at the origin of the ground coordinate system (x, y).

Images acquired by radar satellite sensors are affected by different types of distortion, that can be grouped into geometric and radiometric distortions. Geometric distortions are related with the interaction between the satellite Line of Sight and the local geometry of the enlightened area. Targets closer to the radar sensor (near range) appear compressed along the ground range direction if compared with targets in the far range.

Geometric distortion occurs because the radar is measuring the distance to features in slant-range rather than the true horizontal distance along the ground. Three main types of geometric distortions can be identified for the side-looking radar satellites:

- **Foreshortening (Figure 16a):** foreshortening occurs when the radar beam reaches the base of a tall feature tilted towards the radar (e.g. a mountain) before the top of it. Again, because the radar measures distance in slant-range, the slope (A to B) will appear compressed and the length of the slope will be represented incorrectly (A' to B'). Foreshortening severity depends on the angle of the hillside or mountain slope in relation to the incidence angle of the radar beam. Maximum foreshortening occurs when the radar beam is perpendicular to the slope and its base and top are imaged simultaneously (C to D). In such a case, the length of the slope will be reduced to an effective length of zero in slant range (C'D').
- **Layover (Figure 16b):** when the radar beam reaches the top of a tall feature (B) before it reaches the base (A), layover occurs. In this case, the return signal from the top of the feature will be received before the signal from the bottom. As a result, the top of the feature is displaced towards the radar from its true position on the ground, and "lays over" the base of the feature (B' to A'). Layover effects on a radar image look very similar to effects due to foreshortening. As for foreshortening, layover is most severe for small incidence angles, at the near range of a swath, and in mountainous terrain.
- **Shadowing (Figure 16c):** Radar shadow occurs when the radar beam is not able to illuminate the ground surface behind vertical features or slopes with steep sides. Since the radar beam does not illuminate the surface, shadowed regions will appear dark on an image as no energy reaches the surface to be backscattered. As incidence angle increases from near to far range, so will shadow effects, as the radar beam looks more and more obliquely at the surface. This geometrical distortion is recognizable in radar images as black area, paying attention to not confuse this effect with water areas.

To reduce the effect of the geometric distortion several techniques were developed based on, as instance, the use of several images to taking advantage of different view angles or by means of DEM to correct it.

Radiometric distortions are related to the amount of energy received by the sensors and are usually associated with geometric distortions. Considering foreshortening effect, for example, radar sensors receive the backscattered energy stored in a smaller area than the real one, absorbing intense reflecting energy in few pixels. The main problem with radiometric distortions is that their effects cannot be fixed without information deriving from the observed sources that are needed to calibrate and validate the acquired radar images.

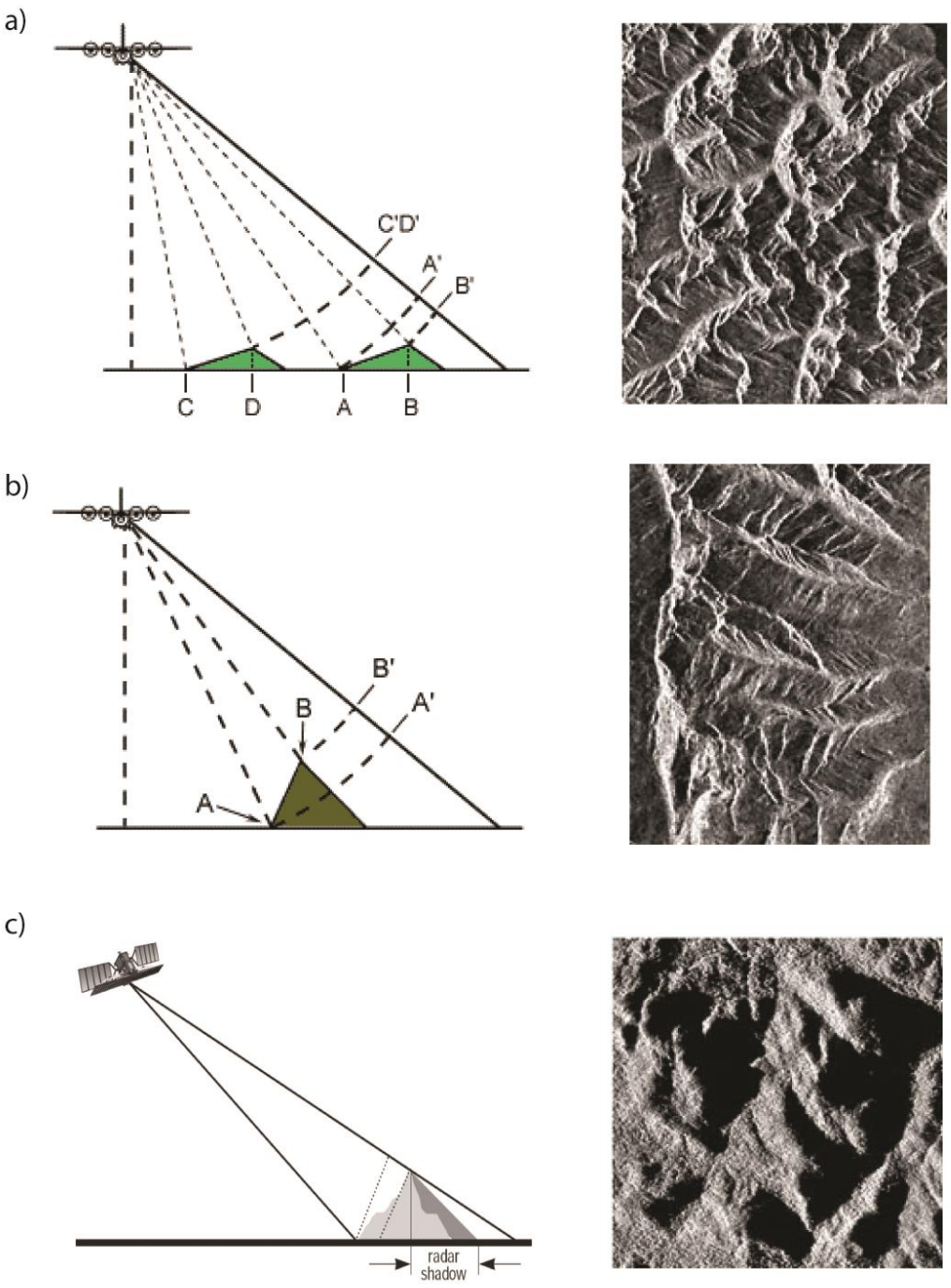

Figure 16 – Geometric distortions of radar airborne images: a) foreshortening effect, b) layover effect, c) shadowing effect.

Satellite radar constellation acquire Earth surface images both in ascending (from South to North) and descending (from North to South) orbit, shifted few degrees from the North-South direction (Figure 17). For this reason and considering that radar sensors acquire image with a side-looking geometry perpendicular to their LOS (usually right towards), it appears clear that Earth surface movements with East-West direction result more easily detectable than movements occurring in North-South direction. Combining ascending and descending orbits and their measured components of the Earth surface it is possible to eliminate most part of geometric distortion described above, obtaining the true information of enlightened targets.

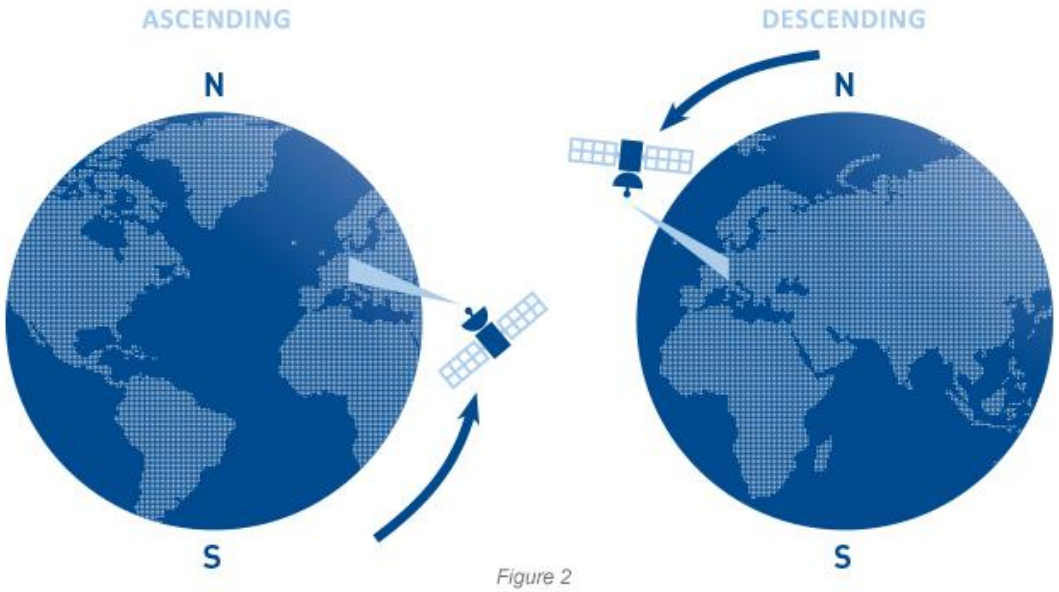

Figure 17 – Ascending and descending polar orbits of a radar satellite constellation.

3.3.3 Persistent Scatterers interferometry

SAR technique applied for Earth surface movement detection is based on the Differential Interferometric SAR (DInSAR) approach (Massonnet and Feigl, 1998). With this methodology, two SAR images of the same area are acquired at different times, depending on the revisitation time of the satellite constellation. Differences in the phase of the waves returning to the radar sensor are used to generate maps of surface deformation or digital elevation (Figure 18 - Ground surface displacement detection by means of two acquisition with InSAR techniques (http://www.un-spider.org)).

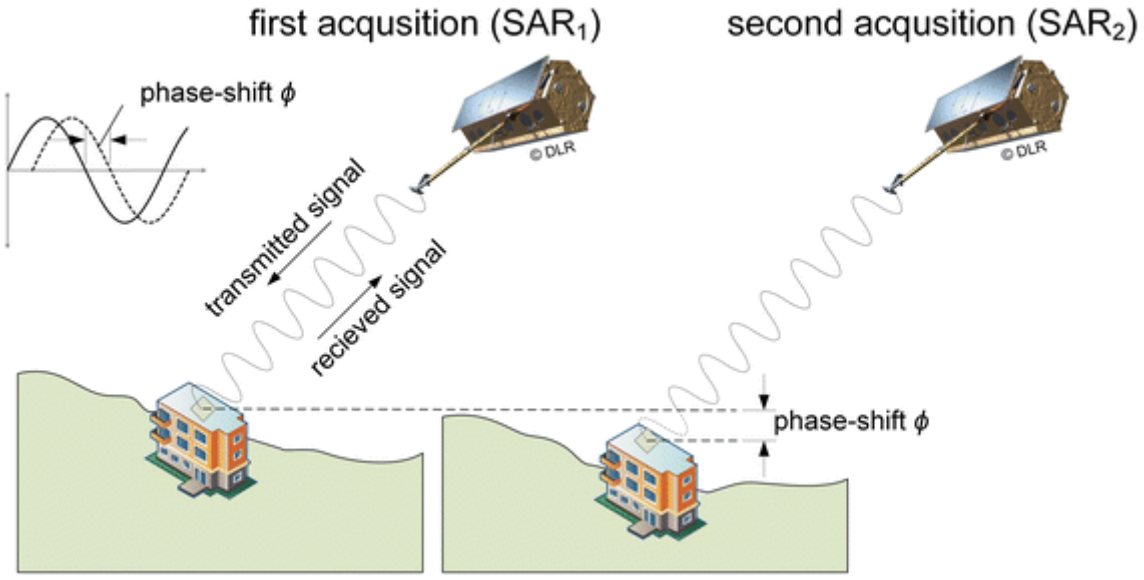

Figure 18 - Ground surface displacement detection by means of two acquisition with InSAR techniques (http://www.un-spider.org).

Drawbacks of such methodology are represented by atmospheric and temporal decorrelations (Massonnet and Feigl, 1998; Ferretti et al., 2001; Colesanti et al., 2003) that affect and usually disturb the final products. A possible solution to avoid these kinds of problems is to use techniques that take advantage from multi-

temporal radar acquisitions to improve their results, like the Persistent Scattering Interferometry (PSI) (Ferretti et al., 2001). In PSI methodology, long-term stable natural reflectors (called Persistent Scatterers, PS) are identified from several multi-interferogram analyses of SAR images in order to precisely track the motion of each PS to determine ground deformations. PS are represented by natural or anthropic features, with pixel or sub-pixel size, that are present in every SAR image of the stack. The PSI technique is able to correct DInSAR atmospheric, orbital and topographical induced errors in order to derive velocity and displacement measurements on specific ground targets. Persistent Scatterers Interferometry represents a class of SAR techniques that indicates several approaches proposed in literature during last 20 years, such as Coherent Pixel Technique (CPT, Mora et al., 2003), Interferometric Point Target Analysis (IPTA, Werner et al., 2003), Stable Point Network (SPN, Duro et al., 2004) or the most recent and commonly used SqueeSAR (Ferretti et al. 2011).

In PSI analysis, two big families of targets can be generally extracted from InSAR processing on each radar satellite images: Persistent Scatterers (PS), points having the reflected energy of only a single or a few connected pixels, and the Distributed Scatterers (DS), corresponding to a homogeneous area covered by several pixels. The SqueeSAR algorithm combines PS and DS coherent matrix in order to extract an optimum vector of phase values to use for interferometric analysis, improving the density of measured points and preserving the high quality of data. Combination of PS and DS gives results with lower standard deviation with respect to the traditional PSInSAR algorithms, making SqueeSAR a very effective tool for ground surface displacement detection at different analysis scales.

3.3.4 Vertical and horizontal decomposition

Considering the polar orbit of InSAR satellites, from North to South for descending orbit and from South to North for ascending orbit, InSAR images recorded by radar sensors measure ground displacement in time along satellite Line of Sight. Thus, measured displacement is satellite geometry dependent and does not represent the real displacement of observed targets (Figure 19).

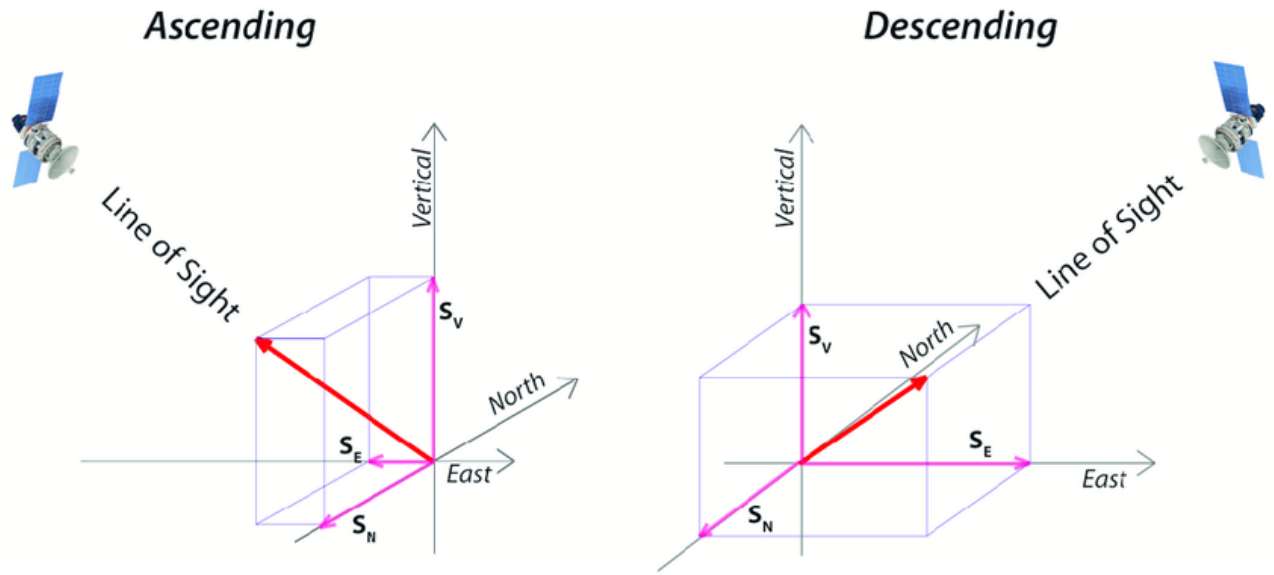

Figure 19 – Ascending and descending geometries for Line of Sight velocity decomposition; S_E, S_N and S_V represent the target displacement along East, North and vertical directions respectively (Del Soldato et al., 2018).

If both ascending and descending geometries are available for each observed target, the real velocity of displacement can be calculated as follow:

$$\bar{V} = V_x\bar{s_x} + V_y\bar{s_y} + V_z\bar{s_z} \tag{45}$$

Where V_x, V_y and V_z are the velocity components along East, North and vertical directions, while $\bar{s_x}$, $\bar{s_y}$ and $\bar{s_z}$ are the unit vectors of the three coordinate axes.

Combination of ascending and descending acquired displacement values allows to decompose detected LOS motion into its horizontal and vertical components (Manzo et al., 2006; Notti et al., 2014). Using the mean velocity of the two available orbits data, a system of two equations with three variables can be created:

$$\begin{cases} V_a = V_x h_{LOS,a} + V_y n_{LOS,a} + V_z e_{LOS,a} \\ V_d = V_x h_{LOS,d} + V_y n_{LOS,d} + V_z e_{LOS,d} \end{cases} \tag{46}$$

Where $h_{LOS,a}$, $n_{LOS,a}$, $e_{LOS,a}$, $h_{LOS,d}$, $n_{LOS,d}$ and $e_{LOS,d}$ represent the LOS directional cosines for ascending and descending orbits and V_a and V_d are the ascending and descending LOS satellite measured velocity. Equation (46) can be solved only considering the North-South horizontal component of the motion negligible, because of the near polar orbits of the SAR satellites that produce a low sensitivity along the North-South direction (Notti et al., 2014). With this assumption, and considering the availability of both ascending and descending acquisition geometry, the horizontal and vertical components of motion can be calculated:

$$V_H = \frac{\left(\left(\frac{V_d}{h_{LOS,a}}\right) - \left(\frac{V_a}{h_{LOS,a}}\right)\right)}{\frac{e_{LOS,d}}{h_{LOS,a}} - \frac{e_{LOS,a}}{h_{LOS,a}}} \tag{47}$$

$$V_H = \frac{\left(\left(\frac{V_d}{e_{LOS,a}}\right) - \left(\frac{V_a}{e_{LOS,a}}\right)\right)}{\frac{h_{LOS,d}}{e_{LOS,a}} - \frac{h_{LOS,a}}{e_{LOS,a}}} \tag{48}$$

With:

$$h_{LOS} = \cos(\alpha) \tag{49}$$

$$e_{LOS} = \cos(1.571 - \alpha)\cos\omega \tag{50}$$

$$n_{LOS} = \cos(1.571 - \alpha)\cos\eta \tag{51}$$

$$\eta = 3.142 - \theta \qquad \omega = 4.712 - \theta$$

α and θ are respectively the incidence angle and the LOS azimuth angle and are unique for each satellite.

Beside its possible drawbacks and all its post-processing procedures needed to validate data, nowdays the use of InSAR techniques it is probably the most effective and widespread available methodology for monitoring phenomena occuring on Earth surface. In the geosciences field, multiple application have been proposed, involving different kind of deformation caused by sudden (e. g. earthquakes) and slow natural

events (e. g. landslides or natural subsidence) or induced by human activities (e. g. subsidence due to gas or groundwater overexploitation) (Schmidt and Burgmann, 2003; Funning et al., 2007; Bianchini et al., 2012 Tomas et al., 2014; Del Soldato et al., 2018). Despite the high amount of proposed methodologies and countless publications made on it, InSAR remote sensing technique still represent a field of active research with possible unlimited development and potential in natural processes monitoring and mitigation.

3.4 Fragility curves and vulnerability maps

In the last few decades, a dramatic increase in the losses caused by natural catastrophes has been observed worldwide. The vulnerability of buildings and structures to natural hazards are often assessed with the development of fragility and vulnerability curves, since they represent a good compromise between the accuracy of the results and the amount of time and money required for the studies. Fragility curves provide the probability of reaching or exceeding a given damage state as a function of the intensity of the natural event, and they are usually modeled by lognormal functions. A very important point is that fragility curves clearly take into account that not all buildings of the same type will suffer the same level of damage for a given event intensity. Figure 20a shows the damage distribution on stone masonry buildings for an earthquake EMS-98 of intensity equal to 11. Mathematically, the probability (P) of reaching a given level of damage (D_i) can be written according to the following equation (Peduto et al., 2017):

$$P(Damage \geq D_i|\Delta) = \emptyset\left(\frac{1}{\beta}\cdot Ln\left(\frac{\Delta}{\overline{\Delta_i}}\right)\right) \quad (52)$$

Where $\emptyset(\cdot)$ is the standardized cumulative normal distribution, $\overline{\Delta_i}$ and β are the median and the standard deviation, respectively, of the natural logarithm of the intensity parameter Δ.

After calculating the damage probability distribution for each levels of damage, fragility curves for this type of building can be created (Figure 20b). Finally, starting from fragility curves, for each intensity levels a mean damage value can be calculated, and vulnerability curves can be developed (Figure 20c). Vulnerability curves represent relationships between the mean amount of damage for a given type of building and the value of the event intensity.

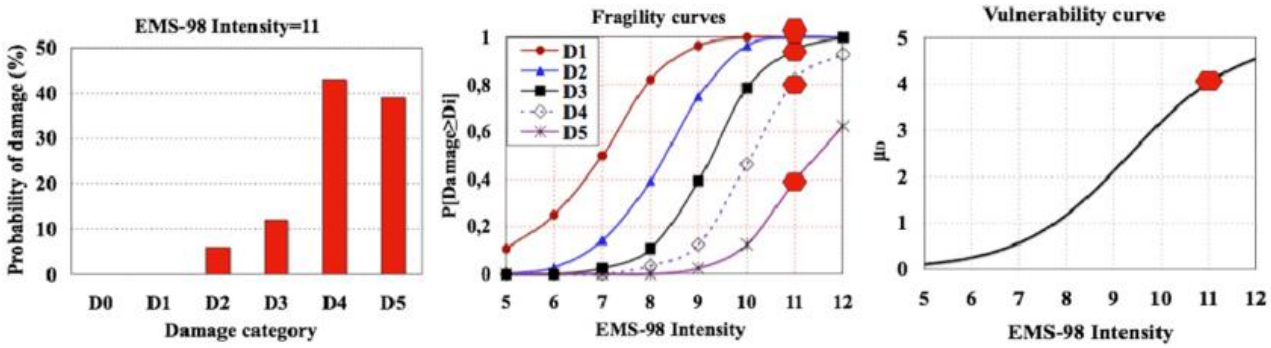

Figure 20 - a) Damage distribution, b) Fragility curves and c) vulnerability curves (Saeidi et al., 2009).

There are several methods available in literature to derive fragility and vulnerability curves, that can be grouped in four main categories:

- Empirical methods: are methods based on field data from post-events surveys; the main advantage of this type methods is that they represent a realistic image of the real vulnerability of buildings (Billah and Alam, 2014) since they are based on actual recorded damage. The most common problem when applying an empirical approach is the necessity to collect many sufficient and reliable data to construct the fragility and the vulnerability curves.
- Engineering judgmental: are methods based on experts opinion, applied when there are not enough data to develop fragility curves; these methods are strictly dependent on the personal experience and judgment of the consulted individual.
- Analytical methods: with these kinds of methods, damage distributions are obtained by performing numerical simulation with different intensity scenarios, so they can be extremely computationally intensive and time consuming.

- Hybrid methods: approaches that try to compensate the major drawbacks of the other methods by combining observed data and analytical estimations.

Despite the different approach that can be chosen, in order to develop vulnerability and fragility curves, three categories of input data are needed: damage scale, building typology and intensity criterion. Damage scales are based on threshold of global and/or local parameters of the analyzed structure, depending also on the nature of the damaging event. Building typology is defined according to the main widespread constructive technique in the study area for the parameters that are relevant to the buildings resistance against the considered hazard. The intensity of a given event can be expressed in different ways, depending on the type of the considered phenomena (e.g. magnitude for earthquakes, velocity for landslides, ecc.)

Various methods for vulnerability assessment have been proposed in seismic engineering literature. Sabetta et al. (1998) used post-earthquake surveys of approximately 50,000 buildings damaged by destructive Italian earthquakes in order to derive vulnerability curves. Empirical fragility curves with a binomial distribution were derived as a function of Arias Intensity and effective peak acceleration. Rota et al. (2006) have also used data obtained from post-earthquake damage surveys, carried out in several municipalities over the past in Italy, in order to obtain fragility curves for typical building classes. Rosetto et al. (2003) derived vulnerability functions for European-type RC structures based on observational data of 99 post-earthquake damage distributions observed in 19 earthquakes. In 2010, Negulescu and Foerster proposed some preliminary fragility curves with respect to the magnitude of differential ground displacement due to landslides. Referring to subsidence phenomena, Saeidi et al. (2012) developed vulnerability and fragility curves based on the use of analytical methods, tested and validated with a set of three cases that occurred in Lorraine between 1990 and 1996. They referred to two building types that are typical of a large number of countries: unreinforced masonry buildings and reinforced masonry buildings with lengths between 10 and 20 m and heights between 7 and 10 m.

4 Study area

The city of Pistoia rises in the North-Western corner of the Middle Valdarno basin, also known as Firenze – Prato – Pistoia basin, located in the Northern part of Tuscany region, central Italy. The valley is bordered by the Northern Apennines to the North and to the East sides, by the Chianti and Senese hillslopes to the South, and by the Valdinievole valley and the Serravalle Pistoiese relief to the West. It is a 35 km wide and 100 km long intermontane sedimentary basin and has an extension of approximately 824 km^2, with a mean elevation of ca. 50 m a.s.l. (Capecchi et al., 1975). Firenze – Prato – Pistoia basin represents one of the main tectonic basins of the Northern Appennines, developed parallel to the main chain axis starting from the Neogene period, in the Tyrrhenian side of the Apennines thrust and fold belt (Boccaletti et al., 2001). The genesis of all depression was related to the extensional tectonic regime imposed from the Upper Tortonian age following the opening of the Tyrrhenian Sea (Boccaletti and Guazzone, 1974). The substratum of the basin is mainly made of metamorphic Ligurian Units (shales, calcareous-quarzitic sandstone and calcareous turbidites) that tectonically overlie the turbiditic formations of the Tuscan Unit (Macigno sandstone). Above the rocky basement, the basin is filled up with fluvial and lacustrine unconsolidated sediments with different thickness, reaching in the middle portion of the basin a depth of more than 500 meters. In general, the bottom of the stratigraphical sequence is composed by clay and silt with organic or gravel levels. On top of this clayey layer, the sequence follows the paleogeographic evolution of the basin, with thick gravel and sand fan deltas deposits at the mouth of lateral streams and sand and silt level deposited by paleo-rivers wandering along the basin (Capecchi et al., 1975).

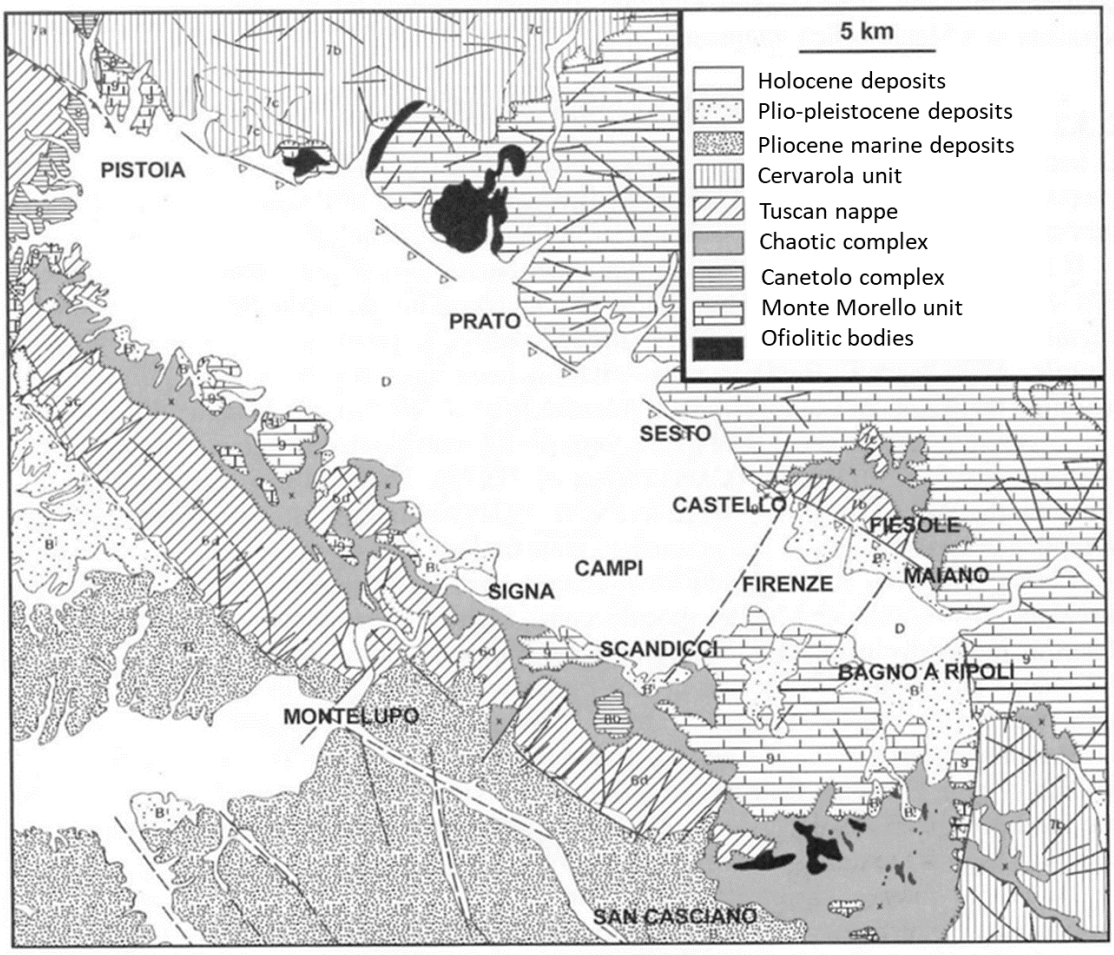

Figure 21 – Geological map of the Firenze – Prato – Pistoia basin (Coli & Rubellini, 2007).

Thus, the stratigraphically asset is quite complex and varies a lot depending on the relative position within the basin, with strong lateral variation that determine a highly variable hydrogeological context with multilayer aquifers with different hydraulic properties. The imposed river system strongly reflects the high anthropic impact in the area, and it is represented by the Ombrone river and its tributaries in Pistoia province, by the Bisenzio River close to Prato city and by the Arno River in the Florence area (Figure 21).

The study area corresponds to Pistoia city, capital of the homonymous province located in the North-Eastern portion of Tuscany Region and, more in general, to the Ombrone river basin, located in the North – West part of the Firenze – Prato – Pistoia basin. Pistoia is a typical medieval city with a population of about 91,000 inhabitants hosting important cultural heritages, such as the Duomo and the San Giovanni Baptistery, that attract several tourists during the year. A network of underground channels (called “gore” in Italian) run below the historical city center; these channels, built in Medieval Age, were used for water supply and are today considered as a touristic attraction. The city is famous for its plant and flower nursery activities that are widespread all around the city center.

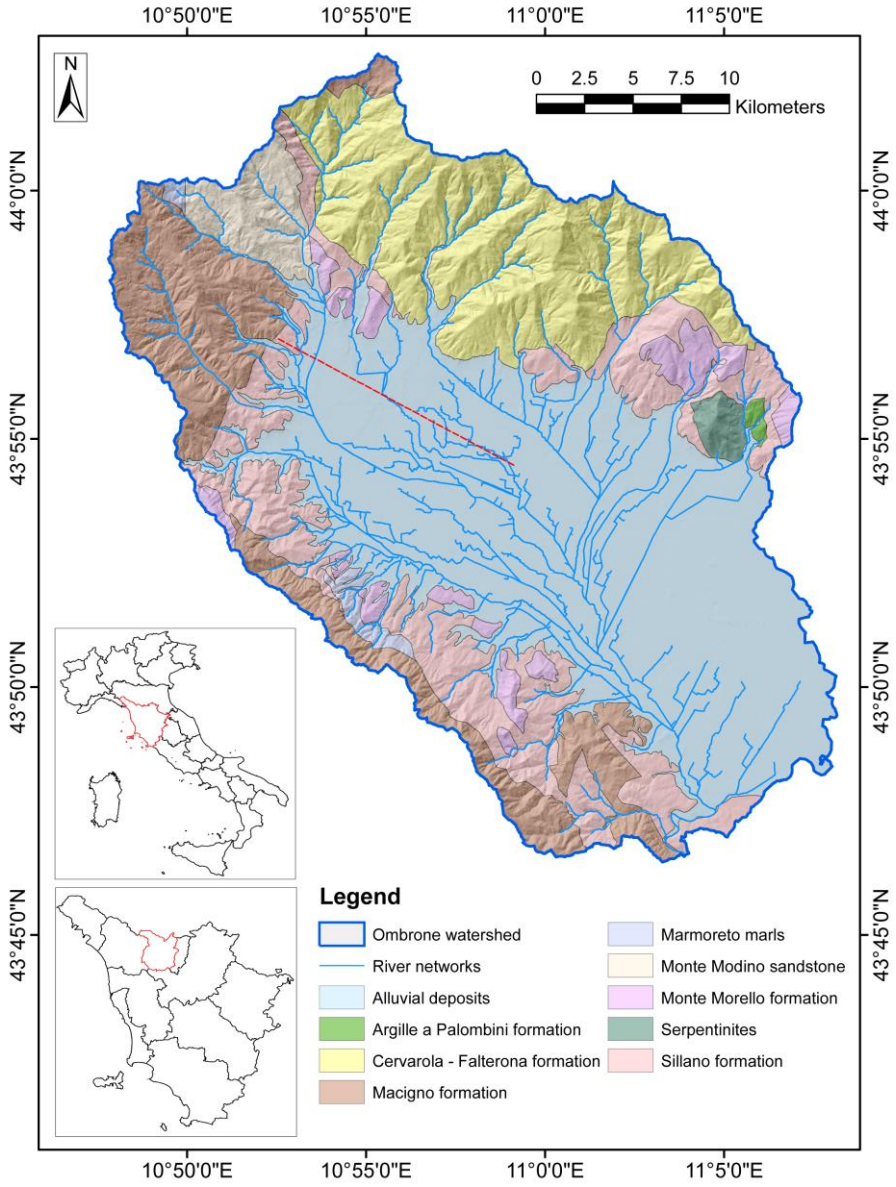

Figure 22 - Geological map of the Ombrone river basin.

From a geological point of view, the area reflects its position within the Firenze – Prato – Pistoia basin and it is characterized by a Cretaceous – Paleogene basement constituted by a stratigraphic column starting with the sandy flysh of the Macigno formation (Oligocene-Miocene), the Canetolo Complex clayschists (Eocene–Oligocene), the Ophiolitic Complex (Lower Jurassic–Lower Cretaceous) and the Calvana Supergroup (Upper Cretaceous–middle Eocene, Figure 22).

Here, the compressible lacustrine and fluvial sediments have a thickness that increase moving from the relieves surrounding the basin, up to a maximum that reaches more than 400 meters in the South – Eastern part of the plain, along the axis of the basin. Generally, the deposits are constituted by pebbles with variable dimensions with the presence of gravel, sand and clay (Figure 23).

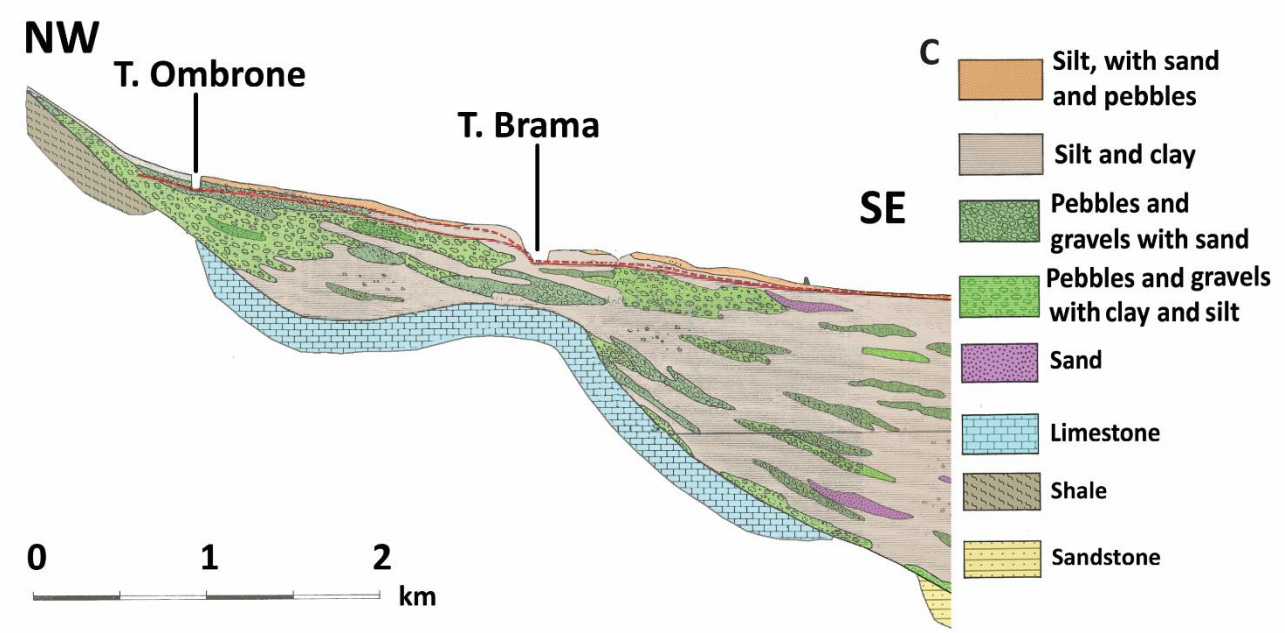

Figure 23 – Geological section of Ombrone basin across A-A' section in Figure 22.

As stated before, the stratigraphic situation presents a high lateral variability: thick gravel and pebbles levels in the northern portion of the area of interest, coinciding with the Ombrone River fan delta, and prevalent silt and clay terrains with sparse and thin gravel and sand layers (with variable thickness frequently lower than 10 m) in the southeastern portion of the city. The fan delta sequence hosts a phreatic aquifer that is largely exploited, thanks to its high transmissivity and quality of the resource, for the Pistoia freshwater supply and for agriculture in the surroundings of the city. Pumping rate patterns are quite homogeneous all over Pistoia aquifer, with the evidence of a major pumping region located in the southern part of Pistoia city. In this area, a pumping well can reach a specific discharge of 5 to 10 l/s for 1 m drop of the groundwater level (usually found 1 to 5 m below surface). It has been estimated that the 85% of the drinking water supplied by the aqueduct of the city is extracted by pumping wells, with a maximum discharge of 150 l/s during summer. This phreatic aquifer is barely used within the historic city center, where no industrial activities are found and where some wells extract water for air condition systems or for other usages.

The surficial aquifer is partially recharged by the water of the Ombrone river (losing stream disconnected, following the definition of Winter et al., 1998), flowing in the Western part of the city. In the South - Eastern part of the basin, where clay and silt are more abundant, the phreatic aquifer is limited and barely exploited. In this area, the main source of groundwater consists in multiple thin confined aquifers taking place in gravel or sand layers found at different depth with low lateral continuity. These aquifers, characterized by quite long recharge times, are intensively exploited by the flower and plant nursery activities that can be found

South-East of Pistoia city. The sandstone rocks that underlies the basin represent the main recharge source area of Pistoia aquifer, transmitting water from surrounding reliefs through the alluvial deposit. Some additional recharge may occur from East side of the basin, from Prato aquifer, but this amount is expected to be quite small.

4.1 Firenze – Prato - Pistoia subsidence

Land subsidence along the Firenze-Prato-Pistoia basin is well known. Colombo et al. (2003) and Canuti et al. (2006) analyzed ERS 1/2 data, spanning between 1992 and 2000, to derive the first deformation map of the basin, highlighting the presence of two main subsidence bowls: one coinciding with the city of Prato (20 km Southern than the study area), where subsidence rates reach 20 mm/yr, one southern than the urban perimeter of Pistoia, recording lowering up to 25 mm/yr. Subsidence in Prato area was connected to textile manufacturing, exploiting the thick phreatic aquifer of the Ombrone fan delta. These industrial activities, started in early 60s and spread over the southern portion of Prato, depressed the phreatic level of several meters, inducing long-term subsidence (Canuti et al., 2006). Subsidence in southern Pistoia has been related to plant and flower nurseries that represent the main economic sector of the municipality, largely exploiting several confined aquifers present at different depths.

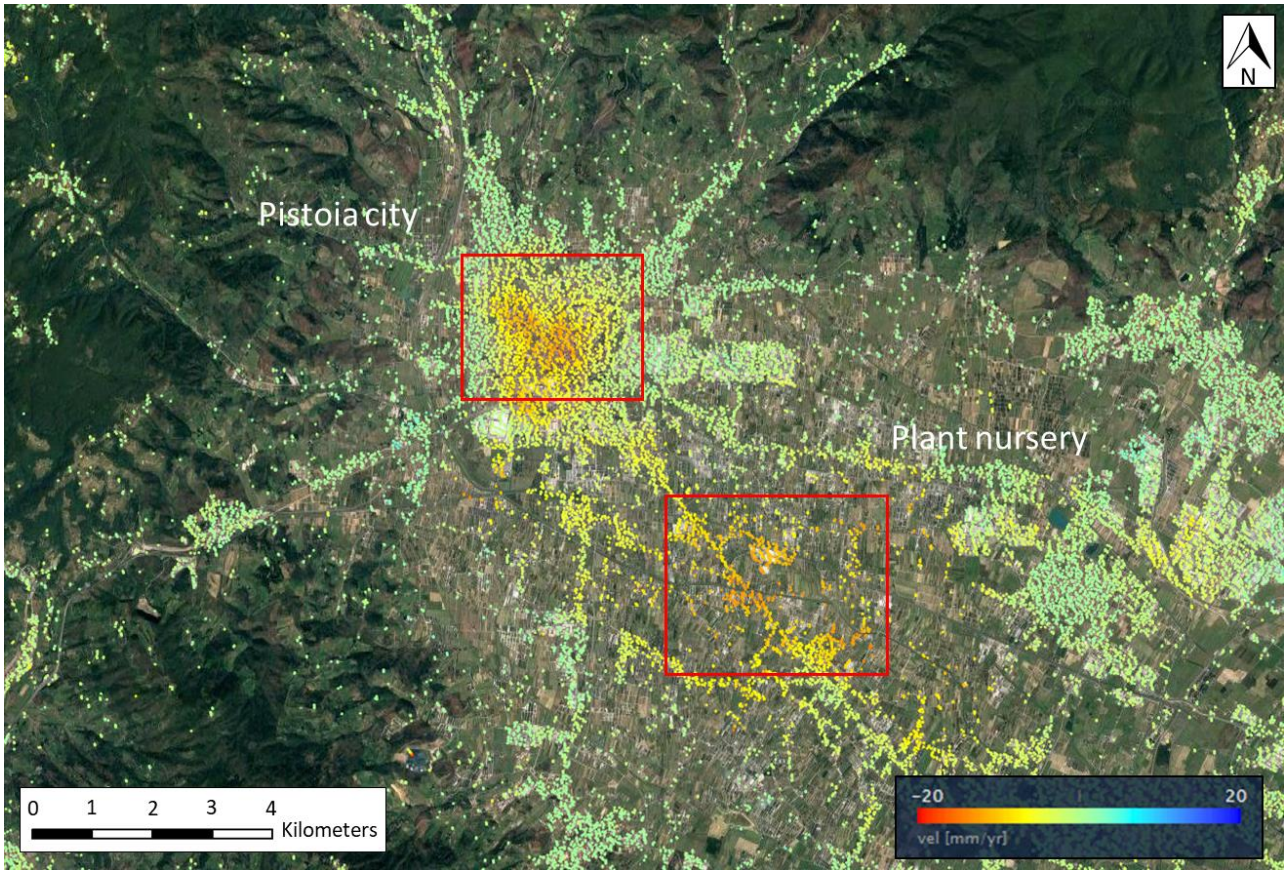

Figure 24 – Subsidence bowls detected in Pistoia area, located in correspondence of the plant nursery area and in Pistoia historical center.

Rosi et al. (2016) and Del Soldato et al. (2018) updated the interferometric analysis over the Firenze-Prato-Pistoia basin using Envisat data, acquired between 2003 and 2010. In this period, ground lowering in the city of Prato drastically decreased or stopped because of the recession of the textile industry that led to a lower

exploitation of the aquifer (Rosi et al., 2016). In Pistoia area, Envisat data confirmed the presence of a large subsidence bowl characterized by maximum subsidence rates higher than 30 mm/yr.

The results of a new interferometric investigation in the Firenze-Prato-Pistoia basin, with a focus on the municipality of Pistoia, are presented in Figure 25. Both contours have been traced starting from the same interferometric products used by Canuti et al. (2006) and Rosi et al. (2016) and generated by interpolating the original PS points velocity values with an Inverse Distance Weighting algorithm. A stability threshold of 4.5 mm/yr, equal to two times the standard deviation of the datasets, has been used to define the velocity lower limit for the delimitation of the subsidence bowl. The highest velocities are located between the hamlets of Bottegone and Bottaia, ca. 8km southern than the city center. Thus, in the 18 years investigated period no signs of subsidence in the city center of Pistoia were recorded.

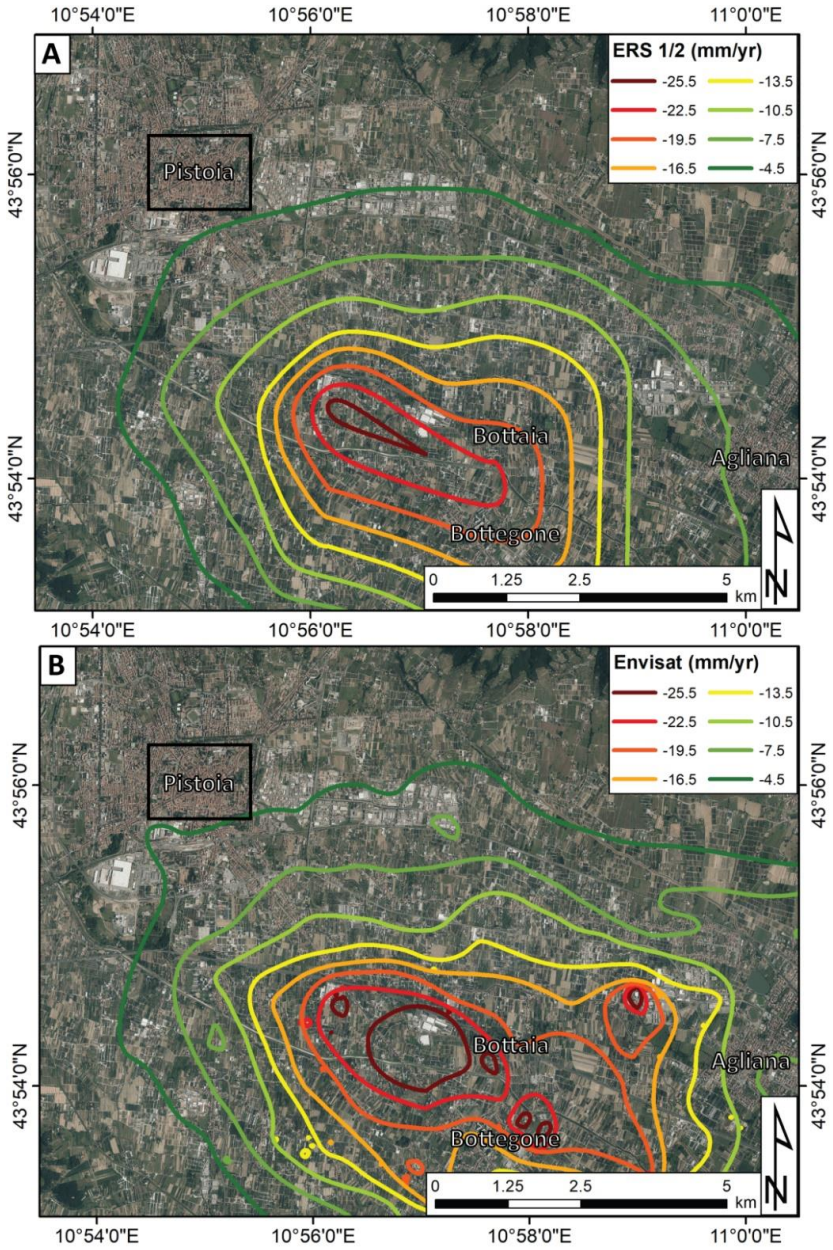

Figure 25 – Subsidence contours derived from ERS 1/2 (A) and Envisat (B) data, covering a time period spanning between 1992 and 2010. The contours have been derived by Canuti et al. (2006) and by Rosi et al. (2016).

According to the interferometric results, derived from Sentinel-1 radar images acquired between 2015 and 2017, the city recorded an anomalous variation of the spatial distribution of moving points, with the creation

of a new subsidence bowl coinciding with the historical city center, far from the already known lowering area of Bottegone/Bottaia (Figure 24).

This area was also affected by other anomalous deformation event in 1964-1973 period, as suggested by the limited data found in literature (Fondelli, 1975; Fancelli et al., 1980). Leveling measurements in the city center (Fondelli, 1975) detected more 1.5 cm of subsidence occurred in the analyzed period, but no official hypothesis about the triggering factors was presented.

Ground displacement information from satellite data are available for the study area since April 1992, acquired by means of the first European Remote Sensing (ERS) satellite developed by the European Spatial Agency (ESA) in July 1991. ERS data are available until November 2000.

Starting from February 2003, ground displacement data are available from ENVISAT (ENVironmental SATellite) acquisition. ENVISAT data cover a 8 years monitoring period, until June 2010.

For the 2015-2017 period, both Sentinel-1 and Cosmo SKY-MED (COnstellation of small Satellites for Mediterranean basin Observation) InSAR data are available. Sentinel-1 data, with biweekly ground displacement continuous information up to present, are available for the whole Tuscany region and cover all the Ombrone basin domain. Cosmo SKY-MED data were requested only for the 2015-2017 and are available for the Pistoia city historical center only.

No information about ground displacement in the study area are available for the December 2000 – January 2003 and for the July 2010 – December 2014 periods. The temporal consistency of Permanent Scatterers InSAR data over Pistoia area from 1992 to nowadays is presented in Figure 26.

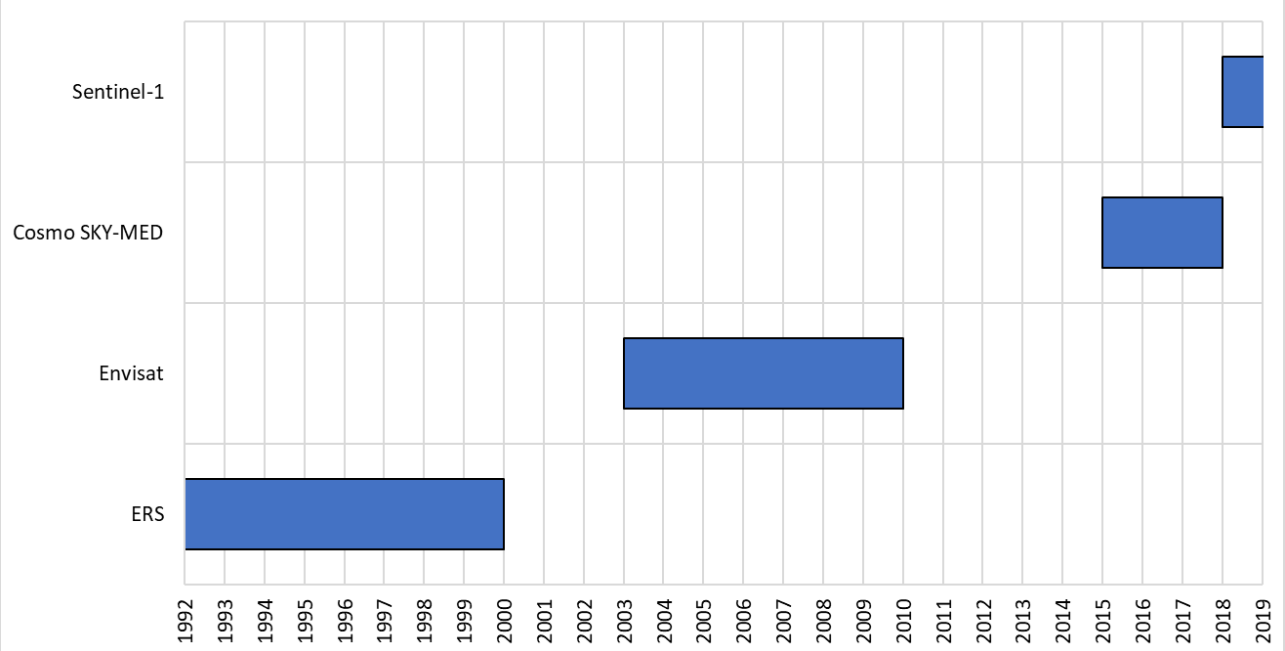

Figure 26 – PS-InSAR data consistency in the study area from 1992 to present.

4.2 PS-InSAR data processing

The ground deformation pattern detected in Pistoia historical center with Sentinel-1 system needed to be validated with external data. The absence of GNSS and leveling measurement in the area led to the request of Cosmo-SkyMed (CSK) and ENVISAT constellation (Covello et al., 2010) ascending and descending X-band images and their processing with a different processing algorithm.

4.2.1 Sentinel data and processing

Sentinel-1 C-band images were processed by means of a parallelized SqueeSAR algorithm (Ferretti et al., 2011). SqueeSAR is a Homogeneous Distributed Scatterers Inteferometry (HDSI) approach which relies on a new category of stable radar targets: the Distributed Scatterers (DS). Unlike the point-like PS, a DS is considered a distributed target whose signal is averaged from multiple targets with homogeneous signal. DS are usually detected in uncultivated or debris-covered areas. The selection of DS is based on the Kolmogorov-Smirnov test which is used to select statistical homogeneous families of pixels depending on the distribution of amplitude values within a pre-defined searching window (Kwam and Vidakovic, 2007). In summary, the SqueeSAR algorithm firstly analyze the amplitude characteristics of the single pixel of the radar image, then, through the Kolmogorov-Smirnov test, define the families of homogeneous pixels which are going to be the DS candidate. Finally, PS and DS are jointly processed by means of a classical PSInSAR approach. SqueeSAR allows improving the accuracy of time series and velocity estimations as well as increases the MP density in peri-urban areas and especially in mountain areas with widespread debris deposits and low vegetation cover. The data used in this work derive from a specific application of the SqueeSAR algorithm. Such data are part of the first worldwide example of a monitoring system totally based on interferometric products (Raspini et al. 2018, 2019).

4.2.2 CSK data and processing

In order to validate subsidence pattern identified in Pistoia city by Sentinel-1 InSAR data, Cosmo-SkyMed (CSK) constellation ascending and descending X-band images have been processed with a different processing chain: Coherent Pixels Technique (CPT).

Ascending stack is composed by 60 Stripmap-Himage (STR-HIMAGE) acquired from January 2015 to March 2018 with an almost regular temporal span of 16 days. Descending dataset consists of 34 Stripmap-Himage acquired from February 2015 to December 2017 with a time span between 16 and 32 days. The maximum temporal baseline is 96 days. Despite the availability of higher CSK temporal resolution (3-4 days maximum), the spatial distribution and temporal evolution of the studied subsidence allowed selecting a longer image gap in order to reduce processing times maintaining at the same time an appropriated level of temporal decorrelation.

SAR images were processed using CPT, developed by the Remote Sensing Laboratory (RSLab) at Universitat Politecnica de Catalunya (Mora et al., 2003; Blanco-Sánchez et al., 2008; Confuorto et al., 2017). CPT algorithm is based on the exploitation of spatial coherence, increasing the measurement points especially in rural areas through the use of Distributed Scatterers (DS). Two parts of the processing chain (PRISAR and SUBSOFT) are responsible of the coregistration, generation of interferograms, coherence maps and differential interferograms; and the estimation of linear velocities, time series and atmospheric filtering respectively.

During the processing phase, a double minimization of temporal and spatial baselines was implemented in order to increase the deformation sensitivity and to reduce the temporal decorrelation, relevant when analyzing high resolution X-band images over rural areas. Descending dataset baselines were adapted to assure the connection and redundancy of 7 first images that presented extreme perpendicular baselines. Selected multilook (3x3) was adapted to improve the DS detection preserving a good resolution in urban areas. The stability threshold of the results was settled on 0.5 cm/year, in accordance with 1.5 times the standard deviation values estimated for the points located in a stable area.

4.2.3 ENVISAT data and processing

ENVISAT products cover the time period 2003-2010 and were processed in the framework of the PST-A (Piano Straordinario di Telerilevamento - Extraordinary Plan for Remote Sensing of the Environment) project managed by the Italian Ministry of Environment, Sea and Territory (MATTM). The PST-A project is the first worldwide example of a PSI national product, derived by analyzing ERS 1/2, ENVISAT and COSMO-SkyMed radar images in both orbits. The whole Italian territory was covered by PSI results with ~28 million points for composing the final ENVISAT deformation map with an average density of 50 PS/km2. The radar images were processed by means of the combined efforts of two production team who exploited the PSInSAR (Permanent Scatterer Interferometry, Ferretti et al., 2001) and PSP (Persistent Scatterer Pairs, Costantini et al., 2008) algorithms. Both approaches can define stable radar targets, i.e. the Persistent Scatterers (PS), as measurement points (MP). Each MP is characterized by a value of velocity, estimated by applying a linear deformation model, and by a time series of deformation measured along the Line of Sight (LoS). The density of MP mainly depends on: i) land cover, vegetation and wet surfaces prevent the definition of radar targets as well as the presence of frequent surface changes, e.g. mining activity or construction works; ii) type and style of deformation, i.e. fast motions are difficult to capture since they cause phase aliasing; and iii) topography of the area of interest, i.e. steep slopes can cause geometrical effects as shadowing or layover. Two high performance computing infrastructures were used to process the ENVISAT data, each one consisting of clusters of computing nodes interconnected with large bandwidth and low latency networks (Costantini et al., 2017). The minimum processing unit was the frame, i.e. 100 by 100 km for C-band data. One single reference point for each frame was defined and selected automatically depending on the: i) reliability of the measurement point; ii) small model residuals; iii) position within the frame; and iv) type of scatterer (e.g. a building in a historical city center was preferred over a shed in a recent urbanization). Atmospheric noise was removed using data-driven approaches based on adaptive filters (Costantini et al., 2017). The single frames were mosaicked without the support of GNSS data. The overlap areas between frames were used for consistency check. The reader can refer to Costantini et al. (2017) for more detailed information regarding this wide-area processing approach.

4.2.4 Vertical and horizontal velocity

To convert the velocity measured along the Line of Sight into its vertical and horizontal components, both ascending and descending geometries need to be available for each observed target. In order to respect this condition, a set of synthetic Permanent Scatterers are usually created, following a sampling grid (Rosi et al., 2014, Figure 27). The sampling grid allows the creation of spatially regular series of synthetic PS, where the mean deformation velocity in both orbits can be calculated. Finally, by solving equation 47 and 48, the vertical (V_v) and horizontal (V_h) velocity can be obtained.

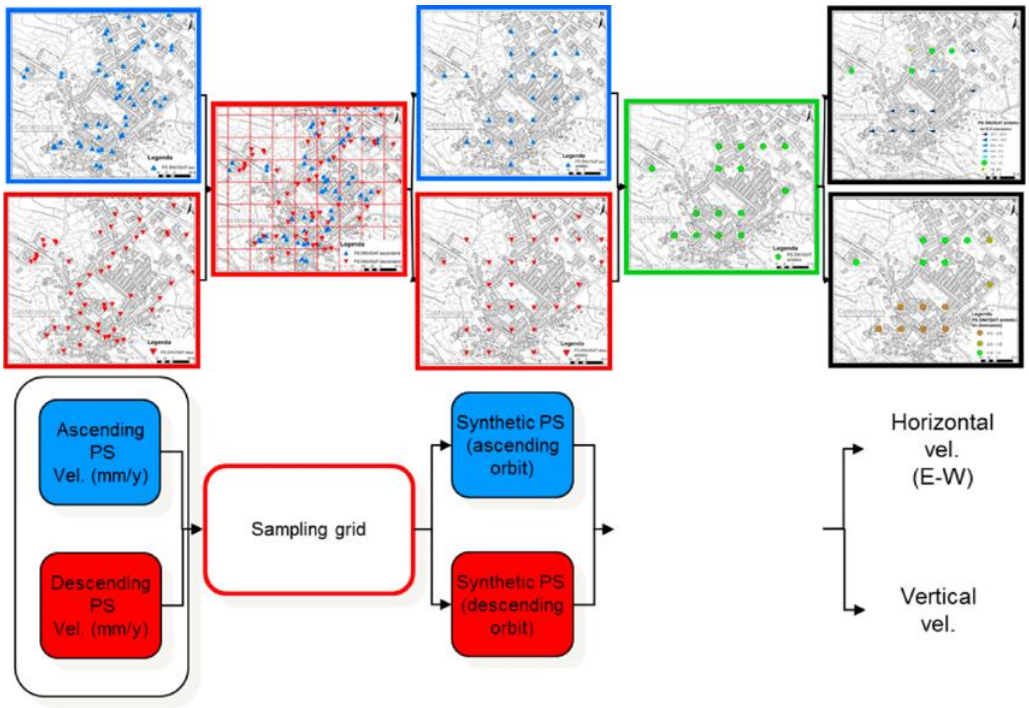

Figure 27 – Flow chart of the process to extract vertical and horizontal component of the velocity by means of synthetic Permanent Scatterers (Rosi et al., 2014).

The choice of the sampling grid cell size depends on the areal extent of the investigated site, the number and distribution of Persisten Scatterers in the area and on the spreading of the studied phenomenon.

4.2.5 Time series analysis

Ground displacement maps can give important information about the extent and the intensity of subsidence patterns, but only with the direct examination of Permanent Scatteres time series, different trends of the temporal evolution of the phenomenon can be detected (Cigna et al., 2012, Berti et al., 2013). Notti et al., 2015, in order to properly characterized the evolution of ground displacement in time, proposed a new methodology to analyze Permanent Scatterers time series, with a particular focus for landslides and subsidence phenomena analysis. To better observe the real behavior of the ground surface, some post-processing elaborations are recommended:

- Removing noise and regional trend: needed for time series affected by regional trend or external noise not related to the ground motion caused by the observed phenomenon. These values can be identified by selecting a high coherence (> 0.9) PS in a stable area that can reveal the presence of a specific trend; correct time series can be obtained by removing the stable time series (that contain only the regional trend) from the original ones.
- Removing single date anomalies: for entire databases with anomalous displacement at a certain date. Anomalies can be detected by selecting stable time series with high coherence; if more than one third of them show the same extreme displacement value at the same time, that value should be removed.
- Detect and correct possible phase unwrapping errors: unwrap occurs when, between two successive satellite acquisitions, ground surface is subjected to a displacement higher than a quarter of the radar wavelength. When this happens, involved time series need to be unwrapped in order to obtain the real ground displacement information.

4.2.6 Self-consistency

Comparison of the deformation rates between ascending and descending acquisition geometry of PS-InSAR data of the same sensor is a common practice to quantitatively verify the consistency of radar measurements (Aslan et al., 2019). In order to evaluate the self-consistency between InSAR measurements from two different viewing geometries, Sentinel-1 and COSMO-SkyMed detected displacement in Pistoia area from ascending and descending point of view are compared to each other (Figure 28).

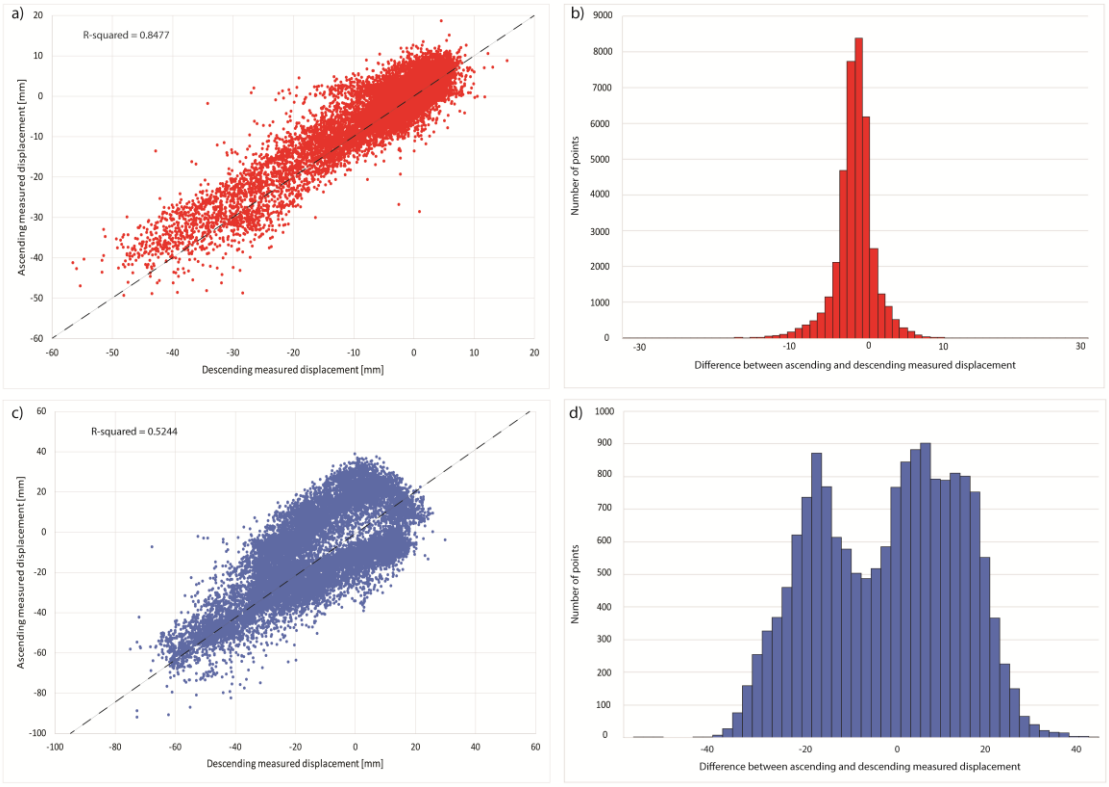

Figure 28 – Quantitative comparison between ascending and descending geometry for Sentinel-1 (a) and COSMO-SkyMed (c) constellations for the 2014-2017 period. In b) and d) are displayed the differences distributions between the two geometries.

The self-comparison of the two LOS measured displacement has been performed for the 2014-2017 period, using a two steps procedure. Firstly, PS data were resampled with a 100x100 meters regular grid, in order to eliminate the mismatch between the two datasets. Then, subsidence distribution for both tracks has been compared, to evaluate the self-consistency of both ascending and descending geometries for the same satellite constellation. Results of the analysis for Sentinel-1 satellite showed a good correlation between the two acquisition geometries (Figure 28a), with a coefficient of determination (R^2) close to 0.85 and an error distribution that converges through the 0 value (Figure 28b). Cosmo-SkyMed constellation, with a value of R^2 of about 0.52, shows a lower correlation between its two datasets (Figure 28d), with the distribution of difference between ascending and descending measured ground displacement characterized by the presence of two peaks around 20 mm and 7 mm (Figure 28d). Similar ground displacement values measured from two different acquisition geometries indicate that subsidence pattern is dominated by mainly vertical motion, evidencing the high reliability of the available PS-InSAR data. The major scattering of CSK data is caused by the higher intensity of the horizontal component detected by CSK acquisitions in Pistoia city (Figure 29c), that result in bigger differences in the LOS measured displacement from the two acquisition geometries. Such discrepancies could be ascribed to insufficient acquisitions, uncertainty in georeferentiation of points, seasonal biases, different temporal gaps of two geometries, and, most importantly, different looking sides.

4.2.7 LOS velocity decomposition

LOS velocity decomposition for the area of Pistoia has been performed for both Sentinel-1 and Cosmo-SkyMed PS-InSAR data (Figure 29). Sentinel-1 data were available for the entire extension of the Pistoia aquifer, while CSK data were only focused on the historical center of Pistoia city. The two datasets are in good agreement with each other in detecting ground displacement in Pistoia city, both in terms of intensity and spreading of the phenomenon.

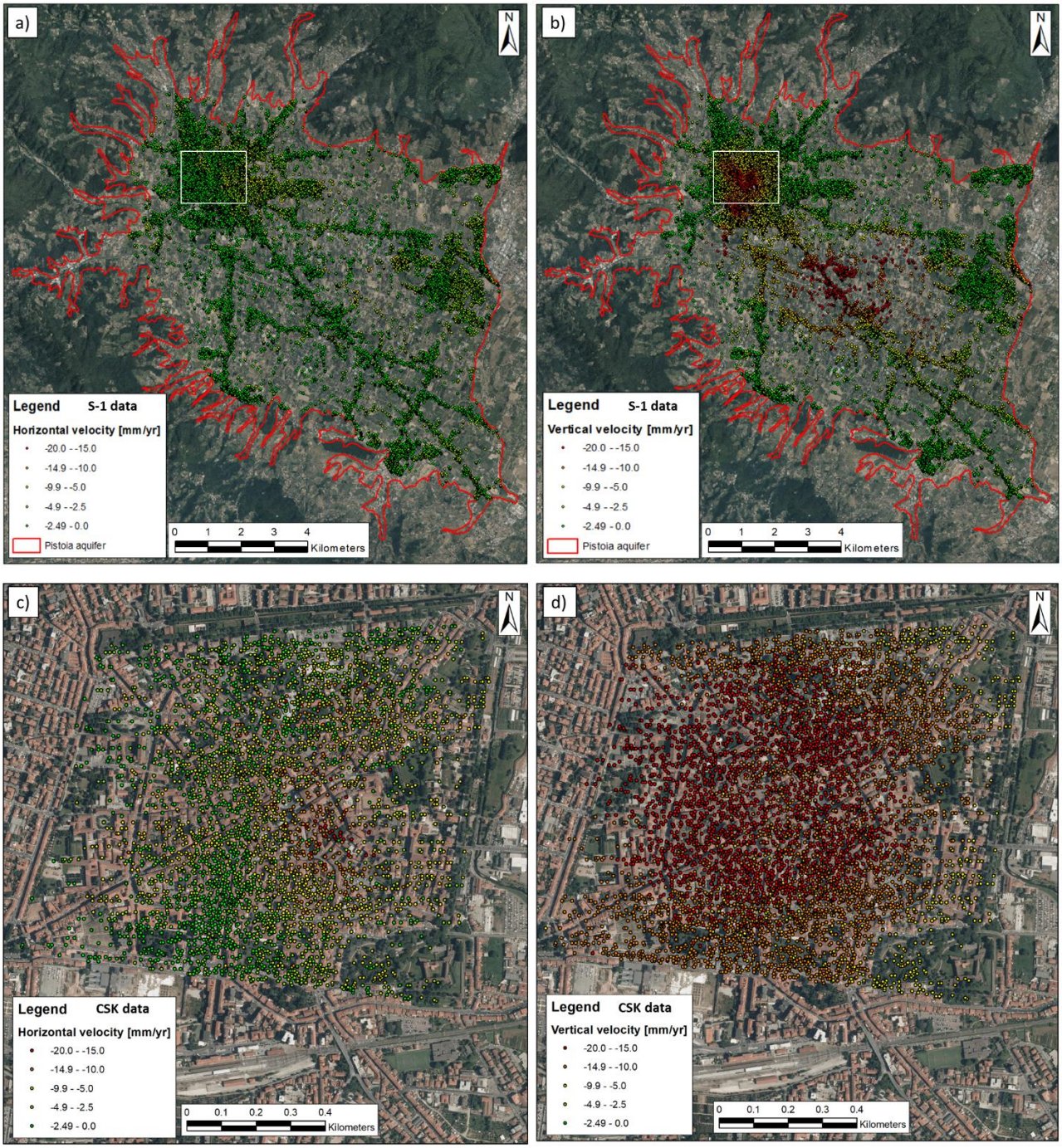

Figure 29 – a) Horizontal and b) Vertical decomposition of the LOS velocity measured by Sentinel-1 constellation during the period 2015-2017 and c) Horizontal and d) Vertical decomposition of the LOS velocity measured by Cosmo-SkyMed constellation for the same period. CSK data were available only for the two white rectangular areas in a) and b).

The prevalent vertical movement that characterize subsidence phenomena in Pistoia city is clearly visible in both S1 and CSK PS-InSAR data (Figure 29b and d), completely overwhelming its horizontal component (Figure 29a and c). Higher values of the horizontal component are detected by CSK acquisitions (Figure 29c) in the central – eastern part of the City, but they are not confirmed by Sentinel-1 data. However, such displacement patterns are sometimes detected in subsidence areas, related to the presence of lateral strains.

The ground deformation detected in Pistoia historical center with Sentinel-1 system needed to be validated with external data. The absence of GNSS and leveling measurement in the area led to the request of Cosmo-SkyMed (CSK) constellation (Covello et al., 2010) ascending and descending X-band images and their processing with a different processing algorithm.

Comparing the ground displacement data obtained from the two different constellations, Cosmo-SkyMed PS-InSAR data substantially confirm the subsidence pattern identified by Sentinel-1 data, both in terms of intensity and spreading of the phenomenon (Figure 7). Time series of ground displacement velocity for Pistoia city area, built from Sentinel-1 and CKS descending data and displayed in Figure 31, show a very good correspondence between the two analyzed dataset. During the February, 2015 – November, 2017 monitoring period, both constellations identified a decreasing ground displacement pattern with an average velocity of 20 mm/year and a maximum cumulative value of about 40 mm, characterized by the presence of clearly visible seasonal cycle. After that period and starting from January, 2018, Sentinel-1 data shows a stabilization of ground displacement in Pistoia historical center, but it was not possible to validate this information because of the unavailability of CSK data.

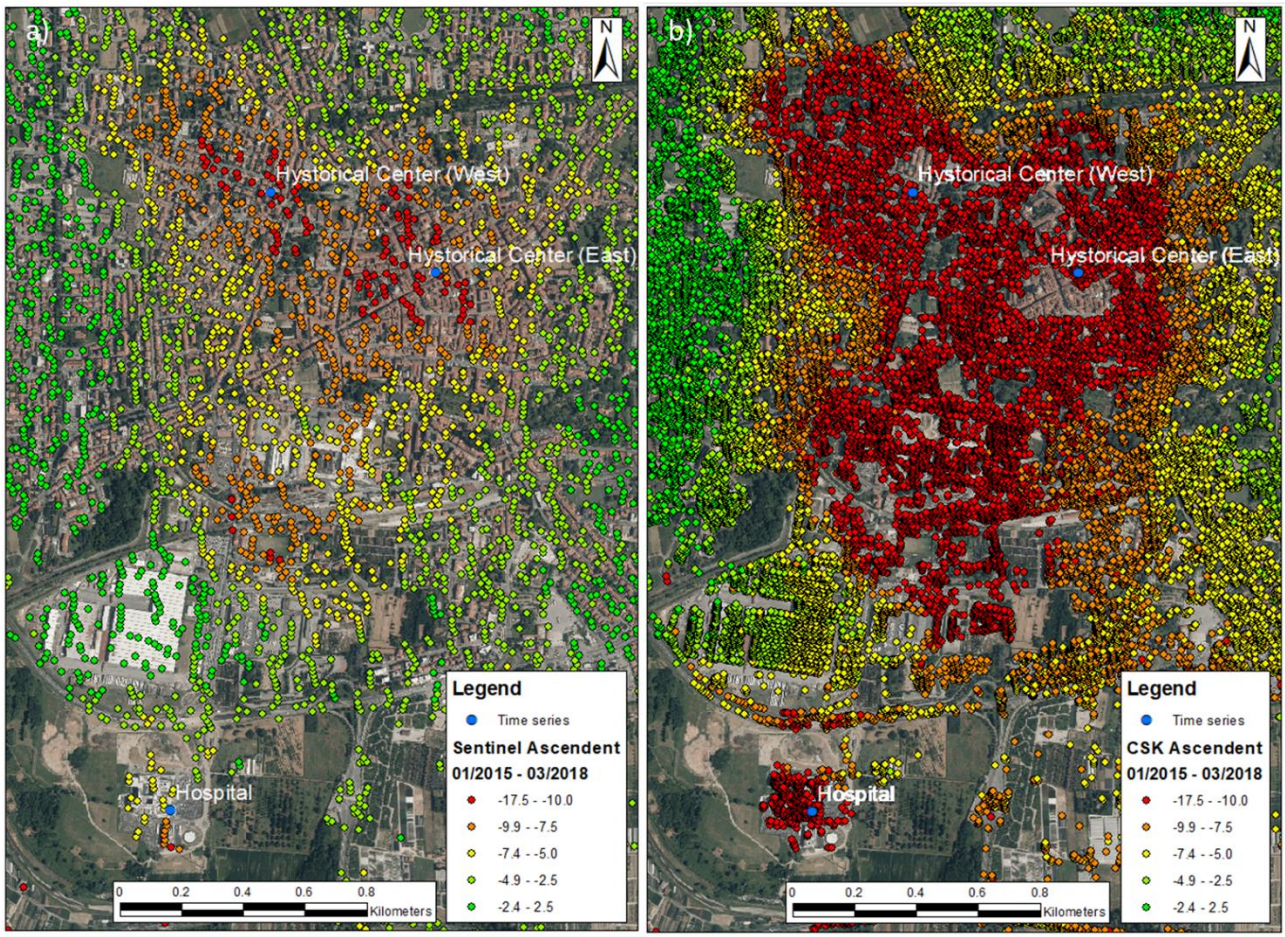

Figure 30 – Comparison between ground displacement velocity (in millimiters/year) in Pistoia area detected by a) Sentinel-1 InSAR data and b) Cosmo-SkyMed InSAR data for the 2015-2018 period.

Concerning the plant nursery area, Sentinel-1 PS-InSAR data for the 2015 – 2018 period confirm both previous Canuti et al. (2006) and Rosi et al. (2016) interferometric analysis (Figure 32a). Here, time series of ground displacement velocity built in two different locations (East and West side of the area) show an observed subsidence rate of about 15 mm/year, and a total lowering of 60 mm in the analyzed period (Figure 32b and c). As for time series of historical center, in ground displacement time series is clearly visible the strong influence of the seasonal variability, with cycles that displace the normal subsidence trend up to 10 mm.

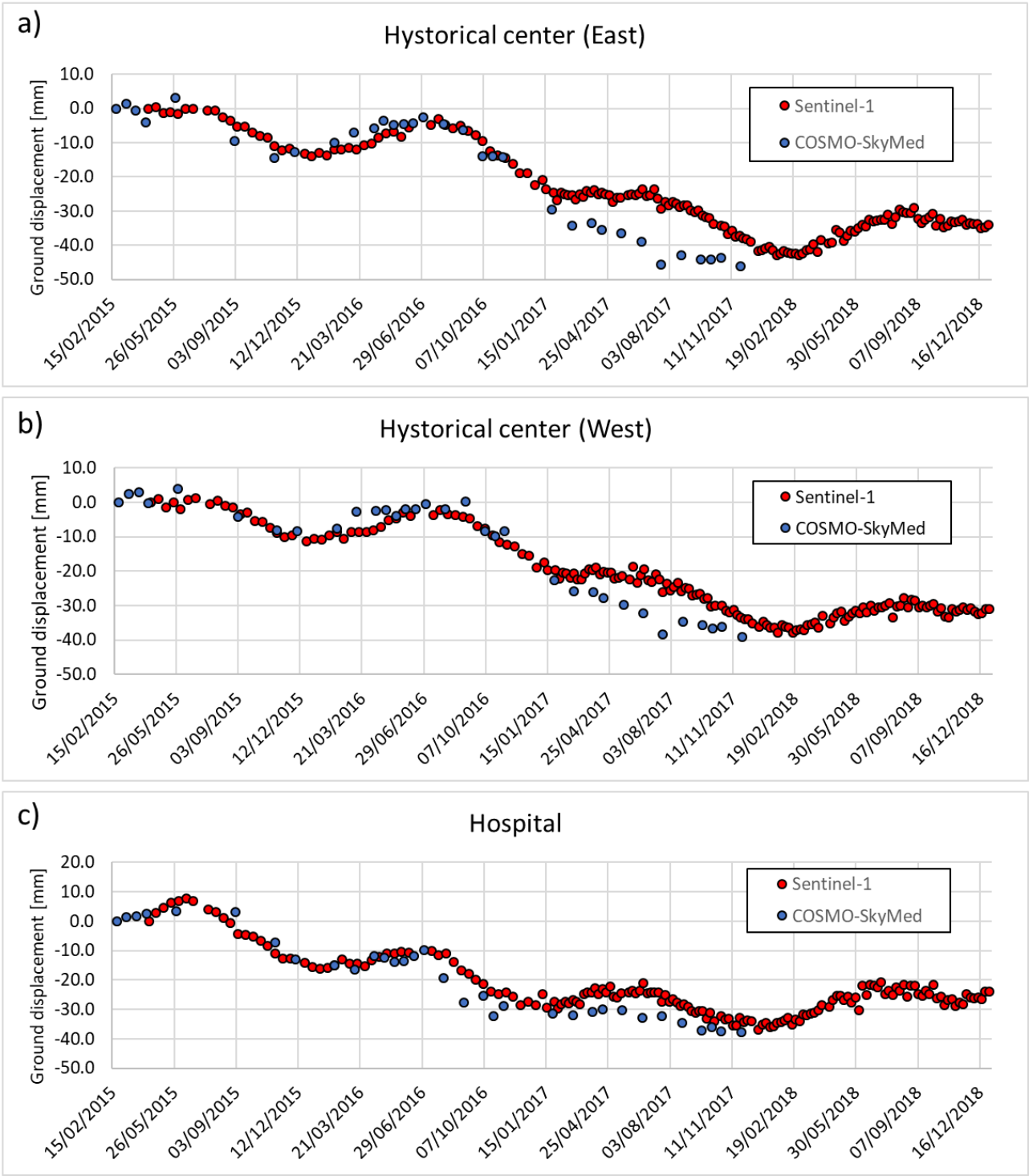

Figure 31 – Time series of ground displacement measured by descending Sentinel-1 and Cosmo-SkyMed constellation for a) Historical center (East side), b) Historical center (West side) and c) San Jacopo hospital area. Location of the three points is displayed in Figure 30.

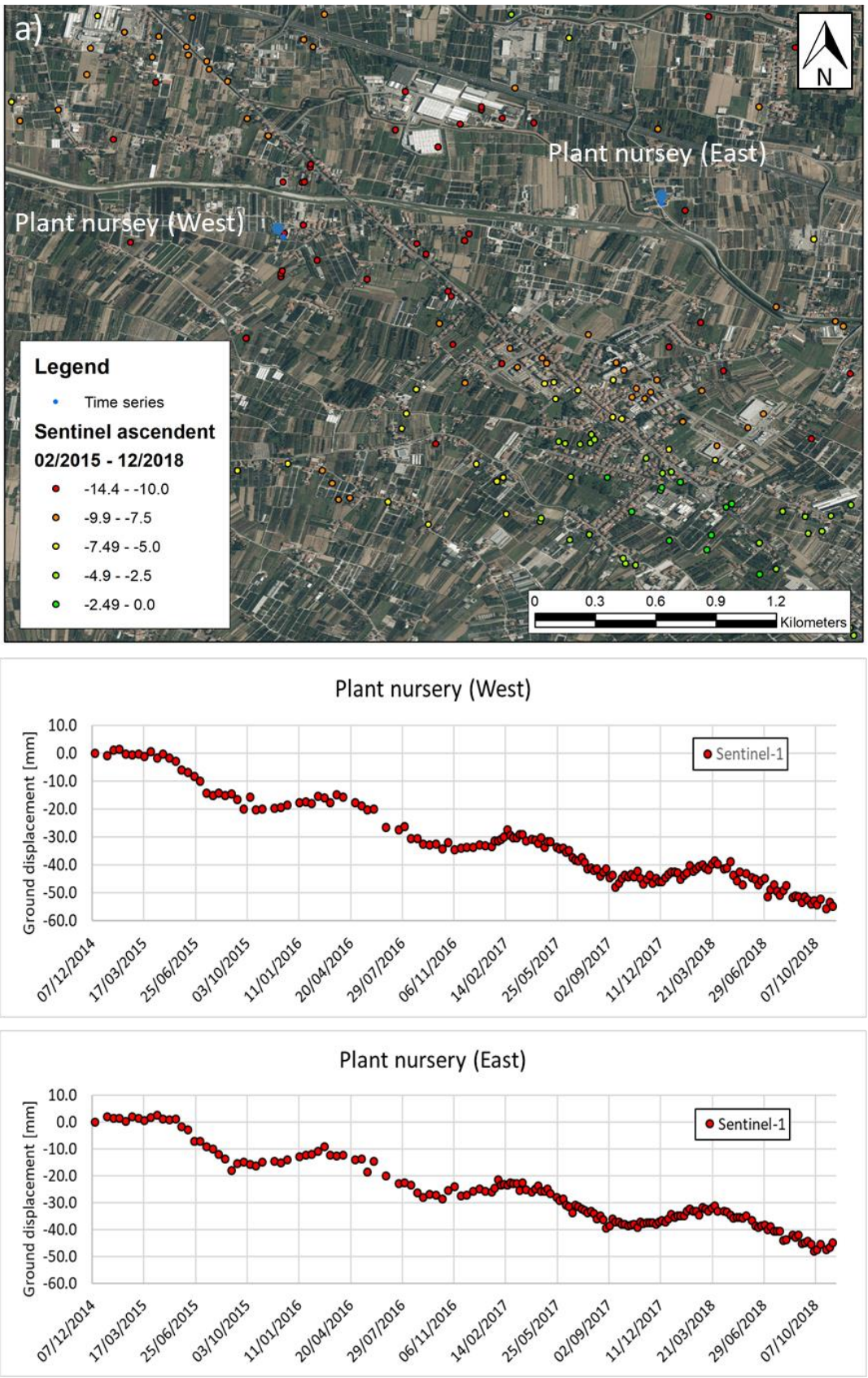

Figure 32 – a) PS-InSAR data for the plant nursery area, South – East of Pistoia city and b) Time series of ground displacement measured by descending Sentinel-1 for plant nursery area (East side) and c) Plant nursery area (West side).

4.3 Causes of Pistoia subsidence

Among the possible causes of the anomalous ground displacement observed in Pistoia city in recent years, ground settlement caused by an increase of the geostatic load related to the development of the historical center and the construction of new structures can be neglected.

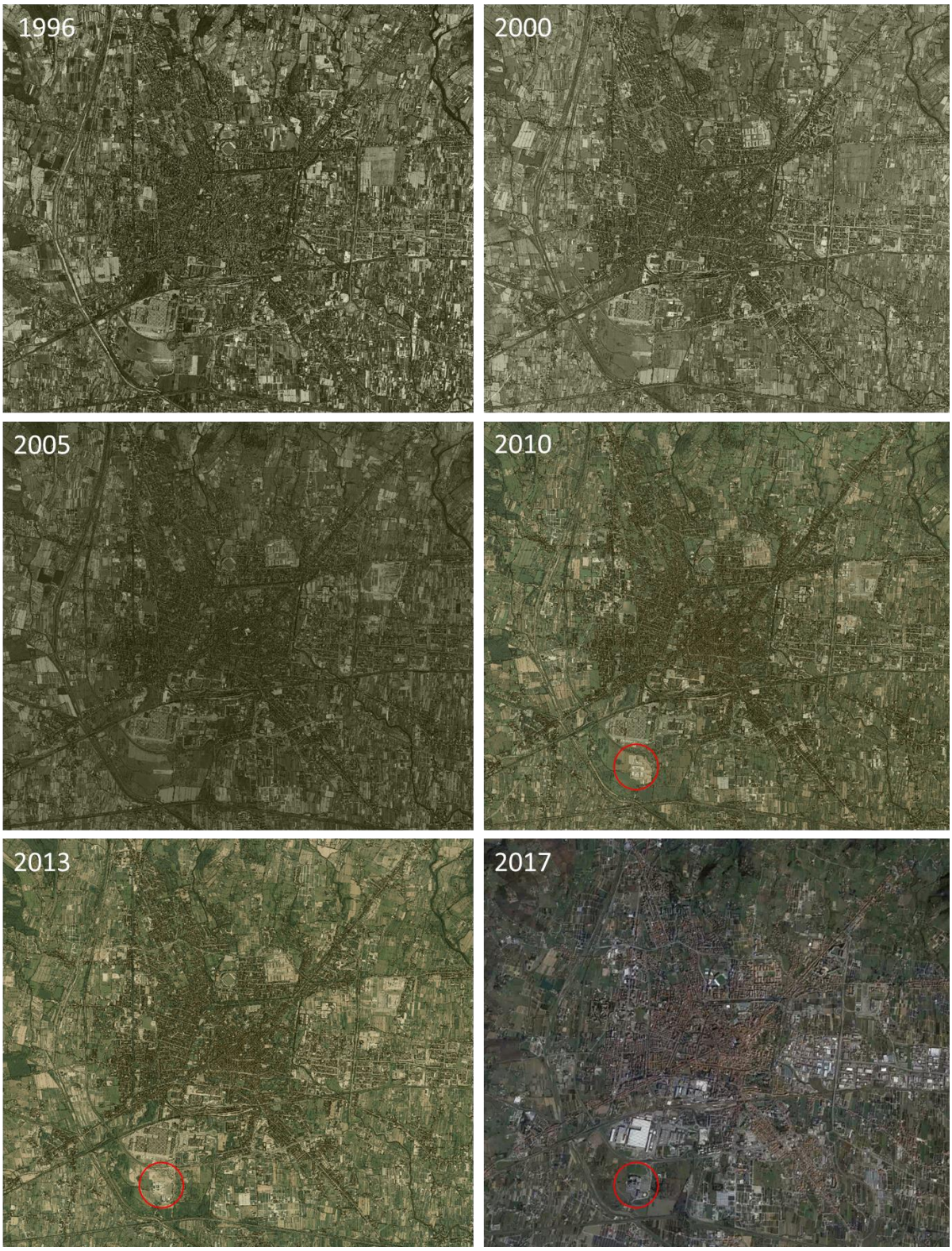

Figure 33 – Aerial image of Pistoia city from 1996 to 2017; red circles highlight the San Jacopo hospital area.

Figure 33 displays some aerial images of Pitoia city, acquired between 1996 and 2017. Pistoia was completely reconstructed and transformed during the 1950' and 1960', after the heavy damages suffered during the Second World War, but no substantial changes have been made in the last decades. The only important variation in the urban morphology occurred between 2010 and 2013, with the realization of the new San Jacopo hospital, in the southern part of the city (highlighted in red in Figure 33).

From the building typology point of view, the plant nursery area located South – East of Pistoia city, where high subsidence rates have been detected since the first 1990', is mainly characterized by the presence of light structures and greenhouses, with only few sparse private buildings. Here, as for the historical center of the city, the increase of the geostatic load due to building overload can be considered negligible.

A possible cause of the recent evolution of subsidence patterns in Pistoia area could be ascribed to the overexploitation of groundwater from aquifers that would have led, in the long term, to a decline of water levels. Usually, when a lowering of the water table occurs, unconsolidated sediments are subject to a decrease in pore water pressure and to a relative increase in effective stress. This leads to the compression of aquifers and confining aquitards and to a gradual land subsidence.

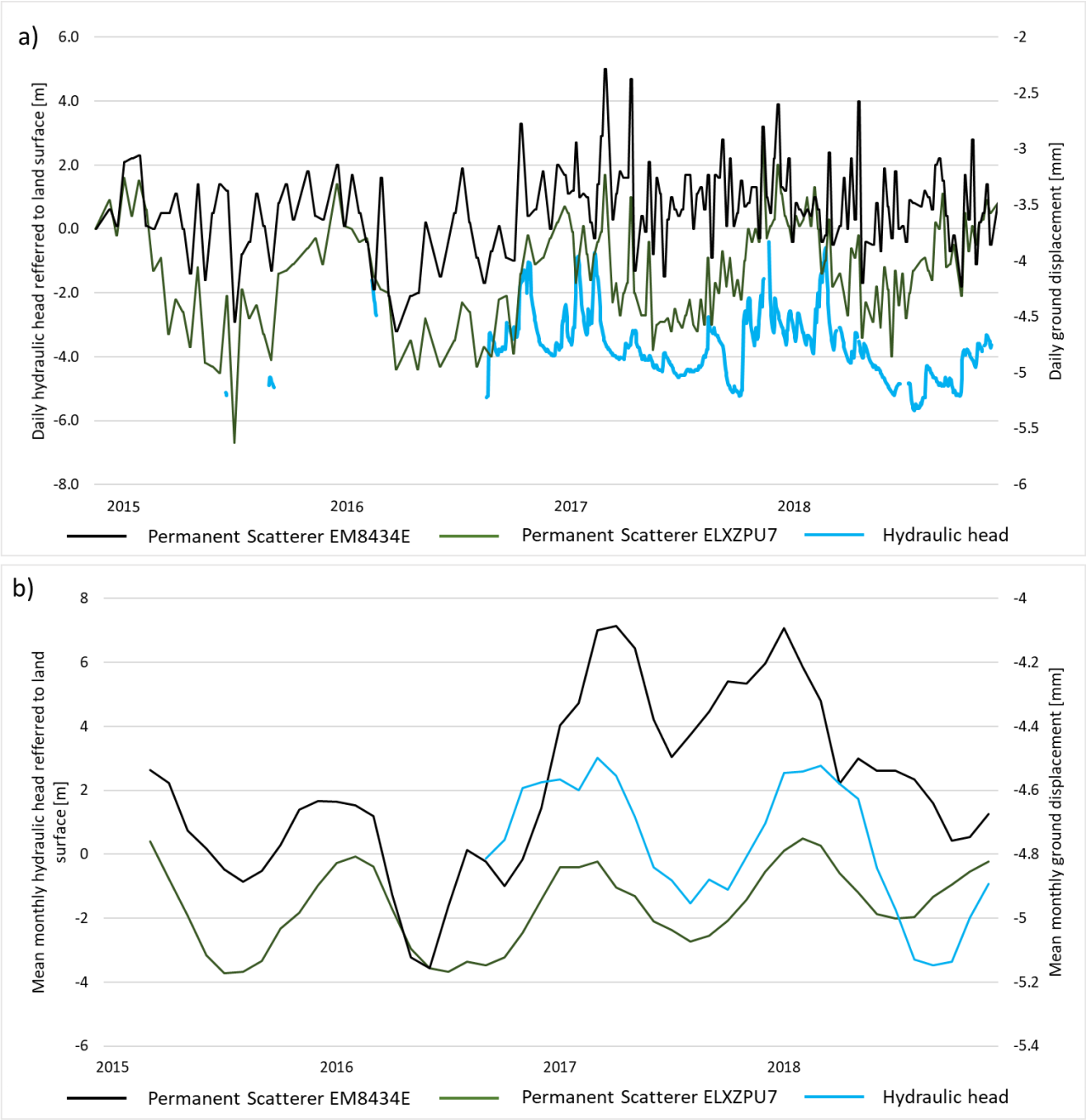

Figure 34 – a) Comparison between raw PS-InSAR data and raw hydraulic head measurement and b) Moving average processed data.

Many studies in literature relate ground lowering to groundwater over pumping (Carrera-Hernández and Gaskin, 2007; Burbey and M. Zhang, 2015; Chen et al., 2016). In Pistoia area, Del Soldato et al. (2018) ascribe subsidence occurring in the historical center and in the South – East part of the city to the widening of the depression cone caused by groundwater overexploitation from greenhouses and plant nurseries activities, that rapidly increased their number starting from the beginning of the 21st century. In order to detect a potential direct correlation between subsidence and hydraulic head variation in Pistoia area, a comparison between the available monitoring well data and ground displacement measured by PS-InSAR was performed (Figure 34a and b). Unfortunately, only one monitoring well with continuous hydraulic head data is available in the study area, located, from the ground displacement point of view, in a quite stable area. However, Figure 34a and b shows a very good correlation between seasonal hydraulic head variation and ground

displacement, considering both raw data and moving averaged data for the September, 2016 – December, 2018 period. The small amount of observed drawdown, completely recovered in the yearly cycle, it is not high enough to result in a permanent ground deformation, but the elastic behavior of the ground surface in response of the hydraulic head variation can be clearly detected.

4.4 In-situ damage field campaigns

In order to assess the level of damage that affect buildings in Pistoia city related to subsidence effects, two field campaigns were carried out. Distortion and cracks of structures from subsidence, occurring as differential settlement, may affect the structural health of buildings. Differential settlement induces angular and linear distortions in buildings structure, that become evident as inclined cracks in weaker areas (partitions and closures, Figure 35).

Figure 35 – Cracks evidence in Pistoia historical center buildings.

Subsidence phenomena in Pistoia historical center were firstly detected by Sentinel-1 PS-InSAR at the beginning of 2015. Due to short period, only low entity damages are emerged, but ground settlement will not stop as long as main causes of subsidence continue to occur, leading to the worsening of structures conditions.

During field surveys, performed on June 26th, 2018 and on August 1st, 2018, information on building characteristics as well as level and extent of damage, according to Del Soldato et al. (2017) damage assessment scheme, were recorded for a total of 227 buildings (Figure 36).

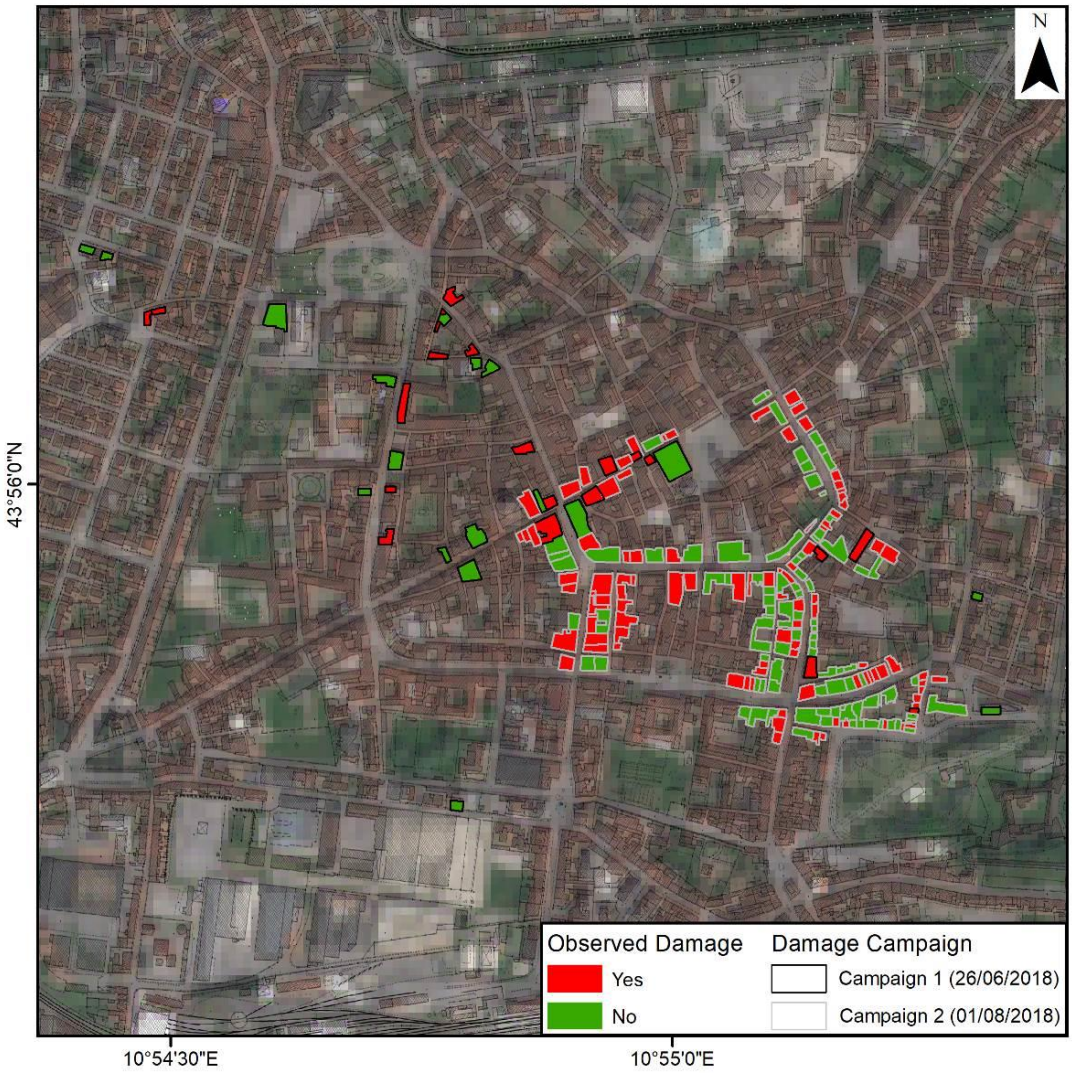

Figure 36 - Results of the in-situ damage detection field campaigns.

The 1:5000 official cadastral map of Pistoia (http://www.regione.toscana.it/-/geoscopio) was used for the identification of the buildings. It is worth mentioning that: a) these buildings were randomly selected trough several inspection tracks; b) the inspection of the buildings was performed from the outer part of the buildings, since no access was possible to the private properties; c) most of the inventoried buildings are located in the historical downtown of Pistoia, presenting very similar structural characteristics (mainly masonry buildings); and d) the inventoried damage are quite low, varying between D0 and D2 according to the scheme proposed by Del Soldato et al. (2017).

For each surveyed building, the vertical displacements were derived from the ascending and descending PS data available from Sentinel-1 and COSMO-SkyMed datasets. The combination of the level of damage of the recorded buildings and their associated vertical displacements (i.e. settlements) allowed to build the fragility curves of surveyed building for each category of damage.

5 Models development

5.1 Hydrologic model

5.1.1 Hydrologic model structure

MOBIDIC code works with a modular structure constituted by two main processing phases, the geographic data pre-processing and the real hydrologic computation, in order to optimize the calculation procedure. Before to execute the hydrologic computation, the geographic data must be analyzed by the pre-processing module, to produce a single database containing all the geologic and topographic information about the study area. All input data, simulation parameters and computation options are managed by a configuration file, that need to be set before the calculation phase starts. Global hydrologic calibration parameters are also contained in the configuration file.

Following the modular structure of the processing phase, input data are divided in:

- Geographic data, containing information concerning soil properties, geology and geomorphology of the watershed;

- Hydro-meteorological data, containing information about all meteorological variables affecting the hydrologic process.

Geographic data

MOBIDIC geographic input are described by a set of data in vectoral or raster format, depending on their graphic nature. The *raster* format is mainly used to represent geographic data with areal valence, while the vector format is used to represent geographical data with linear or punctual valence, for which more precision in georeferentiation is required. Both type of formats have required or optional data, depending if their parameters values can be given, also as a unique *default* value (optional data) in the configuration file, or if they need to be explicitly expressed by a raster or a vector file (required data). Further geographic input data, called additional data, are completely at user discretion and can be totally omitted, even as default values.

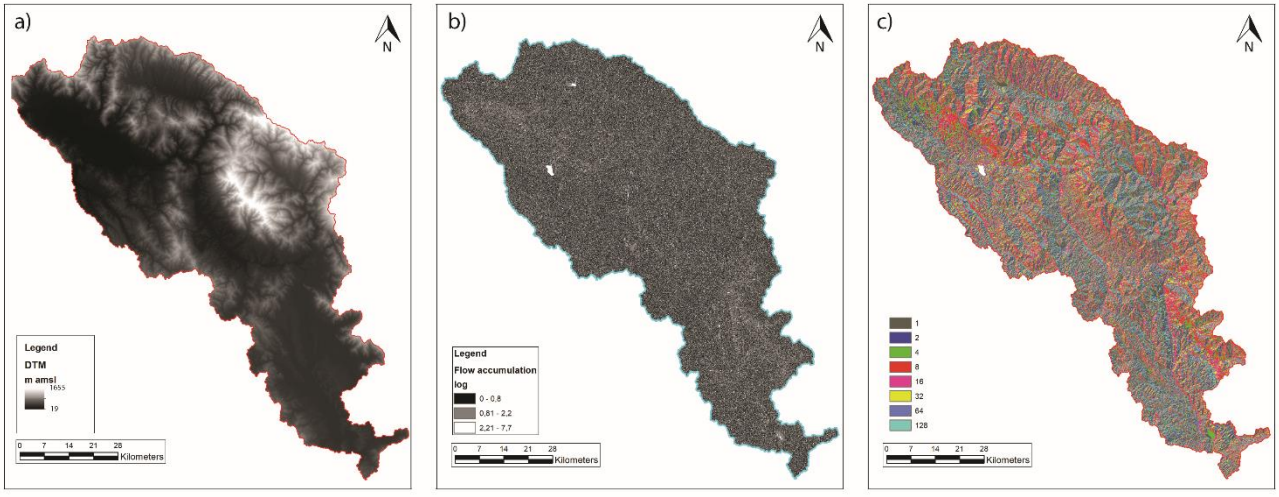

Figure 37 – MOBIDC required geographic input data: a) Watershed digital elevation model, b) Flow accumulation raster file and c) flow direction raster file.

The digital terrain models (DTM) raster file is the primary reference for the identification of the watershed geographical extension and, starting from it, both flow direction and flow accumulation required raster files can be directly obtained (Figure 37).

As states before, optional raster data can be defined as a unique default value for all the watershed in the configuration file or they can be expressed with an input file. Even if considered optional raster data, some parameters have a high influence in the hydrologic simulation and should always be explicitly described. Among such parameters, an important role in the hydrologic processes control is played by W_g, W_c, K_s and A_b variables (Figure 38).

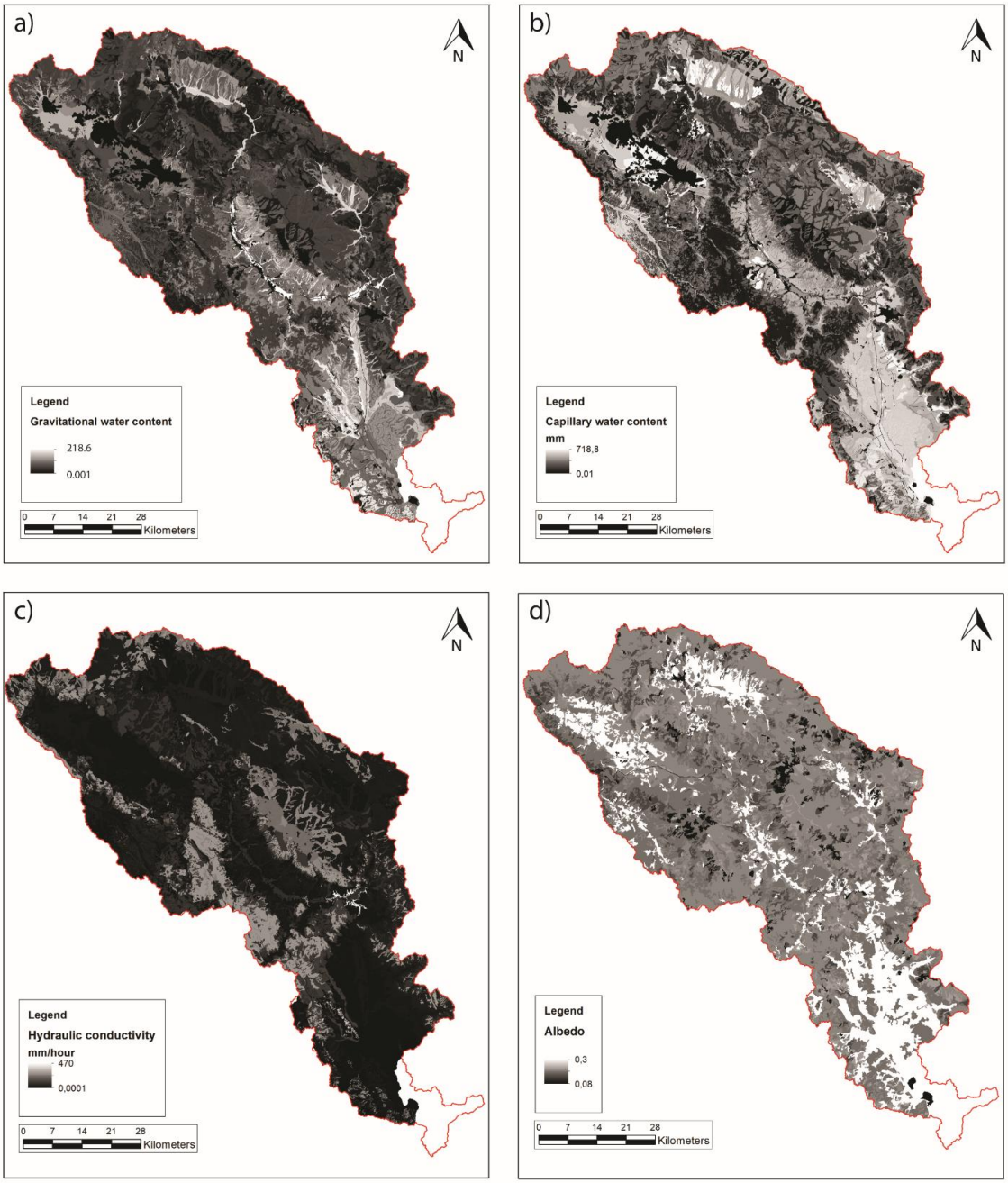

Figure 38 - MOBIDC optional geographic input data: a) Gravitational water content, b) Capillary water content, c) Hydraulic conductivity and d) Land surface albedo.

W_g, W_c represent respectively the capacity of the soil fraction with prevalent gravitational behavior (that can be assimilated to the saturation water content at field capacity) and the capacity of the soil fraction with

prevalent capillary behavior, that can be assimilated to the difference between field capacity and residual water content at the wilting point. K_s is the saturation hydraulic conductivity of the soil superficial layer and A_b represents the albedo coefficient of land surface.

For the portions of the watershed without geographic raster data coverage, MOBIDIC code uses a user defined default value contained into the configuration file to fill the gaps.

Among vector data describing the basin, required input files are those concerning the river network, represented by a vector file in which every river branch is a different segment of a polyline (Figure 39).

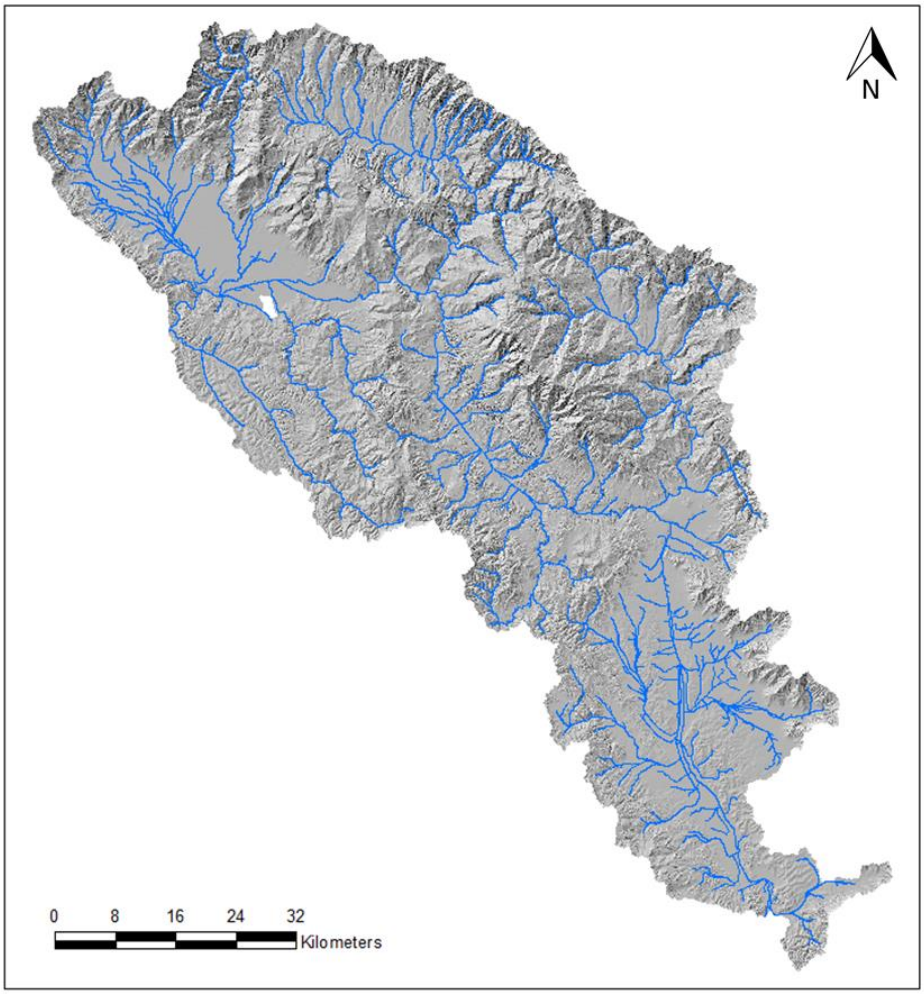

Figure 39 – River network of the Arno river basin, upstream of Pistoia area, as a shapefile format.

Hydro-meteorological data

In MOBIDIC code, the temporal length of the simulation is defined by the hydro-meteorological data time series. The hydrometeorological data for long-term hydrologic simulation must be referenced to point measurement stations located within the modelled watershed, as defined by the areal extension of the geographic data (Figure 40).

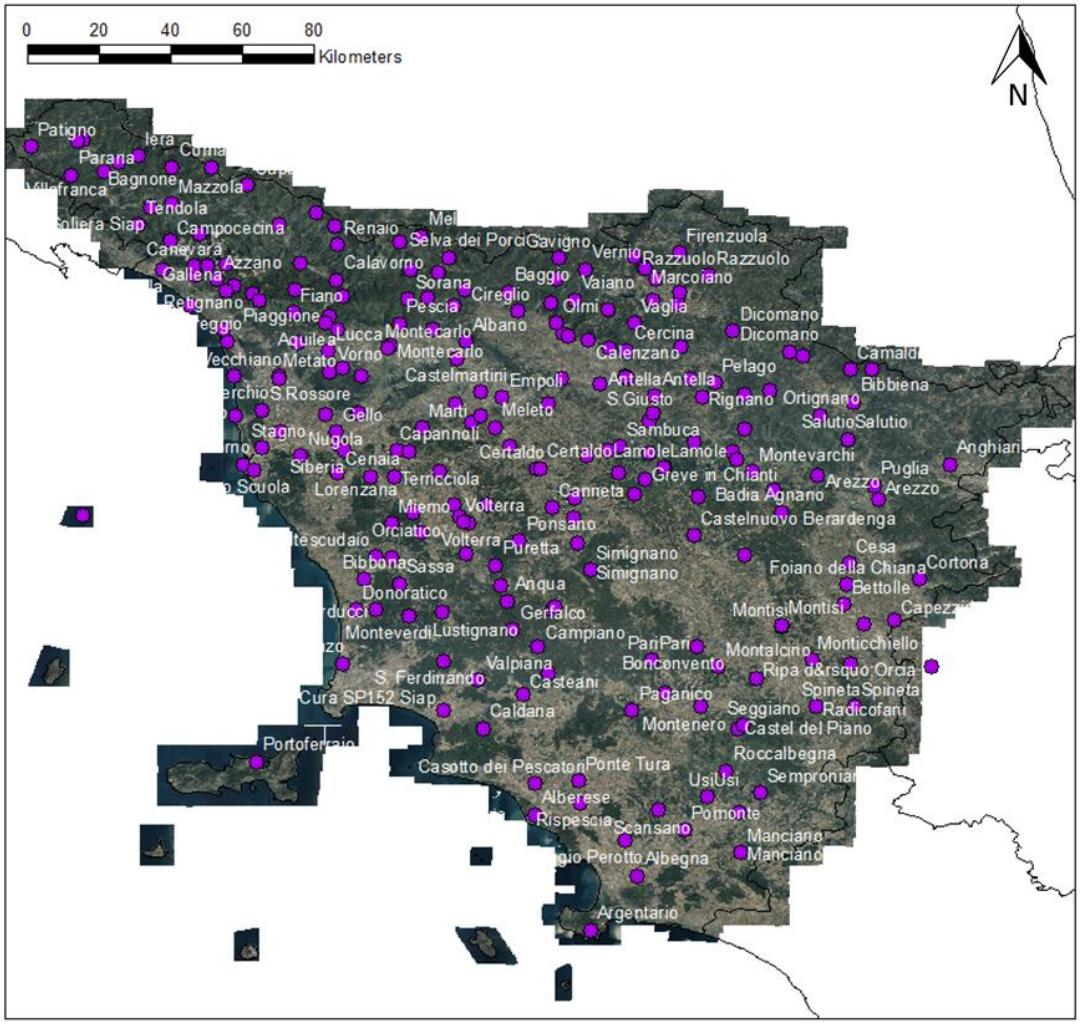

Figure 40 – Measurement stations for precipitation in Tuscany region.

Then, MOBIDIC uses the Voronoi polygons interpolation techniques in order to distribute the punctual information all over the model domain, following the equation:

$$X_C = \frac{X_A}{d_{AC}^k} + \frac{X_B}{d_{BC}^k} + \cdots \tag{53}$$

Where X_A and X_B are the values of the considered variables in the measurement stations A and B, d_{AC} and d_{BC} represent the distances between the measurement stations A and B and the interpolated point C, and *k* exponents are coefficients that count 8 for precipitation and between 2 and 6 for the other variables.

The hydrometeorological variables that currently used in the hydrologic calculations are (1) precipitation, (2) minimum and (3) maximum temperature, (4) air humidity, (5) shortwave solar radiation and (6) wind speed.

5.1.2 Hydrological model setup

The hydrological model has been set up considering two different scale approaches, in order to assess the response of MOBIDIC code at different resolutions (Figure 42). The large-scale approach simulates the hydrological processes occurring in Pistoia area considering, as model domain, the entire portion of the Arno river basin upstream of the Gonfolina closing section. The Ombrone basin and the Pistoia aquifer are closely connected with the Prato and Firenze sub basins, and the simulation of this whole area should avoid losing any type of interaction between the hydrologic and hydrogeologic components of the three sub basins.

The small-scale approach models the hydrology of the only Ombrone basin, focusing on the processes occurring in a smaller area, with a higher resolution of the input variables that guarantee a better fit in the calibration phase between observed and simulated parameters.

As stated before, MOBIDIC deals with the energy balance by solving the heat diffusion equations in the soil–vegetation system. The approach to be used for the surface energy balance can be chosen between (1) a 5-layers scheme, (2) a 4-layers snow scheme, (3) a 2-layers scheme and (4) a 1-layer scheme. For the current study, a 1L (1-layer) surface energy balance scheme has been adopted.

The fluvial discharge, simulated by means of the general Saint-Venant equation, may be computed with four different methods, to be used as conceptual schemes for the river flow routing: the lag method, the linear reservoir method, the Muskingam method (McCarthy, 1938) and the Muskingam–Cunge method (Cunge, 1969). In this study, the linear method was selected.

In MOBIDIC, surface water withdrawals can also be simulated, specifying their location within the watershed, the volume of water extracted and the relative derivation laws, that specify the percentage of water withdrew from the surficial network, as a function of the year period, for each different type of water derivation (Figure 41).

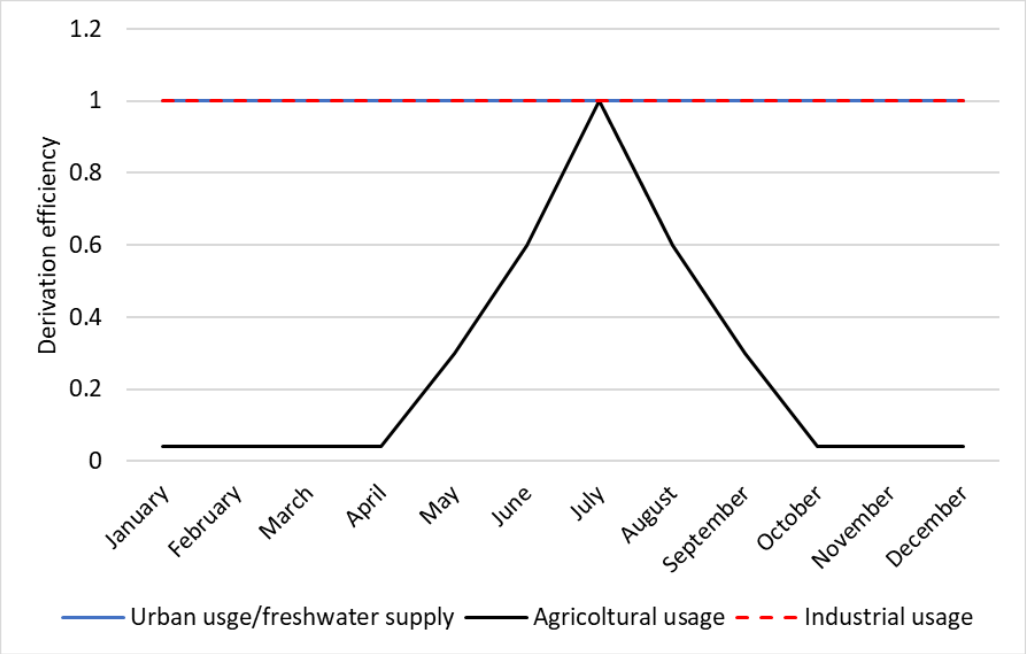

Figure 41 – Temporal laws of each type of water derivation from surficial network depending on the year period.

For Tuscany region, quasi-continuous meteorological data time series are available for the January, 1992 – December, 2017 period. Following MOBIDIC structure, in which the temporal duration of each simulation is

defined by the hydro-meteorological data time series length, a 26 years long model has been implemented (1992-2017). The first two years of simulation (1992-1993 period) were used as model "warm-up", in order to give enough time to the model to fill up its reservoirs and to reach stable initial values of involved variables. The calibration phase involved 5 years of the simulated temporal domain (2010-2015), chosen for its good availability of continuous field data, in a period as close as possible to the maximum magnitude of the observed subsidence events.

The calibration of the MOBIDIC global hydrologic parameters has been carried out by means of the calibration module integrated in the code. Such module searches the minimum of the objective function given by the weighted sum, for each available hydrometric series, of the normalized differences between measured and computed data. In the objective function, four different parameters can be considered: discharge, cumulative flow volume, flow duration and peak discharge, and for each term the relative weight in the objective function must be specified.

In the calibration phase, 4 river gauging stations (Pontelungo, Poggio a Caiano, Dicomano and Scandicci) have been considered for the large-scale model (called "Gonfolina model") and 2 measurement stations (Pontelungo and Poggio a Caiano) for the small-scale model (called "Ombrone model"). These stations, located within the respective watershed, record quasi-continuous river discharge data for the whole calibration period (2010 to 2015, Figure 42).

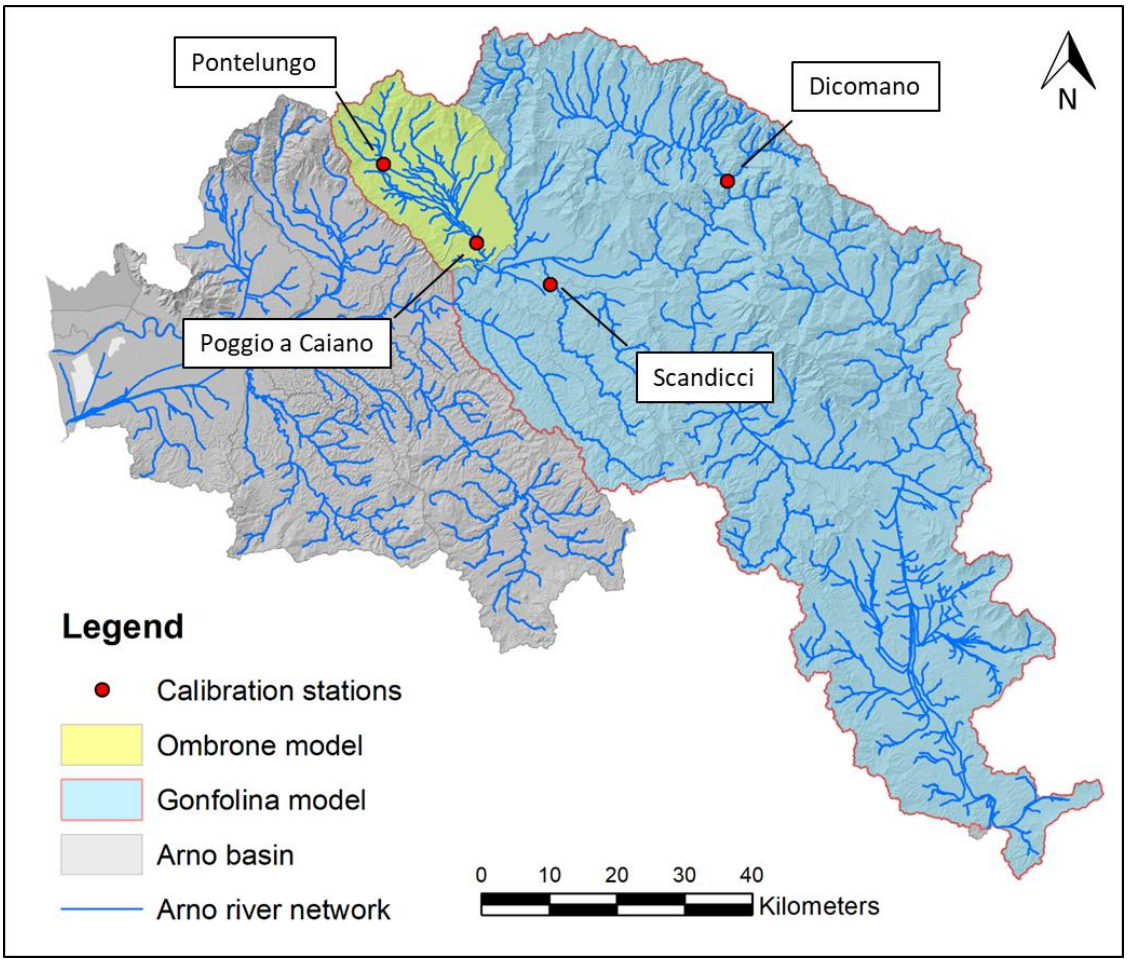

Figure 42 – Model domains for small (Ombrone model) and large scale (Gonfolina model) simulation and river gauging station used for the two models calibration.

The focus of the calibration phase was to identify the better value of the four hydrologic parameters considered by MOBIDIC simulations, in order to reach the best fit between model values and observations. The initial values for the global hydrologic calibration parameters have been obtained from the Arno river hydrological model, carried out with MOBIDIC by Castelli et al. (2009), and currently in use as a flood risk assessment tool by the Arno river Basin Authority (AdB, Table 1).

Table 1 – Global hydrologic parameters and their initial values in the calibration phase.

Parameter	Unit of measure	Description	Initial value
γ	$[T^{-1}]$	Percolation coefficient	$1.026 \cdot 10^{-7}$
κ	$[T^{-1}]$	Adsorption coefficient among gravitational and capillary soil	$1.336 \cdot 10^{-6}$
β	$[T^{-1}]$	Hypodermic flow coefficient	$2.44 \cdot 10^{-6}$
α	$[T^{-1}]$	Hillslope flow coefficient	$5.0 \cdot 10^{-5}$

5.2 Hydrogeologic model

5.2.1 Hydrogeological conceptualization

The Ombrone basin covers an area of about 500 km^2 and represents a sediment-filled structural basin with two major lithologic units: a Cretaceous – Paleogene bedrock and a fluvial-lacustrine valley fill of heterogeneous sediments. Despite the big amount of boreholes data available in Pistoia city area, a proper hydrogeologic characterization, needed for the development of the conceptual model for the hydrogeological modelling of the basin, still does not exist. Because of this, the first phase in the groundwater model development procedure concerned the realization of a conceptual model that discretize the numerous geological and stratigraphic information available for the study area. The first step in the conceptual model development started with the definition of the limits of the Ombrone aquifer (also known as Pistoia aquifer). A planar discretization of the aquifer has been already carried out by the Arno river basin Authority and these data are freely available online. The northern, western and southern borders of the domain have been set in correspondence of the limit between alluvial sediments constituting the aquifer and the Cretaceous – Paleogene rock that underlie the basin. Such formations are considered to be of many orders of magnitude less permeable than the basin fill. The eastern side of Pistoia aquifer corresponds to Agna stream, that also define the institutional border between the province of Prato and Pistoia.

The aquifer geometry has a high level of detail and has been simplified, especially in its borders, to avoid convergence issues in MODFLOW simulations (Figure 45a). Since all the sediment pack that fill the basin plays an important role in subsidence control and need to be considered in the hydrogeologic model, the lower limit of the model domain has been set in correspondence of the stratigraphic contact between the basement and the valley fill. The effective thickness of the sediment fill has been identified thanks to the available boreholes data and to the information extracted from old stratigraphic maps of the area (Figure 43).

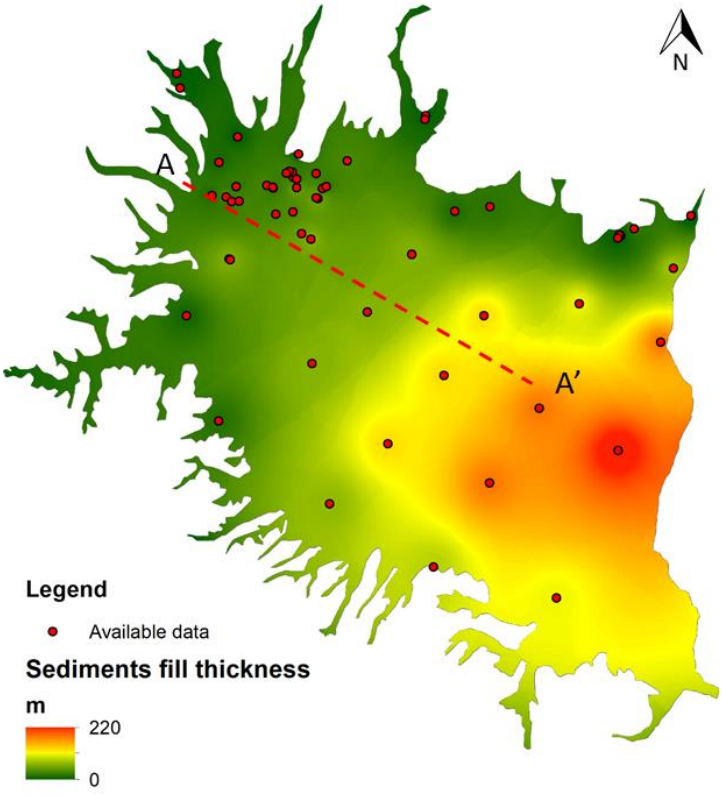

Figure 43 – Sediment fill thickness of the Pistoia aquifer within the Ombrone watershed.

The top of the model grid was defined using the ground surface elevation and was determined by using a 10 meters digital elevation model of the area.

The vertical domain was discretized into three model layers that were used to represent three aquifer zones (Figure 44). Model layers 1 corresponds to the near surface phreatic aquifer, directly connected with the Ombrone river network, and characterized by a general average thickness of 8-10 m all over the plain. An exception is represented by the thick gravel and pebbles levels in the northern portion of the area, coinciding with the Ombrone River fan delta.

Beneath the surficial aquifer, alluvial deposits can be divided into two sub layers with different sedimentary facies (Capecchi e al., 1976 a; Capecchi e Pranzini, 1986). The deeper layer is mainly constituted of Upper Pliocene lacustrine sediments, generating sand lenses embedded into a finer matrix that limit the aquifer permeability. The shallower layer is comprised of coarser Pleistocene materials, where the fluvial component becomes predominant and constitutes a higher permeability layer. This part of the vertical model domain is simplified by means of two layers, representing the middle-zone (layer 2) and the deep-zone (layer 3) aquifers, respectively. The bottom of layer 2 was estimated based on boreholes data available for the study area, while the bottom of layer 3 was set in correspondence of the stratigraphic contact between the basement and the valley fill.

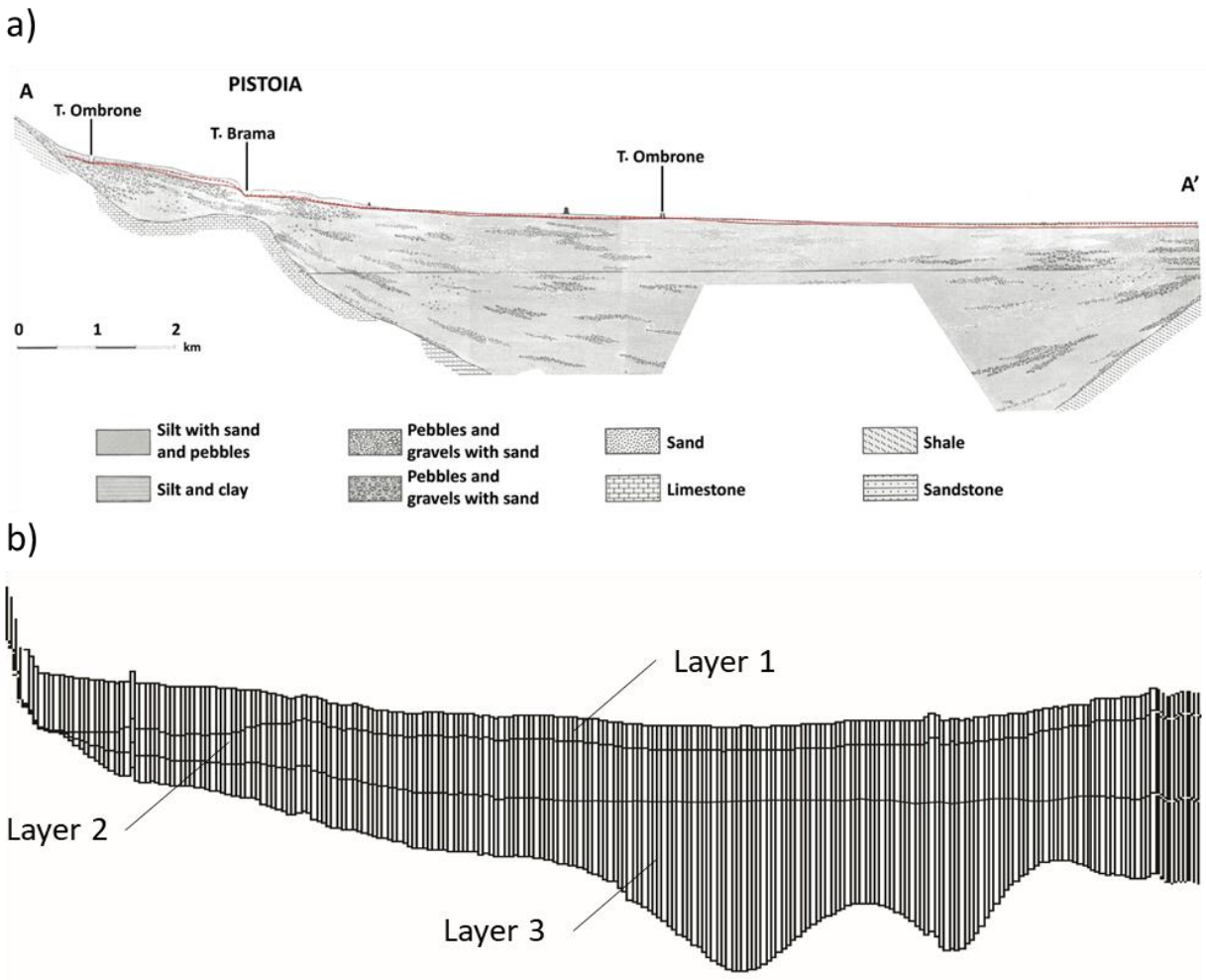

Figure 44 – a) Cross section of the Pistoia aquifer along the A-A' trace in Figure 43 and b) vertical discretization of the groundwater model in MODFLOW.

The model area is 18.0×18.0 km^2 wide and has been discretized into 360×360 cells using a uniform cell size of 50 m. The model includes a total of 388,800 cells, where 123,417 are active.

5.2.2 Hydrogeological model setup

The definition of boundary condition represents a critical aspect during the development of a groundwater model, and it needs to take into account, besides the physical limits that circumscribe the model domain, also water fluxes out from or into the aquifer system. Main water input for the Pistoia phreatic aquifer are represented by the influence of the surficial network, representing a constant source of water especially during the rainiest months of the year. The river system has been modelled in MODFLOW code using the river boundary conditions (RIV package, Figure 45b). Confined unit recharge is quite limited in short term periods and can be identified by the percolation water that flows from the high permeable sandstone formations that underlie the basin into the aquifers. This contribution has been taken into account in layers 2 and 3 by setting injection well cells (modelled with MODFLOW WEL package) all around the model domain (Figure 45c and Figure 45d). Some additional water exchanges, in both directions, may occur in the East side of the basin, where a real physical limit with Prato aquifer does not exist, but this amount is expected to be quite small. The influence of Prato aquifer has been considered by setting a General Head Boundary condition (GHB package) all along the East side of the model domain. Another low entity recharge source for the surficial layers is represented by the direct precipitation on the valley floor, modelled in MODFLOW with the RCH package.

Outflows from the aquifer system mainly occur from groundwater extraction for freshwater supply and irrigual purposes, especially for the numerous flower and plant nursery activities present at South-East of Pistoia city, representing one of the main economical aspect of the municipality. Other outputs are represented by water restitution to the river system and by underground fluxes through adjacent aquifers.

Pumping wells are widespread all over the basin, with the higher extraction rate located along the Ombrone river, in the West side of the basin. Location of pumping wells and their extraction rate are freely available online from Arno river basin Authority database. Pumping wells location in the vertical domain of the model has been selected by means of their estimated depth. Groundwater extraction occur from a total of 5910 extraction points (2397 for the surficial aquifer, 2844 for middle-zone aquifer and 669 for deep-zone aquifer) with a total pumping rate of about 50.00 Mm^3/yr. Wells have been modelled by means of the WEL package.

Since the basin sediment fill is interrupted by the surrounding reliefs that are considered to be of much lower permeability than the basin-fill sediments, the lateral boundaries of the model are all modelled as no-flow conditions for all three layers.

Preconditioned Conjugate-Gradient (PCG) was used as numerical solver, with a HCLOSE (head change criterion for convergence) and RCLOSE (Residual criterion for convergence) values set to 0.001 and 1. The number of outer and inner iterations were set to 200 and 30, respectively.

The groundwater model includes recharge (RCH), general head boundary (GHB), well (WEL) and river (RIV) boundary conditions.

The groundwater model has been constructed using MODFLOW-2000 (McDonald and Harbaugh 1984; Harbaugh et al. 2000) with Groundwater Vistas as user interface (Rumbaugh and Rumbaugh, 2004).

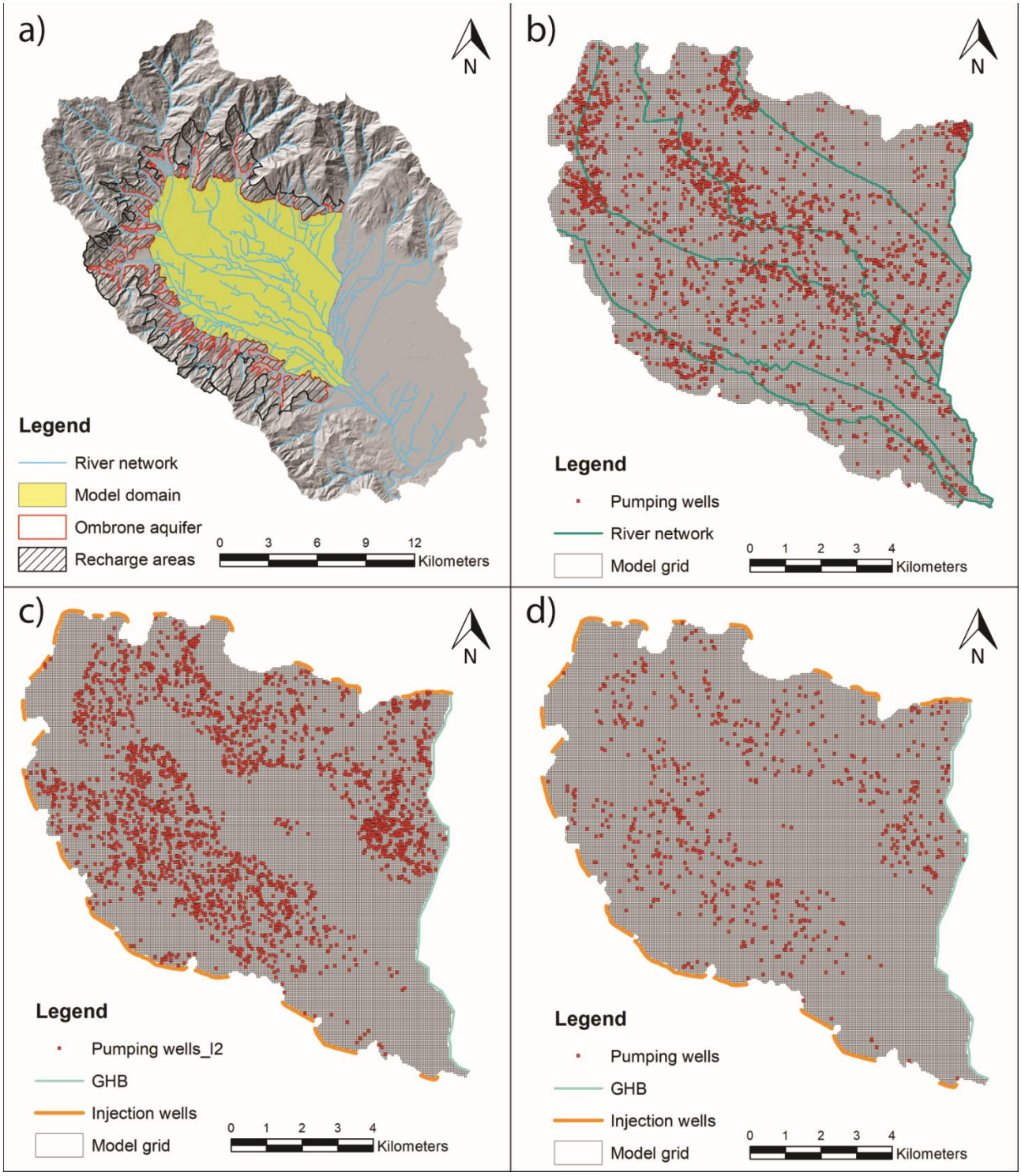

Figure 45 – Groundwater model of the Ombrone aquifer: a) Location of the Ombrone aquifer, of the simplify model domain and of the aquifers recharge areas within the Ombrone watershed; b) First layer of the three-layers hydrogeological model; c) Second layer and d) Third layer of the hydrogeological model.

Time discretization

The final goal of the developed groundwater model concerns the representation of the subsidence pattern affecting the surrounding area of Pistoia city, and the temporal discretization of the model was chosen to reflect this purpose. Since the total amount of measured subsidence in the area has characterized by values

in the order of millimeters per year, a monthly-based temporal step (or less) would have given an oversized resolution if compared with the aim of the model. Moreover, since subsidence modelling involves many years of simulation, the computational burden of a too fine temporal resolution would be too onerous. This resulted in the setup of a 25 stress periods model, composed by a stationary stress period and 24 transient ones, corresponding to the 1994-2017 period, with year as a unit time step. The lengths of the stress periods varied from 10 days for the stationary stress period to 365 days for the transient stress periods.

In order to characterize the mean yearly behavior of the main hydrogeological processes occurring in Pistoia aquifer, a 13 stress periods groundwater model has also been implemented (1 stationary stress period + 12 transient ones), considering the monthly averaged information obtained by MOBIDIC for the 1994-2017 simulation period.

Model calibration and validation

Data from 1994 and 1996 hydraulic head maps of Ombrone aquifer have been used for steady state calibration; this period represents a quite stationary period with respect to groundwater level, with very low variations registered in the measured hydraulic head. Moreover, continuous measurements of hydraulic head changes for the piezometer P13, available starting from January, 2011, were used to validate the transient simulation (Figure 46).

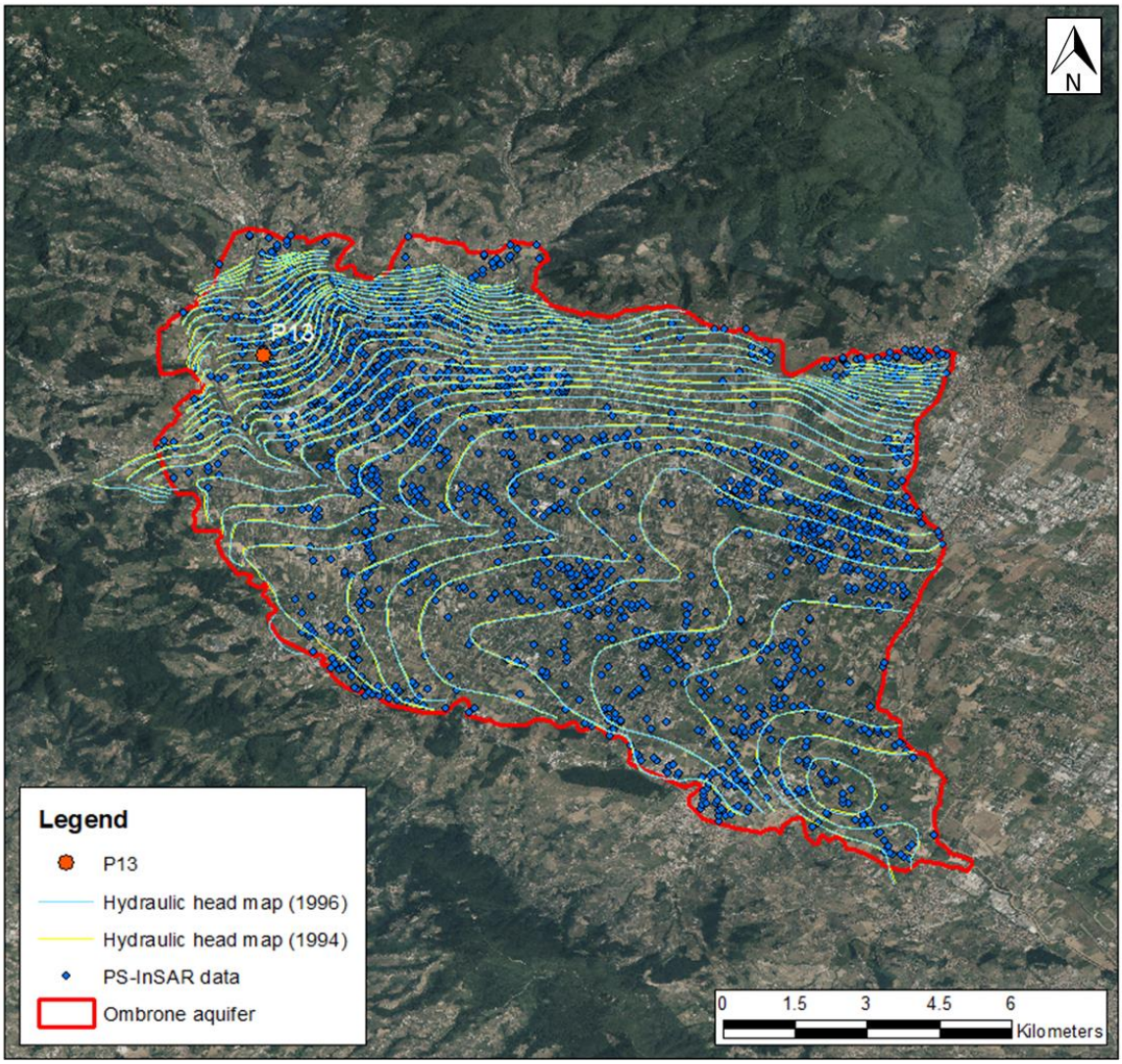

Figure 46 – Hydraulic head data and PS-InSAR measurement used for groundwater model calibration.

Hydraulic head or drawdown data are the most popular type of observation data used for parameter estimation in groundwater flow models (Poeter and Hill, 1997). However, in regions where a complete network of hydraulic head monitoring system does not exist, obtaining sufficient data can be problematic, because the installation of a sufficient number of observation wells for basin-wide investigations can be very expansive. With the improvement of technology for detecting land deformation over large spatial regions by means of InSAR or PS-InSAR techniques, the acquisition of millimeter-scale subsidence data is becoming easily available and inexpensive. Thus, InSAR data can be used together with sparse drawdown or hydraulic head data to improve the estimation of calibration parameters (Yan et al., 2007, Bell et al. 2008, Burbey et al., 2015).

Since not so many hydraulic head data were available for the Ombrone aquifer, the efficiency of model calibration was improved by means of the large amount of PS-InSAR subsidence observation. In particular, Sentinel-1 data for the 2015-2017 period were used, in conjunction to the available hydraulic head data, for the calibration of hydraulic conductivity (and trasmissivity) and elastic and inelastic skeletal specific storage.

6 Integrated modelling procedure

6.1 Introduction

The evaluation of the effects of hydrologic and hydrogeologic related phenomena taking place in a natural system requires the development of reliable modelling procedures, able to properly simulate the influence of the entire set of processes on which the studied phenomenon depends and their interactions. In order to perform a holistic analysis that consider both surficial and underground parts of the hydrologic cycle as a single system, taking into account water dynamics and fluxes occurring between them, an integrated numerical modelling approach is presented in his study. The fully distributed, physically based, MOBIDIC code was used to simulate surface water states and hydrologic variables, to obtain detailed information for the development of a reliable groundwater model, by means of the USGS' modular finite difference MODFLOW code.

Among the entire set of hydrologic variables, water percolation through the aquifer and river network discharge represent the main variables that more affect the contribution of the surficial processes to the groundwater system. Usually, in groundwater modelling practice, these variables are not explicitly modelled, but they are discretized as boundary conditions and then adjusted during the model calibration phase. For the simulation of the river network contribution, all relative information are obtained from discharge data recorded at gauging stations within the watershed. However, if present, hydrometric data are not widespread homogeneously all over the modelled watershed, especially in small basins, resulting in a poor approximation of the real river systems condition. Percolation variable is probably the most difficult to estimate, since its direct measure can be hard to perform. Percolation contribution is usually determined by means of different empirical equations and calculated as a fraction of the total precipitation.

A package called "ETS package" is available in MODFLOW code to estimate the amount of evapotranspiration occurring in a certain area, starting from measured rainfall data. ETS package can also be used to obtain the percentage of water reaching the aquifer from direct precipitation. The main issue with ETS concerns the definition of its calibration parameters, unknown a prori, that increase the number of variables involved in the calibration phase.

With the MOBIDIC-MODFLOW procedure, detailed information about surficial processes and hydrologic variables can be obtained from MOBIDIC output, reducing the number of parameters involved in the groundwater model calibration. Moreover, physically based calculation of the main hydrologic parameters allows to obtain important information for the development of groundwater models, leading to the achievement of more realistic and reliable results.

The combined MOBIDIC-MODFLOW modeling approach was tested in the case study of Pesa river basin (Toscana, central Italy). Pesa river is one of the main Arno river tributaries, characterized by a small Pliocenic basin with the presence of an unconfined aquifer and a strong relation between groundwater and surficial network. MOBIDIC-MODFLOW modelling procedure were applied in the study area with the aim to perform a global water balance of the Pesa basin.

6.2 Study area

The Pesa river basin is located in the central part of Italy, 20 km South-West of Florence, and covers an area of about 335 km^2 with an elevation that ranges between 18 to 880 m above mean sea level. It represents one of the sub basins of the Arno river basin (*Figure* 47a).

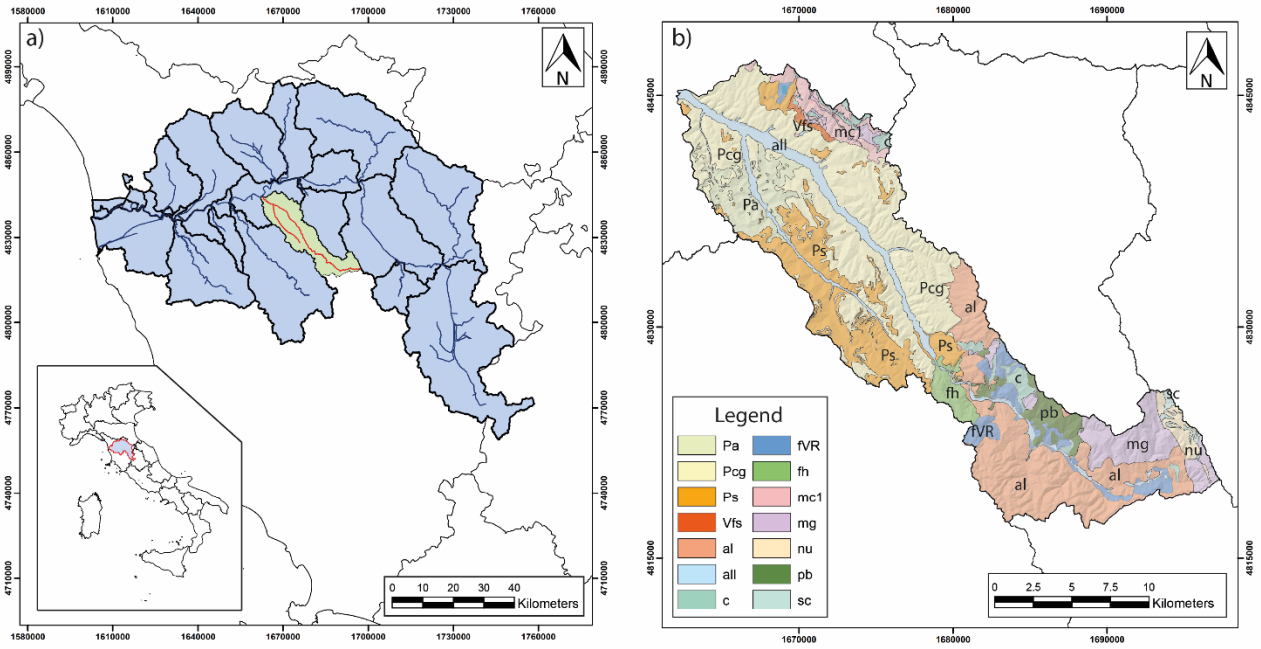

Figure 47 – a) Location of the Pesa river basin within the Arno river basin; in red, the Pesa and Virginio river and in dark blue the Arno river basin network with Strahler (Strahler, 1957) order bigger than 5 and b) Geological map of the Pesa basin: all, recent alluvial deposits; Vfs, lacustrine sands and clayey sands; Pa, marine clay and sandy clay; Ps, sands and clayey sands; Pcg, marine gravels and conglomerates; pb, argille a Palombini; fh, flysh a Elmintoidi; al, turbidites; fVR, Argilliti Varicolori; c, Argille Scagliose; mc1, Arenarie del Falterona; mg, Macigno; nu, Calcareniti a nummuliti; sc, Scaglia Toscana.

The River Pesa arises from the confluence of several tributaries in the area located between the Badiaccia in Montemura (675 m) and Badia a Coltibuono (628 m), at the border of the provinces of Siena and Florence.

Both Pesa and Virginio river, its main tributary, are effectively seasonal torrents and remain dry, especially in its final part, during summer.

Based on the Servizio Idrologico della Regione Toscana climate data, the mean annual precipitation in the basin is about 1000 mm and the mean daily temperature varies between 2 to 30°C, with an annual average of 14.5°C. From a geological point of view, the Val di Pesa (the valley of the Pesa river) is a structural pliocenic basin, with Northwest to Southeast direction, included between Monti del Chianti and Montagnola Senese ridges. The valley cuts through the entire Upper Pliocene sequence with the bottom of it reaching down the Lower Pliocene (Figure 47b).

Then, over the Pliocenic substrate, the basin has been filled up with sea to river-lake sediments during the relaxation phase of the Apennine orogenesis and with alluvial terraced deposits in the quaternary age.

These deposits are mainly composed of silty and clayey sediments with sparse coarse sandy lens, in which some barely exploited confined aquifer are set. The main aquifer is represented by the high permeability sandy and gravelly sediments of limited thickness (ranging between 6 to 8 meters) that can be found at the top of the stratigraphic column, made by the most recent activity of Pesa river.

Such phreatic aquifer is strictly connected with the surficial network and it strongly reflects its seasonal trend, with the level of the water table that drop down by several meters in summer.

6.3 Hydrological model setup

The hydrological model of Pesa basin has been constructed by means of MOBIDIC code, considering a 15 years modelling period (from 2002 to 2017), with 2 years of model warm up (2002 and 2003), 6 years of calibration (2004 to 2009) and 8 years of validation (2010 to 2017). The hydro-meteorological data used for the simulation were available from the SIR (Sistema Informativo Regionale) of Tuscany region website, containing time series of the observed meteorological data, needed for the hydrological modelling. The approach used to solve the surface energy balance was the 1L (1-layer) surface energy balance scheme and the linear method was adopted as conceptual scheme for the river flow routing.

The model calibration, performed by means of MOBIDIC calibration module, has been carried out using the discharge measurement of the Turbone river gauging station, located in correspondence of the closing section of Pesa basin (Figure 48a). Turbone station records Pesa river discharge data since January 2004, even if the time series are not continuous for all the monitored period and some data are missing. Observed data have been used to calibrate the 4 main hydrologic parameters of the model γ, κ, β and α by minimizing the differences between simulated and measured flow duration curves. The initial values for the calibration parameters, obtained from the Arno river hydrological model carried out with MOBIDIC by Castelli et al., (2009), have been defined as follow:

- Hillslope flow, α: $5 \cdot 10^{-5}$ s^{-1};
- Hypodermic flow, β: $2.44 \cdot 10^{-6}$ s^{-1};
- Percolation, γ: $1.026 \cdot 10^{-7}$ s^{-1};
- Adsorption flow, κ: $1.336 \cdot 10^{-6}$ s^{-1}.

For the calibration of the hydrologic parameters, the calibration module integrated in MOBIDIC has been used. The module searches the minimum of the objective function given by the weighted sum, for each available hydrometric series, of the normalized differences between measured and computed data.

In the objective function, four different variables can be considered: discharge, cumulative flow volume, flow duration and peak discharge and, for each term, the relative weight in the function must be specified. Since the final purpose of the modelling procedure was the development of a mean annual water balance of the Pesa basin, the maximum weight of parameters included in the objective function has been given to the flow duration, in order to emphasize the importance of the outflows over the long-time scale.

6.4 Hydrogeological model setup

Pesa basin is a closed basin that can be discretize as an isolated system in terms of surface water and groundwater. His only external interaction is located in correspondence of the Pesa river outlet, in the Northwestern part of the basin, with the Empoli aquifer.

Based on the available stratigraphic data and the hydrogeological information of the area, a simple one-layer conceptual groundwater model has been developed. The model area is 18.0×16.5 km^2 wide and has been discretized with 360×330 cells, using a uniform cell size of 50 m. With 1 layer, the model includes a total of 118,800 cells, where 5,530 are active.

Top of the model corresponds with the ground surface and was determined using a 10 meters resolution digital elevation model (DEM) of the area. The bottom boundary of the layer, on the other hand, corresponds to the lower part of the aquifer sediments, in contact with low permeability clays, whose depth was estimated by means of the available stratigraphic data.

For the definition of the boundary conditions in MODFLOW, both physical limits and water fluxes from or into the aquifer have been considered (Figure 48b).

The main inputs for the Pesa aquifer system are represented by the infiltration of water for direct precipitation on the valley floor and by leakage from the river network. Such inputs have been discretized in MODFLOW with the RCH (recharge) package and the RIV (river) package, respectively, and were obtained from the hydrological simulation performed by means of MOBIDIC code.

The outflows from the aquifer occur through evapotranspiration, groundwater extraction and water restitution to the river during the driest periods.

Pumping wells are widespread homogeneously all over the basin, with the higher extraction rate located in Ginestra Fiorentina and Montelupo Fiorentino wells field. Pumping wells location and their annual mean pumping rate have been obtained from Arno river basin Authority database, freely available online and containing withdrawal information of Pesa aquifer for the last 10 years. Groundwater extraction occurs from 464 wells, for agricultural, domestic and freshwater supply purposes, with a total pumping rate of about 4.0 Mm^3/yr. Pumping wells are modelled in MODFLOW code as a constant flux boundary condition, by means of the WEL package.

Model borders are represented by the stratigraphic contact between the permeable sediments constituting the aquifer body and the Pliocenic rocks of surrounding reliefs, considered to be of many orders of magnitude less permeable than the basin fill. Since no flows are expected to happen along the model borders, lateral boundaries are all simulated as no-flow cells.

Only in the final part of the aquifer, in the Northwestern side of the area, a Time-Variant Specified-Head (CHD) condition has been specified, in order to take into account the transition of the Pesa basin aquifer with the confining Empoli aquifer. The Time-Variant Specified-Head package is used to simulate specified head boundaries that can change within or between stress periods.

The aim of the groundwater model was to represents the mean annual hydrogeologic balance of the Pesa basin, in order to identify the seasonal trends of the main hydrogeological processes and to analyze the availability of the water resource during the year. This resulted in the identification of 13 stress periods, a stationary one and 12 transient ones, from January to December, with the day as a unit time step. The lengths of the stress periods varied from 10 days for the stationary stress period to 30 days for the transient ones.

The groundwater model has been constructed using MODFLOW-2000 (McDonald and Harbaugh 1984; Harbaugh et al. 2000) with Groundwater Vistas as user interface (Rumbaugh and Rumbaugh, 2004).

Preconditioned Conjugate-Gradient (PCG) was used as numerical solver, with a HCLOSE (head change criterion for convergence) and RCLOSE (Residual criterion for convergence) values set to 0.1. Number of outer and inner iterations were set to 300 and 35, respectively.

As stated before, river network discharge and water percolation through the aquifer represent the two variables of interest that are considered in the integrated approach between MOBIDIC model and MODFLOW code, representing the main input data for a reliable description of a natural groundwater system.

Rivers and waterways are modelled in MODFLOW using the river boundary condition (RIV), a head-dependent boundary condition. In a river cell, the flow of water into or out of the aquifer is dependent on

the head assigned to the river and the conductance term. The head is compared to the computed head in the aquifer for the cell containing the river. If the aquifer head is higher than the river head, then the river removes water from the aquifer, otherwise the river add water to the system. The amount of water added to or removed from the aquifer is based on the conductance term, computed from the following equation:

$$C = \frac{KLW}{D} \tag{54}$$

Where K is the hydraulic conductivity of the riverbed material, L is the length of the river in the cell (usually set as the cell length), W is the width of the river in the cell, and D is the thickness of the riverbed material. Thus, giving a default value for the riverbed thickness and the hydraulic conductivity that cannot be known a priori without available field data, the remaining needed variables are represented by river stage and river width.

River stage represents the elevation of the water level above the riverbed, and can be calculated from MOBIDIC discharge output, starting from the basic discharge formula:

$$Q = A\,v \tag{55}$$

Where Q is the river discharge (simulated by MOBIDIC), A is the area of the river section and v is the flow celerity. The area of the river section can be simplified in terms of river width W and river stage h, by the simple geometric equation:

$$A = W\,h \tag{56}$$

Combining equation (55) and (56), the variable river stage, needed for the RIV package in MODFLOW can be calculated:

$$h = \frac{Q}{Wv} \tag{57}$$

Pesa river network has been divided into 8 river branches (2 for Virginio river and 6 for Pesa river), characterized by constant width and flow celerity, to improve the resolution of the model in simulating water exchanges between surficial and groundwater reservoirs. For each branch, by means of the digital elevation model of the area, a cross section of the river channel has been constructed, in order to identify the relative river width. Flow celerity, assumed as a constant value for all the river network during the year, has been obtained from Turbone river gauging station data, in correspondence of the closing section of the Pesa river.

Recharge rate in MODFLOW represents the net amount of water that reaches the water table in the aquifer and is modelled using a specified flow boundary condition. Values of recharge rate con be directly obtained from MOBIDIC output percolation variable, cumulated for the selected time step.

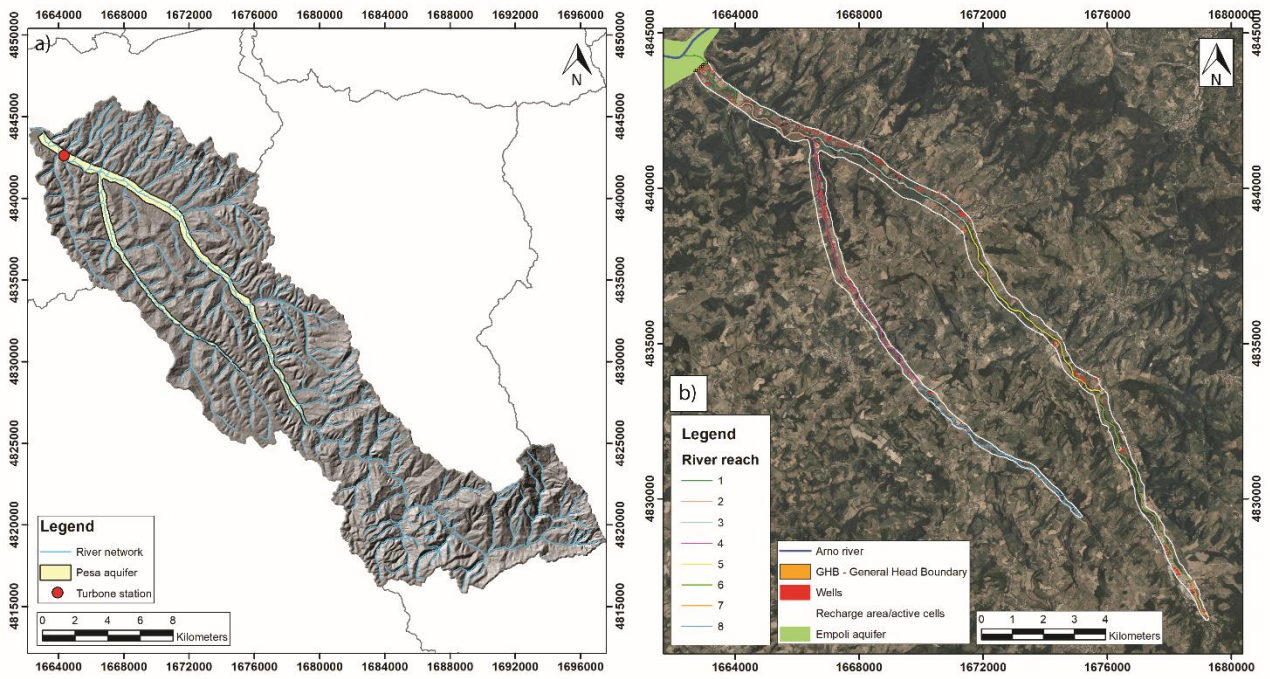

Figure 48 – a) Location of the Pesa aquifer and the Turbone river gauging station within the Pesa basin; b) Conceptual model of the aquifer for groundwater modelling with MODFLOW. Colored polylines represent the 8 branches in which Pesa and Virginio river have been subdivided.

Groundwater model calibration was performed by means of the hydraulic head data available for Pesa aquifer, obtained from the online database of Arno River Basin Authority. Data from 55 head observation of the year 2008 have been used, considering only wells falling within the model area and imposed in the phreatic aquifer. 2008 was a quite stationary period with respect to groundwater level, with variations in hydraulic head generally less than 4 meters and with a mean variation of about 2 meters, representing the most recent year with enough head measurement available.

Two parameters were involved in the calibration phase, the horizontal ($K_h=K_x=K_y$) and the vertical (K_z) hydraulic conductivities, considered with an anisotropy of $K_h/K_v=10$. To simplify the calibration of the system, a single conductance of $3\cdot10^{-3}$ m/s was used for the entire aquifer as starting value, obtained by on-site measurements available in literature.

7 Climate models

Climate change and global warming are becoming two of the main threats to be faced in the last decades, for their huge impact on environment and human lives. Besides temperature and precipitation, many others environmental variables are strongly affected by this evolving phenomenon. As a direct consequence, long term climate variation may also alter river discharge, seasonal and local water availability, and freshwater supply (Olmstead 2013; Aristeidis et al. 2012; Arnell 2003). Therefore, all water matrix related risks are changing as well, enhancing the importance of the investigation on the impact of climate change on hydrology and hydrogeology at regional or basin scale (Teutschbein and Seibert 2012; Babel et al. 2013; Xu et al. 2013; Olmstead 2013).

Global Climate Models (GCMs) are the most powerful available tool for simulating climate scenarios, since they may provide the basis for climate change impact assessment at all different scales, from local to global. GCMs are able to simulate many different physical processes in atmosphere, cryosphere, oceans and land surface, and they are becoming always more important in climate change research to properly evaluate the response of the global climate system to the increasing of greenhouse gas concentration in the atmosphere (Figure 49*).* Many simpler models have been proposed in the past to provide estimation of climate response at regional or global scale, but only Global Climate Models showed the capability to guarantee consistent climate simulation for climate changing impact assessment.

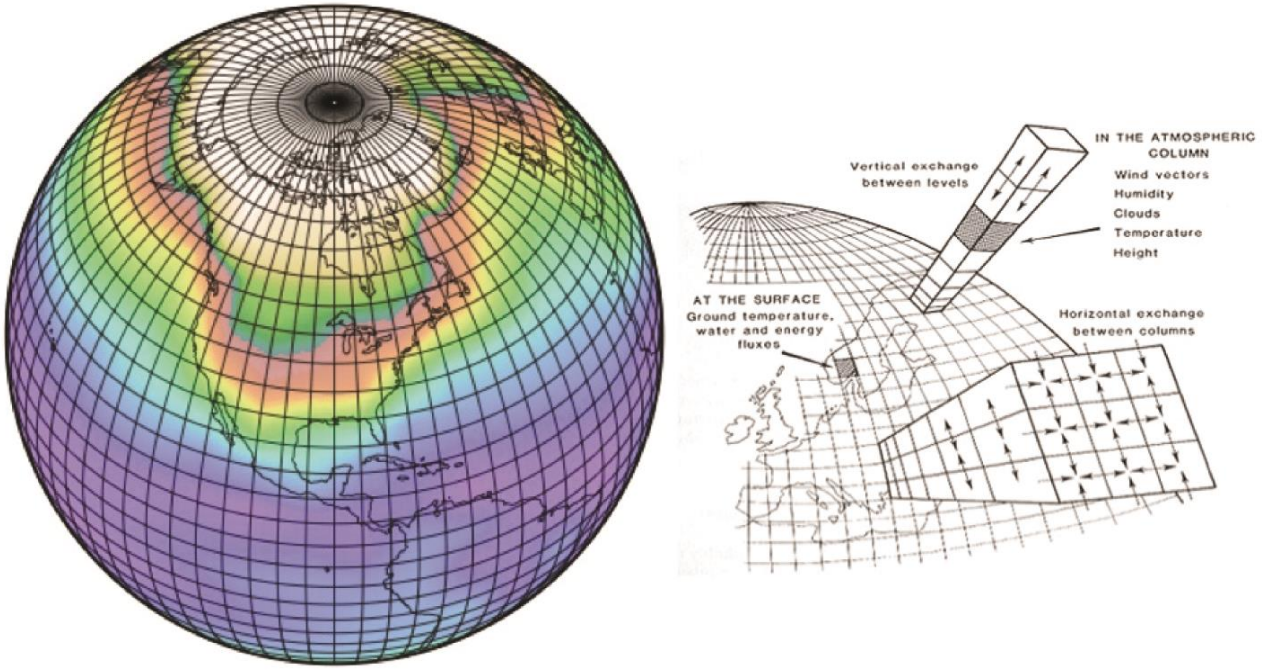

Figure 49 – Horizontal and vertical discretization of a Global Climate Model (GCM, Henderson-Sellers, 1985).

To perform climate simulation, GCMs use a three-dimensional grid of the whole globe with a horizontal resolution ranging between 110 to 600 km. The vertical domain is discretized with 10-20 vertical layers for the atmosphere and up to 30 layers for the oceans. This resolution is quite coarse if compared to the basin scale at which most climate changing impact analysis are performed. Moreover, many natural processes in natural climate systems occur at a smaller scale and cannot be properly simulated with this kind of resolution. This is one of the main uncertainties of Global Climate Models simulations.

In order to solve this problem, GCMs are often coupled with higher resolution models, to perform climate changing simulations at the required scale without the necessity of big assumptions or parametrizations. Such models, known as Regional Climate Models (RCMs), use a particular GCM model as boundary conditions and simulate climate processes at regional scale, with a resolution that range between 30 to 50 km.

Many different factors are involved in climate modelling and all of them have to be taken into account when performing climate forecasting, since GCMs and RCMs may give different responses to the same initial condition, simply because of the way certain processes are modelled or directed. Many anthropic variables, such as the amount of greenhouse gasses that will be emitted in the atmosphere, or changes in energy production methods or technology development, need also to be considered, to ensure that starting conditions, historical data and future projections are constant for all different climate models, guaranteeing their consistency and allowing their comparison.

In order to address this issue, several modelling scenarios have been introduced in climate change research field, providing a framework that can be used during the model building process. Each scenario consists in a set of starting values and estimated greenhouse gasses emission, based on many different social and economic factors directly affecting the Earth climate.

The first set of climate scenarios, called IS92, was published in 1992 by the Intergovernmental Panel on Climate Change (IPCC), an organization of governments Created in 1988 by the World Meteorological Organization (WMO) and the United Nations Environment Program (UNEP). The second generation of climate scenarios, the Special Report on Emissions Scenarios (SRES), were released by the IPCC in 2000. These scenarios were used as a reference for the development of climate models and were contained in two following reports: the Third Assessment Report (TAR, 2001) and the Assessment Reports Four (AR4, 2007). SRES provided reference scenarios for climate modelling for more the 10 years, until the publication in 2014 of the Assessment Report Fifth (AR5). AR5 released a new set of scenarios, replacing the previous SRES, and introduced the Representative Concentration Pathways (RCPs). Four RCPs have been introduced, describing different possible climate scenarios based on the amount of greenhouse gasses that will be emitted in the atmosphere in the years to come. The four RCPs, called respectively RCP2.6, RCP4.5, RCP6 and RCP8.5, get their names from the attended possible values of radiative forcing that they are simulating for the year 2100 (2.6, 4.5, 6, 8.5 W/m^2, Figure 50).

RCP2.6 has been developed by the IMAGE modeling team of the PBL Netherlands Environmental Assessment Agency. The emission pathway is representative of scenarios that would lead to very low greenhouse gas concentration levels, aiming to limit the increase of global mean temperature to less than 2°C. RCP2.6 is represented as a "peak-and-decline" scenario, with radiative forcing level reaching a maximum value of about 3.1 W/m^2 in the mid-century, and returning to 2.6 W/m^2 within 2100. In order to reach such radiative forcing levels, greenhouse gases emissions from 2010 to 2100 need to be strongly reduced, requiring substantial changes in energy use and emissions policies (Van Vuuren et al. 2011b).

RCP4.5 was developed by the GCAM modeling team at the Pacific Northwest National Laboratory's Joint Global Change Research Institute (JGCRI) in the United States. RCP4.5 is an intermediate stabilization scenario in which radiative forcing expect to stabilize to a value of 4.5 W/m^2 in the year 2100 without ever exceeding that value (Thomson et al., 2011). In order to reach this target, technological and economic politics in the environmental field need to be adopted.

RCP6 was developed by the Asia-Pacific Integrated Modelling team (AIM) at the National Institute for Environmental Studies (NIES) in Japan. It is a stabilization scenario describing a trend in total radiative forcing that is stabilizing in 2100, without exceeding the value of 6 W/m^2. To reach this goal, greenhouse gasses

emissions need to be reduced worldwide during the entire simulation period with the application of new environmental strategies (Masui et al., 2011).

RCP 8.5 was developed combining the MESSAGE model and the IIASA Integrated Assessment framework by the International Institute for Applied Systems Analysis (IIASA), Austria. RCP8.5 represent the scenario with the highest amount of greenhouse gas emissions, assuming low technological improvements and non-existent environmental policies. Radiative forcing reaches a value of 8.5 W/m^2 in the year 2100 but it may increase during the following years (Riahi et al., 2011).

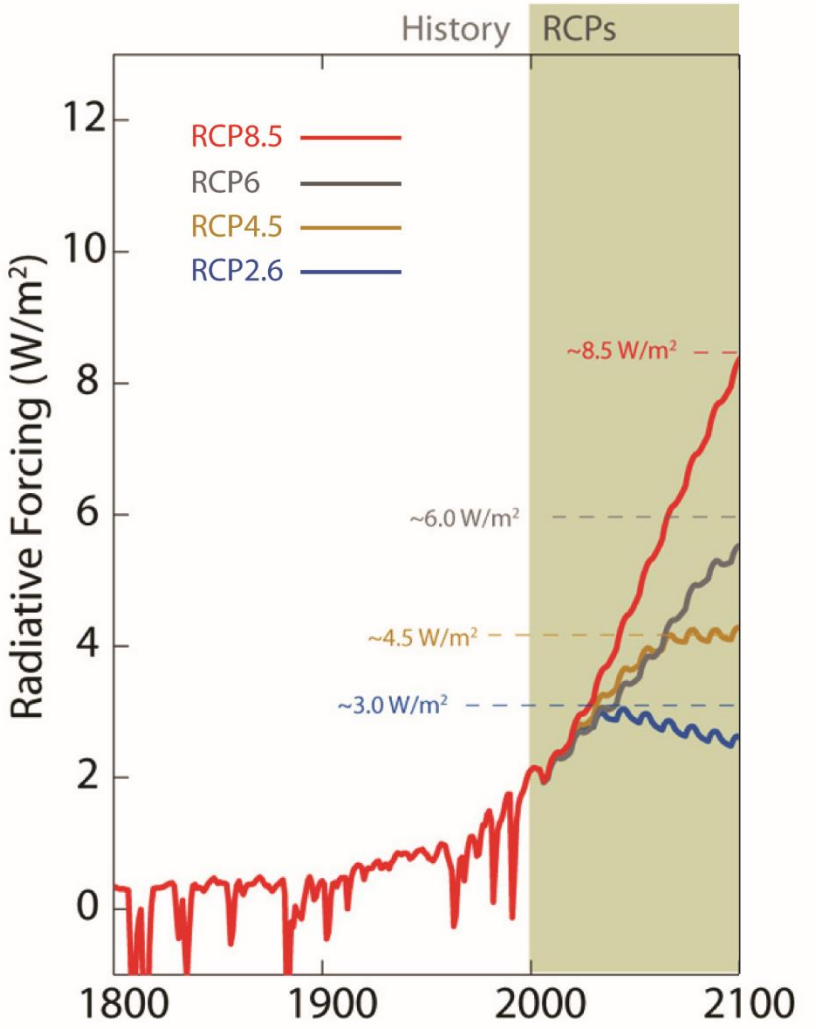

Figure 50* - Global Anthropogenic Radiative Forcing for the high RCP8.5, the medium-high RCP6, the medium-low RCP4.5 and the low RCP3-PD scenarios, modified after *Meinshausen (2011).

Besides starting values, estimated greenhouse gasses emission and all several social and economic factors determined by each RCP, a GCM (and/or RCM) simulation may also depend on the time on which these external factors are introduced into the model. In fact, even if final results of each GCM/RCM model show slight differences from each other in the long term, there could be many discrepancies in the resulting climate projection in a year to year comparison. For this reason, usually modelling projects consist of a certain number of "ensemble" simulation composed of many identical experiments carried out with the same scenario. The only difference between each ensemble set is represented by the moment of the run in which forcing factors are introduced.

The following set of figures represents the regional pattern of climate change for the South Europe/Mediterranean area from GCMs of the CMIP5, showing the map of surface air temperature and

precipitation changes in different seasons until the year 2100 (Figure 51, Figure 52, Figure 53 and Figure 54). Dotted areas in the maps represent geographical zone characterized by climate variation in conformity with natural variation range. First percentile, median value and third percentile are showed, considering three different twenty-year average periods for the near term (2016-2035), midterm (2046-2065) and long term (2081-2100). Time series and relative probability box plot for precipitation and temperature are also displayed for each RCP, with RCP4.5 clearly representing the intermediate modelling pattern.

Considering the median modelled values, in Italy an increasing of temperature is expected in future years, ranging between 0.5-1 °C in the near term (2016-2035) and between 2-3 °C in the long term (2081-2100) for the December-February period. For the June-August period temperature are forecasted to rise up to 1-1.5°C in the near term and up to 2-3 °C in the long term (Figure 51 and Figure 52).

Figure 53 shows maps of RCM precipitation change for the October-March period. Median values conflict with each other, indicating a small precipitation reduction (0, -10%) in the near term and an as much precipitation value increasing in the long term (0, +10%) for the studied area. However, dotted lines demonstrate that predicted RCM results are in agreement with natural variability for the October-March period in the Mediterranean area.

RCM results for precipitation change in the April-September period are showed in Figure 54. RCM simulation suggest a 0-10% reduction in precipitation for the short term and a 10-20% reduction for both mid and long term. However, if in the short term the prevision fall into the natural variability range, in the mid-long term they assume an important statistically significance.

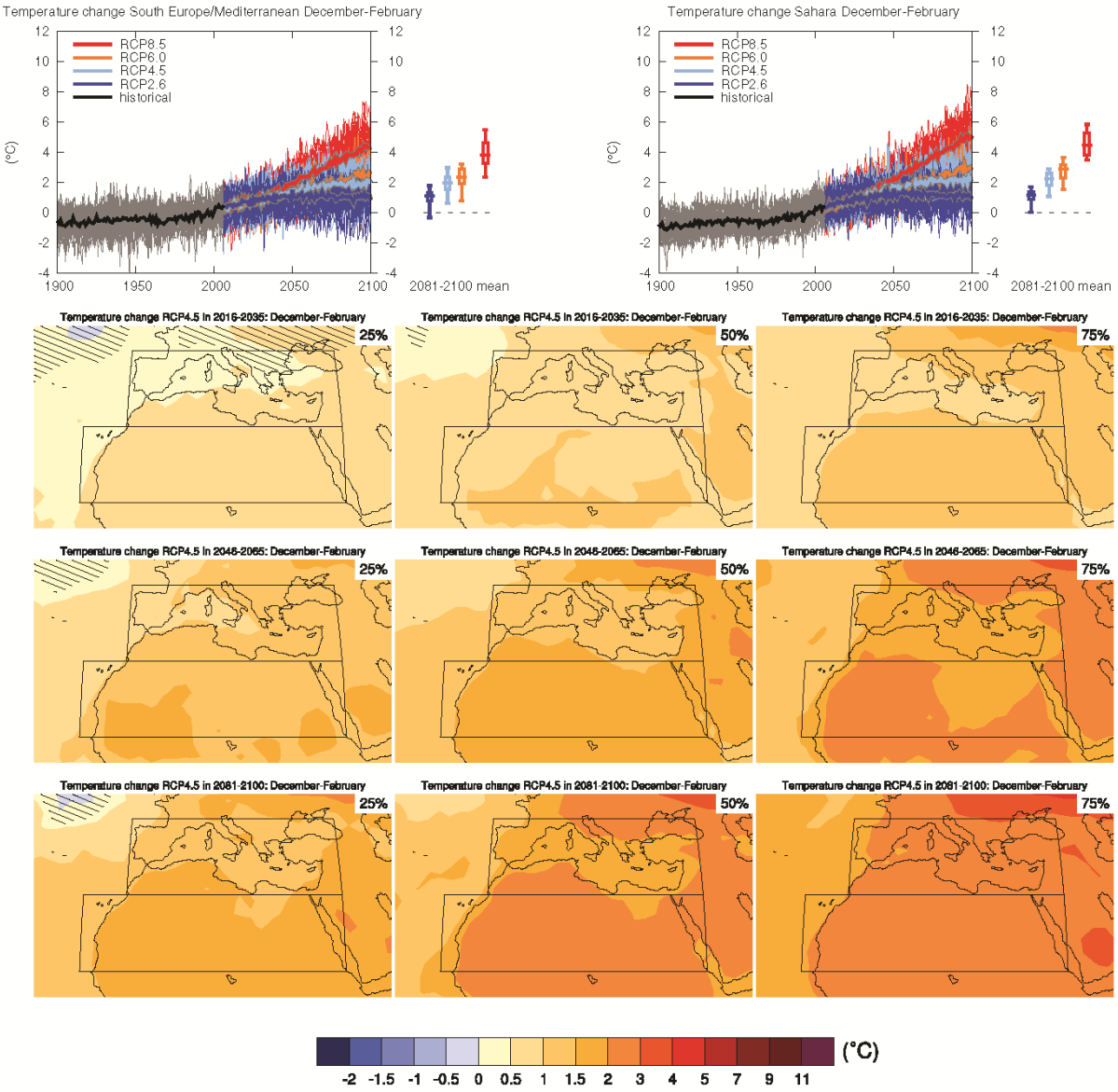

Figure AI.40 | (Top left) Time series of temperature change relative to 1986–2005 averaged over land grid points in the region South Europe/Mediterranean (30°N to 45°N, 10°W to 40°E) in December to February. (Top right) Same for land grid points in the Sahara (15°N to 30°N, 20°W to 40°E). Thin lines denote one ensemble member per model, thick lines the CMIP5 multi-model mean. On the right-hand side the 5th, 25th, 50th (median), 75th and 95th percentiles of the distribution of 20-year mean changes are given for 2081–2100 in the four RCP scenarios.

(Below) Maps of temperature changes in 2016–2035, 2046–2065 and 2081–2100 with respect to 1986–2005 in the RCP4.5 scenario. For each point, the 25th, 50th and 75th percentiles of the distribution of the CMIP5 ensemble are shown; this includes both natural variability and inter-model spread. Hatching denotes areas where the 20-year mean differences of the percentiles are less than the standard deviation of model-estimated present-day natural variability of 20-year mean differences.

Sections 9.4.1.1, 9.6.1.1, 10.3.1.1.4, Box 11.2, 14.8.6, 14.8.7 contain relevant information regarding the evaluation of models in this region, the model spread in the context of other methods of projecting changes and the role of modes of variability and other climate phenomena.

Figure 51 – Temperature variation for Winter season (December-February) relative to 1986-2005 period.

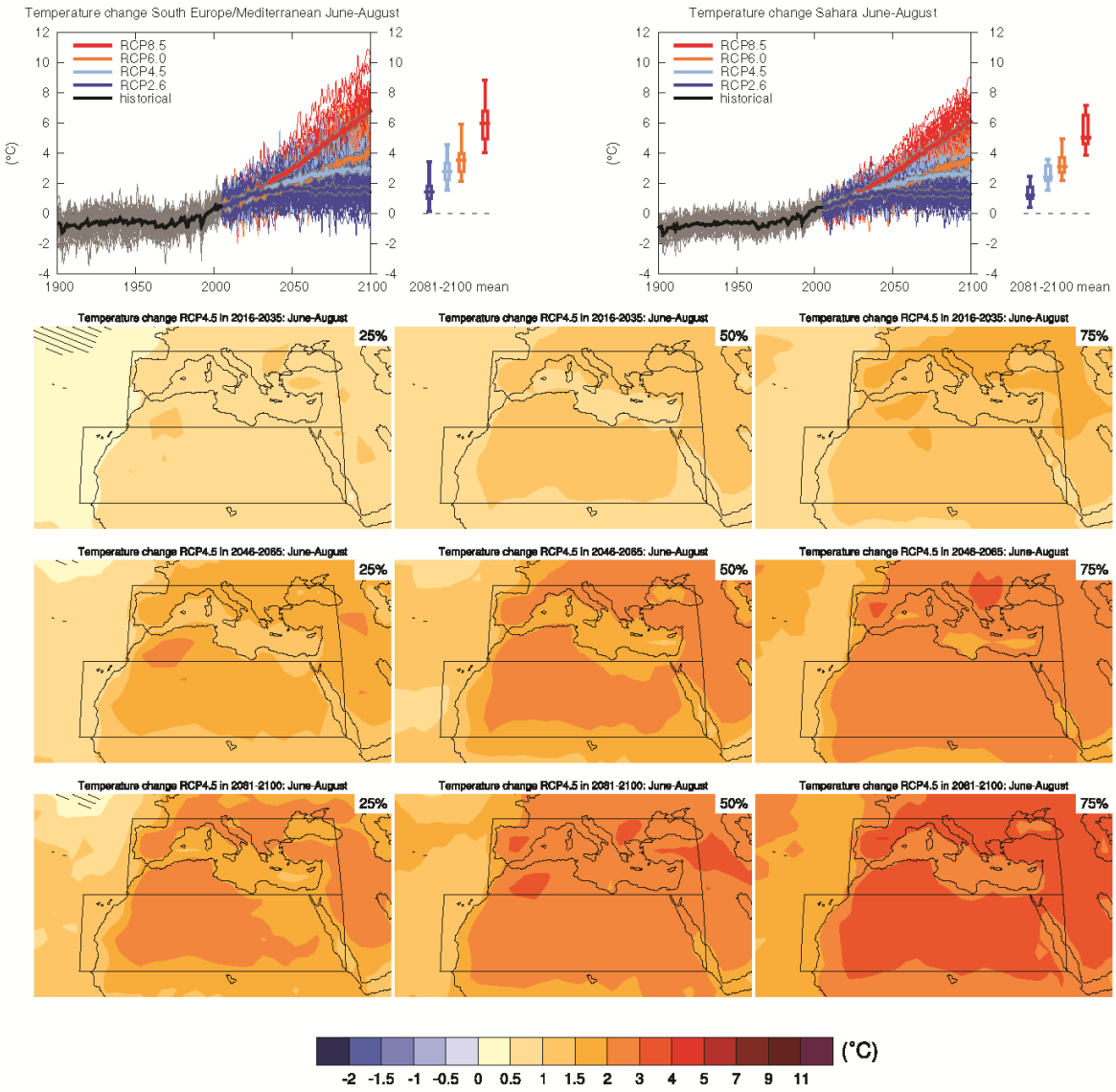

Figure AI.41 | (Top left) Time series of temperature change relative to 1986–2005 averaged over land grid points in the region South Europe/Mediterranean (30°N to 45°N, 10°W to 40°E) in June to August. (Top right) Same for land grid points in the Sahara (15°N to 30°N, 20°W to 40°E). Thin lines denote one ensemble member per model, thick lines the CMIP5 multi-model mean. On the right-hand side the 5th, 25th, 50th (median), 75th and 95th percentiles of the distribution of 20-year mean changes are given for 2081–2100 in the four RCP scenarios.

(Below) Maps of temperature changes in 2016–2035, 2046–2065 and 2081–2100 with respect to 1986–2005 in the RCP4.5 scenario. For each point, the 25th, 50th and 75th percentiles of the distribution of the CMIP5 ensemble are shown; this includes both natural variability and inter-model spread. Hatching denotes areas where the 20-year mean differences of the percentiles are less than the standard deviation of model-estimated present-day natural variability of 20-year mean differences.

Sections 9.4.1.1, 9.6.1.1, 10.3.1.1.4, Box 11.2, 14.8.6, 14.8.7 contain relevant information regarding the evaluation of models in this region, the model spread in the context of other methods of projecting changes and the role of modes of variability and other climate phenomena.

Figure 52 – Temperature variation for Summer season (June-August) relative to 1986-2005 period.

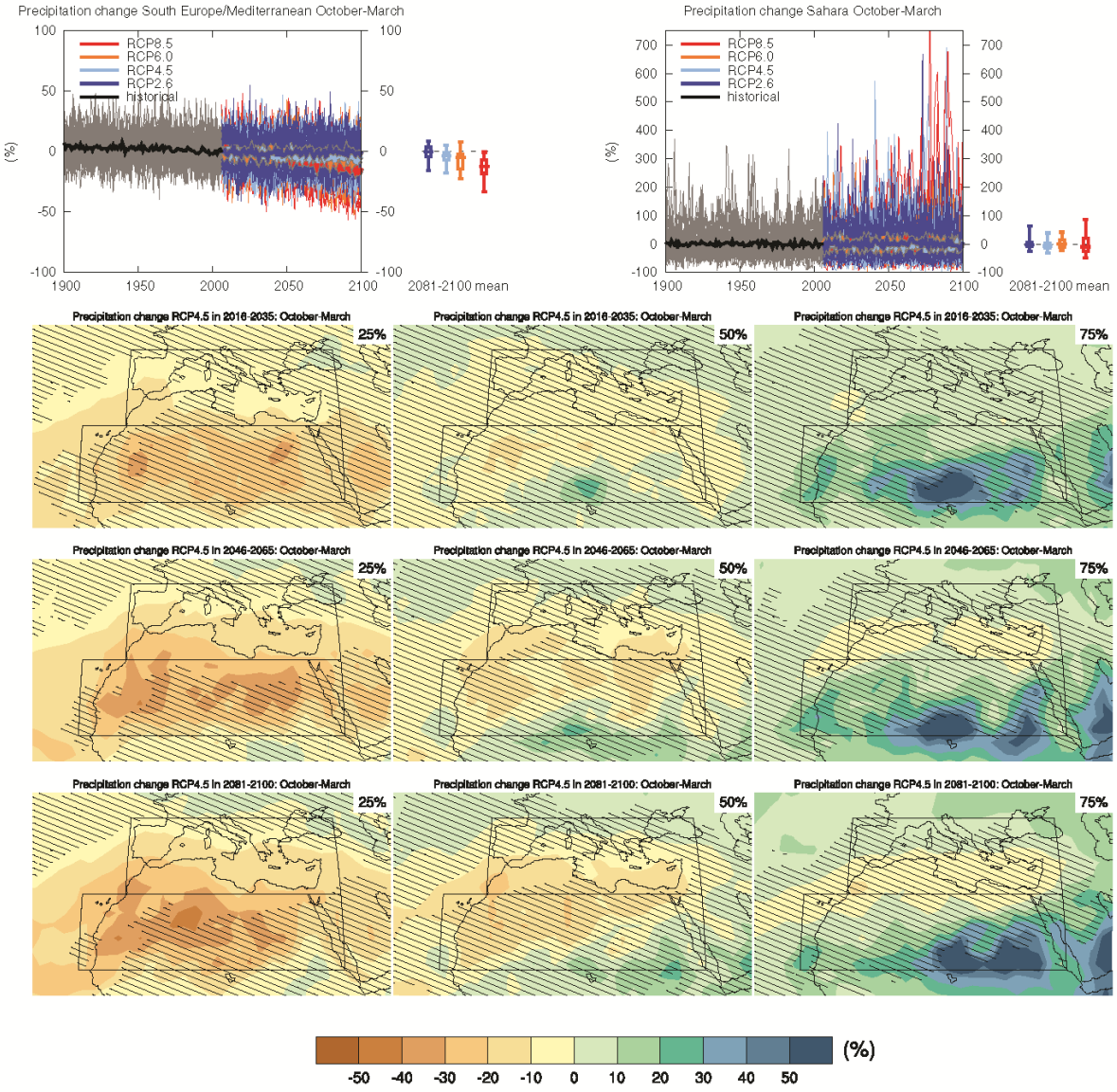

Figure AI.42 | (Top left) Time series of relative change relative to 1986–2005 in precipitation averaged over land grid points in the region South Europe/Mediterranean (30°N to 45°N, 10°W to 40°E) in October to March. (Top right) Same for land grid points in the Sahara (15°N to 30°N, 20°W to 40°E). Thin lines denote one ensemble member per model, thick lines the CMIP5 multi-model mean. On the right-hand side the 5th, 25th, 50th (median), 75th and 95th percentiles of the distribution of 20-year mean changes are given for 2081–2100 in the four RCP scenarios. Note different scales.

(Below) Maps of precipitation changes in 2016–2035, 2046–2065 and 2081–2100 with respect to 1986–2005 in the RCP4.5 scenario. For each point, the 25th, 50th and 75th percentiles of the distribution of the CMIP5 ensemble are shown; this includes both natural variability and inter-model spread. Hatching denotes areas where the 20-year mean differences of the percentiles are less than the standard deviation of model-estimated present-day natural variability of 20-year mean differences.

Sections 9.4.1.1, 9.6.1.1, Box 11.2, 12.4.5.2, 14.8.6, 14.8.7 contain relevant information regarding the evaluation of models in this region, the model spread in the context of other methods of projecting changes and the role of modes of variability and other climate phenomena.

Figure 53 –Precipitation variation for Autumn-Winter season (October-March) relative to 1986-2005 period.

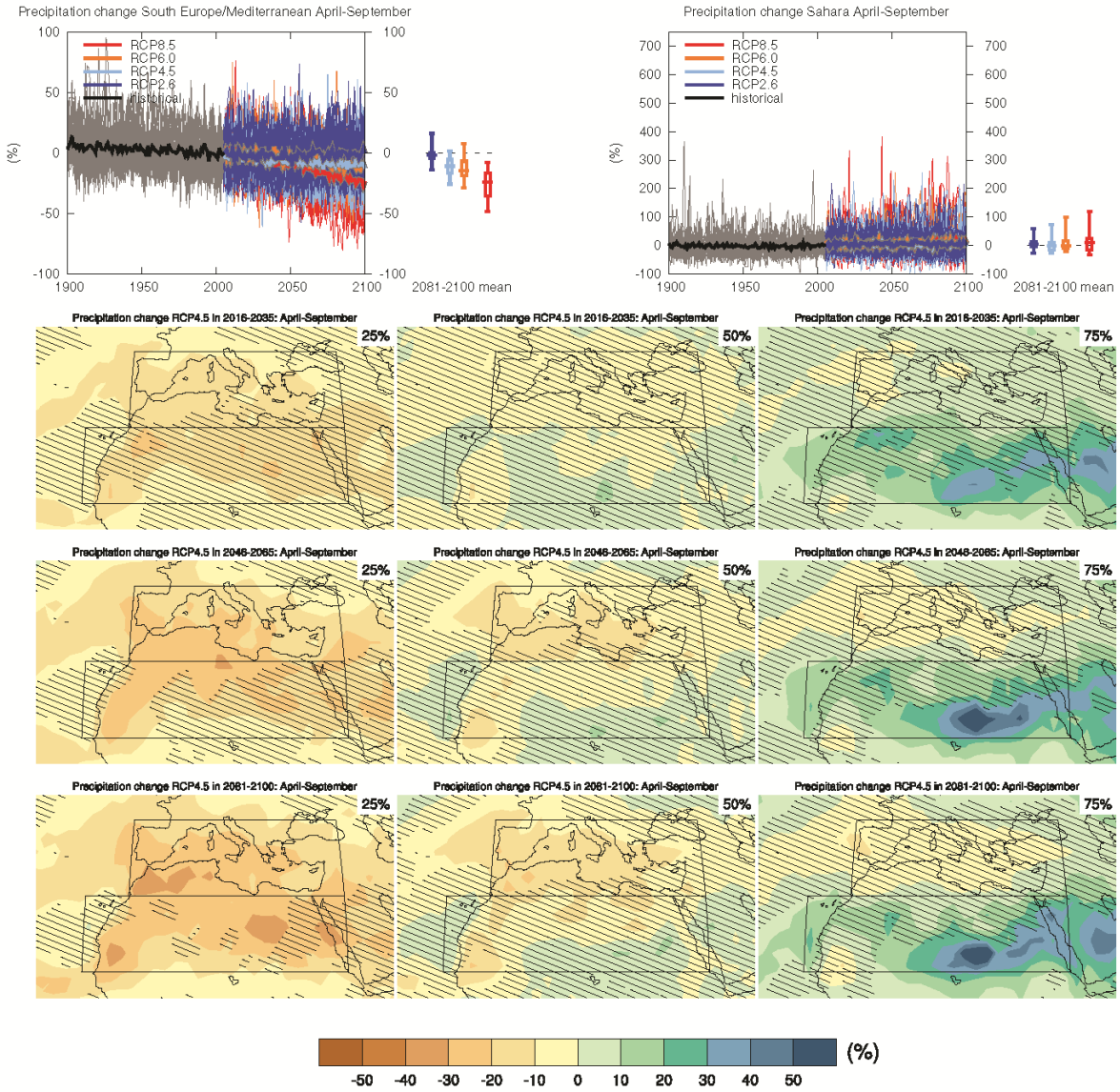

Figure AI.43 | (Top left) Time series of relative change relative to 1986–2005 in precipitation averaged over land grid points in the region South Europe/Mediterranean (30°N to 45°N, 10°W to 40°E) in April to September. (Top right) Same for land grid points in the Sahara (15°N to 30°N, 20°W to 40°E). Thin lines denote one ensemble member per model, thick lines the CMIP5 multi-model mean. On the right-hand side the 5th, 25th, 50th (median), 75th and 95th percentiles of the distribution of 20-year mean changes are given for 2081–2100 in the four RCP scenarios. Note different scales.

(Below) Maps of precipitation changes in 2016–2035, 2046–2065 and 2081–2100 with respect to 1986–2005 in the RCP4.5 scenario. For each point, the 25th, 50th and 75th percentiles of the distribution of the CMIP5 ensemble are shown; this includes both natural variability and inter-model spread. Hatching denotes areas where the 20-year mean differences of the percentiles are less than the standard deviation of model-estimated present-day natural variability of 20-year mean differences.

Sections 9.4.1.1, 9.6.1.1, Box 11.2, 12.4.5.2, 14.8.6, 14.8.7 contain relevant information regarding the evaluation of models in this region, the model spread in the context of other methods of projecting changes and the role of modes of variability and other climate phenomena.

Figure 54 – Precipitation variation for Spring-Summer season (April-September) relative to 1986-2005 period.

7.1 Bias correction methods

In the hydrologic modelling field, information about the spatial and the elevational variation of all the variables involved in the hydrologic cycle are strictly necessary. Unfortunately, the coarse resolution of GCMs make them unable to represent small scale variations (Seager and Vecchi, 2010). RCMs guarantee finer resolution to climate models, preserving the coherence between atmospheric variables and topographic characteristics (Bergstrom et al., 2001; Anderson et al., 2011). However, raw RCMs output are barely used directly in hydrologic simulation, since they show systematic errors (bias) due to rough resolution and to the assumptions and simplification needed for physical and thermodynamic processes modelling (Shrestha et al., 2016). As a result, errors in GCMs and RCMs output may be particularly large, if compared to historical observed data (Ramirez-Villegas et al. 2013). In order to be able to perform reliable simulation, GCMs/RCMs raw data need to be corrected before using them as input for a hydrological model, especially in regions where local topography has a big influence in surface hydrological processes control (Figure 55).

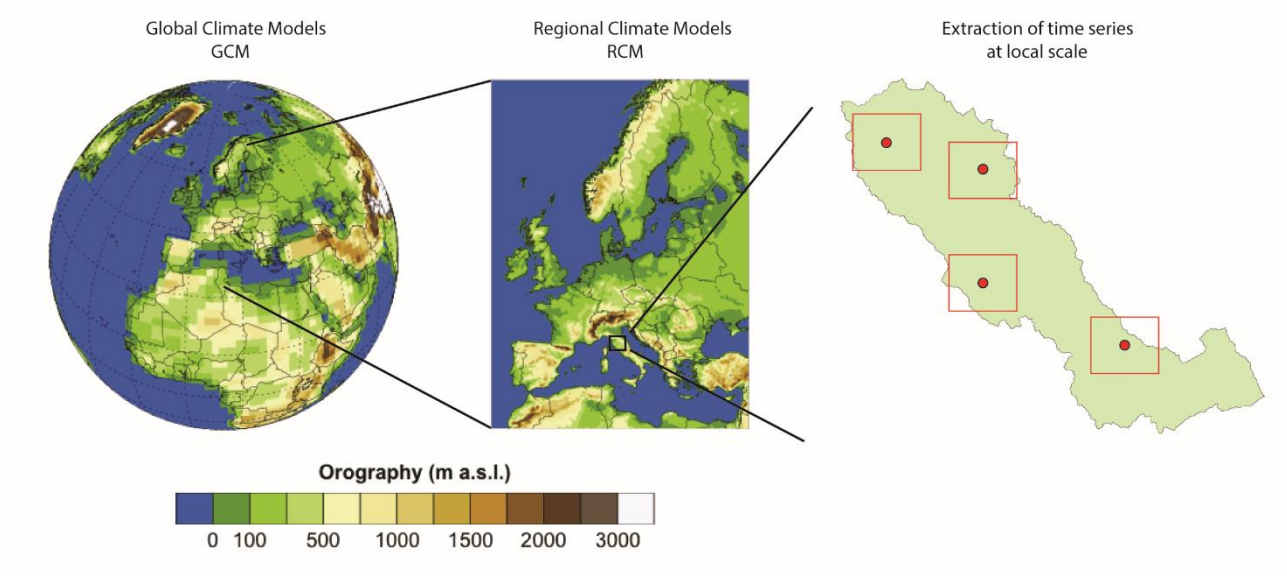

Figure 55 – Climate models downscaling from GCMs to RCMs and from RCMs to local scale.

Many different bias correction procedures have been proposed in literature to transpose GCMs/RCMs output to local scale, from simple downscale methods to more sophisticated geostatistical approaches (Teutschbein and Seibert, 2012). In the present study, the Linear Scale method (LS) has been used (Ines and Hansen 2006). This method is based on a constant correction factor given by the differences between GCMs/RCMs output and observation for each month in the historical reference period. The correction factor is then applied to the raw climate model data in additive or multiplicative way, in order to obtain bias corrected time series of the studied variables (Figure 56). The LS method is capable to perfectly match the monthly mean of corrected RCM output with that of observed values (Lenderink et al., 2007).

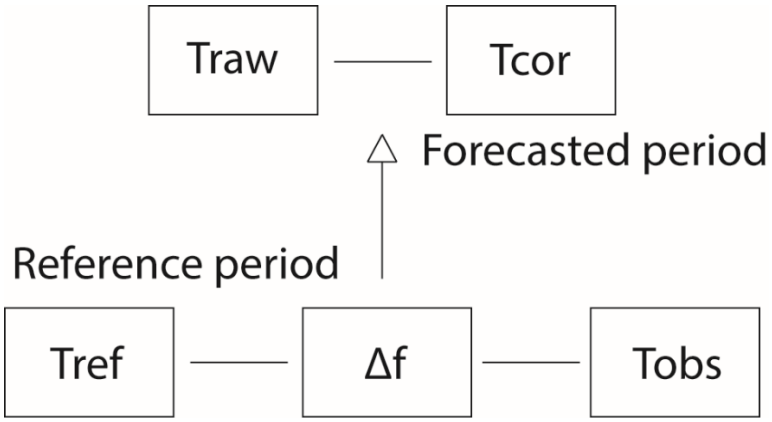

Figure 56 – Bias correction methodology scheme: observation (Tobs) and raw RCMs data (Tref) in the reference period are used to estimate the correction factor that is used to correct raw RCMs data in the future forecasted period.

Additive correction is commonly used for temperature, whereas multiplicative correction is more suitable for not negative variables like precipitation, wind speed, humidity and solar radiation to avoid the presence of negative bias corrected data (Hempel et al. 2013). Linear Scale method is applied by means of the following equations:

$$T_{cor,m,d} = T_{raw,m,d}\ \frac{\mu(T_{obs,m})}{\mu(T_{ref,m})} \tag{58}$$

$$T_{cor} = T_{raw,m,d} + \mu(T_{obs,m}) - \mu(T_{ref,m}) \tag{59}$$

Where: $T_{cor,m,d}$ is the bias corrected RCMs data in the day *d* of the month *m*, $T_{raw,m,d}$ is the raw RCMs data in the day *d* of the month *m*, $\mu(T_{obs,m})$ represents the mean value of observation at the month *m* in the reference and $\mu(T_{ref,m})$ the mean value of observation at the month *m* in the reference period.

8 Results and discussion

8.1 MODFLOW – MOBIDIC integrating procedure

With the increasing of freshwater demand, water resource management strategies are needed to increase the efficiency of water usage, preserving its good quality and quantity state. Groundwater represents one of the main sources of freshwater worldwide and it is strongly influenced by processes occurring on the Earth surface. The evaluation of medium- and long-term variation of groundwater levels must be analyzed together with the main hydrological variables on which the response of the groundwater system depends. The hydrologic model MOBIDIC and the groundwater model MODFLOW have been combined together with an integrated modelling approach, in order to simulate natural and artificial processes occurring in both surface and underground sides of the water cycle.

8.1.1 Hydrological model results

The estimation of the parameters required for MOBIDIC calibration was approached by minimize the differences between simulated and measured flow duration curves, assuming the same standard values of global hydrologic parameters for every sub-basin within the watershed. The calibration phase of the model focused on Turbone river gauging station discharge data over the period 2004-2009; this period has been chosen because it contained an adequate number of homogeneous discharge time series. Table 2 shows the values of MOBIDIC calibration parameters for the Pesa river basin and their respective initial value.

Table 2 – MOBIDIC calibration parameters, together with their initial values, range of variation and controlled hydrologic process.

Parameters	Process	Starting values	Range of variation	Calibrated values
α	Hillslope flow	$5.00 \cdot 10^{-5}$	$1.0 \cdot 10^{-5} – 1.0 \cdot 10^{-7}$	$4.10 \cdot 10^{-6}$
β	Hypodermic flow	$2.44 \cdot 10^{-6}$	$1.0 \cdot 10^{-6} – 1.0 \cdot 10^{-8}$	$7.06 \cdot 10^{-8}$
γ	Percolation	$1.026 \cdot 10^{-7}$	$1.0 \cdot 10^{-6} – 1.0 \cdot 10^{-8}$	$1.97 \cdot 10^{-7}$
κ	Adsorption flow	$1.336 \cdot 10^{-6}$	$1.0 \cdot 10^{-5} – 1.0 \cdot 10^{-7}$	$1.37 \cdot 10^{-5}$

MOBIDIC output provides time series of modelled discharge in all branches of the river network, together with maps of hydrological balance variables (evapotranspiration, runoff and precipitation) and main environmental states (soil water content, soil temperature, evaporative fraction), with daily time step. Figure 57 represents the simulated discharge values obtained with MOBIDIC for the calibration (a) and the validation period (b), in addition to the daily observed rainfall at Turbone gauging station. Analyzing the hydrographs, a good agreement between simulated and observed discharge can be observed, both during calibration and validation periods. In particular, base flow is estimated with high accuracy and temporal flow variation are correctly described. Only simulated flow peaks show some differences if compared to the real observed discharge values, with the model that do not always adequately simulate short-term high discharge values. The main goal of the current study, however, was the realization of a basin scale water balance and the evaluation of river flow over the long timescale, following a quantitative procedure analysis. Flow peaks are usually difficult to model, especially by hydrologic models with daily time step in river network characterized by a time of concentration of only few hours. Moreover, during the calibration of MOBIDIC model, peaks

discharge was considered by the objective function of the calibration module only with a 5% weight (the same as for discharge and cumulative flow volume), with an 85% attributed to flow duration parameter.

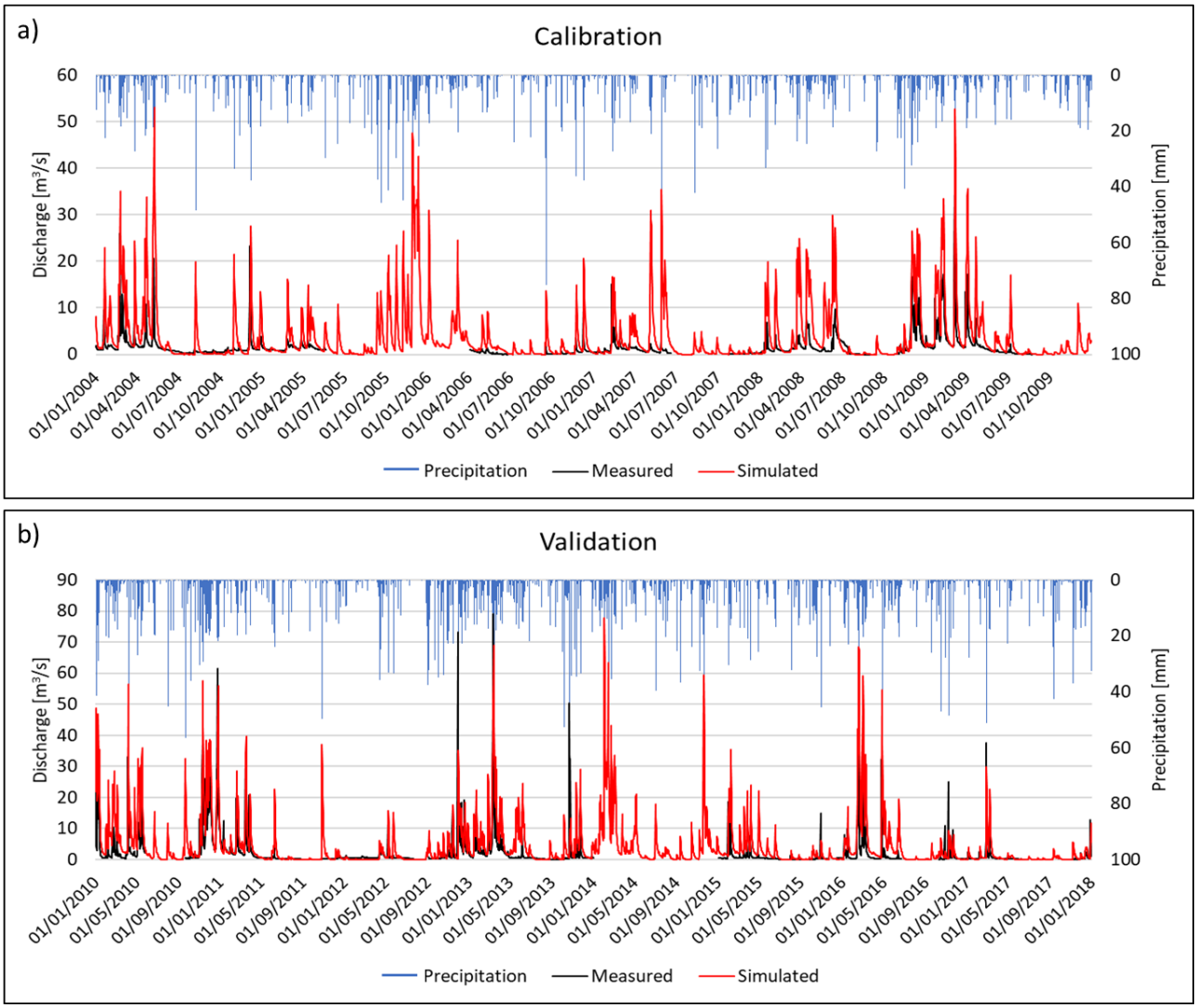

Figure 57 - Observed and simulated hydrographs for Turbone gauging station during a) calibration and b) validation periods.

In order to evaluate the goodness of the model for each single year of simulation, duration curves of observed and simulated discharge values in correspondence of Turbone river gauging station are presented, both for calibration and validation period (Figure 58 and Figure 59). Analyzing the curves, there is a quite good match between simulated and measured discharge values, with the model that simulates reasonably well the range of magnitude of daily flows for all the duration of the simulation. Some mismatches can be identified in correspondence of low discharge values for 2004, 2011 and 2012 curves, but the calibration procedure generally reached, for the entire temporal domain, a good degree of approximation between observed and modelled duration curves.

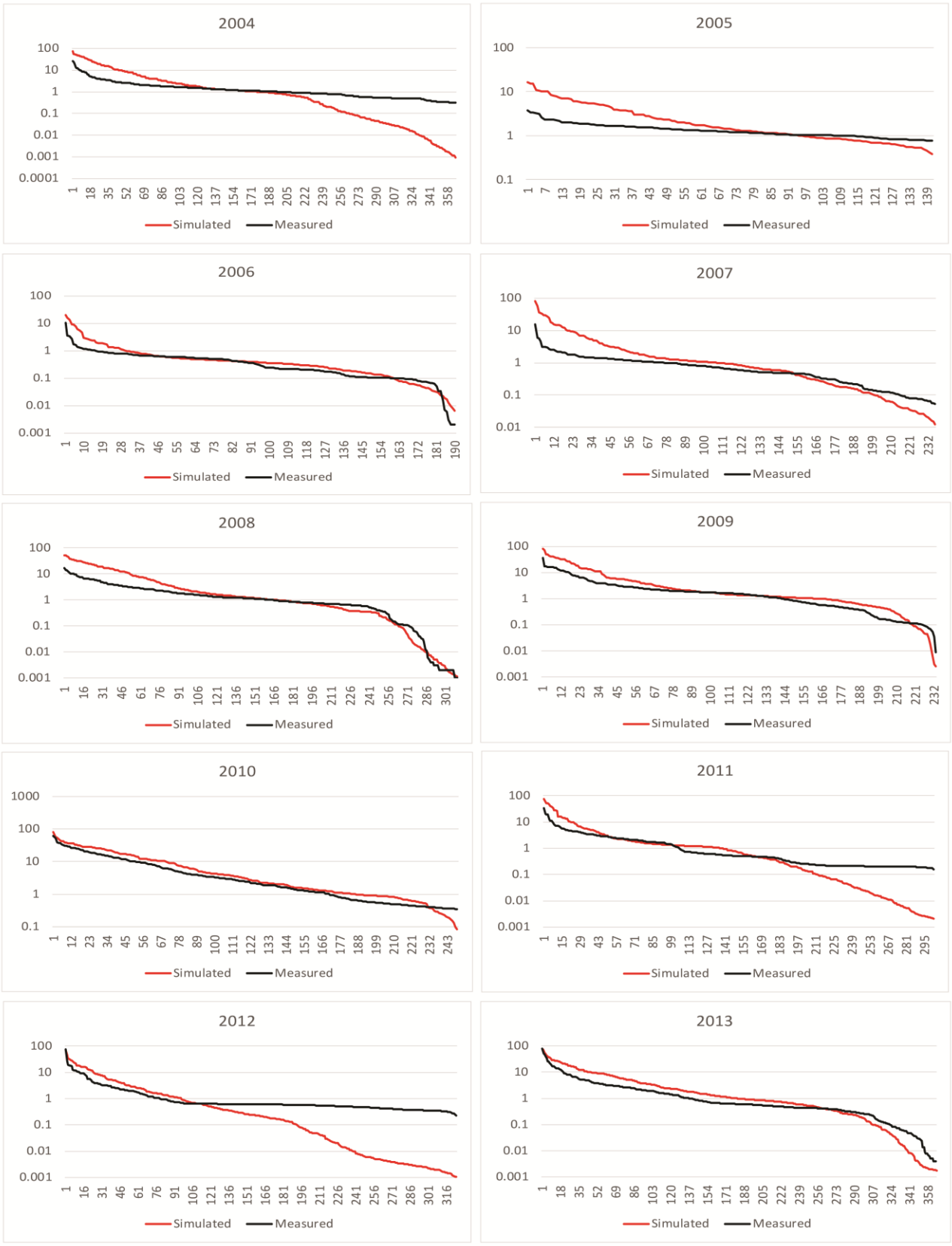

Figure 58 - Observed and simulated duration curves at Turbone gauging station for 2004-2009 calibration period and 2010-2013 validation period.

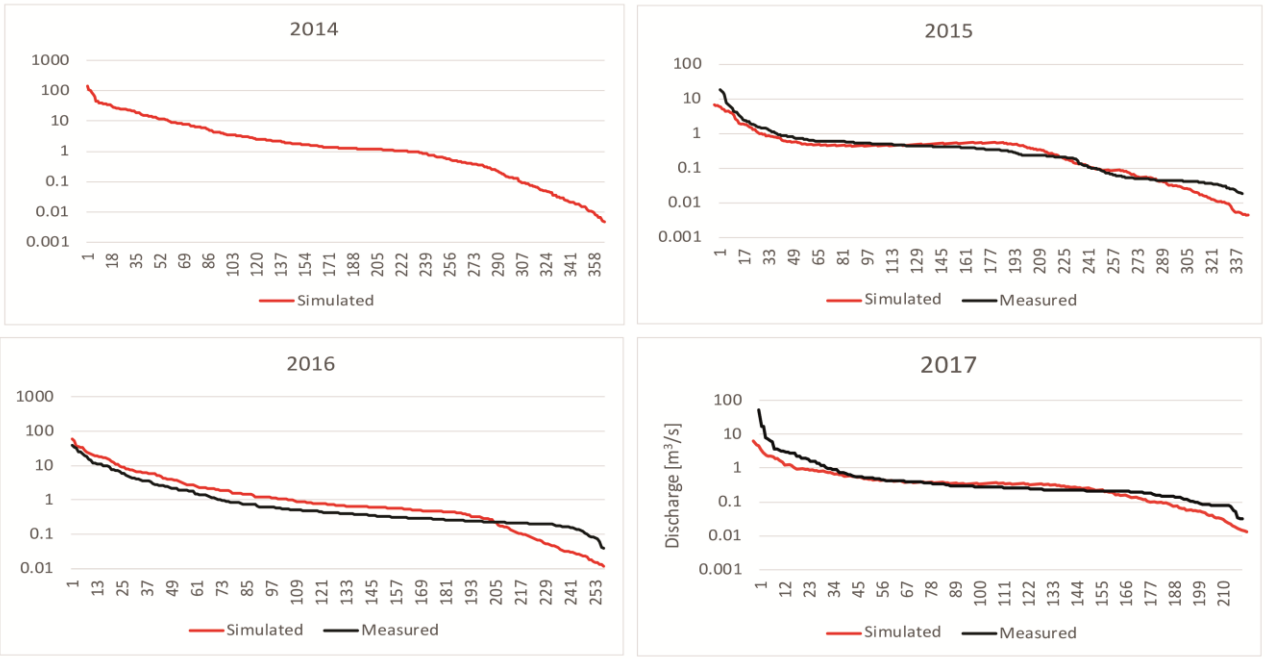

Figure 59 - Observed and simulated duration curves at Turbone gauging station for 2014-2017 validation period.

The evaluation of hydrologic model efficiency and performance is commonly made through comparisons of simulated and observed variables, and reported by means of many different statistical indexes. The Nash–Sutcliffe efficiency index (NSE) is a widely used and high reliable statistic tool for assessing the goodness of fit of hydrologic models. Nash–Sutcliffe efficiency can range from $-\infty$ to 1. An efficiency of 1 ($NSE = 1$) corresponds to a perfect match of modeled discharge to the observed data. An efficiency of 0 ($NSE = 0$) indicates that the model predictions are as accurate as the mean of the observed data, while an efficiency less than zero ($NSE < 0$) occurs when the observed mean is a better predictor than the model or, in other words, when the residual variance (described by the numerator in the expression above), is larger than the data variance (described by the denominator). Essentially, the closer the model efficiency is to 1, the more accurate the model is. The Nash-Sutcliffe efficiency (NSE) can be defined as follows:

$$NSE = 1 - \frac{\sum_{t=1}^{T}(Q_m^t - Q_o^t)^2}{\sum_{t=1}^{T}(Q_m^t - \bar{Q}_o^t)^2} \tag{60}$$

Where Q_m^t and Q_o^t are respectively modeled and observed discharge data at time t and $\bar{Q}_o^t$ is the mean of observed discharges.

Another important indicator to assess overall modelling performance is represented by the root-mean-square error (RMSE). RMSE is a frequently used measure of the differences between values predicted by a model and the observed values. RMSE is a measure of accuracy, to compare forecasting errors of different models for a particular dataset and not between datasets, as it is scale-dependent. The root-mean-square error is defined by:

$$RMSE = \sqrt{\frac{\sum_{t=1}^{T}(Q_m^t - Q_o^t)^2}{N}} \tag{61}$$

Normalizing the RMSE, for example by the range of the measured data (defined as the difference between its maximum and its minimum value), allows the comparison between models with different scales. The new obtained index is commonly referred to as the normalized root-mean-square error (NRMSE), expressed as a percentage, where lower values indicate less residual variance. NRMSE can be calculated by means of the following equation:

$$NRMSE = \frac{RMSE}{Q_{o\,max} - Q_{\,omin}} 100 \tag{62}$$

Where $Q_{o\,max}$ and $Q_{\,omin}$ are the maximum and the minimum value of the observed data respectively.

Efficiency evaluation indexes values for MOBIDIC hydrological model in Pesa basin are showed in Table 3:

Table 3 – Statistical index for MOBIDIC hydrological modelling at Turbone river gauging station.

	Years	NSE	RMSE	NRMSE
Calibration	2004-2009	0.306	5.453	14.823
Validation	2009-2017	0.352	7.824	9.878

Nash-Sutcliffe coefficient is characterized by a value of 0.306 and 0.352 for calibration and validation years, respectively. Such low values probably depend on differences encountered between observed and modelled flow peaks that, with high discharge values, have a strong influence on NSE coefficient calculation.

As discussed in chapter 6, in order to use time series of modelled river discharge data as input data for MODFLOW code (and its RIVer package), MOBIDIC discharge output needed to be converted into river stage values, representing the elevation of the water level above the riverbed, by means of equation (57). According to the groundwater model resolution, for each river branch in which Pesa river network has been divided, the mean monthly discharge was identified. Then, considering a constant flow celerity and a branch-dependent river width, the mean monthly river stage has been calculated (Figure 61). All branches have similar distribution of maximum and minimum water levels during the year, with a bi-modal distribution that highlight the two major rainy seasons on February and November. During summer, river stage drops down to a very low level, with long traits of the river becoming dry during the warmer weeks (Figure 60).

Figure 60 - Final part of Pesa river, close to the Pesa basin outlet (July 2017).

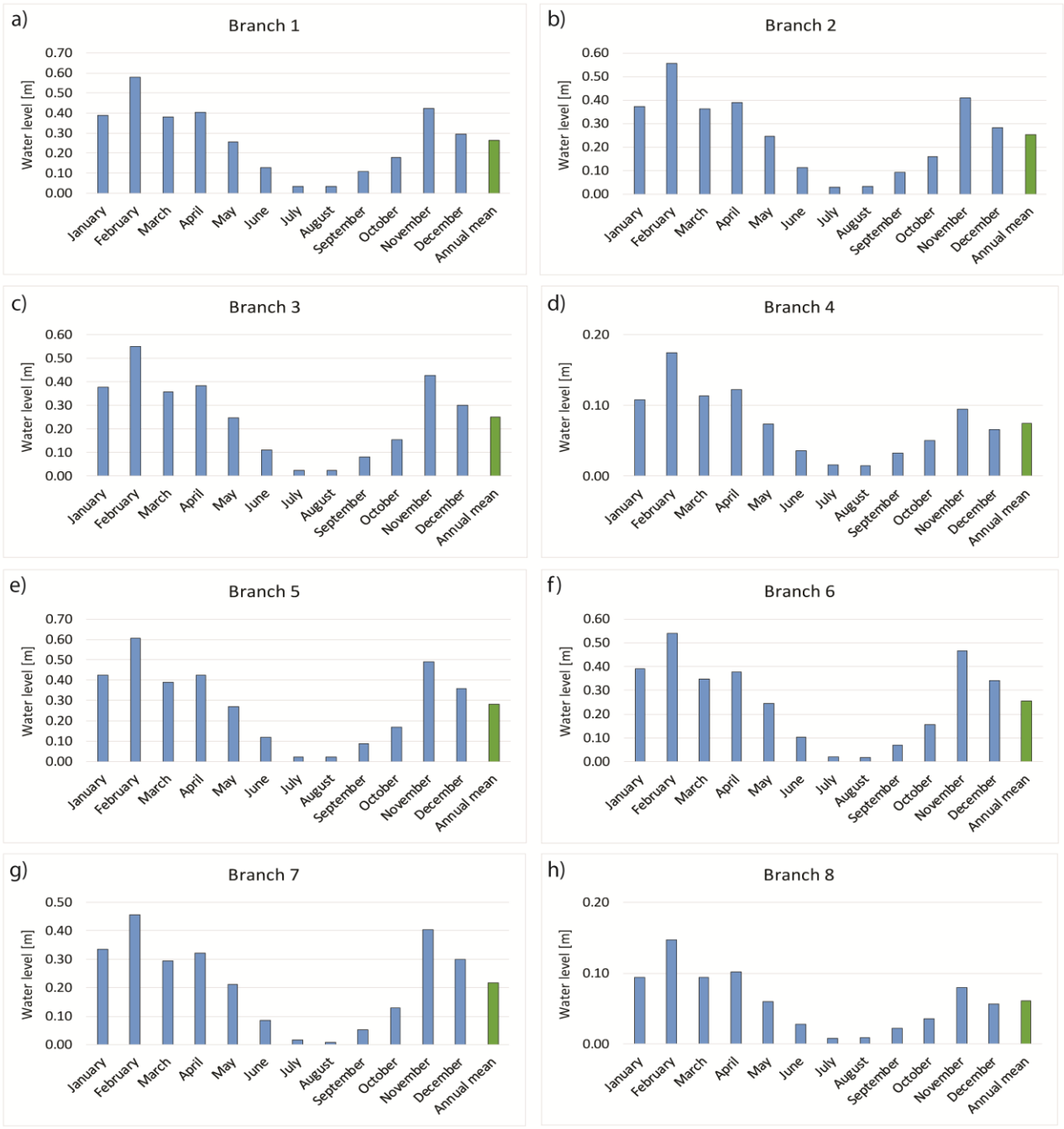

Figure 61 - a) River stage for each river branches, as calculated from MOBIDIC discharge output.

Among MOBIDIC output variables, time series of water percolation through the aquifer are also provided, representing the net amount of water that actually reaches the groundwater table. In MOBIDIC, percolation is considered to be proportional to the water contained in the gravitational storage, by means of the percolation coefficient γ. Mean monthly percolation values of 2004-2017 period, obtained from the hydrological modelling of Pesa basin, are shown in Figure 62.

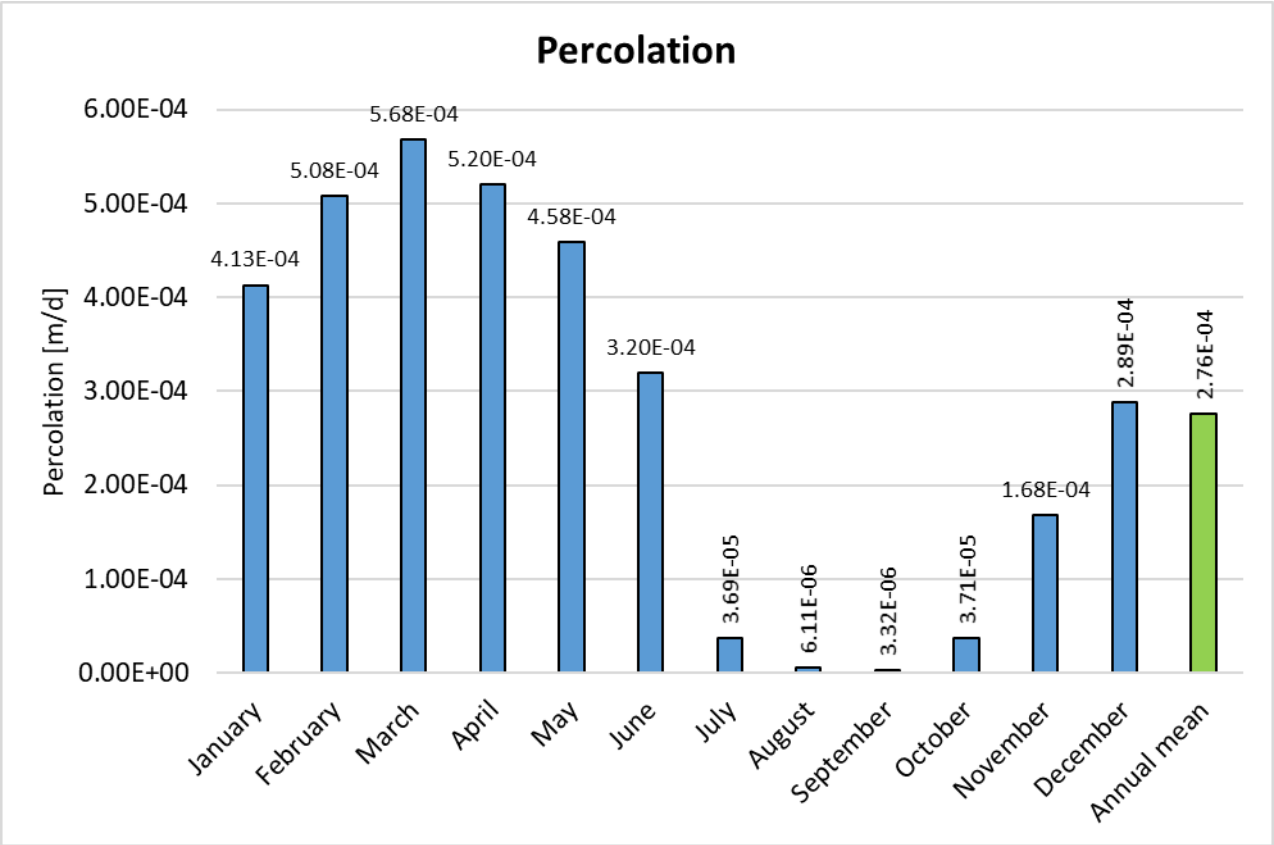

Figure 62 – Percolation values obtained from MOBIDIC output.

Differently than for river stage, mean monthly percolation follows a single peak distribution, located on March, at the end of the main rainy season. Very low values are normally observed during the driest months, from July to October. Over the basin, a mean annual percolation of $2.76 \cdot 10^{-4}$ m/day (100.74 mm/year) has been calculated for the 2004 – 2017 period. Based on real precipitation and evapotranspiration data, the Arno River basin Authority estimated a mean annual percolation of $1.95 \cdot 10^{-4}$ m/day (71.35 mm/year) for Pesa basin in 2007 (the most recent update).

RCH (recharge) package in MODFLOW is used to represent constant flux boundary condition, in which only the amount of water that flows into each model cell over the reference time step need to be defined. In order to do this, MOBIDIC percolation output can be directly used as input for the RCH package, without need of further post processing elaboration. As discussed before, the groundwater model consists of 13 stress period, representing the twelve months of the year and a starting 10 days-long stationary stress period. Mean annual percolation value has been used as recharge input parameter for the first stress period.

8.1.2 Hydrogeological model results

MODFLOW Preconditioned Conjugate-Gradient (PCG) solver package has been used for groundwater flow equation computation. The solver checks the maximum head change in the solution at every cell after each iteration. If the maximum change in the solution is below the set of convergence tolerance (0.1 m in this case), the solution converges and the solver stops, otherwise, a new iteration starts.

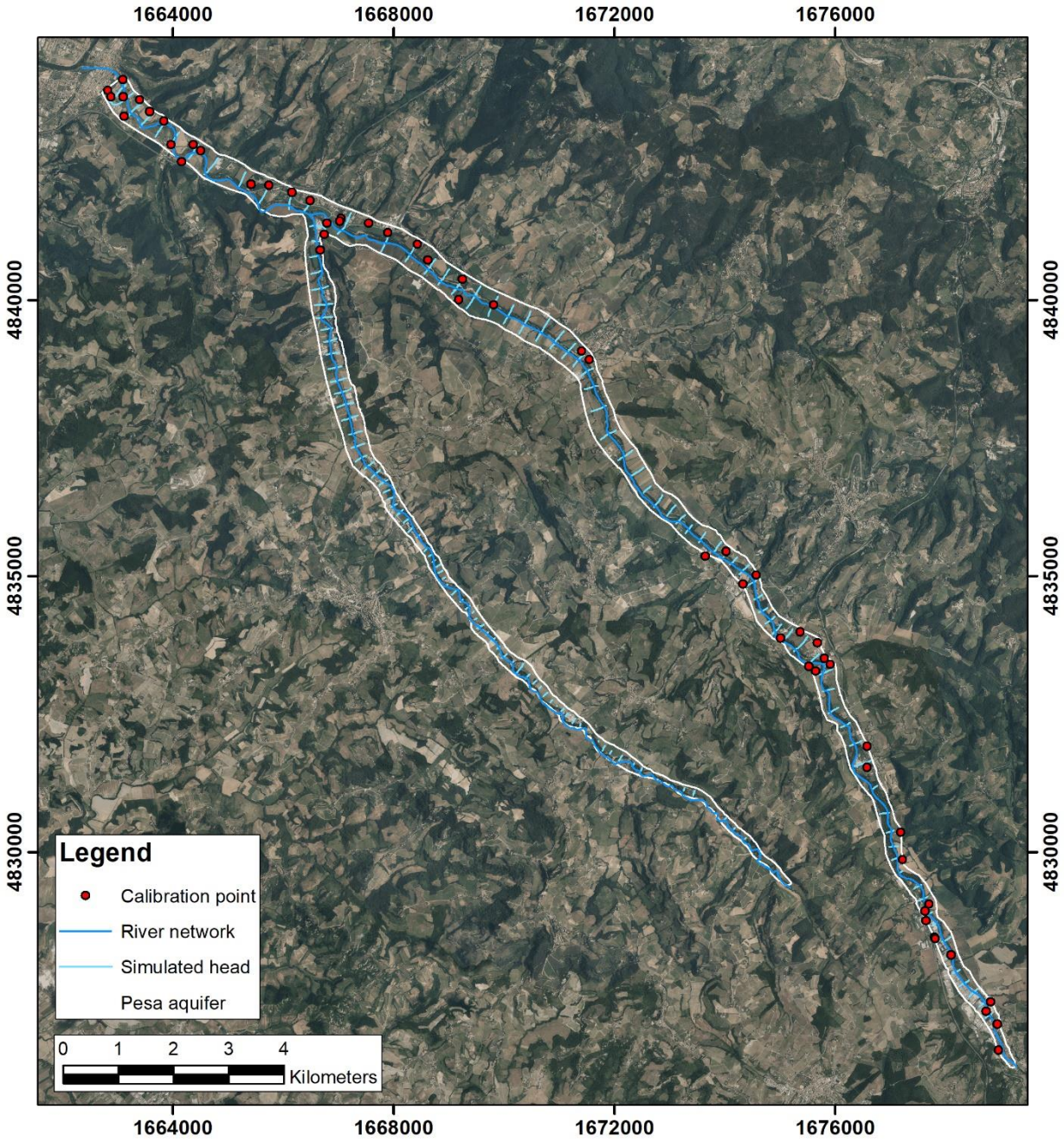

Figure 63 – Simulated hydraulic head map for the Pesa aquifer.

The groundwater flow model was calibrated by adjusting the horizontal and vertical aquifer hydraulic conductivity within a certain range of values, accordingly to the textural classes that constitute the aquifer, until the best fit between observed and simulated head values was obtained.

Since there were not transient hydraulic head observation available for the study area, the calibration was focused only on the first steady state stress period of the simulation.

The accuracy of the computed groundwater levels was judged by the comparison between observed and simulated values, with the examination of residuals (difference between observed and simulated values) and by means of statistical indexes like residual mean, residual standard deviation, root means square error (RMSE) and determination coefficient of the regression line (R^2). Ground water model calibration results are displayed in Figure 64:

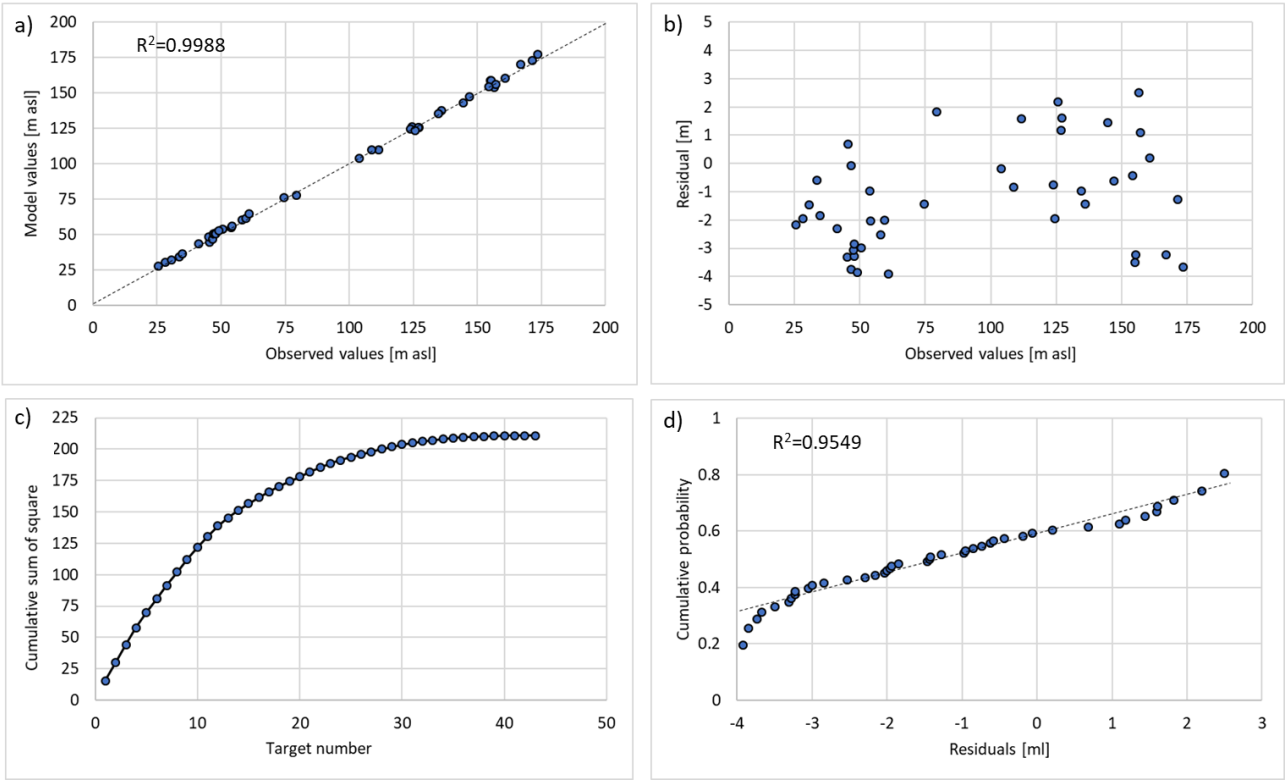

Figure 64 – Output of groundwater model calibration.

A good agreement has been obtained between the observed and simulated heads at all the 55 observation wells, as shown in Figure 64a. Plot of model values as a function of observation are all displayed along the 45° x-y bisector, with a determination coefficient value R^2 of 0.9988. Model residuals, representing the difference between simulated and observed head values, should be represented by a mean that approaches to zero and a standard deviation as minimal as possible. Typically, residuals should be characterized by values lower than 10% of the variability in the field data across the model domain. Residuals displayed in Figure 64b shows low values, ranging between +3 and -4 meters with an average value of -1.26 meters, that represent the 0.8 % of the difference between the maximum and minimum value of observed hydraulic head in the area. Calculated root mean squared error (RMSE) and residual standard deviation value for steady state model are equal to 2.61 and 2.06 m, respectively. Since the RMSE value is about 1.7% of the difference between the highest and lowest head in the study area (150 m), the model can be considered calibrated appropriately (Ehtiat et al., 2018). In Figure 64c, monitoring wells are sorted by the square of the residual and plotted with a cumulative curve. Squared residual, with a maximum value of 211.0, is homogeneously distributed among all targets, showing their reliability in the model calibration phase. Finally, a normal probability plot representing residuals departures from a normal distribution is given in Figure 64d. With a determination coefficient of 0.9549, the normal distribution of residuals data is assessed, and the goodness of the model calibration is confirmed.

MODFLOW-MOBIDIC modeling output have been used to develop a mean annual water budget estimation of Pesa basin, accounting the mean water fluxes and states occurred in the area during the 2004-2017 period. Water budget has been approached by examining separately both surficial and groundwater systems, in order to properly evaluate all the processes taking place within each reservoir and to deeply characterize their interaction. Then, a global water balance of the Pesa aquifer has been carried out, by combining results obtained from the integrated hydrological and hydrological simulations.

8.1.3 Hydrologic balance

Surface water balance was obtained by following the hydrologic cycle scheme showed in Figure 65, combining all hydrologic variables obtained from MOBIDIC model output.

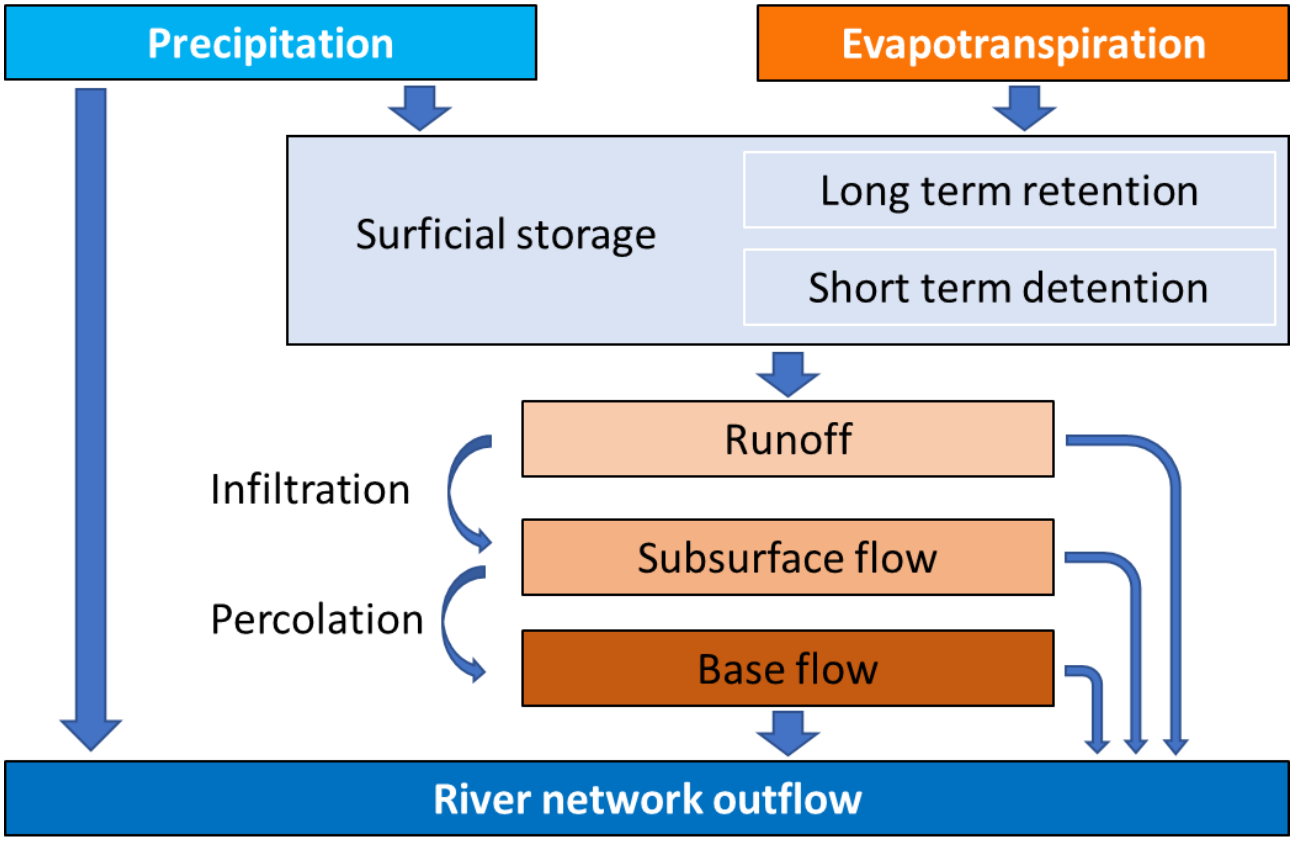

Figure 65 – Hydrological variables and fluxes considered in the surface water balance of MOBIDIC.

In the long term, the outflows/inflows water balance can be described by the following equation:

$$P = ET + Q_{out} \tag{63}$$

Where ET is represented by the evapotranspiration and Q_{out} is the total river network discharge, composed by the sum of surficial runoff, subsurface flow and base flow. Surficial storage hydrological performance is linked to the ability to delay and attenuate rainfall runoff. This effect can be explained by two simultaneous processes taking place, retention and detention. Retention is the ability to permanently hold back (retain) water by storing it for subsequent removal by evapotranspiration. If the precipitation intensity exceeds the storage capacity, runoff occurs. Detention is the ability to temporarily hold back (detain) the water, resulting in a reduced and delayed peak runoff.

Simulated values of the annual hydrological variables in Pesa basin, obtained from the hydrological model, are described in Table 4.

Table 4 - Simulated mean annual hydrological variables for the 2004-2017 period.

Year	Precipitation	Evapotranspiration	Stream outflow	Runoff	Subsurface flow	Base flow	Percolation
	[Mcm/yr]	[Mcm/yr]	[Mcm/yr]	[Mcm/yr]	[Mcm/yr]	[Mcm/yr]	[Mcm/yr]
2004	294.61	147.63	145.12	126.42	9.65	4.20	16.31
2005	328.89	176.62	143.33	124.46	9.82	4.27	16.61
2006	226.52	167.64	76.76	56.88	10.94	4.80	18.51
2007	225.57	162.56	75.46	61.67	7.41	3.24	12.55
2008	311.59	148.31	141.77	122.11	10.33	4.48	17.46
2009	259.86	146.25	127.21	106.23	11.19	4.89	18.92
2010	440.94	137.78	291.26	260.92	15.21	6.60	25.68
2011	192.83	176.64	82.32	67.88	7.67	3.38	12.98
2012	309.15	192.24	71.72	67.27	2.04	0.87	3.44
2013	362.60	172.24	179.41	156.41	11.97	5.21	20.23
2014	353.49	152.93	198.50	173.70	12.84	5.59	21.70
2015	232.86	170.26	84.59	66.27	9.98	4.39	16.90
2016	344.14	190.23	159.72	140.04	10.16	4.43	17.18
2017	219.95	212.15	34.66	30.36	2.28	0.99	3.85
Mean	293.07	168.11	124.96	111.47	9.39	4.10	15.88

The seasonal cycle of precipitation over the region shows a bi-modal distribution, with two distinct peaks in the most wet months (February and November, the rainiest month), that drive the temporal distribution of all the main hydrologic variables in Pesa watershed (Figure 66a).

Evapotranspiration represent the main factor of water loss within the study area, with an annual mean value of about 168.11 Mcm, representing more than 50 % of the total amount of rainfall. The annual evaporation trend evidence a small drop in February and maximum intensity during July and August, that is consistent with the idea that the spatial pattern of evaporation is primarily driven by temperature. Compared to other water balance term, evapotranspiration has a relatively low variability over the years, even if it is characterized by an increasing trend in the simulation period (Figure 66b). Because of its close relation with temperature, this could be probably linked to the effects of climate warming affecting the Earth in last decades.

River discharge, together with its hydrologic components (surficial runoff, subsurface flow and base flow), strictly follow the precipitation trend. The only difference is represented by their maximum values, occurring on February, when probably the highest amount of rainfall, gravitational and capillary water and groundwater storage are combined.

An important role in the water budget is also played by runoff component that, with an average value of 111.47 Mcm/year, represents the 87% of river discharge during the year. Percolation through Pesa aquifer ranges between 12 - 25 Mcm/year, except for a minimum value of 6 Mcm occurred in 2012, making up 9-10% of the total water budget.

Besides evapotranspiration, the shape of the annual cycle of the main hydrologic variables is clearly related to the precipitation trend, presenting a bimodal distribution that represent the two main rainy seasons. Therefore, short- and long-term variation in the precipitation pattern, driven by climate changes, can lead to

impactful alteration in water balances that need to be taken into account in hydrologic analysis in future years.

Surface water withdrawals from the surficial network are negligible in Pesa watershed and they have not been considered in the water balance analysis.

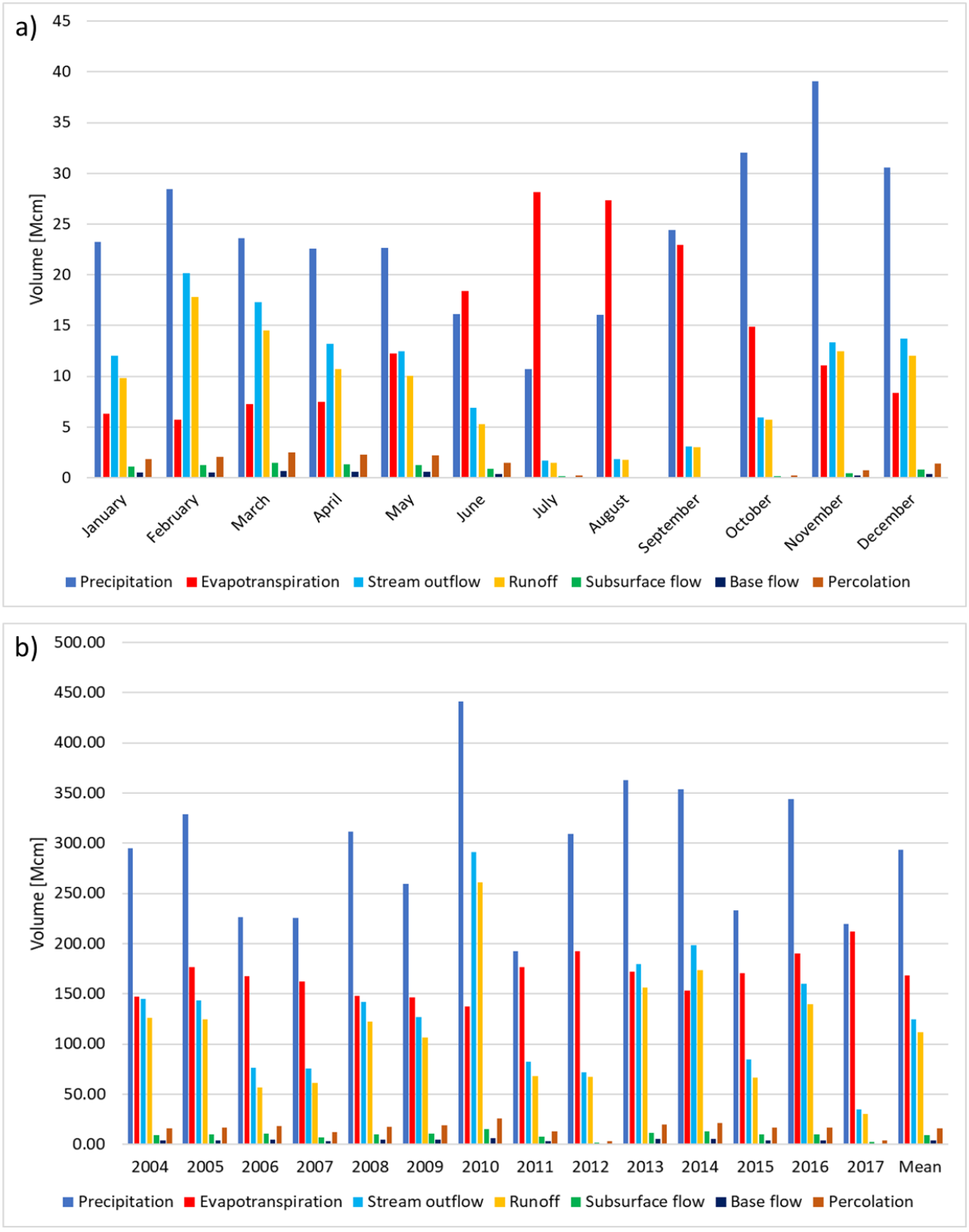

Figure 66 – a) Monthly and b) annual hydrologic balance in Pesa basin.

8.1.4 Hydrogeologic balance

Water balance of Pesa aquifer was carried out by means of the main output parameters obtained by the groundwater model developed with MODFLOW, considering the following equation:

$$R_{ch} + Q_{riv} = D_p + Q_g + G_{dout} + Storage \quad (64)$$

Where R_{ch} and Q_{riv} are the aquifer recharge due to percolation and drainage from the river network, respectively, representing together the total water input of the aquifer system. The output from the aquifer are represented by water extraction from pumping wells (D_p), water drained by the river (Q_g) and deep flows through confining aquifers (G_{dout}). *Storage* is the difference between aquifer recharge and discharge over the time, it is affected by intrinsic properties of the aquifer (storage capacity, transmission capacity, and aquifer geometry) and can be roughly described as the total amount of water stored in aquifers. Figure 67 shows the components of the hydrogeologic water balance for Pesa aquifer. Blue bars represent water input to the aquifer, while red bars represent water output. Since any information was available about seasonal changes in pumping rate in the area, groundwater withdrawals have been considered constant for every stress period of the simulation, and they were not represented in the figure below.

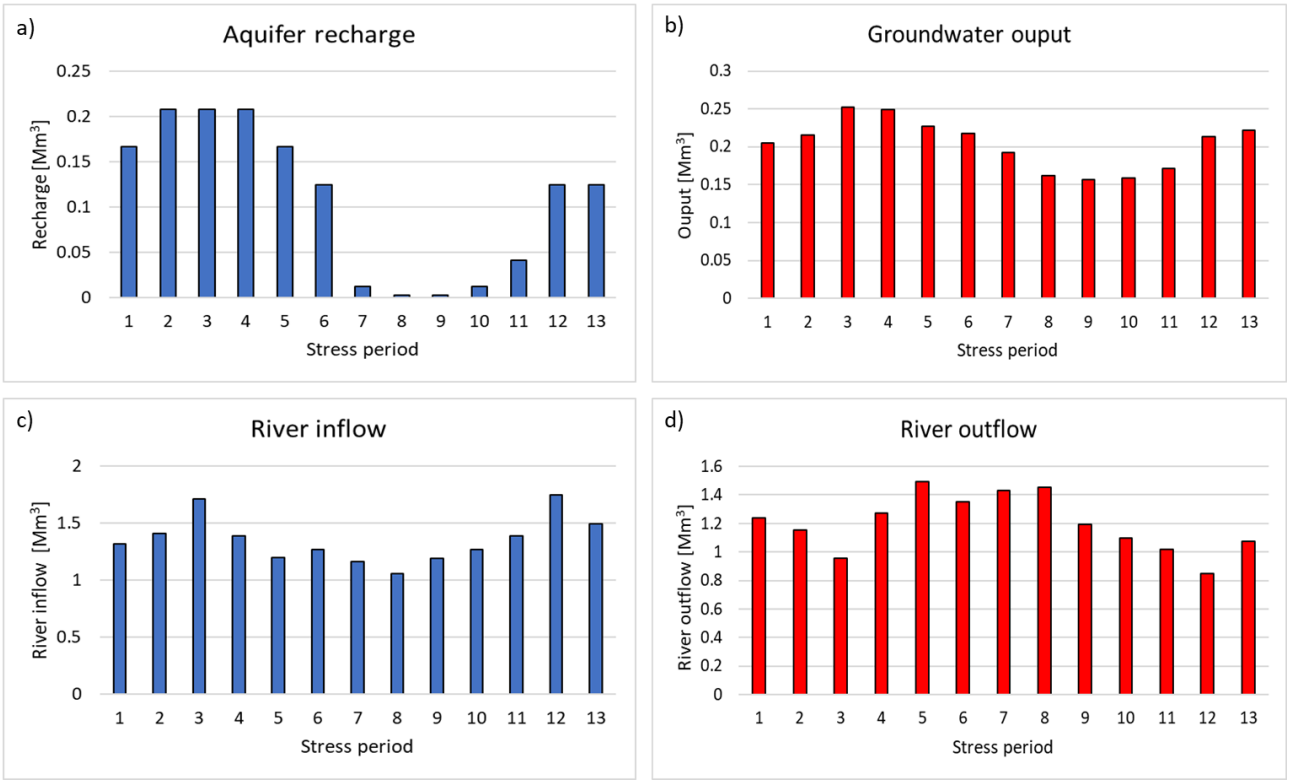

Figure 67 – Main monthly inflow and outflow of Pesa aquifer.

Aquifer inflows, derived from percolation of rainfall and drainage from the surficial network, are dominated by the direct influence of Pesa river, annually representing about the 90% of the total aquifer recharge. Both percolation and river inflow clearly follow the seasonal precipitation trend, with maximum values occurring during the rainiest months (Figure 67a and c). However, if percolation values tend to zero during summer, river inflow contribution remains quite important, guaranteeing an important amount of recharge for Pesa aquifer even in correspondence of the driest months. Percolation trend displayed in Figure 67a is referred to the only Pesa aquifer, explaining why it exhibits lower values than percolation pattern shown in Figure 66a, referred to the whole Pesa basin.

Groundwater discharge from Pesa aquifer through the confining Empoli aquifer shows a very low variability during the year, with a difference of only 0.9 Mcm between the maximum (0.19 Mcm on March and April, stress periods 4 and 5) and the minimum value (0.1 Mmc on July, August and September, stress periods 9 and 10). Occurring in the underground, this deep flow is probably less influenced by seasonal climate variation (Figure 67b) than other hydrogeological variables. As can be clearly seen in Figure 67d, the main water output from Pesa aquifer is constituted by the restitution of groundwater from the aquifer to the river network, that represents about the 83% of the total annual outflows. This can be explained by the direct connection between aquifer and river network in Pesa basin, where flows occurring between surficial and deep reservoirs are predominant. Water inflows and outflows occurring in Pesa aquifer and estimated by MODFLOW model are displayed in Table 5:

Table 5 – Simulated input and output flows occurring in Pesa aquifer.

Stress period	Month	Aquifer recharge	River inflow	River outflow	Wells extraction	Groundwater output	Storage
		[Mcm]	[Mcm]	[Mcm]	[Mcm]	[Mcm]	[Mcm]
1	Mean	0.17	1.55	1.24	0.34	0.14	0.00
2	January	0.21	1.65	1.65	0.34	0.16	0.21
3	February	0.21	1.95	1.95	0.34	0.19	0.67
4	March	0.21	1.63	1.63	0.34	0.19	0.04
5	April	0.17	1.44	1.44	0.34	0.17	-0.39
6	May	0.12	1.51	1.51	0.34	0.16	-0.21
7	June	0.01	1.40	1.40	0.34	0.13	-0.49
8	July	0.00	1.30	1.30	0.34	0.10	-0.59
9	August	0.00	1.43	1.43	0.34	0.10	-0.20
10	September	0.01	1.51	1.51	0.34	0.10	-0.02
11	October	0.04	1.63	1.63	0.34	0.11	0.20
12	November	0.12	1.99	1.99	0.34	0.15	0.77
13	December	0.12	1.73	1.73	0.34	0.16	0.28

Additional information given in Table 5 are represented by the amount of water extracted by pumping wells, considered constant during the whole simulation with a value of 0.34 Mcm per month (4.08 Mcm per year), and by the value of groundwater storage.

During the first stress period, simulated as a starting mean annual condition with a single stationary stress period, storage has a value very close to zero. At the end of each steady state simulation, the mass balance equation must reach the equilibrium, with the occurrence of the same amount of inflows and outflows occurring through the model domain. The developed groundwater model is characterized by a very low output/input difference of 0.003%, that confirm the goodness of the model and its high reliability.

Following the Mediterranean climate pattern, groundwater storage exhibits an accumulation trend in Winter and Autumn seasons, while Spring and Summer months are characterized by a loss of storage. Storage shows a high variability during the year, reaching its maximum increase on November (with a surplus of about 0.77 Mcm) and its minimum in July (with a deficit of -0.59 Mcm). The inversion between positive and negative storage trends occurs in March and September, when the aquifer system is characterized by very similar amount of water inflows and outflows, and storage assumes values close to 0 (Figure 68a).

The cumulative distribution of monthly storage was computed and displayed in Figure 68b, in order to evaluate the net water balance of Pesa aquifer. The maximum amount of stored resource results available in

March, right at the end of the wet season, while September can be identified as the month with the minimum volume of groundwater available. Finally, at the end of December, the yearly balance is concluded with a small storage surplus of about 0.28 Mcm, resulting in an increasing of available water in Pesa aquifer during the study period.

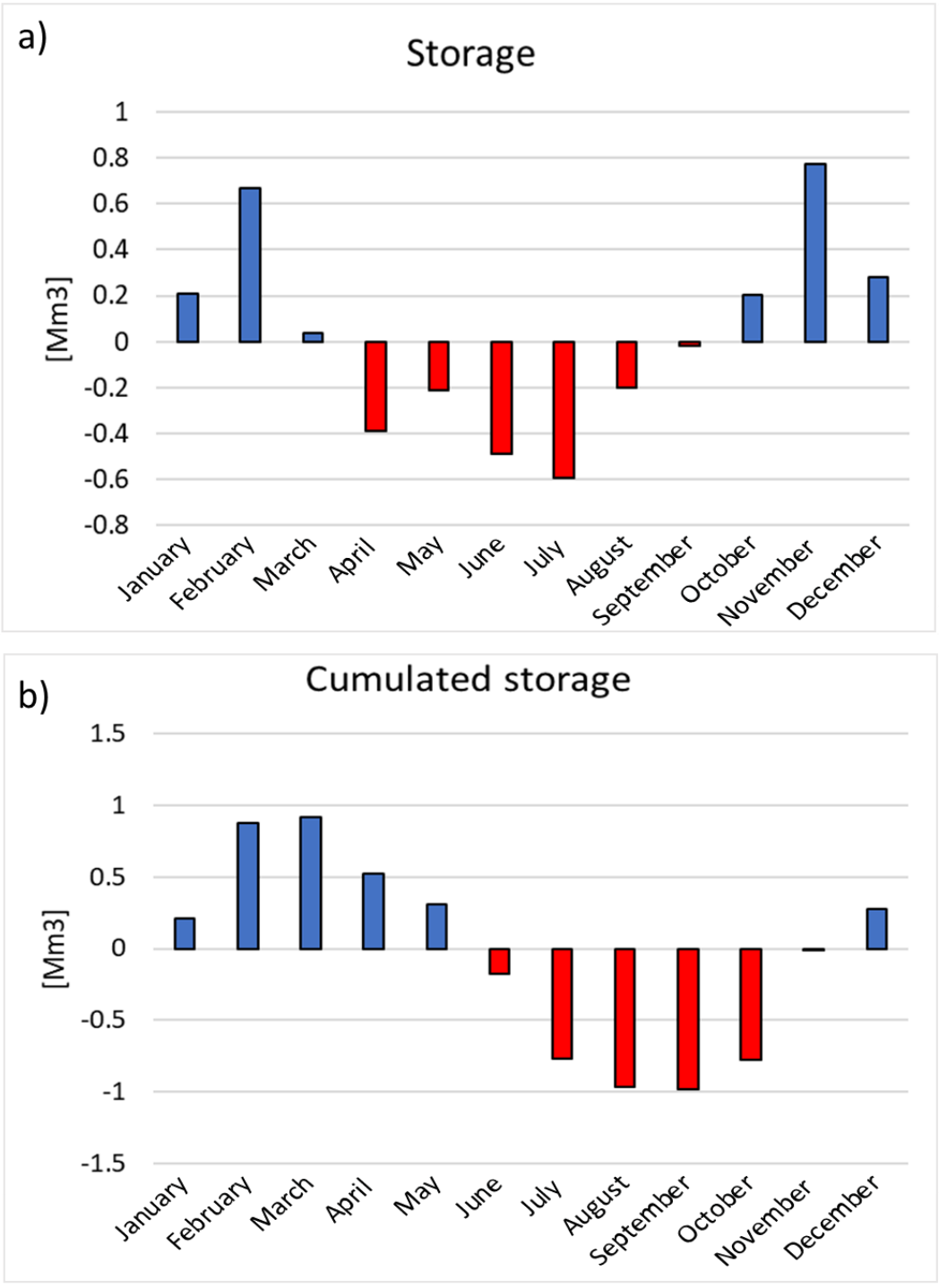

Figure 68 – a) Mean monthly storage and b) Cumulated storage in Pesa aquifer.

8.1.5 Global water balance

Combining results obtained from the analysis of both surficial and underground water balances, a global evaluation of water availability in Pesa aquifer can be performed, considering all natural and anthropic processes occurring in the study area:

Surficial balance $$P + Q_{in} + Q_g = ET + Q_{out} \quad (65)$$

Underground balance $$G_{in} = Q_g + G_{dout} + D_p + Storage \quad (66)$$

Global balance $$P + Q_{in} + G_{in} = ET + Q_{out} + D_p + G_{dout} + Storage \quad (67)$$

Where Q_{in} and G_{in} represent respectively surficial and deep-water input flowing into the aquifer system from the surrounding area of the basin (Figure 69).

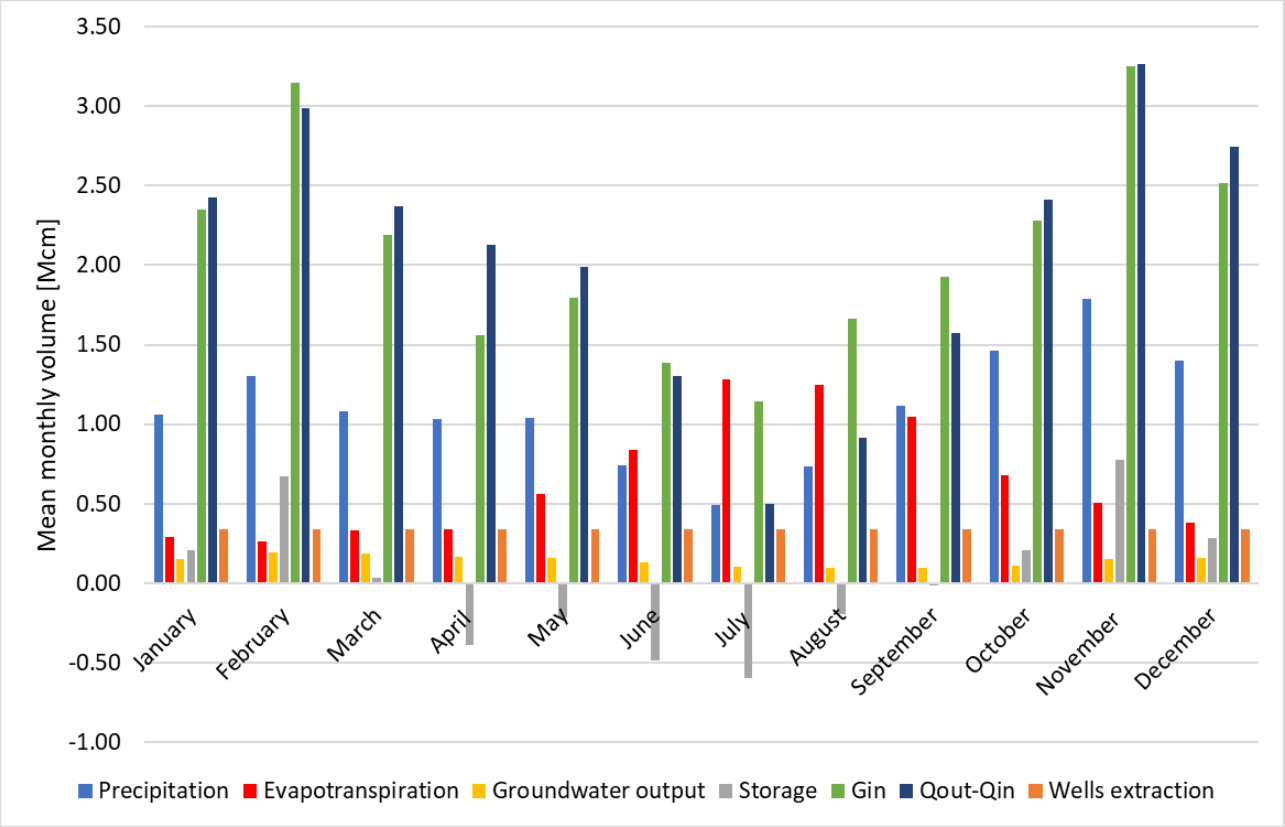

Figure 69 – Global hydrologic-hydrogeologic water balance on the Pesa aquifer.

For the analysis, precipitation and evapotranspiration variables have been rescaled in order to consider only the portion of the water cycle directly affecting the aquifer system. Q_g parameter, representing the amount of water drained by the river system from the aquifer, has not been included in the global water balance equation, since it can be considered at the same time as an input for the surficial balance and as an output for the groundwater balance.

8.2 Pistoia Subsidence Modelling

Groundwater overexploitation is a common issue that characterize many aquifer systems all over the World, inducing several long-term consequences for the natural environment and for human activities. One of the main problems related to groundwater over pumping, and affecting many areas characterized by the presence of unconsolidated alluvial deposits, is the development of land subsidence. When groundwater removal rate is greater than the average aquifer recharge rate for long periods, subsidence phenomena may occur, as a result of the compaction of silty and clayey sediments due the increase of the effective stress.

Firenze – Prato – Pistoia basin (Tuscany region, central Italy) has a long experience of land subsidence and ground deformation related to groundwater overexploitation, observed in the area since the early 1960s. In recent years, with the availability of widespread and cheap ground displacement measurement obtainable from satellite InSAR acquisitions, subsidence occurring in Firenze – Prato – Pistoia area has been clearly detected. In particular, two main subsidence bowls close to Pistoia city and characterized by high ground displacement velocity (>15 mm/yr) have been identify in recent years.

With the purpose to identify causes and potential consequences of subsidence phenomena occurring in Pistoia area, a subsidence-focused groundwater model has been developed, by means of the presented MOBIDIC-MODFLOW modelling approach. Then, thanks to MODFLOW SUB PACKAGE capabilities, subsidence affecting Pistoia city and its surroundings has been modelled and potential scenarios of land subsidence that could interest Pistoia area in the years to come have been analyzed.

8.2.1 Hydrologic model results

As discussed in chapter 5, the hydrological modelling has been approached at two different scales, considering the whole region of the Arno basin upstream of Gonfolina closing section (called “Gonfolina model”) or limiting the model domain at the only Ombrone river basin portion (called “Ombrone model”). The temporal domain of both hydrological models includes 26 years, from 1992 to 2017, with 6 years of calibration (2010-2015). For the Gonfolina model, the calibration phase has been accomplished by means of the river discharge observations available at Pontelungo, Poggio a Caiano, Dicomano and Scandicci stations. For the Ombrone model, only Pontelungo and Poggio a Caiano stations have been included in the calibration procedure. Calibrated global hydrologic parameters and their relative initial values are presented in Table 6:

Table 6 – MOBIDIC global hydrologic parameters, with their initial and calibrated value, for Gonfolina and Ombrone models.

Parameter	Unit of measure	Initial value	Calibrated value gonfolina	Calibrated value ombrone
γ	$[T^{-1}]$	$1.026 \cdot 10^{-7}$	$1.13 \cdot 10^{-7}$	$2.58 \cdot 10^{-7}$
κ	$[T^{-1}]$	$1.336 \cdot 10^{-6}$	$1.72 \cdot 10^{-6}$	$2.70 \cdot 10^{-7}$
β	$[T^{-1}]$	$2.44 \cdot 10^{-6}$	$2.11 \cdot 10^{-6}$	$1.79 \cdot 10^{-6}$
α	$[T^{-1}]$	$5.0 \cdot 10^{-5}$	$1.53 \cdot 10^{-6}$	$7.77 \cdot 10^{-5}$

Models calibration has been performed by means of MOBIDIC calibration module, attributing a different weight to the four parameters considered by the objective function. In particular, in order to enhance the importance of flow duration in the long-term, a 0.85% weight has been given to the flow duration parameter, while a 0.05% weight has been attributed to discharge, cumulative flow volume and peak discharge.

To evaluate the goodness of the model calibration for each year of simulation, duration curves of Ombrone river at Poggio a Caiano and Pontelungo gauging stations are displayed for both Ombrone and Gonfolina model in Figure 70. Moreover, for the period 2009-2017, an additional hydrologic modelling has been performed by means of Soil and Water Assessment Tool (SWAT), in order to compare the results of the fully distributed MOBIDIC model with a different semi-distributed modelling approach. The calibration of SWAT model has been carried out by means of SWAT-CUP calibration program.

Despite the efforts of the calibration phase, Gonfolina large scale model overestimates river discharge at both Poggio a Caiano for all the years of simulation. Likely, using lumped hydrological parameters aggregates on wide portion of the basin, the model was not able to reach an appropriate degree of accuracy with the measured information for all 4 calibration stations.

Poor results are also encountered with the simulated duration curves obtained by SWAT code, describing hydrologic dynamics that most probably require a more detailed representation of their spatial variability, that is not captured with a semi-distributed approach.

Analyzing the river duration curves in correspondence of Poggio a Caiano station, the small scale Ombrone model appears to be the most suitable for simulating river discharge in Ombrone basin, with flow duration curves that match the observations in a very good way for all the years of simulation. During the calibration phase, the 85% of the weight into the objective function has been attributed to flow duration parameter, trying to reduce the difference between observed and modelled duration curves as much as possible. Only a 5% weight has been given to discharge, cumulative flow volume and flow peaks, resulting in small discrepancies between simulated and measured duration curves for high discharge values. Base flow is simulated with a very good accuracy for all the duration of the simulation. The importance of setting a warm-up period at the beginning of a MOBIDIC simulation is demonstrated by the 1992 and 1993 simulated duration curves, that show high differences if compared with the observed ones. Because of this, data obtained from the first two years of the simulation have not been considered in the mass balance analysis.

Regarding Pontelungo gauging station, both SWAT and Gonfolina simulations overestimate the observations for years 2009, 2010, 2011 and 2012 at high discharge values, while they underestimate river flow at lower values. Better results are achieved for 2014, 2015 and 2016 years, in correspondence of which, duration curves of both models are very close the observations for the entire discharge range. A very good match between modelled and observed discharge has been obtained by the small scale Ombrone basin model for all the years of simulation. As for Poggio a Caiano station, even after the calibration phase, some differences in the shape of duration curves at high discharge values still remains, due to the assumptions made in the MOBIDIC calibration module settings phase.

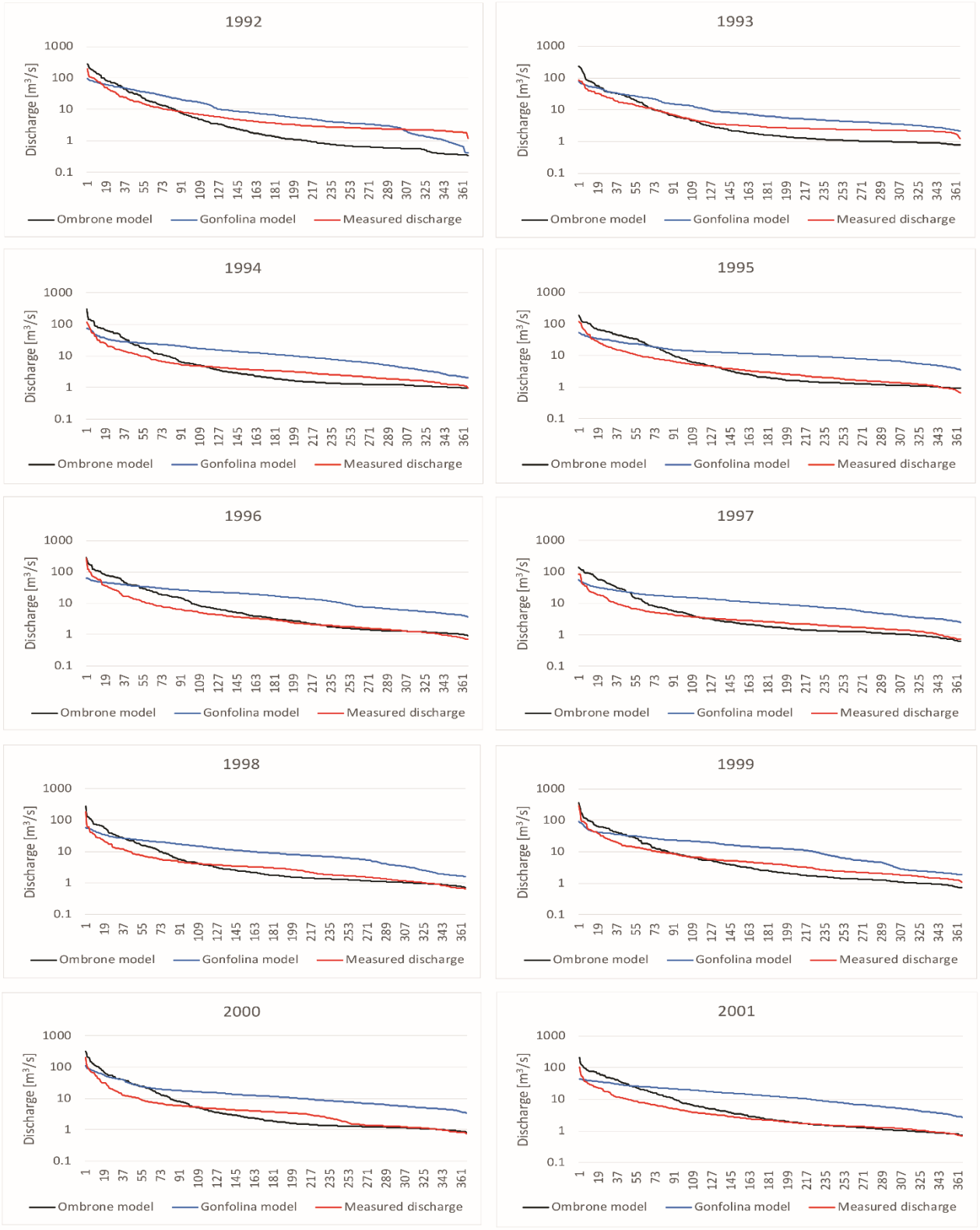

Figure 70 - Observed and simulated duration curves at Poggio a Caiano gauging station for 1993-2001 period.

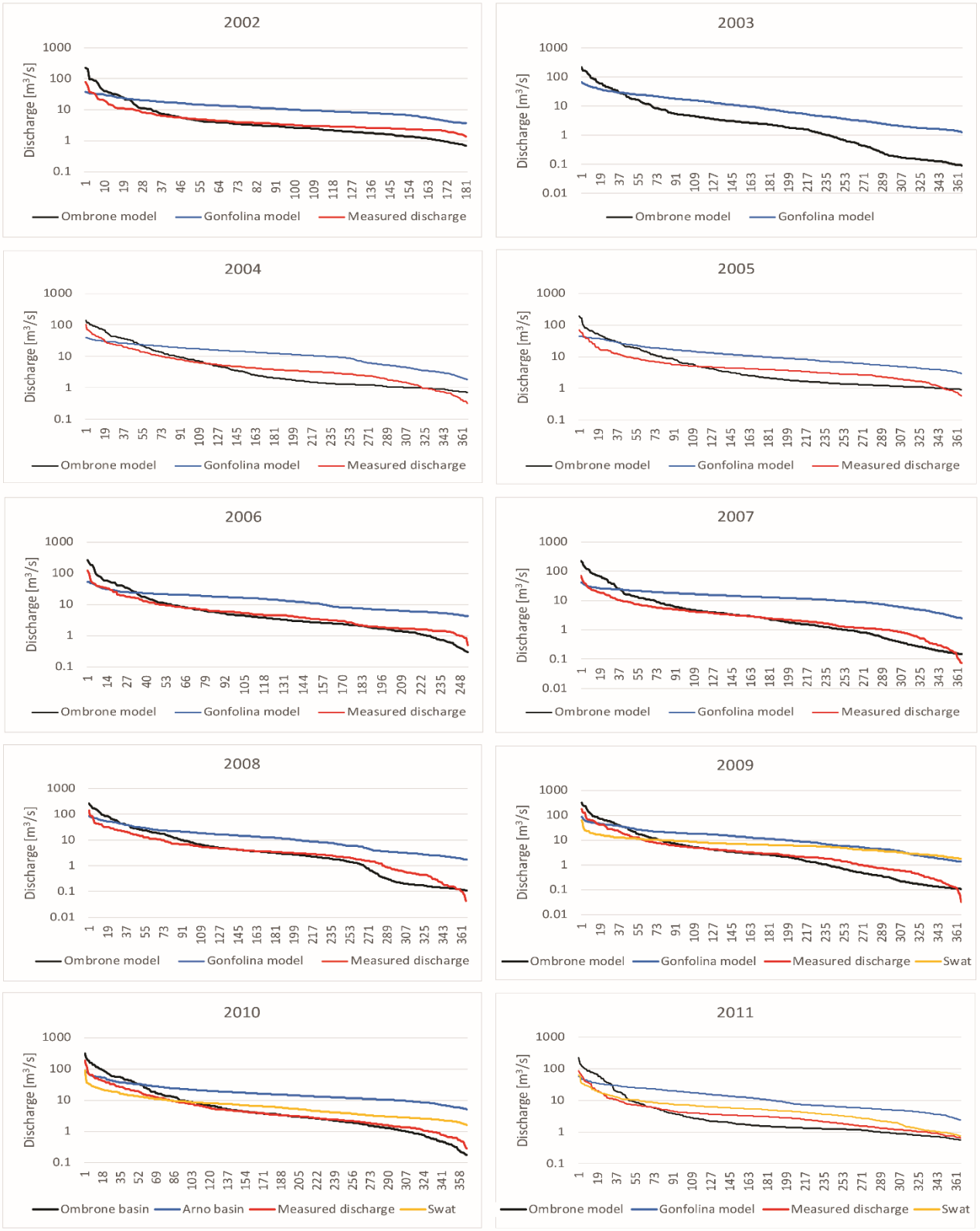

Figure 71 - Observed and simulated duration curves at Poggio a Caiano gauging station for 2002-2011 period.

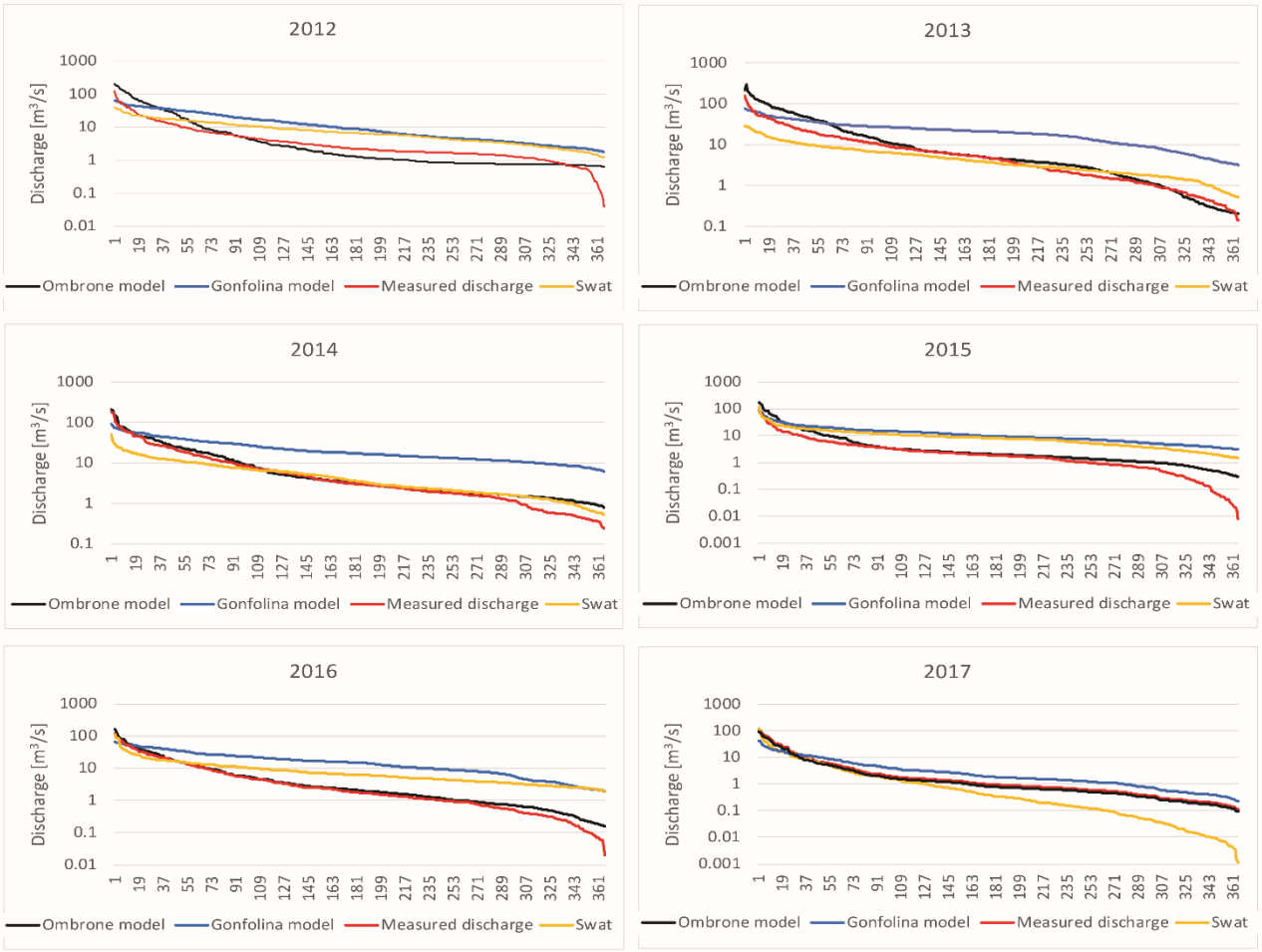

Figure 72 - Observed and simulated duration curves at Poggio a Caiano gauging station for 2012-2017 period.

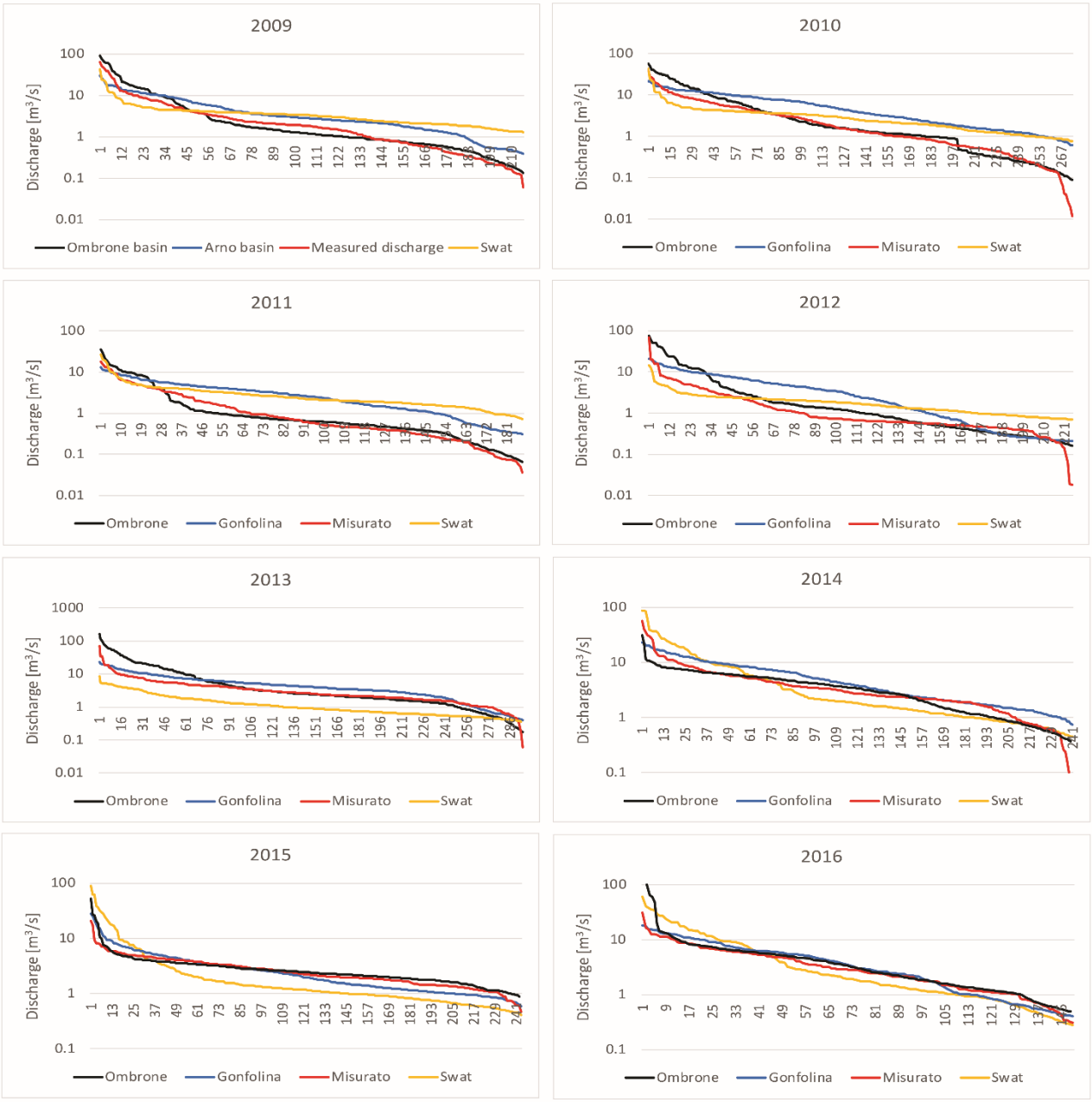

Figure 73 - Observed and simulated duration curves at Pontelungo gauging station for 2009-2016 period.

The analytical evaluation of the ideal hydrologic modelling approach, that led to the selection of the best model for the implementation of the groundwater simulations with MODFLOW, has been carried out by means of different statistical indexes. In particular, the Nash–Sutcliffe efficiency index (NSE), the root-mean-square error (RMSE) and the normalized root-mean-square error (NRMSE) have been considered in the analysis (Table 7 and Table 8). Only statistical indexes of Ombrone model are reported in the table.

Nash-Sutcliffe coefficient values indicate an acceptable performance rate for the developed model to describe the Ombrone basin river flow during the analyzed period. Higher values are achieved at Poggio a Caiano station, since it is characterized by a more reliable and continuous discharge time series for all the 1992-2017 period (except for years 2002 and 2003, with no measured data). Normalized Root-Mean-Squared error presents low values, around 10%, at both monitoring stations, with Poggio a Caiano still showing the best accuracy.

Table 7 – Statistical index for MOBIDIC hydrological modelling at Pontelungo river gauging station.

Pontelungo	Years	NSE coefficient	RMSE	NRMSE
		[-]	[m^3/s]	[%]
Calibration	2010-2015	0.46	7.30	10.47
Overall	1992-2017	0.49	7.70	11.04

Table 8 - Statistical index for MOBIDIC hydrological modelling at Poggio a Caiano river gauging station.

Poggio a Caiano	Years	NSE coefficient	RMSE	NRMSE
		[-]	[m^3/s]	[%]
Calibration	2010-2015	0.50	13.58	7.58
Overall	1992-2017	0.52	22.71	7.87

Before to convert MOBIDIC discharge output into input data for MODFLOW RIV package, the Ombrone network has been sub divided into 11 branches, in order to represent the river system with an appropriate resolution. Each branch is characterized by constant width, flow velocity and river stage (Figure 74).

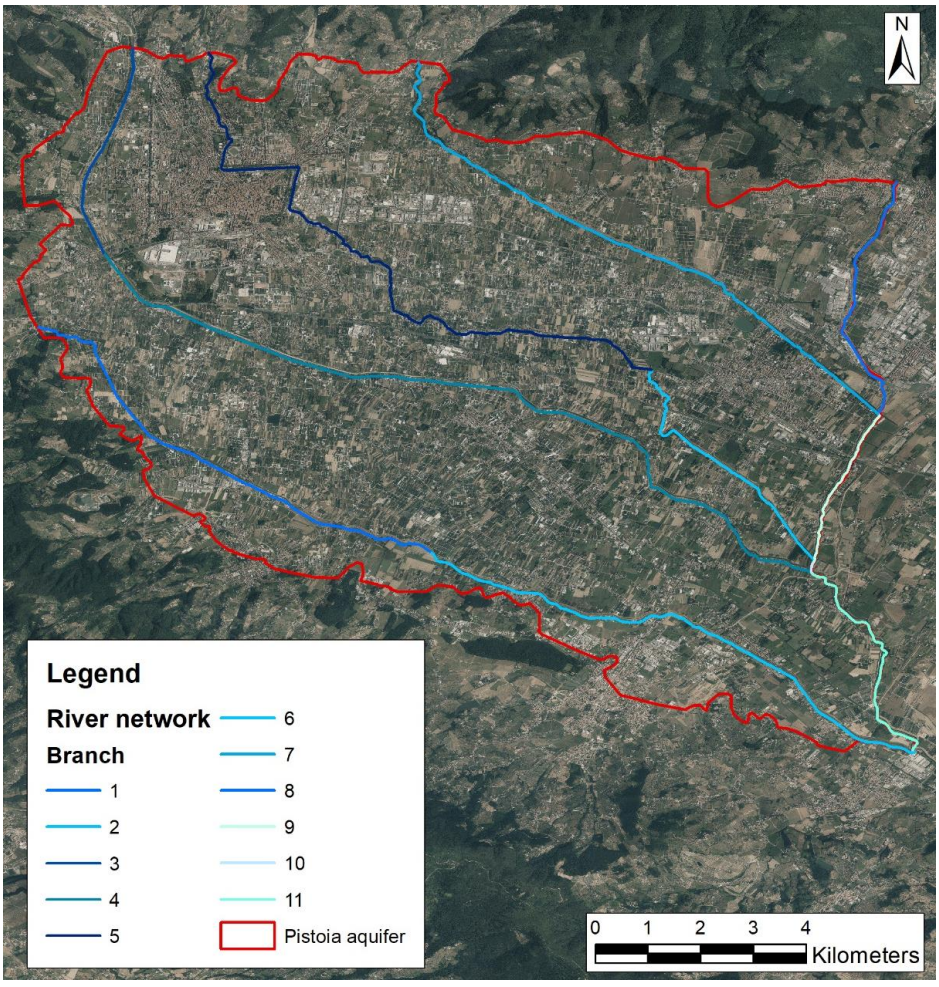

Figure 74 – Ombrone river network discretization for MODFLOW river package.

For the definition of the total amount of water that reach the water table as a result of infiltration through the aquifer, the mean annual percolation over the Ombrone basin, obtained from MOBIDIC simulation output, has been considered (Figure 75).

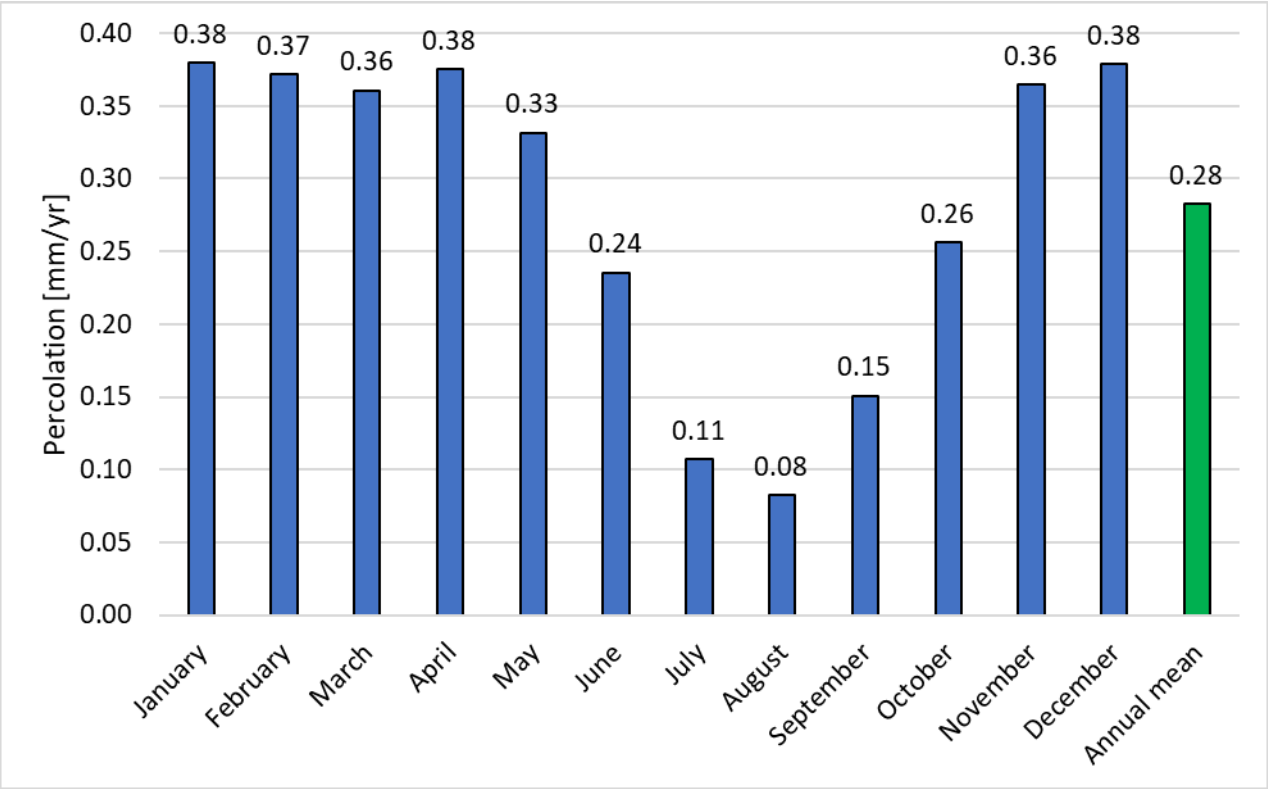

Figure 75 – Mean monthly percolation values obtained from MOBIDIC output.

The same percolation values have been also used to quantify the infiltration rate of water that flows from the high permeable sandstone formations underling the basin into the deep confined aquifers, occurring as lateral recharge.

Mean monthly percolation in Ombrone aquifer follows the typical seasonal distribution, with higher values in corresponding of the most rainy seasons and lower values during summer, with a minimum of ca. 0.08 mm/day in August. For the 1994-2017 period, a mean annual percolation value of 0.28 mm/day (corresponding to $2.80 \cdot 10^{-4}$ m/day or 102.2 mm/year) has been estimated over the basin.

8.2.2 Hydrologic balance

The hydrologic balance of Ombrone basin, obtained from the analysis of MOBIDIC output, is presented in Table 9 and displayed in Figure 76. Since the first two years of the simulation, 1992 and 1993, represent the model warm-up, needed for the model to reach its optimal state, only the 1994-2017 period has been considered in the analysis.

Table 9 - Simulated mean annual hydrological variables for the 1994-2017 period.

Year	Rainfall	Evapotranspiration	River discharge	Surficial withdrawals	Base flow	Runoff	Subsurface flow	Percolation
1994	517.05	283.54	233.51	6.13	55.77	177.04	33.66	48.84
1995	574.08	294.98	279.10	6.34	57.06	181.60	34.74	54.61
1996	666.22	289.16	377.07	6.70	70.45	229.49	43.91	60.53
1997	470.70	301.03	169.68	5.50	45.42	137.01	26.09	43.38
1998	466.30	283.53	182.77	5.30	42.63	136.97	26.14	46.37
1999	595.81	279.31	316.50	5.70	60.87	203.83	38.82	50.13
2000	603.48	286.41	317.07	5.32	61.37	211.73	40.20	50.95
2001	522.36	307.22	215.14	6.42	55.75	159.20	30.57	50.47
2002	613.64	283.84	329.81	5.36	56.42	195.03	37.31	56.89
2003	477.08	283.81	193.27	5.52	50.86	157.62	29.91	38.40
2004	500.55	268.30	232.24	5.23	49.60	155.32	29.72	50.04
2005	466.88	274.50	192.38	3.79	41.74	143.16	27.15	46.93
2006	443.80	301.91	141.89	4.15	40.46	128.99	24.53	45.30
2007	484.62	383.62	100.99	4.17	35.32	115.42	21.94	42.10
2008	615.47	333.73	281.74	4.64	52.80	188.87	35.83	47.59
2009	594.14	309.17	284.97	5.53	60.75	203.23	38.57	41.28
2010	807.98	319.33	488.65	6.26	86.52	300.55	57.25	64.17
2011	436.07	355.33	80.74	5.47	39.97	111.57	21.23	38.36
2012	534.73	293.47	241.26	3.15	44.35	165.76	31.35	36.10
2013	767.09	317.75	449.35	6.77	87.90	277.54	53.08	61.41
2014	806.90	235.66	571.24	6.81	97.13	321.43	61.45	77.07
2015	483.40	232.10	251.30	6.29	58.72	169.14	32.33	61.60
2016	643.00	217.21	425.78	6.61	79.41	248.33	47.56	67.68
2017	417.95	141.19	276.76	4.29	51.61	161.41	30.92	43.99

The annual cycle of precipitation over the basin shows a one peak distribution, in November, that control the seasonal variations of all the analyzed hydrologic variables.

Evapotranspiration presents a mean monthly value of 24.54 Mcm and a mean annual value of 286.50, representing about 50% of the total precipitation. Evapotranspiration evidence a trend mainly driven by temperature, with highest values observed during summer, where more than 50% of total yearly evapotranspiration occurs.

River discharge at basin outlet shows a mean annual value of 276.38 Mcm, while Poggio a Caiano gauging station, located about 10 km upstream of the basin outlet, registered a mean annual discharge of about 240 Mcm per year, for the 1992 – 2017 period.

Percolation through Ombrone aquifer ranges between 36 to 77 Mcm/year, with its minimum value occurred in 2012. Percolation represents about 10% of total monthly and annual rainfall, and it is characterized by a seasonal trend that shows an average value of 4.21 Mcm/month, with a pronounced drop in Summer up to ≈ 1.50 Mcm/month.

Surficial withdrawals occurring directly from the river network and from riverbed sediments are quite impactful on the Ombrone basin water balance, since they represent, together with deep pumping from the aquifer, the main source of freshwater for Pistoia city. In the analyzed period, surficial withdrawals are characterized by a mean value of 5.48 Mcm/year, showing small variation related with the effective availability of the water resource that, especially during Summer, can be decisively lower than freshwater demand.

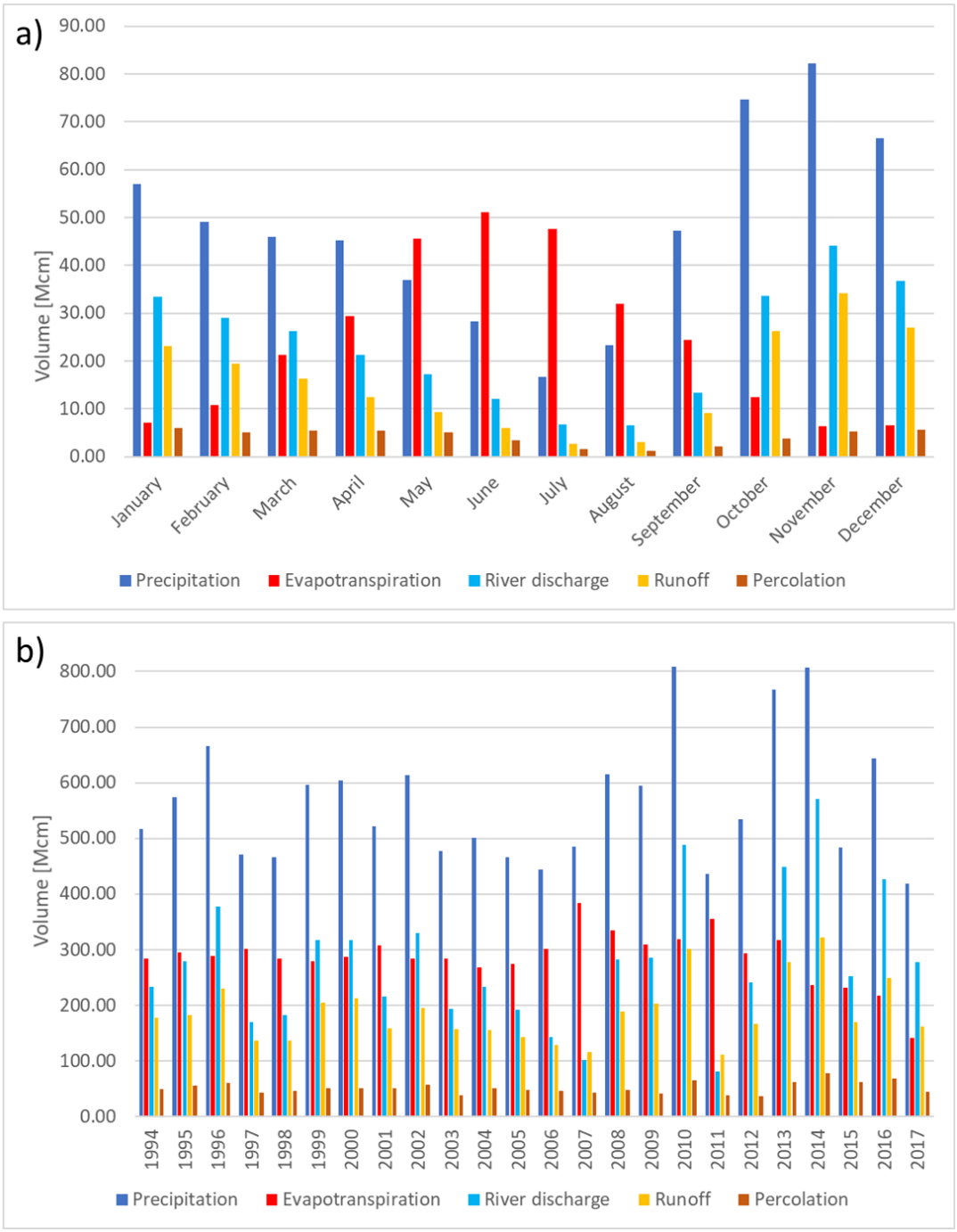

Figure 76 – Values of main average a) Monthly and b) Annual simulated hydrologic variables in Ombrone basin.

8.2.3 Hydrogeological model results

Groundwater model calibration was carried out by means of PEST code (Model Independent Parameter ESTimation, Doherty et al., 2010) that was used together with Modflow-2000 to conduct an inverse modeling procedure, in order to estimate hydraulic conductivity and elastic and inelastic storage coefficients of Pistoia aquifer. Since only few hydraulic head data were available in the study area, ground displacement InSAR data have been used together with sparse hydraulic head data to improve the estimation of calibration parameters. PEST estimates the optimal parameter values by minimizing the objective function using a modified Gauss-Newton iterative procedure.

Firstly, model residuals are calculated as:

$$r_i = (X_{mod} - X_{obs}) \tag{68}$$

Where X_{mod} and X_{obs} are respectively modelled values and observation of variables involved in the calibration process (hydraulic head and ground displacement).

Then, PEST objective function is defined as:

$$\phi = \sum(w_i r_i)^2 \tag{69}$$

Where w_i is a weighting factor that can be assigned to each observation.

In order to better characterize the geological heterogeneity of the aquifer system, PEST code was applied together with the pilot points technique (Doherty, 2003). Pilot points are points within the model domain in which the unknown variables of the calibration procedure are estimated by PEST code. Then, these points are spatially interpolated to create a heterogeneous distribution of the calibration variables to all model domain, by means of kriging interpolation method.

Initial hydrodynamic parameters of the aquifer (transmissivity and specific storage coefficients), used as starting values for the calibration phase, have been obtained by available pumping tests performed in Pistoia area by local freelance geologists during last years and from literature values. Starting values of the calibration parameters are showed in Table 11:

Table 10 – Starting values for groundwater model calibration parameters: Horizontal hydraulic conductivity (Kx, Ky), Specific storage (Ss), Porosity (n) and Elastic and Inelastic Skeletal Specific Storage Coefficients (Ske and Skv).

Layer	$K_x=K_y$	K_v	S_s	n	S_{ke}	S_{kv}
-	[m/s]	[m/s]	[L^{-1}]	[%]	[m^{-1}]	[m^{-1}]
1	$2.3 \cdot 10^{-3}$	$2.3 \cdot 10^{-4}$	0.72	0.25	$1.0 \cdot 10^{-6}$	$1.0 \cdot 10^{-4}$
2	$6.14 \cdot 10^{-5}$	$6.14 \cdot 10^{-6}$	0.02	0.25	$3.0 \cdot 10^{-6}$	$3.0 \cdot 10^{-4}$
3	10^{-6}	10^{-7}	0.01	0.25	$6.0 \cdot 10^{-6}$	$6.0 \cdot 10^{-4}$

The anisotropy of the hydraulic conductivities is specified to be as $K_h/K_v=10$, where K_h and K_v are the horizontal and vertical hydraulic conductivities, respectively. Highlighted cells contain values derived from literature.

Since interbeds included in layers 2 and 3 of Pistoia aquifer are characterized, in some cases, by several meters of thickness, the assumption that heads within interbeds equilibrate instantaneously when a change in aquifers head occurs can not be made, and delay interbeds must be considered for subsidence modelling. On the other hand, interbeds contained in layer 1 show a decimetric avarage thickness all over the model domain. For such a case, no delay interbeds are adopted. Usually, interbeds storage values are specified in

the model by their skeletal storage coefficients $S_{se} = S_{ke} \cdot b_0$ and $S_{kv} = S_{sv} \cdot b_0$, rether than by their elastic and inelastic specific storage values S_{ke} and S_{kv} (where b_0 represents the total thickness of interbeds in each model layer). Definition of S_{se} and S_{sv} starting values, together with the calculation of b_{equiv} and n_{equiv} parameters for delay interbeds are displayed in Table 11.

Table 11 – Definition of starting values for subsidence simulation with SUB package.

Layer	Thickness of individual interbeds	Total thickness	b_{equiv}	n_{equiv}	S_{ske}	S_{skv}	S_{se}	S_{sv}
1	< 0.5	< 1	-	-	$1.0 \cdot 10^{-6}$	$1.0 \cdot 10^{-4}$	$1.0 \cdot 10^{-7}$	$1.0 \cdot 10^{-5}$
2	7; 7.5	14.5	7.25	2.00	$3.0 \cdot 10^{-6}$	$3.0 \cdot 10^{-3}$	$4.35 \cdot 10^{-5}$	$4.35 \cdot 10^{-3}$
3	9; 5; 14	28	10.03	2.79	$6.0 \cdot 10^{-6}$	$6.0 \cdot 10^{-4}$	$1.68 \cdot 10^{-4}$	$1.68 \cdot 10^{-2}$

In particular, skeletal storage coefficients (Elastic S_{se} and Inelastic S_{sv}) were computed using the interbeds thicknesses of the reference aquifer section presented in Figure 77, while b_{equiv} and n_{equiv} parameters have been defined by means of equations 25 and 26, presented in chapter 3.

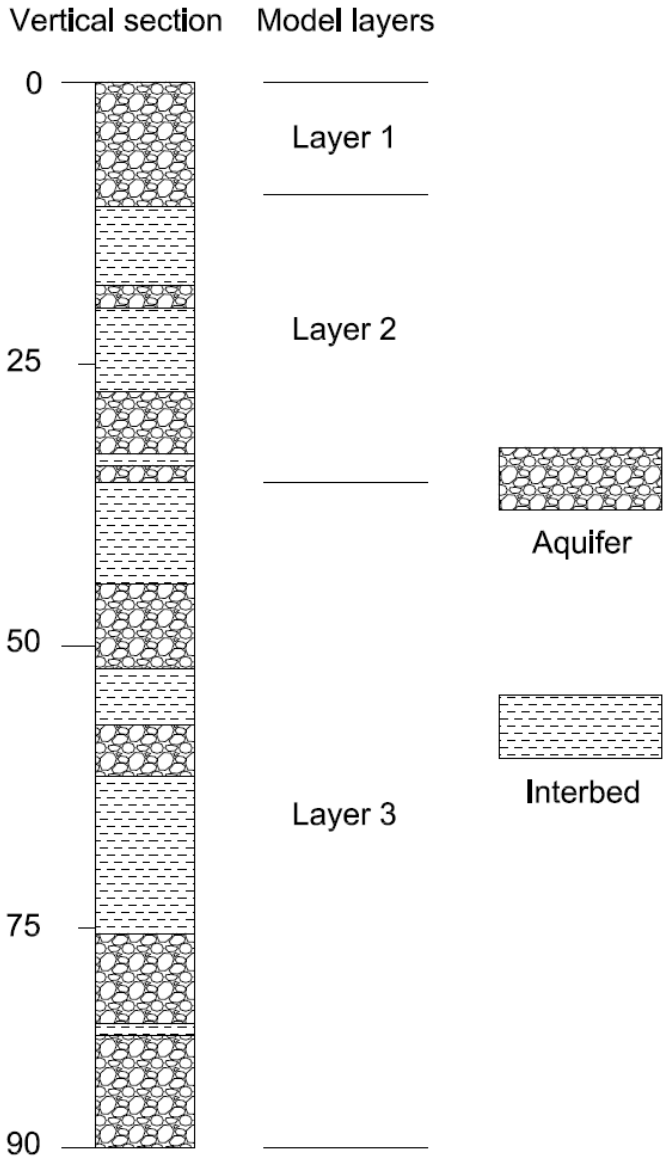

Figure 77 – Reference section of Pistoia aquifer with the definition of groundwater model layers.

Simulated water levels and ground displacement was compared with relative observed values all over Pistoia aquifer, in order to evaluate the accuracy of the groundwater model. The Nash-Sutcliffe efficiency index, mass balance error, residual mean, residual standard deviation, root means square error and determination coefficient R^2 are used to evaluate the model fit. The comparison between measured and computed hydraulic head values are presented in Figure 78:

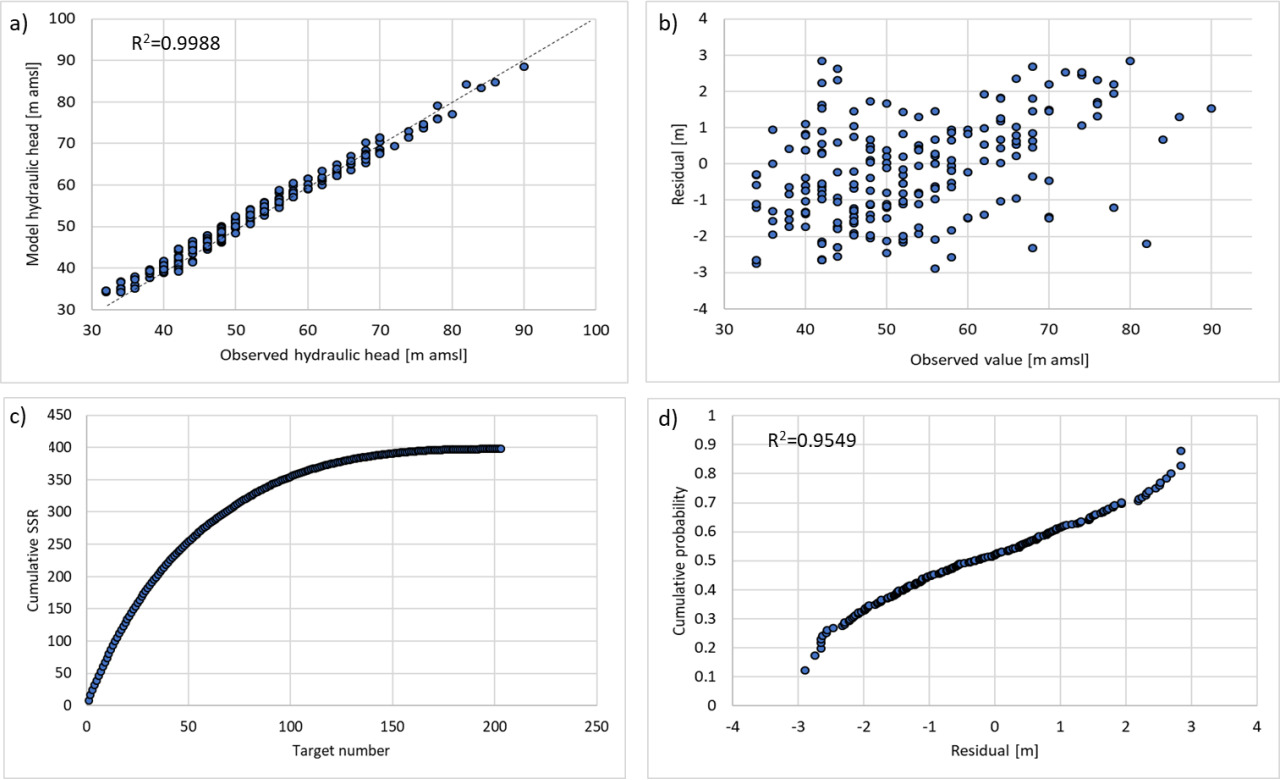

Figure 78 – Output of groundwater model calibration for hydraulic head.

The model shows a good fit with the observations, with simulated groundwater levels vs. observed levels that are grouped around the x-y line for all the 215 validation points, with a high R^2 of 0.9877 (Figure 78a). Model residuals displayed in Figure 78b are characterized by a mean value of -0.22m and a maximum absolute error < 3m (Figure 78b). Assuming a piezometric variability of about 55m in the hydraulic head observations, both errors are below 10% of the total water displacement, an acceptable error for a long duration regional model. The good fit between simulated and observed hydraulic head is confirmed also by the Nash-Sutcliffe index, with a value of 0.99.

Cumulative curve of square residuals, plotted in Figure 78c, has a maximum value of 400.0 and shows an homogeneous distribution of residual errors among all the validation points, confirming the reliability of the model calibration.

Finally, the cumulative probability of residuals is displayed in Figure 78d, with data that are plotted very close to a straight line. With a coefficient of determination of 0.9816, this plot assesses the validity of all the statistical analyses applied to the calibration phase.

In Figure 79, measured hydraulic head data obtained from the only available monitoring well within the study area with continuous data (P13 in Figure 46), are presented. In order to validate the transient simulation, a comparison between modelled hydraulic head and observations has been carried out for the 2011-2017 period.

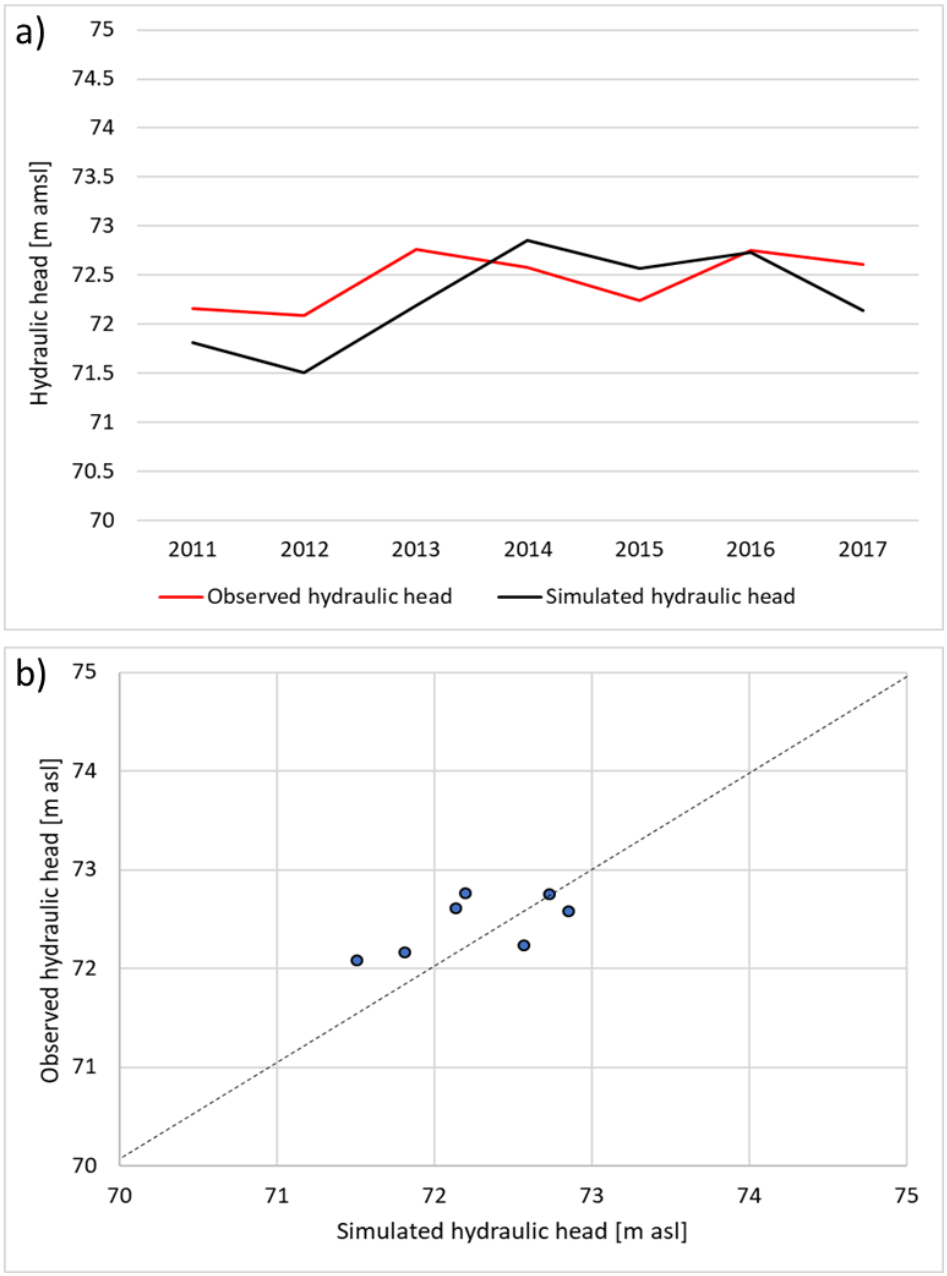

Figure 79 – Observed and simulated hydraulic head at monitoring well P13.

Measured hydraulic head at P13 shows a quite stable trend, characterized by an average value of 72.45 m asl and a standard deviation of 0.29 m, with very small variation occurring during the monitored period and a minimum value observed in 2012 (Figure 79a). Simulated hydraulic head follows the observation trend, with a mean value very close to the observed one (72.25 m asl) and a higher standard deviation of 0.49 m, due to its enhanced minimum value reached in 2012. Unfortunately only few hydraulic head measurement are available for the simulated period, but obtained results still demonstrate the goodness of the groundwater model and its good fit with observations (Figure 79b).

Figure 80 present the comparison between simulated and Sentinel-1 PS-InSAR measured cumulative ground displacement at the end of the 2015-2017 calibration period.

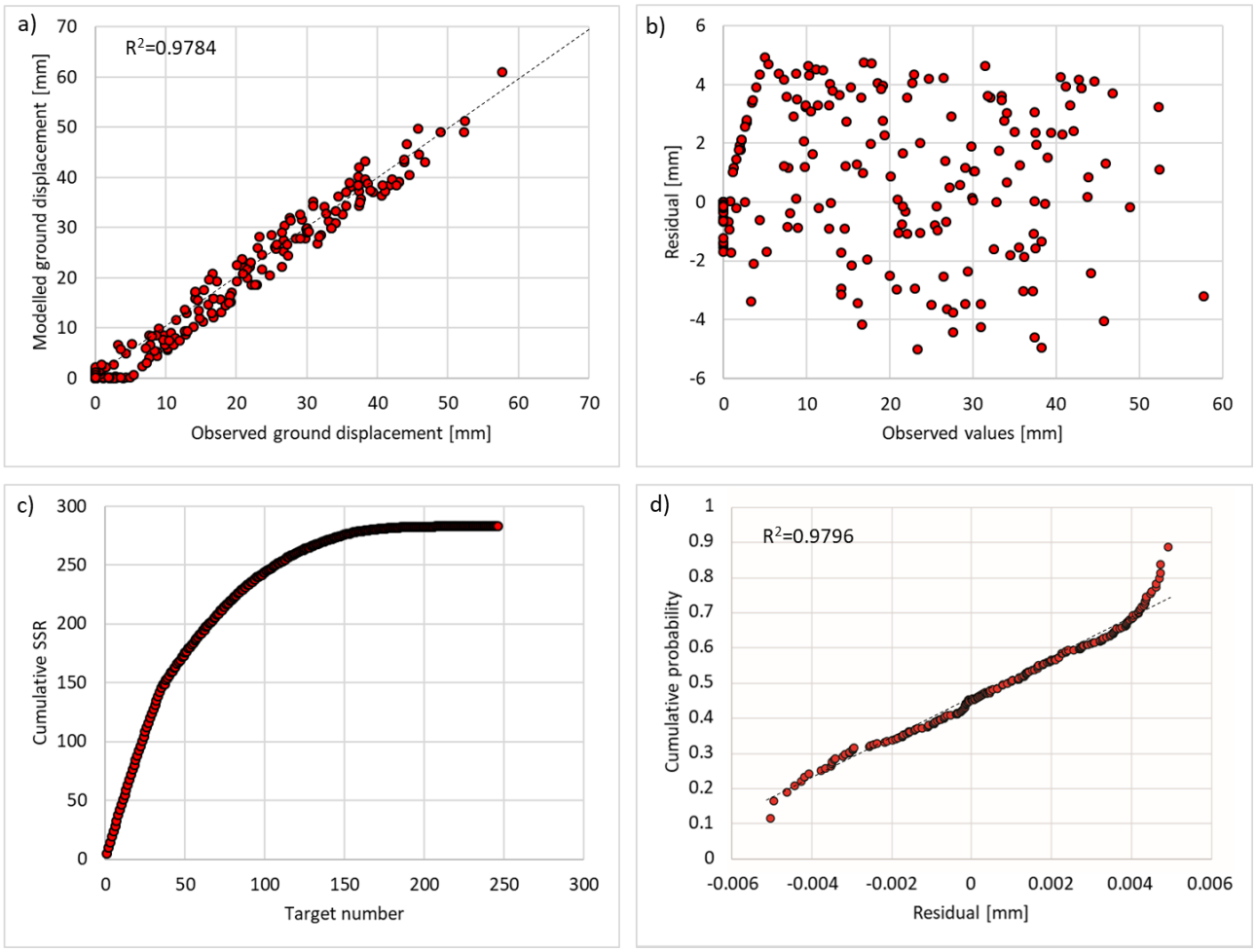

Figure 80 - Output of groundwater model calibration for ground displacement.

As for hydraulic head data, the slope of the regression line between subsidence observations and simulated values is close to one (0.9784), and the intercept close to zero suggests a 1:1 relationship between the modelled and observed subsidence (Figure 80a). 247 Permanent Scatterers have been selected as validation points for model calibration, considering their position within the model domain and their reliability in term of ground displacement time series.

In correspondence of the validation points, model values show an average residual of 0.6 mm and a variability ranging between +5 and -5 mm, if compared with measured subsidence (Figure 80b). Considering a difference of about 50 mm between the maximum and minimum observed subsidence, model residual fall within the 10% of acceptable error. The goodness of the calibration is further confirmed by the 0.993 value of the Nash-Sutcliff index.

Considering the cumulative curve of square residual, about half of the sum of squared residuals (155 out of 282) is accounted by 40 of the 247 targets (Figure 80c). In order to take into account their lower statistical reliability, such targets have been considered with a 0.9 weight in the calibration procedure.

With a coefficient of determination of 0.979, the cumulative probability plot confirms the normal distribution of residuals and asses the goodness of the model calibration.

8.2.4 Hydrogeologic balance

Results of water balance analysis carried out in Pistoia aquifer are presented in Figure 81. The water balance was defined by means of the 13 stress periods groundwater model output, representing the mean annual behavior of the main hydrogeological processes occurring in Pistoia aquifer. Blue bars represent water inflows into the aquifer, while red bars represent water outflows. Stress period 1 was used to simulate the average annual state of groundwater system, modelled with a stationary stress period, while stress periods 2 to 13 represent each month of the year.

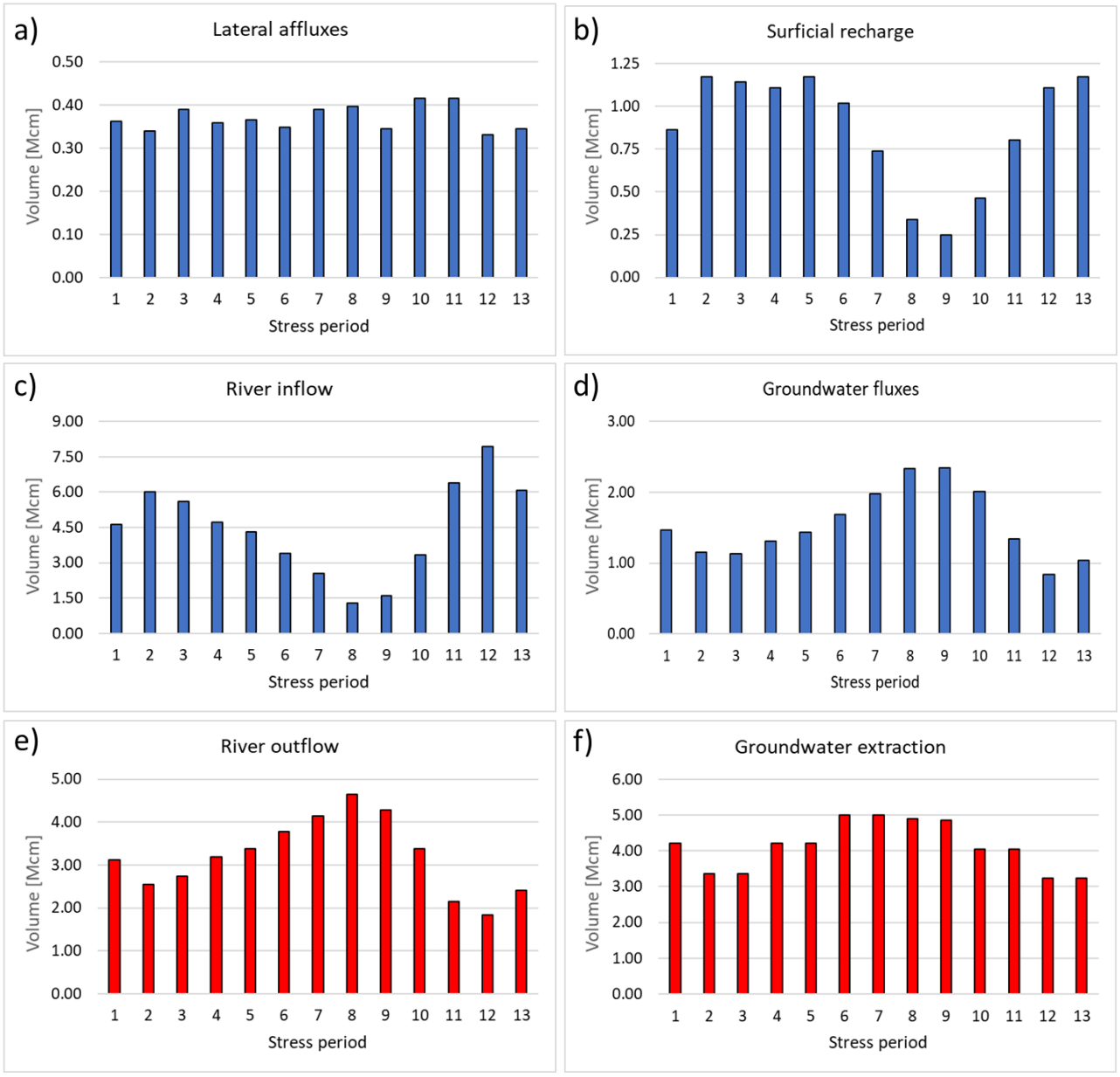

Figure 81 – Main monthly inflow and outflow of Pistoia aquifer.

Aquifer inflows, with an average value of 4.51 Mcm, are dominated by the effects of the Ombrone river system, even if its influence, together with surficial recharge occurring for rainfall percolation, is limited to the phreatic aquifer (Figure 81b and c). Besides internal water exchange between different aquifer layers, the main water inflow for layer 2 and 3 of Pistoia aquifer are represented by lateral affluxes from the high permeable sandstone formations that underlie the basin (Figure 81a). Such contribution, characterized by an average value of 0.36 Mcm, is not influenced by seasonal variation, showing a quite constant value all over the year, with a difference of only 0.09 Mcm between its maximum and minimum value. This is probably due

to the nature of such affluxes, reaching the basin via long deep flow paths, far from the ground surface and from the seasonal meteorological variability.

Additional water exchanges occur on the East border of the model domain, as deep flow from and through Prato aquifer (Figure 81d). Such fluxes show an overall positive input for Pistoia aquifer, contributing to the aquifer recharge especially during the driest period.

Mean water outflows from Pistoia aquifer are represented by water restitution to the river network, characterized by a maximum value of 4.65 Mcm in July (stress period 8) in correspondence of the lower river discharge (Figure 81e), and groundwater extraction from pumping wells. To consider the seasonal variability of pumping rate, in order to take into account the diverse freshwater demand from wet to dry seasons, a different weight has been attributed to the water extraction pattern for every stress period (Figure 81f). In particular, the pumping rate is expected to be higher during Summer, due to the lower rainfall, especially for wells with agricultural purposes, that represent an important part of the total groundwater withdrawals in the study area. Calculated water inflows and outflows occurring in Pistoia aquifer are presented in Table 5:

Table 12 – Simulated inflows and outflows occurring in Pistoia aquifer.

Stress period	Month	Lateral affluxes	Aquifer recharge	River inflow	River outflow	Wells extraction	Groundwater fluxes	Storage
		[Mcm/yr]	[Mcm/yr]	[Mcm/yr]	[Mcm/yr]	[Mcm/yr]	[Mcm/yr]	[Mcm/yr]
1	Annual mean	0.36	0.86	4.63	3.11	4.21	1.47	0.00
2	January	0.34	1.17	6.02	2.55	3.37	1.16	2.78
3	February	0.39	1.14	5.60	2.74	3.37	1.13	2.15
4	March	0.36	1.11	4.72	3.18	4.21	1.31	0.11
5	April	0.37	1.17	4.32	3.37	4.21	1.43	-0.29
6	May	0.35	1.02	3.41	3.78	5.00	1.68	-2.31
7	June	0.39	0.74	2.55	4.13	4.99	1.98	-3.47
8	July	0.40	0.34	1.30	4.65	4.89	2.33	-5.18
9	August	0.35	0.25	1.60	4.28	4.85	2.34	-4.61
10	September	0.42	0.46	3.34	3.38	4.05	2.01	-1.19
11	October	0.42	0.80	6.39	2.15	4.05	1.34	2.75
12	November	0.33	1.11	7.95	1.84	3.24	0.84	5.16
13	December	0.35	1.17	6.08	2.41	3.24	1.03	2.98

In stress period 1, representing the mean annual groundwater states simulated with a stationary stress period, the mass balance perfectly reaches the equilibrium, with a storage value of 0 and a difference between outflows from and inflows to the model of only 0.0002% (-0.75 m^3/day).

Concerning transient stress periods, the mean seasonal storage variation over Pistoia aquifer is shown in Figure 82a. Storage variability follow the typical trend of Mediterranean regions, characterized by positive values in Autumn and Winter and by negative values in Spring and Summer. Storage trend strictly follows the precipitation distribution over the area, reaching its maximum value in November, with a 5.16 Mcm surplus in correspondence of the rainiest month of the year, and its minimum value in July, the driest month, with a deficit of -5.18 Mcm. In March and April, inflows to and outflows from the aquifer are very similar to each other, showing very small values of groundwater storage of 0.11 and -0.29 Mcm respectively.

Figure 82b shows the cumulative distribution of groundwater storage In Pistoia aquifer during the year. The maximum amount of groundwater is available in March, when more than 5 Mcm of water resource are stored

into the aquifer. In September, on the other hand, a deficit of about -12 Mcm identifies the month with the minimum volume of groundwater available. At the end of the year, the hydrogeologic balance of Pistoia aquifer is characterized by an average loss of about -1.11 Mcm, resulting in a decreasing of available water during the studied period that could lead to severe groundwater stress if it continues uncontrolled. This could also represent one of the main causes of subsidence phenomena occurrence in the area.

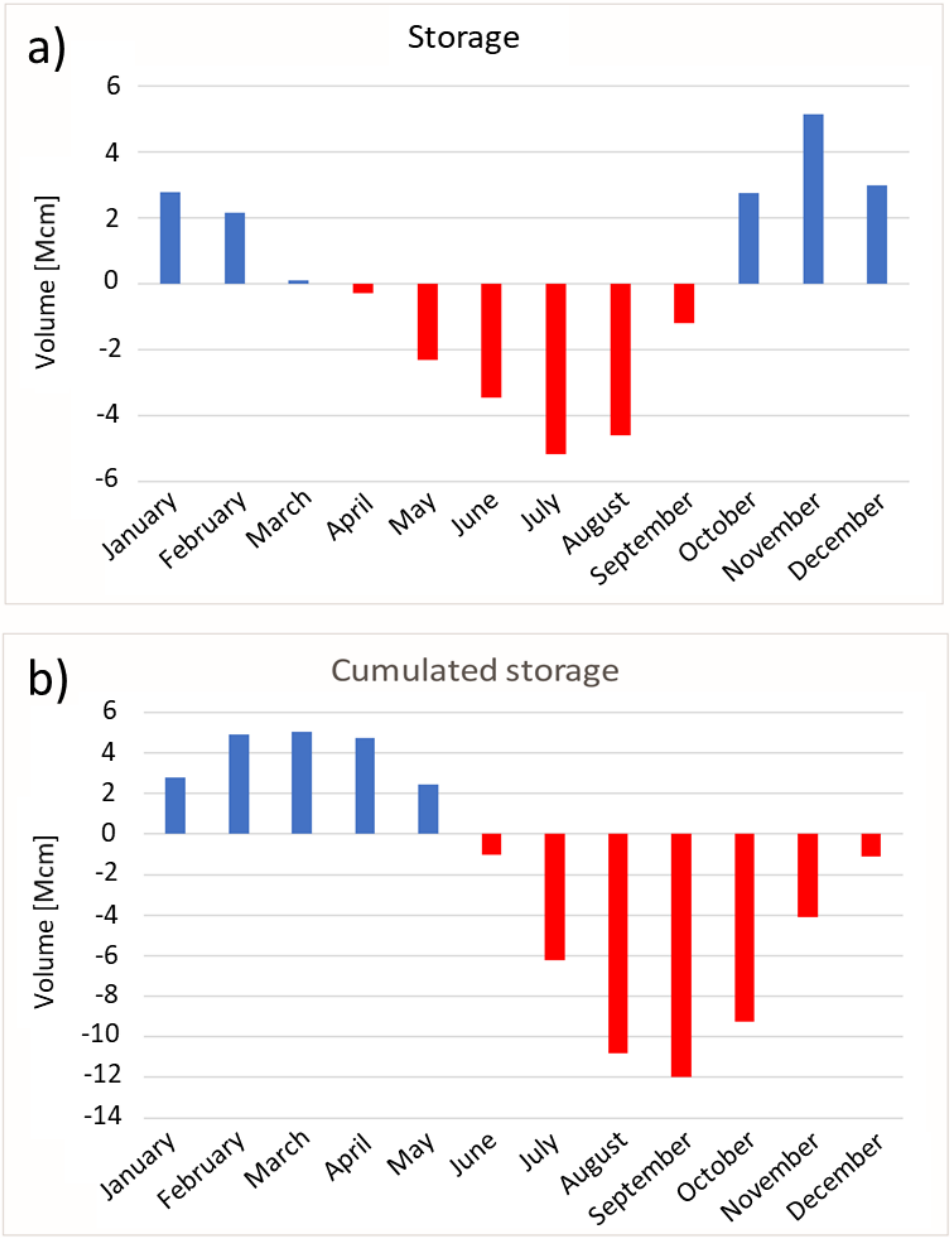

Figure 82 – a) Mean monthly groundwater storage volume and b) Cumulated storage in Pistoia aquifer.

8.2.5 Subsidence modelling

The Ombrone aquifer compaction, as a response to the over exploitation of groundwater resource, has been simulated through a 25 time steps model, with yearly time step, representing the period between 1994 to 2017, for which many PS-InSAR ground displacement measurements were available.

Time series of simulated land subsidence in Pistoia historical center and plant nursery area are presented in Figure 83, together with the vertical component of ground displacement observations obtained from

Sentinel-1 PS-InSAR data, for the 2015-2017 calibration period. The exact location of the analyzed time series is shown in Figure 85.

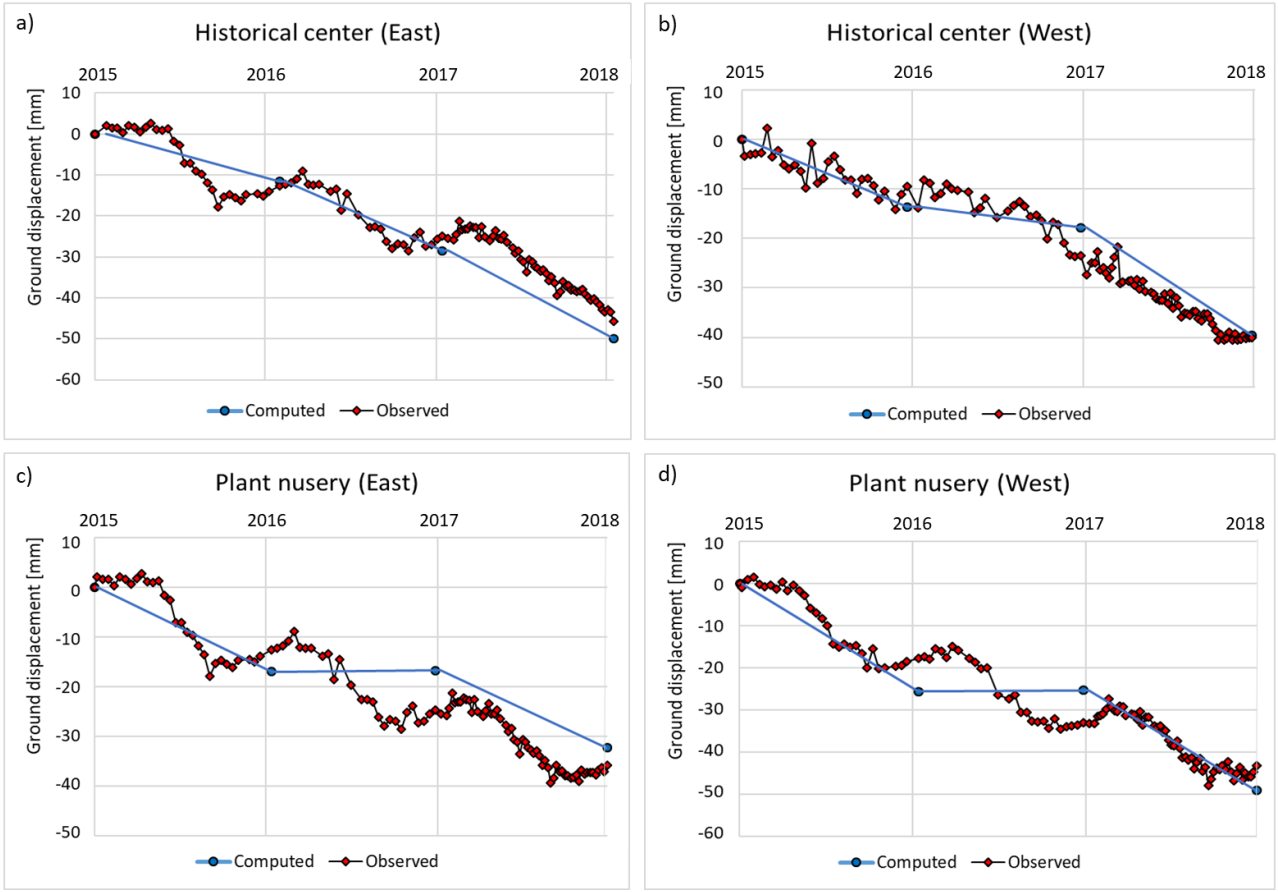

Figure 83 – Time series of modelled and measured ground displacement in correspondence of historical center and plant nursery area for the 2015-2017 period.

By means of the millimetric accuracy and the biweekly acquisition frequency, Sentinel-1 time series describe a fluctuant ground displacement in all the analyzed zones, following a clear seasonal pattern. In the 3 years monitored period, ground movement presents a general subsiding trend with up to 25 mm of maximum displacement during the dry season and smaller recoveries, up to 10 mm, in Autumn and Winter. At the end of 2017, both historical center and plant nursery result affected by a maximum ground displacement ranging between 40 to 50 mm.

Because of the yearly resolution of the groundwater model, time series of simulated subsidence do not show any cyclical short-term oscillations but confirm the general trend of deformation, which is comparable with observed data values. In 2016, for both plant nursery areas and for the western part of the historical center, simulated ground displacement shows a stabilization in the general deformation pattern. Such discrepancies with observations, showing a lower subsidence velocity in the same period only in the West side of the historical center (Figure 83b), are related to a temporary recovery of simulated hydraulic heads simulated by the groundwater model, probably as a result of the higher rainfall fell in 2016 (the highest of 2015-2017 period).

At the end of the simulated period, the model is able to reproduce the magnitude of observed subsidence very well, showing a good agreement with PS-InSAR data. The comparison between modelled and observed cumulated subsidence confirms the goodness of the calibration phase, with only small differences, lower than 10%, observed in the total ground displacement. Only in the Eastern part of the plant nursery area,

model values presents a higher discrepancy with Sentienl-1 data, reaching an error equal to the 13.5% of the total observed ground displacement (Figure 83c).

Figure 84 displays the comparison between modelled and observed ground displacement, for the 2015-2017 period, in correspondence of the hospital area located to the South of Pistoia city.

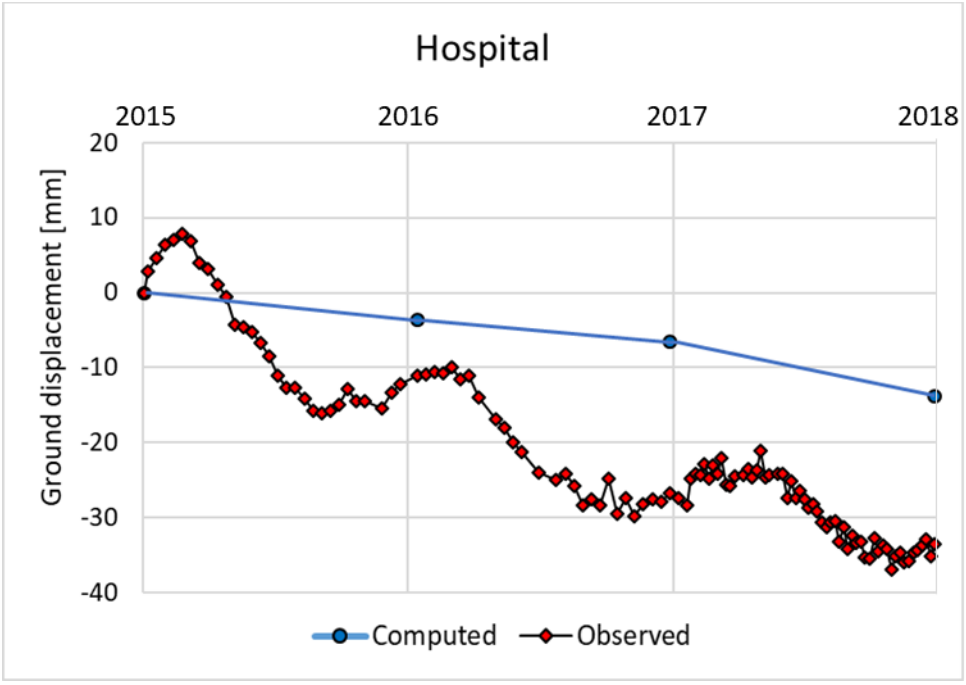

Figure 84 - Time series of modelled and measured ground displacement in correspondence of the hospital area.

Sentinel-1 PS-InSAR data show, as for the other investigated areas, a fluctuant ground movement, with up to 25 mm of ground displacement and an average recovery of about 5 mm every year. Even after the calibration phase, the model is not able to adequately simulate observed subsidence in hospital area, showing big differences of about 20 mm in the total computed ground displacement at the end of 2017, with a relative error of approximately 60%.

This is probably due to the difference nature of subsidence occurring in the hospital area in comparison to the other parts of Pistoia surroundings. San Jacopo hospital is a young structure, finished to build at the end of 2013 and located about 5 km South-West of the main subsiding area located in Pistoia historical center. Very likely, subsidence observed in the hospital area is mainly related to the increase of the geostatic load caused by the construction of the new heavy building, that led to the compaction of the high compressibility sediments that characterize the whole Pistoia aquifer. Since MODFLOW SUB package considers only changes in effective stress caused by pore water pressure variations, changes in geostatic load are not considered and subsidence occurred in Pistoia hospital area can not been adequately simulated.

Figure 85 compares the total simulated land subsidence between January 2015 and December 2017 with Sentinel-1 PS-InSAR observed subsidence in the same period. The developed model is able to reproduce both magnitude and general shape of subsidence occurring in Pistoia area in a very accurately way. The comparison of the subsidence magnitude at the center of historical center and plant nursery subsidence bowl in the map indicates a good match between model results and observations. Small differences still persist right East/South-East of Pistoia city, where the groundwater model estimates a maximum displacement of more than 20 mm at the end of 2017, while no subsidence was observed by Sentinel-1 satellite.

A third subsidence bowl can be detected from the analysis of PS-InSAR data, located less than 1km South of the San Jacopo hospital. This area, characterized by a maximum cumulated displacement of more than 60

mm at the end of 2017, with a mean annual velocity of about 20 mm/year, lies in correspondence of the major pumping center of the region. Here, modelled subsidence matches well with observations, even if it underestimates the total measured ground displacement of about 10 mm and the mean displacement velocity of about 3-4 mm/year.

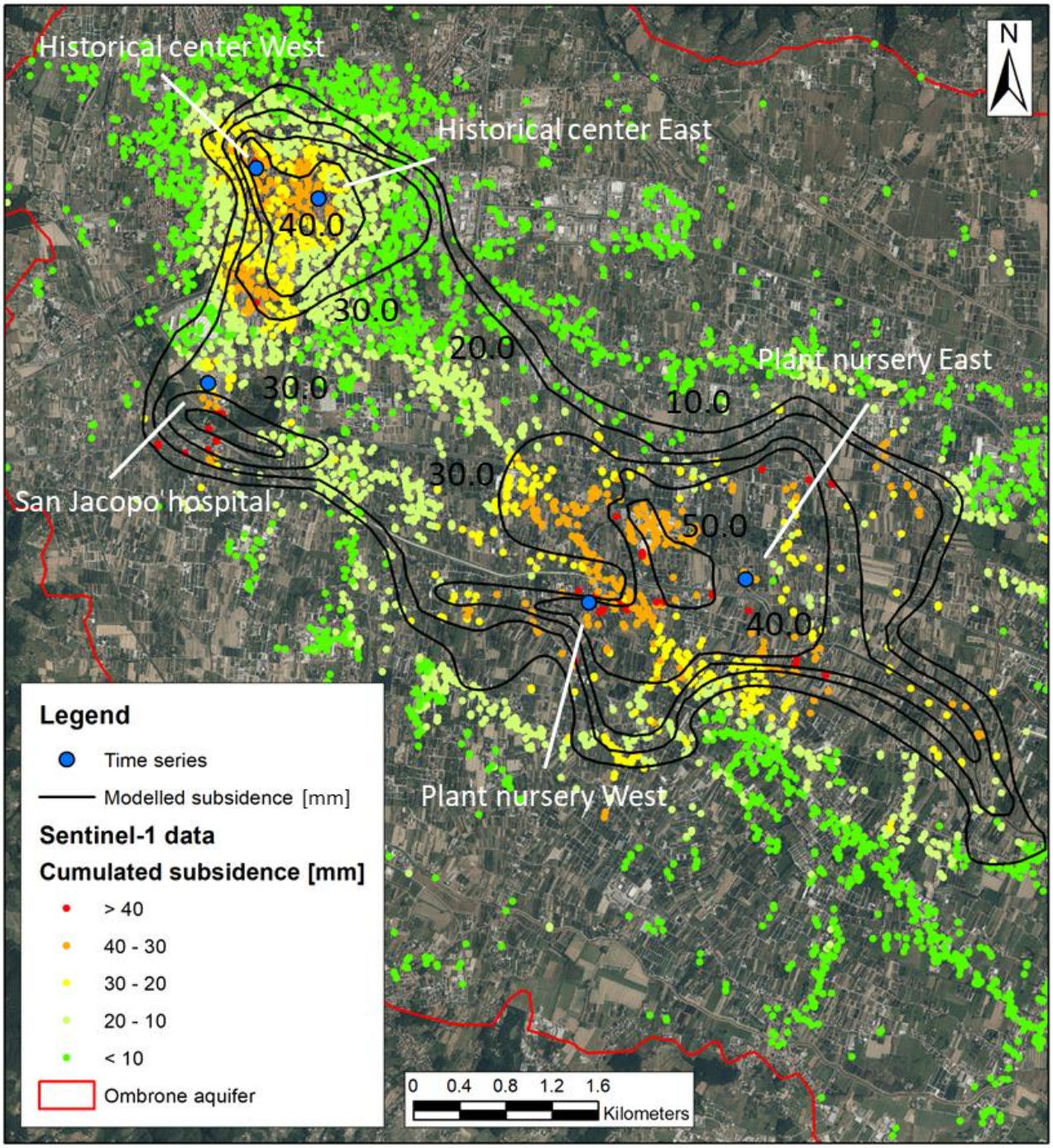

Figure 85 – Cumulated subsidence for the 2015-2017 period as modelled by MODFLOW and measured by Sentinel-1 satellite.

The subsidence model validation has been carried out, for the 2003-2010 period, by means of the available ENVISAT PS-InSAR data available all over Pistoia aquifer. The vertical component of the ground motion, detected by ENVISAT data, has been identified by combining the information obtained by both ascending and descending satellite acquisition geometries, in order to represent the real displacement of observed

targets. Time series of observed and modelled ground displacement for the validation period of both Pistoia historical center and plant nursery area are presented in Figure 86.

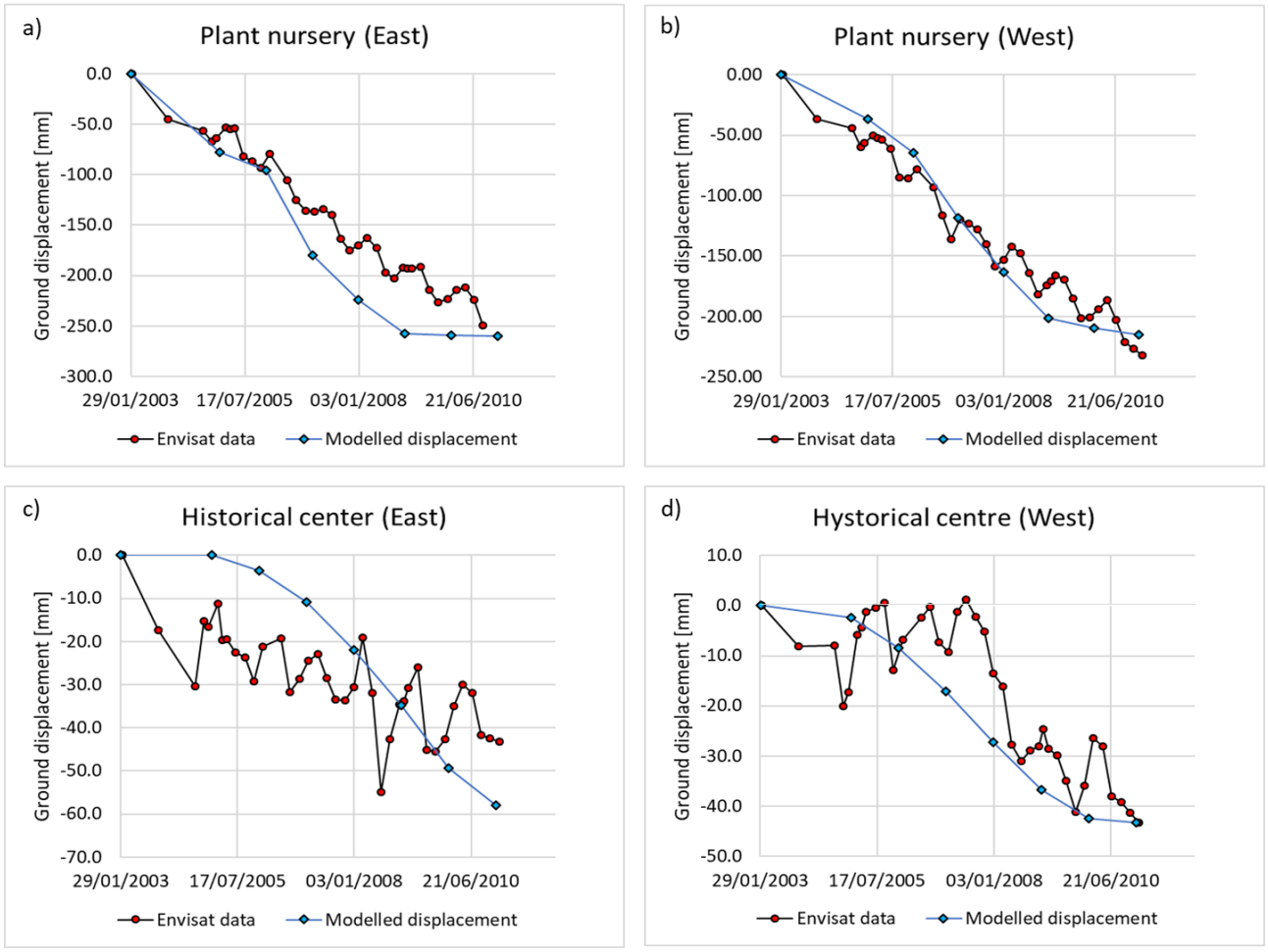

Figure 86 - Time series of modelled and measured ground displacement in correspondence of historical center and plant nursery area for the 2003-2010 period.

ENVISAT PS-InSAR ground displacement data acquired over both sides of the plant nursery area show a constant descending trend, characterized by a mean velocity of more than 25 mm/year and a maximum cumulated subsidence of about 240-250 mm between 2003 and 2010. Despite the monthly or bimonthly acquisition time, ground displacement observed by ENVISAT sensors is characterized by a clear fluctuant trend that follow the seasonal variability. The subsidence model is not able to describe such clear trend, but it can reproduce the general pattern and magnitude of ground displacement in quite good agreement with observations.

For Pistoia historical center, only a small amount of subsidence occurred between 2003 and 2010, with ENVISAT data that detected a mean ground displacement velocity lower than 5 mm/year and a maximum value of 40-45 mm at the end of the monitored period. Model results match very well with observations in the western part of the historical center, while they overestimate the total identified subsidence in the eastern side of about 15 mm, showing a ground displacement pattern not in good agreement with observed values. Anyway, ENVISAT PS-InSAR acquired over the historical center present a very high variability, probably related with the small amount of detected ground displacement in comparison with sensors resolution, that make difficult a good fit between model values and observations.

Figure 87 shows the total simulated and observed subsidence at the end of ENVISAT data monitoring period (June 2010). The general shape and magnitude of modelled values matches well with observed ground displacement for all the model domain.

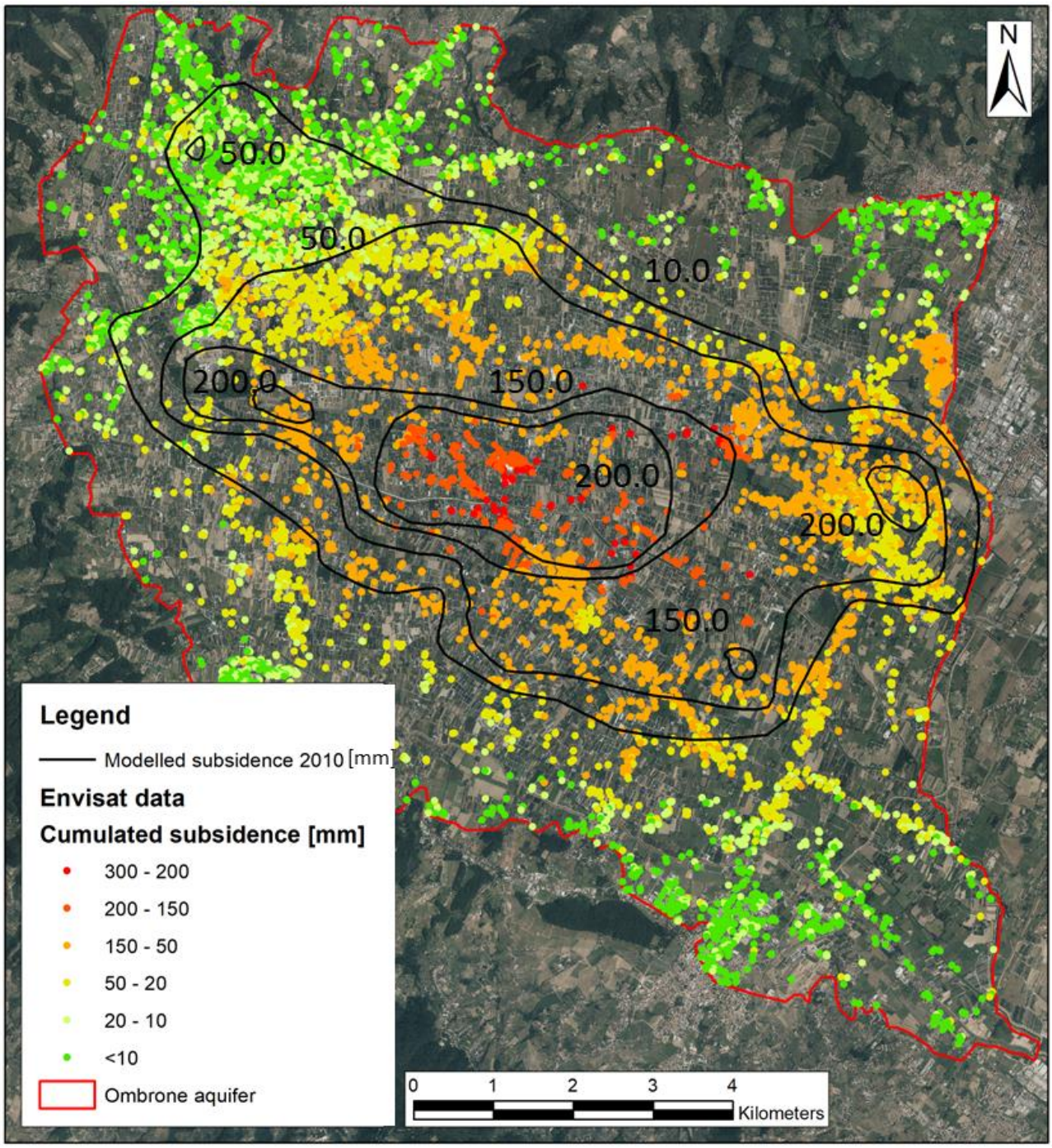

Figure 87 - Cumulated subsidence for the 2003-2010 period as modelled by MODFLOW and measured by Envisat satellite.

A good fit has been also obtained in the spatial representation of modelled ground displacement, with the simulated subsidence bowl in the plant nursery area that exactly match the center of observed subsidence.

As a further confirmation of the different nature of subsidence identified in San Jacopo hospital surroundings by Sentinel-1 InSAR data during the 2015-2017 period, probably not related with groundwater overexploitation, ENVISAT data detect no ground displacement occurring in that area between 2003 and

2010. The hospital construction started in 2010 and was completed in 2013, while ENVISAT data monitoring period last only until June 2010. Unfortunately, no PS-InSAR data, GPS data or leveling data are available for the study area during the 2013-2015 period.

Finally, the comparison between model results and subsidence observed by ERS InSAR data for the 1992-2000 period is presented in Figure 88. Since ground displacement data acquired by the ascending orbit of ERS sensors were not available for the study area, it was not possible to identify the real vertical displacement of observed targets and measured displacement along the satellite Line of Sight is presented.

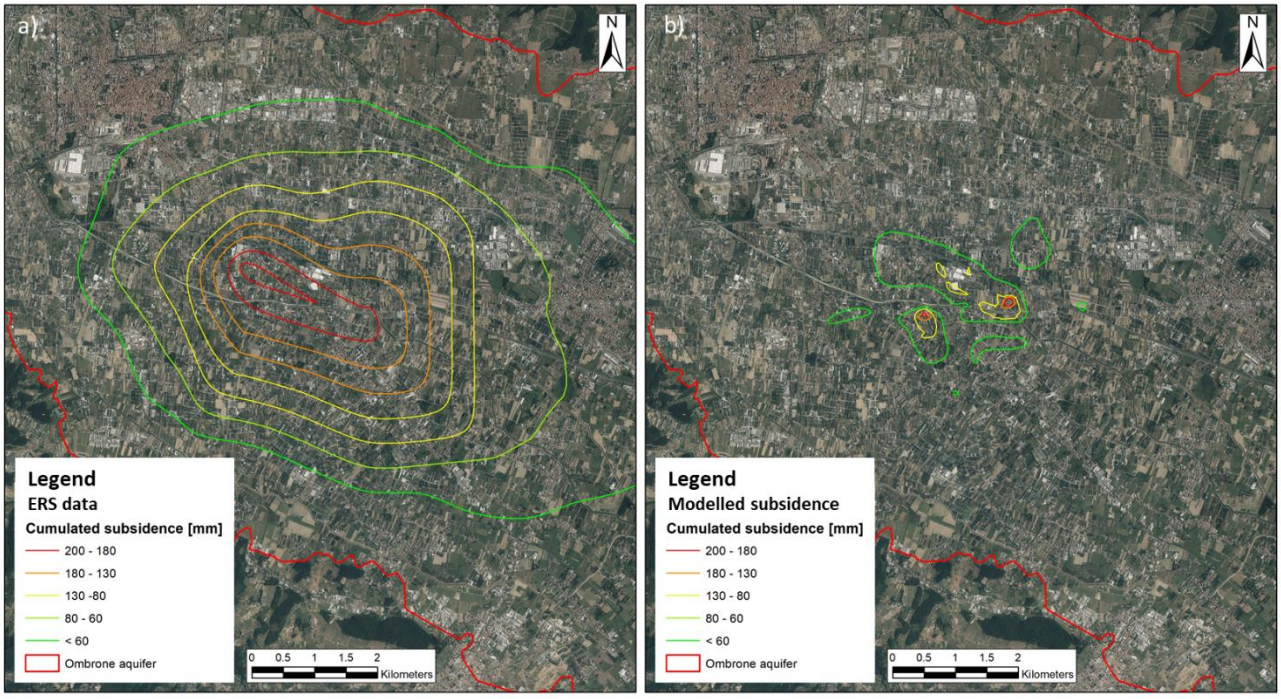

Figure 88 - Cumulated subsidence for the 1992-2000 period as modelled by MODFLOW and measured by ERS satellite.

Unfortunately, simulated ground displacement presents a bad fit with observations, both in terms of magnitude and areal extent of subsidence phenomenon. Such discrepancies can be attributed to imprecise recharge data and boundary conditions, obtained from the warm-up period of MOBIDIC model (1992-1993), and to incorrect results of MODFLOW simulation itself, that was started from 1992 and that probably needed some additional time to reach its optimal status and to simulate subsidence appropriately. Anyway, the raw model output, according to ERS InSAR data, identify for the 1992-2000 period that subsidence occurred only in the plant nursery area of Pistoia aquifer, while no subsidence has been detected and simulated in correspondence of Pistoia city.

8.3 Forecasting Models

In last decades, climate change and global warming are having a growing impact on the environment, affecting all natural and anthropic systems of the Earth. As a direct consequence of long-term climate variation, also river discharge, seasonal and local water availability, and groundwater states can be affected by this phenomenon. Global Climate Models (GCMs) are one of the most powerful tools for climate scenarios forecasting, providing the basis for climate change impact assessment at many different scales. The coarse resolution of GCMs make them unable to represent climate variations at regional or finer scale. Regional Climate Models (RCMs) guarantee higher resolution to Global Climate Models, preserving the coherence between meteorological variables distribution and topographic characteristics of Earth surface. However, RCMs are still affected by many systematic errors (*bias*) caused by their rough resolution and by the assumption made during their development. In order to perform reliable simulations, GCMs and RCMs raw data need to be bias corrected before using them as input for a climate forecasting model. In the present study, GCMs and RCMs corrected output have been used as input parameter for the developed hydrologic model, in order to forecast the response of hydrologic and hydrogeologic states of Ombrone basin to the expected climate variation that will occur in the future.

8.3.1 Methodology

This study mainly focuses on future climate projection and the examination of its effect on the hydrology of Ombrone basin. To evaluate the uncertainty of RCMs and to obtain more reliable information on climate change forecasting variables, five different RCMs afferent to the Coupled Model Intercomparison Project (CMIP5, Taylor et al., 2012), ensemble r1i1p1, has been selected (Table 13). Such models are used to project future precipitation, together with the maximum and minimum air temperatures of the basin, solar radiation, humidity and wind speed. Selected scenario was the intermediate RCP4.5.

Table 13 **–Selected RCM simulated period and resolution, in degrees between adjacent grid points.**

RCM	Resolution	Historical data period	Future data period
MIROC5	1.4008° x 1.40625°	1979-2005	2006-2100
MIROC-ESM	2.7906° x 2.8125°	1950-2005	2006-2100
MRI-CGCM3	1.12148° x 1.125°	1979-2005	2006-2100
INM-CM4	1.5° x 2°	1950-2005	2006-2100
CMCC-CMS	3.7111° x 3.75°	1950-2005	2006-2100

The RCMs and GCMs were selected based on two criteria: data availability for the forecasting temporal period and representativeness of model to the observed stations. Every RCMs simulation present several differences with respect to the others, that can be particularly large, due natural climate variability and different forcing variables introduced into the model. For this reason, results from the different RCMs simulation have been averaged together, to provide a more robust estimate of climate change forecasting.

The outputs of RCM and GCMs were used to project climate scenarios up to the year 2050, following a two periods time frame:

- Control period: 1992-2018, based on RCMs historical data and measured data available in the study area;

- Forecasting period: 2018-2050, based on RCP4.5 scenario.

For bias correction, the linear scaling method was applied to the grid-based climate model data, to predict the future climate at local observed stations (Figure 89).

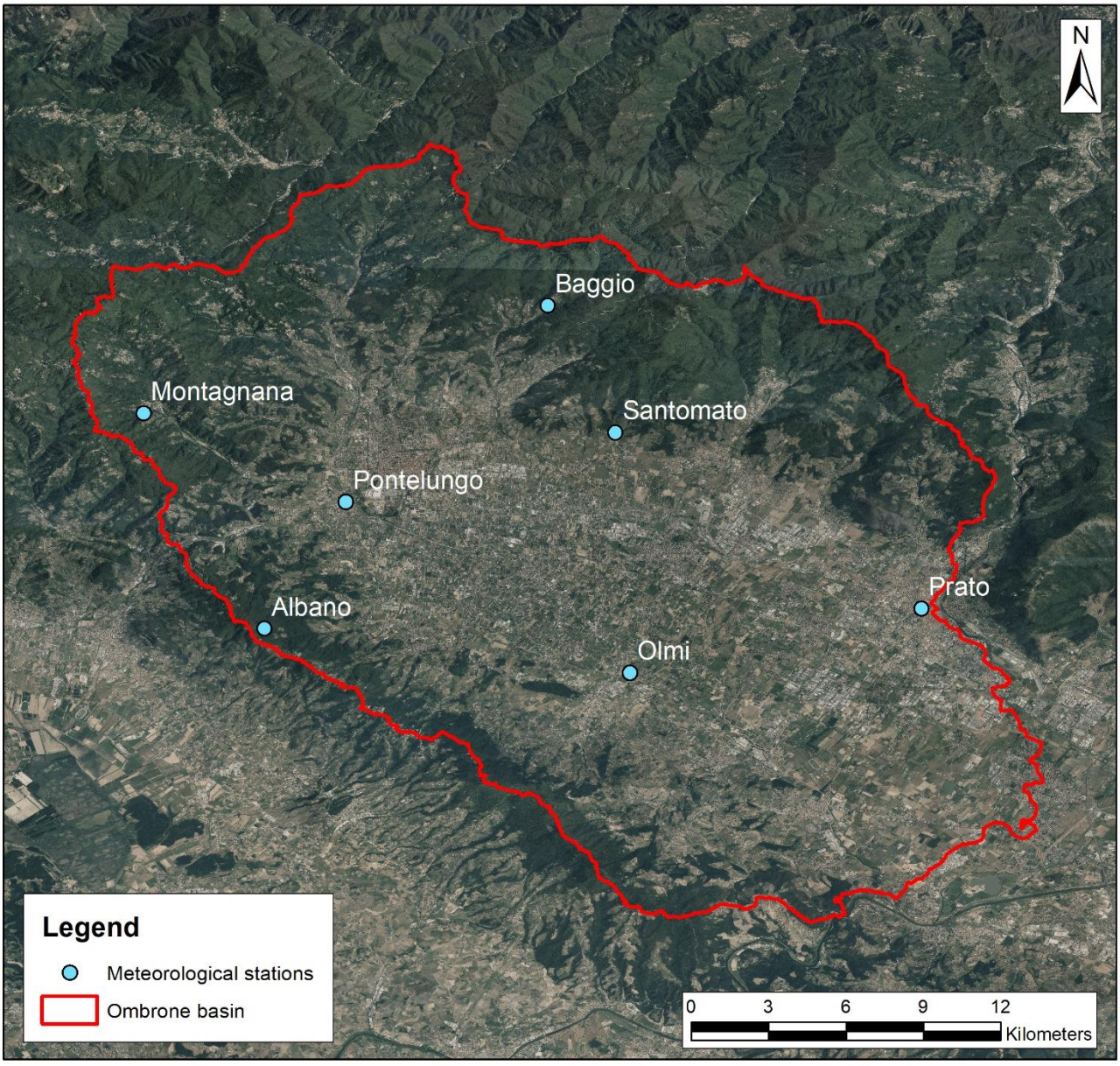

Figure 89 – Meteorological station used for RCMs output downscaling within the Ombrone basin.

Daily precipitation, maximum and minimum air temperature, humidity, solar radiation and wind speed of each RCM were compared with their relative measured data, in correspondence of the available meteorological stations within the Ombrone basin. Then, statistical parameters such as R^2, mean and standard deviation of observed data and model output were compared to each other, before and after the *bias* correction procedure, to check the suitability of climate models.

8.3.2 Precipitation

The simulated daily precipitation for all RCMs has been compared with the observed precipitation at Baggio, Montagnana and Prato stations, starting from 1992 to 2018. Linear Scale method was applied with a multiplicative correction for RCMs precipitation downscaling. Figure 90 shows the mean daily rainfall of raw

RCM simulated (Figure 90a) and calibrated (Figure 90b) precipitation data at the three available meteorological stations. These stations are characterized by a mean daily precipitation of 3.7, 4.23 and 2.83 mm and an annual mean of 1350, 1543 and 1032 mm, respectively. Compared to the observations, raw RCMs output deviates significantly from observed mean values, with all selected RCMs that deeply underestimate the observed rainfall. Thanks to the correction phase performed by means of the linear scale method, calibrated RCM precipitation data result in good agreement with measured data, showing mean values that perfectly match the observations in the control period (1992-2018).

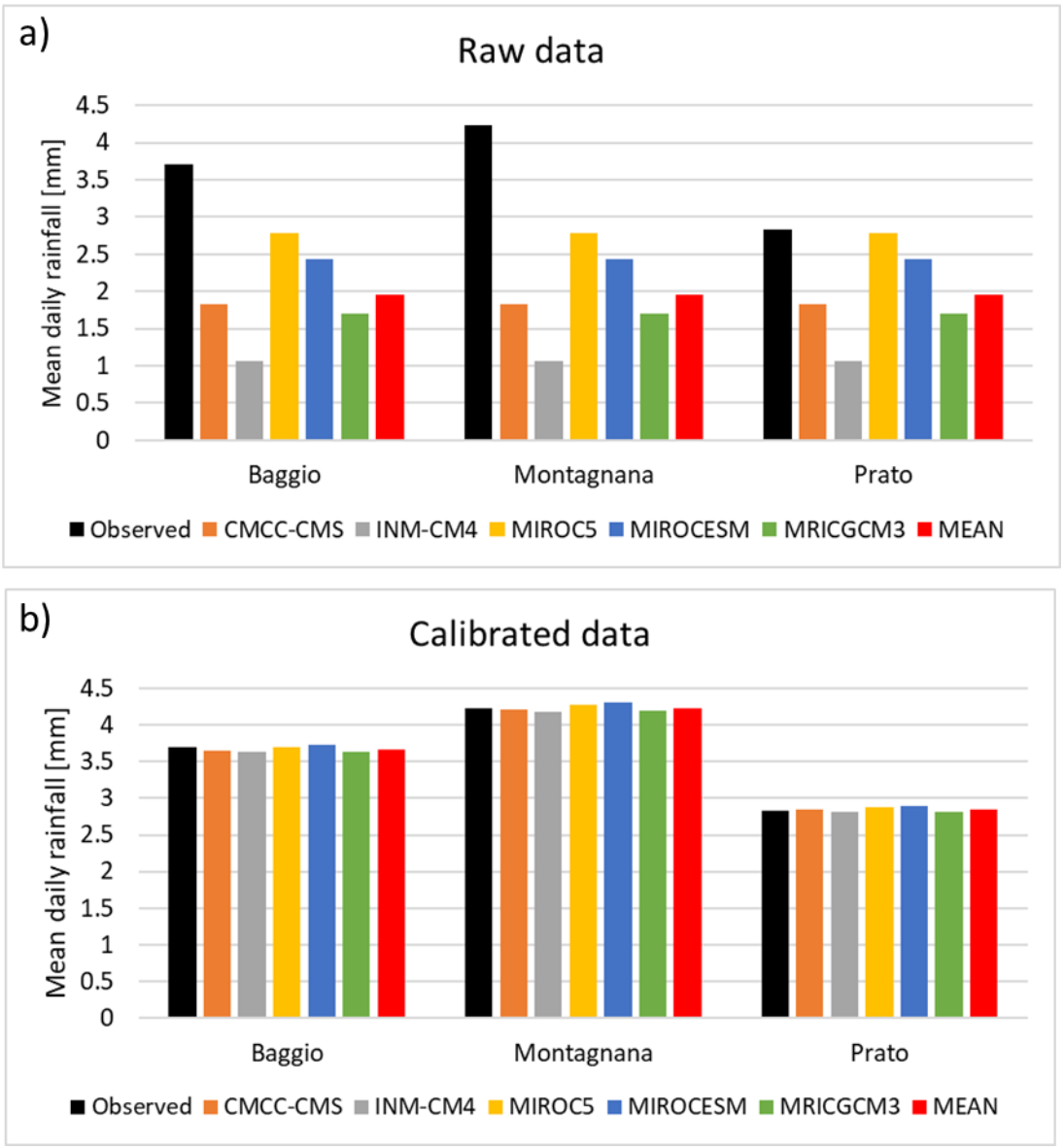

Figure 90 – Mean daily rainfall of a) Raw RCMs simulated and b) RCMs calibrated precipitation data.

Table 14 lists the standard deviation of observed, raw RCMs and corrected precipitation data. The analysis of the raw RCMs output indicates high differences from observed values, with an underestimation of the standard deviation from all selected RCMs. A discussed in chapter 7, the nature of LS method makes it suitable to match the mean of corrected RCM output with that of observed values. If compared to observations, standard deviation values of corrected precipitation data do not reach the same accuracy level of calibrated RCMs means, but all five selected RCMs show clear improvements in the estimation of the statistics. Since all the available meteorological stations fall within a single cell of RCMs grid, raw RCMs output are represented by a single time series (indicated with the “Raw” row in Table 14) for every control stations.

Table 14 – Standard deviation of raw and calibrated RCMs precipitation data and observed precipitation values.

	Observed	CMCC-CMS	INM-CM4	MIROC5	MIROCESM	MRICGCM3
Raw	-	5.10	2.29	6.61	4.41	4.03
Baggio	10.17	9.75	8.21	8.12	6.68	9.09
Montagnana	11.39	11.36	9.81	9.66	7.88	10.92
Prato	7.83	8.09	6.51	6.47	5.37	6.97

Seasonal trends of mean daily rainfall obtained from calibrated RCMs output and observed data are displayed in Figure 91, together with their coefficient of determination R^2.

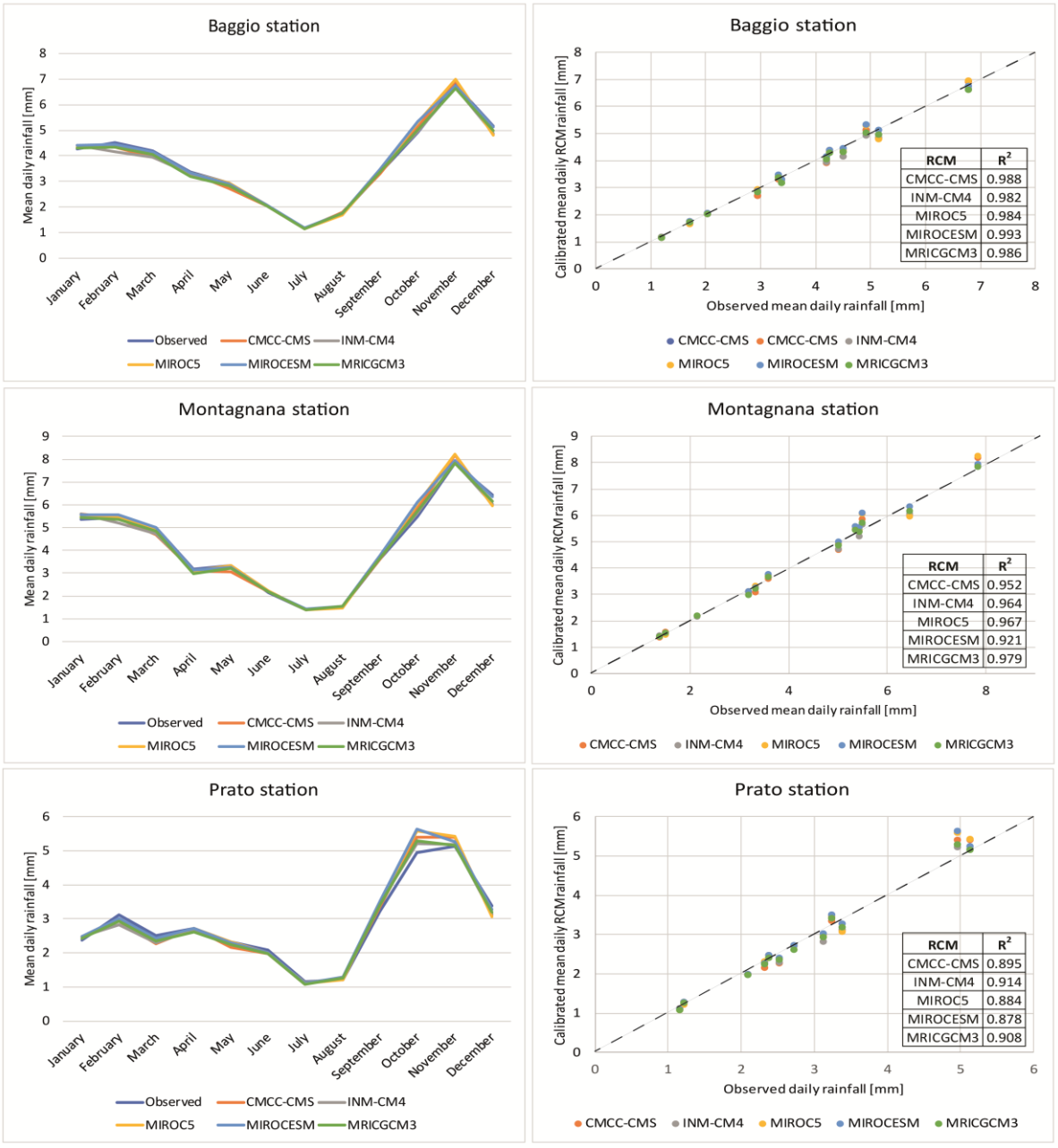

Figure 91 – Seasonal trends of mean daily rainfall for RCMs calibrated output and relative coefficient of determination R^2.

All the control stations show a good correspondence between observations and RCMs calibrated data, proving their capability of perfectly catching rainfall seasonal patterns. Displayed R^2 further demonstrate the

goodness of RCMs calibration, with high values (very close to 1 and always bigger than 0.9) for each RCM at every meteorological station. Some minor discrepancies are encountered at Prato station, in particular for October and November RCMs rainfall, where R^2 values decrease below 0.9 for each model, except for INM-CM4.

In order to identify potential variation of precipitation patterns in future years, RCMs data time frames were divided into 6 periods representing historical data (1992-1999, 2000-2009 and 2010-2019) and future years (2020-2029, 2030-2039 and 2040-2049). Cumulated RCMs rainfall data for different time periods at Prato station are shown in Figure 92. The other stations show very similar trends.

Under RCP4.5 scenario, selected models give different results in precipitation patterns for the future periods. MIROCESM and INM-M4 show a little decrease in cumulated rainfall, whereas CMCC-CMS shows a decisive decrease starting from 2020-2029 period. On the other hand, MRICGCM3 exhibits an increase in precipitation, especially for the 2040-2049 decade, while MIROC5 identify a maximum peak during the 2030-2039 period. However, the average value of all the selected RCMs does not identify a clear trend in precipitation pattern for the years to come, showing little variation lower than 10% between two consecutive time periods. Similar results were obtained by the Intergovernmental Panel on Climate Change (IPCC, 2013) for South Europe and Mediterranean regions, enlightening that the small precipitation changes identified by RCMs simulation fall within the range of natural variability.

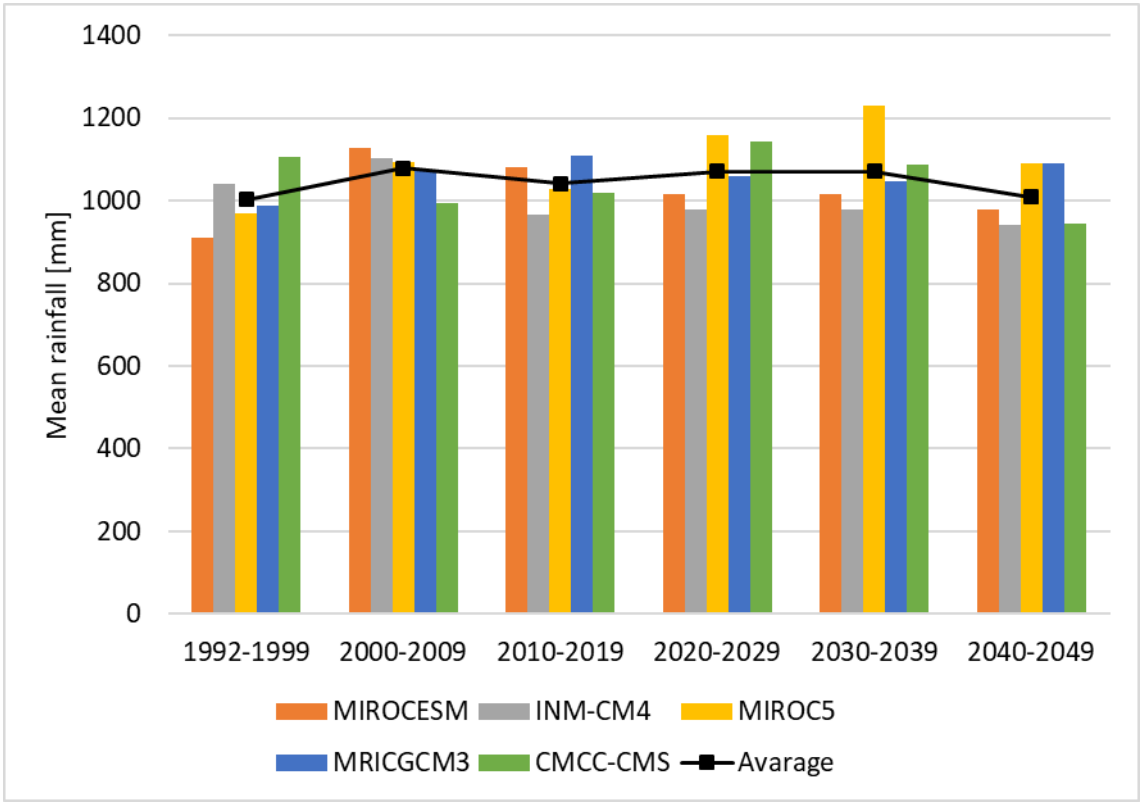

Figure 92 – Mean rainfall for historic and future period obtained by RCMs calibrated ouput under RCP4.5 scenario at Prato station.

8.3.3 Temperature

Raw daily maximum and minimum temperature data obtained from all selected RCMs under RCP4.5 scenarios have been compared with the measured temperature at Albano, Pontelungo and Santomato stations, providing data from 1992 to present. Mean daily maximum and minimum observed temperature for each control station are displayed in Figure 93, together with raw and calibrated RCMs output. Albano, Pontelungo and Santomato meteorological stations show a mean maximum daily temperature of 19.07°C, 20.58°C and 20.44°C and a mean minimum temperature of 10.37°C, 9.79°C and 9.63°C, respectively. All selected raw RCMs simulation slightly underestimate maximum measured temperature, except for INM-CM4 model that shows higher values (Figure 93a). On the other hand, mean minimum temperature is overestimated by all RCMs, in particular by MIROC5 model that shows the greatest discrepancy (Figure 93c).

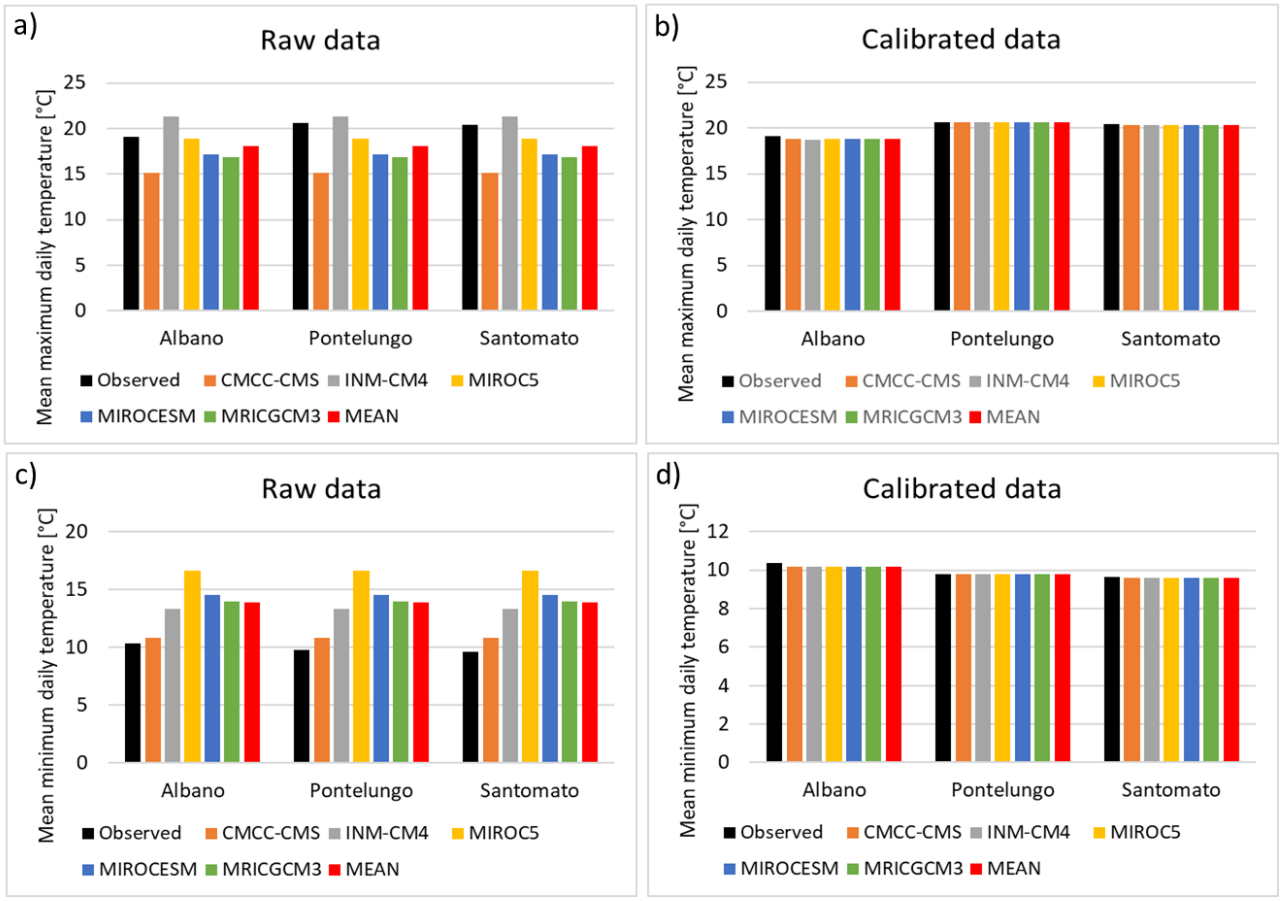

Figure 93 – Mean maximum daily temperature of a) Raw RCMs simulated and b) RCMs calibrated data and mean minimum daily temperature of a) Raw RCMs and b) calibrated RCMs.

Mean daily values of RCMs calibrated maximum and minimum temperature are displayed in Figure 93b and Figure 93c, respectively. The perfect match between observations and RCMs mean at all control stations demonstrates the goodness of the additive correction for temperature data downscaling. Small differences (<2%) still remain only in average values calculated at Albano station, for both maximum and minimum temperature.

Table 15 and Table 16 show the standard deviation of observed, raw RCMs and corrected maximum and minimum temperature data. Standard deviation values of raw RCMs output are characterized by important discrepancies if compared to observed values, underestimating the standard deviation of observations for both maximum and minimum temperature. At Albano station, raw RCMs output display small differences in minimum temperature standard deviation values if compared to observations (Table 15), except for INM-

CM4 model, that overestimates standard deviation at all stations. Bias corrected RCMs output show values of standard deviation that are very close to observed data, with small differences between them (<10%) for both maximum and minimum temperature. Again, the only exception is represented by corrected INM-CM4 output, that show differences bigger than 35% with observed values, not adjusting the standard deviation of raw RCMs minimum temperature data.

Table 15 – Standard deviation values for observed and RCMs maximum temperature.

	Observed	CMCC-CMS	INM-CM4	MIROC5	MIROCESM	MRICGCM3
Raw	-	5.92	10.27	6.44	5.08	5.63
Albano	8.07	8.99	7.59	7.44	7.57	7.61
Pontelungo	8.33	7.94	9.22	7.92	7.77	7.90
Santomato	8.39	7.95	9.18	7.91	7.77	7.89

Table 16 – Standard deviation values for observed and RCMs minimum temperature.

	Observed	CMCC-CMS	INM-CM4	MIROC5	MIROCESM	MRICGCM3
Raw	-	5.74	7.17	5.79	4.92	5.39
Albano	5.96	5.86	8.54	5.65	5.54	5.69
Pontelungo	6.37	6.11	8.64	5.87	5.74	5.96
Santomato	6.17	5.98	8.66	5.78	5.66	5.82

Figure 94 and Figure 95 represent the seasonal trend variation of corrected RCMs time series of mean temperature and their comparison with observations. Coefficient of determination R^2 for each RCM is also displayed. Obtained results show a very good agreement between RCMs and observation mean temperature values, with no significant differences existing in terms of average daily temperature seasonal graphs. The perfect match of both mean daily maximum and minimum temperature with relative observations is also demonstrated by R^2 values, equal to 1 for each RCMs at every control station.

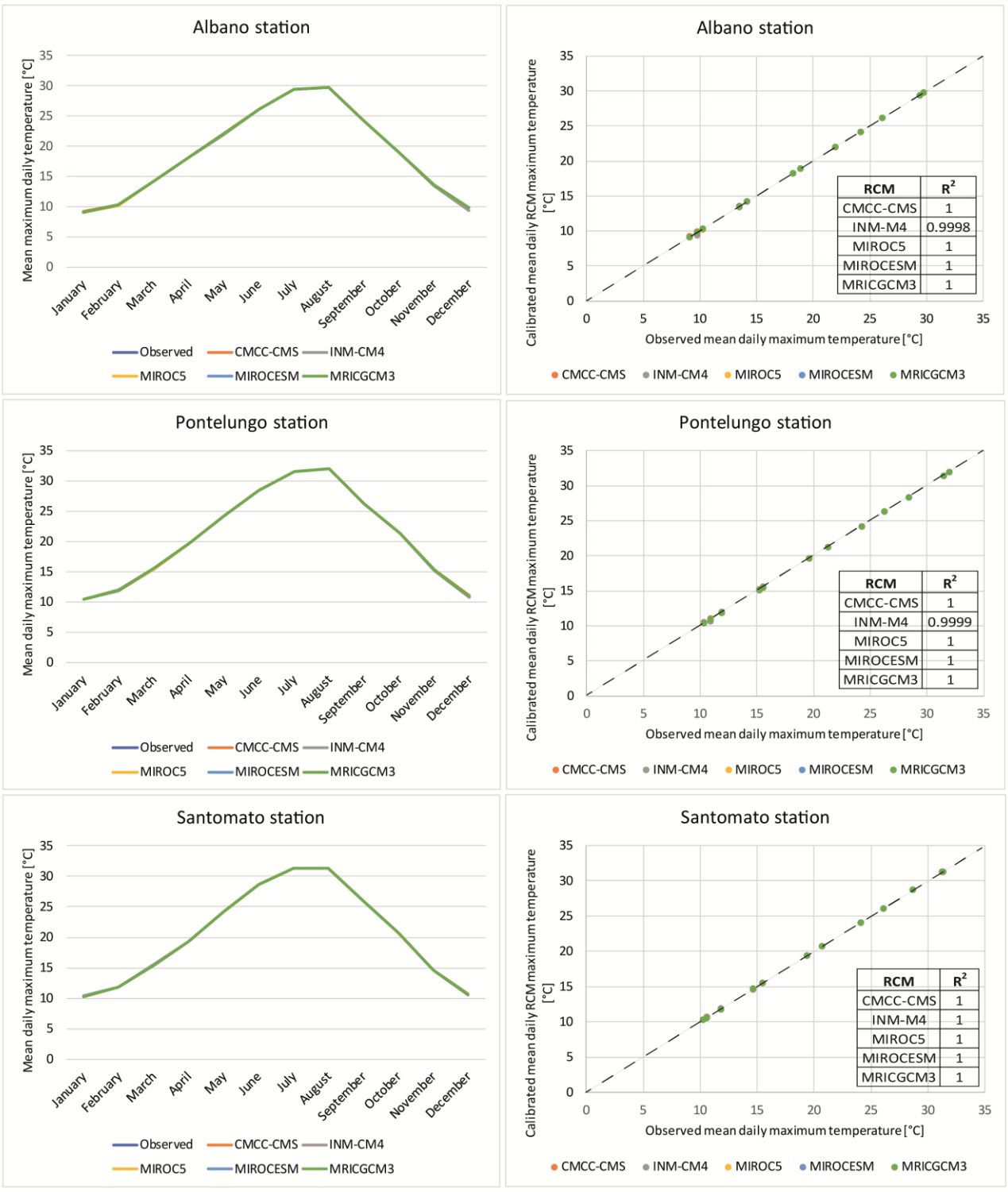

Figure 94 - Seasonal trends of mean daily maximum temperature for RCMs calibrated output and relative coefficient of determination R^2.

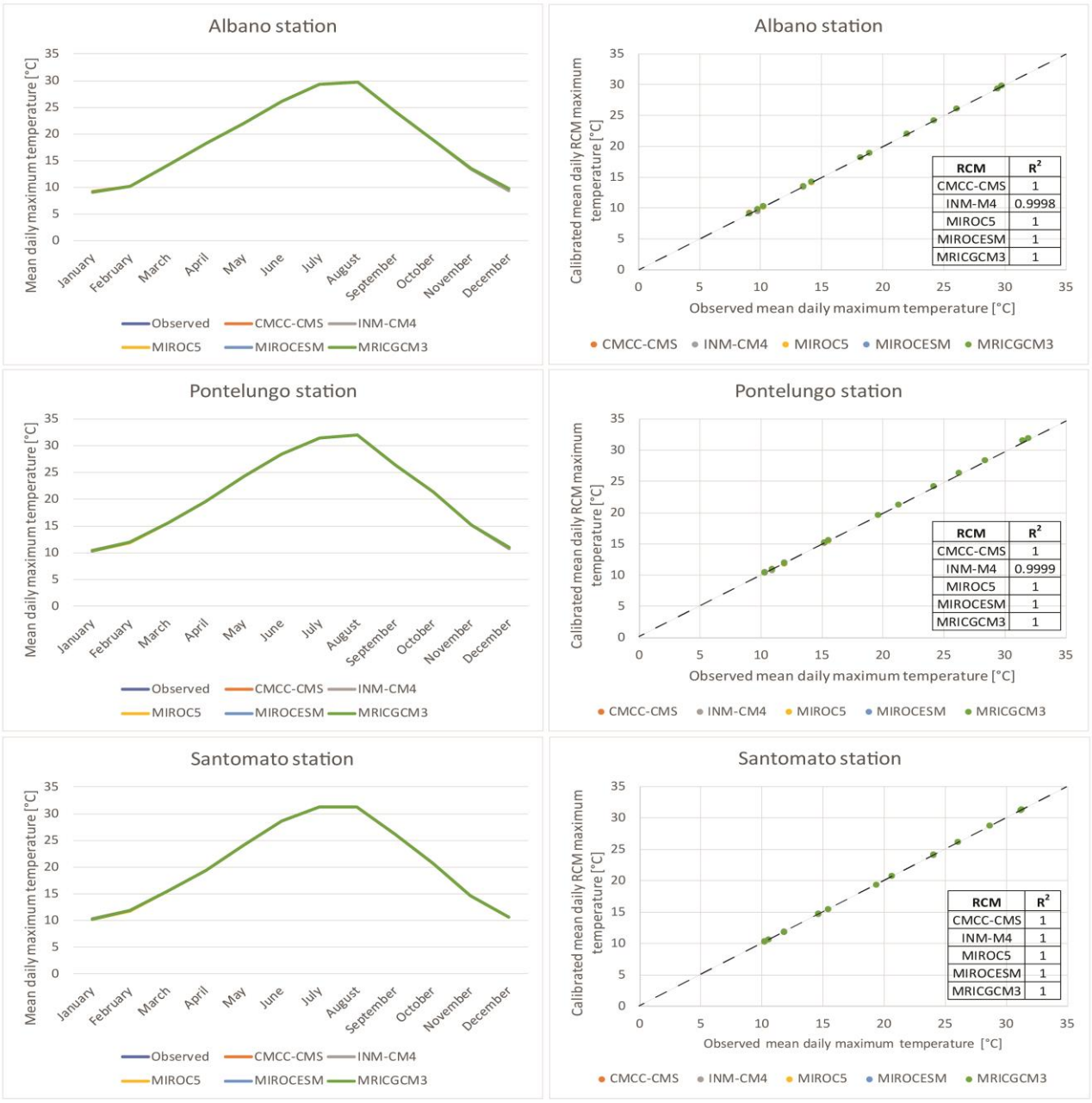

Figure 95 - Seasonal trends of mean daily minimum temperature for RCMs calibrated output and relative coefficient of determination R^2.

Calibrated RCMs mean maximum and minimum temperature data for 1992-1999, 2000-2009, 2010-2019, 2020-2029, 2030-2039 and 2040-2049 periods under RCP4.5 scenario are shown in Figure 96. Since all available meteorological stations show very similar trend for both maximum and minimum temperature data, only values for Pontelungo station are displayed.

The change in average maximum temperature of Ombrone basin is shown in Figure 96a. Mean maximum temperature is expected to increase in next decades, following a quite constant trend of about 0.03°C per decade, started at beginning of 1990'. Among all climate models, MIROCESM shows the maximum increase in maximum temperature under RCP4.5. MIROC5 simulations do not identify any increase in maximum temperature for the study area in future years, but they are characterized by higher temperature values since the first 1992-1999 period, if compared to the other RCMs.

Minimum temperature variability in Ombrone basin is displayed in Figure 96b. A high increasing rate is expected for minimum temperature, characterized by an average constant trend of about 0.25°C every 10 years. Only in the 2040-2049 period, the increasing trend seems to slow down, reaching a lower value of about 0.05°C in 10 years. The maximum variation in mean minimum temperature is expected by MRICGCM3 model, showing an increase of about 2°C in the 1992-2049 period. Overall, all selected RCMs under the intermediate RCP4.5 scenario agree that temperatures are projected to increase in the future.

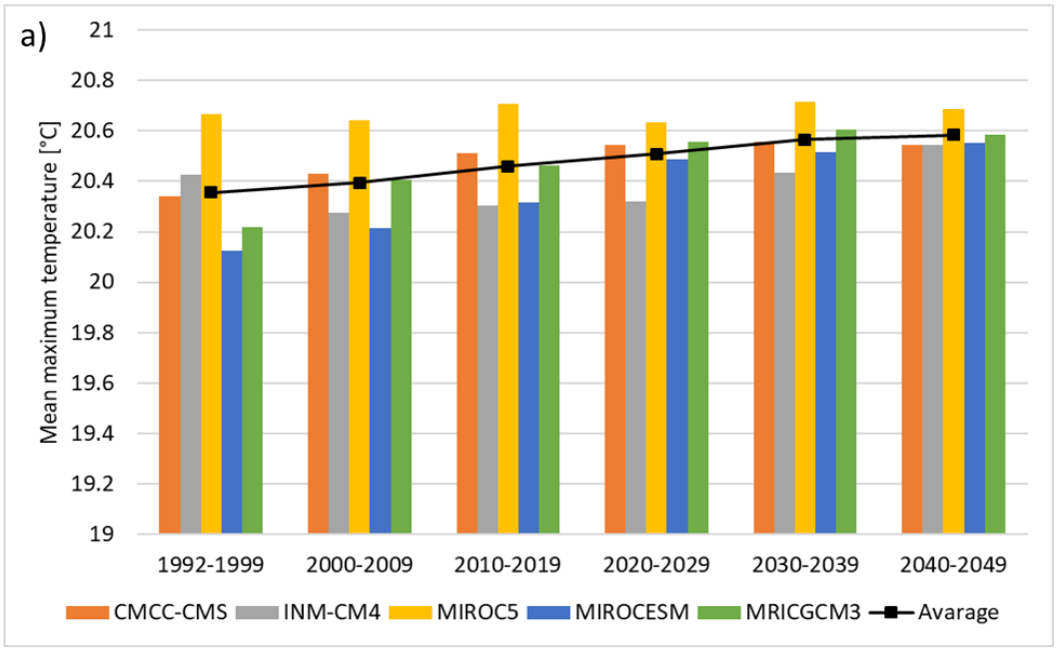

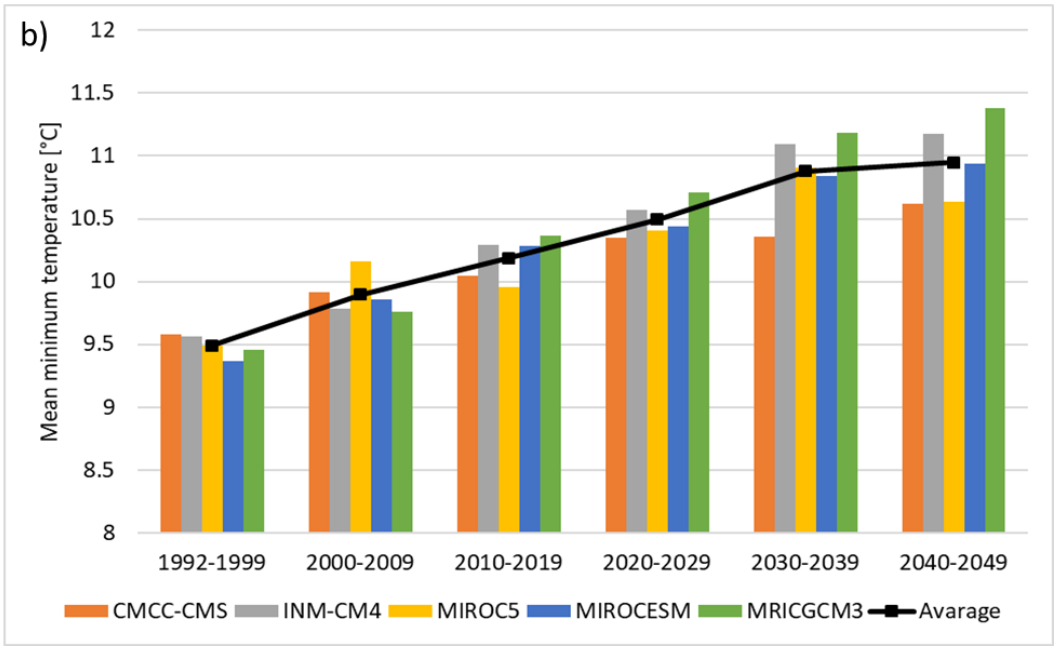

Figure 96 – RCMs mean a) Maximum and b) Minimum temperature for historic and future periods obtained by RCMs calibrated output under RCP4.5 scenario at Pontelungo station.

8.3.4 Solar radiation

Figure 97a and b present the mean daily solar radiation for raw and calibrated RCMs over the control period (1992-2018) at Olmi station. This is the only station for which solar radiation observations were available. Multiplicative linear scale method was applied for solar radiation downscaling. Solar radiation at Ombrone

basin has an average value of 159.04 w/m^2, that is overestimated by all raw RCMs. Only CMCC-CMS shows a lower value (about 150 w/m^2), that is very close to the observed mean.

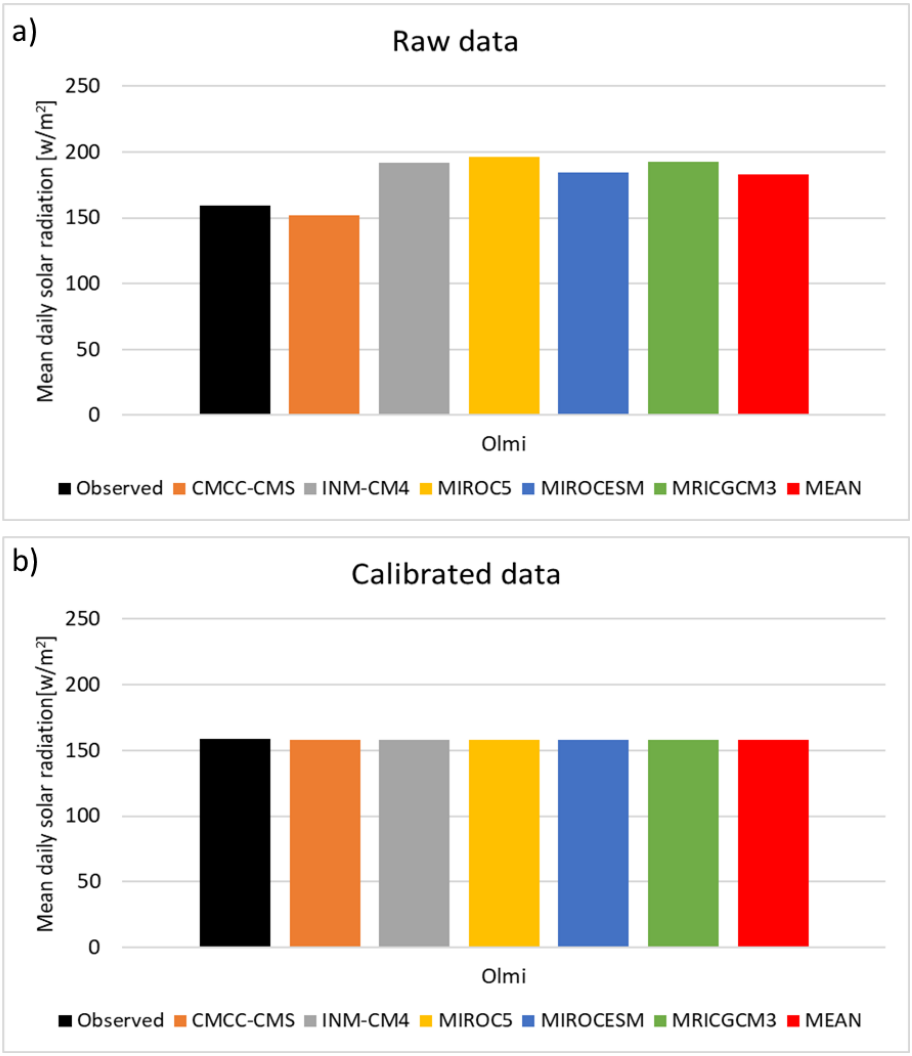

Figure 97 – Mean daily solar radiation for a) Raw RCMs and b) Calibrated RCMs at Olmi station over the period 1992-2018.

The linear scale method provided very good results in RCMs downscaling also for solar radiation, with a perfect correspondence between observed and calibrated mean values. Important improvements are obtained for standard deviation index as well, with all calibrated RCMs showing values closer to the observations (96.51 w/m^2) if compared to raw RCMs data (Table 17). Only calibrated MIROC5 model presents a worsening in fitting standard deviation, displaying a difference of 10% with observations and an increase of 2.5% if compared to raw RCMs (showing a lower difference of about 7.5%).

Table 17 – Standard deviation values for observed, raw RCMs and calibrated RCMs solar radiation data.

	Observed	CMCC-CMS	INM-CM4	MIROC5	MIROCESM	MRICGCM3
Raw	-	100.45	105.60	104.40	110.05	106.70
Olmi	96.51	94.11	88.81	86.96	90.79	87.40

Figure 98a presents the seasonal trend of calibrated RCMs solar radiation at Olmi station, showing a perfect match between observed and modelled values. The goodness of the downscaling procedure is also demonstrated by values of coefficient of determination R^2, equal to 1 for all selected RCMs (Figure 98b).

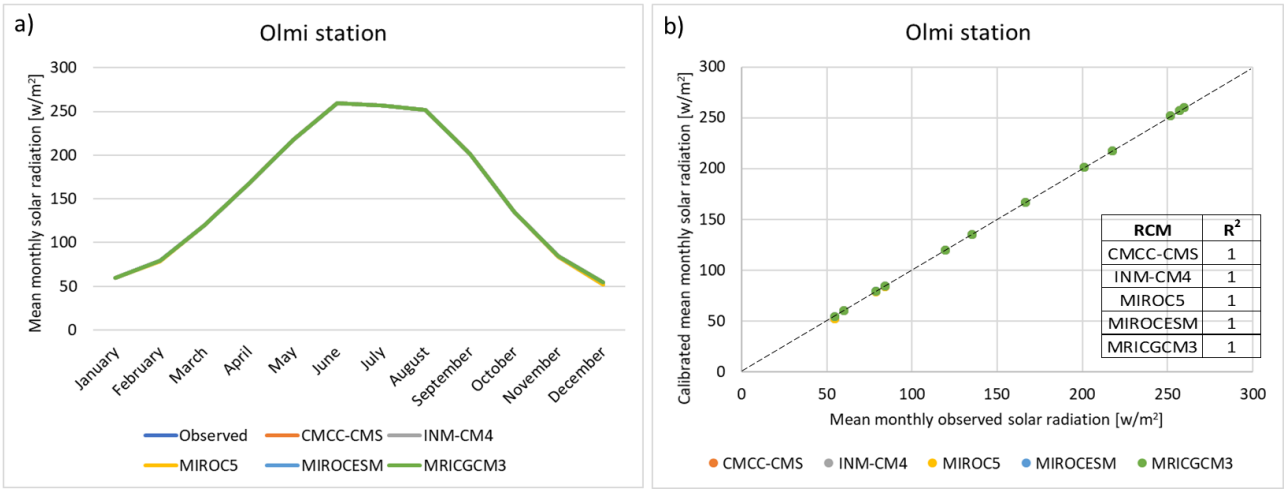

Figure 98 – a) Seasonal trend of calibrated RCMs solar radiation and b) Relative values of R^2 for the control period at Olmi station.

Figure 99 shows the projected mean solar radiation over the periods 2020-2029, 2030-2039 and 2040-2049, according to reference periods 1992-1999, 2000-2009 and 2010-2019. During the last decade, all RCMs shows an average increase in solar radiation of about 3% in respect of 1992-1999 and 2000-2009 periods. For the near future, the analysis of RCMs results projects a stabilization in the increase of solar radiation, with of no particular trends identified. The small changes that are expected to occur can be ascribed to the natural variability of solar radiation variable.

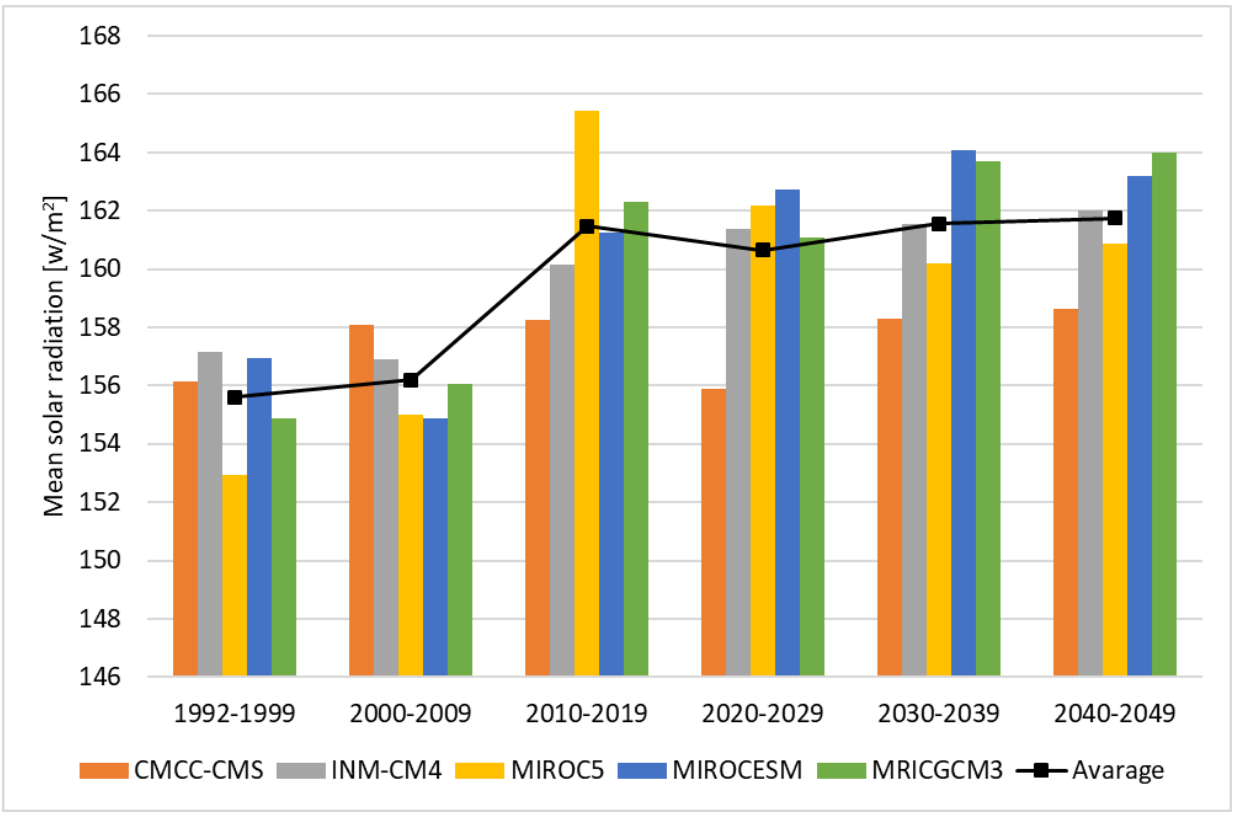

Figure 99 - RCMs mean solar radiation for historic and future periods obtained by RCMs calibrated output under RCP4.5 scenario at Olmi station.

8.3.5 Humidity

Mean values of raw and calibrated RCMs air humidity output for the 1992-2018 period at Prato station have been compared with measured mean air humidity, in order to evaluate the goodness of the downscale procedure, carried out by means of the linear scale method with a multiplicative correction factor (Figure 100). RCMs raw data are characterized by average air humidity values that are very close to observations, oscillating around the mean measured value of 64.43% (Figure 100a). Downscaled RCMs output exhibit further improvements, with average values that fit measurements with very low discrepancies, lower than 3% (Figure 100b).

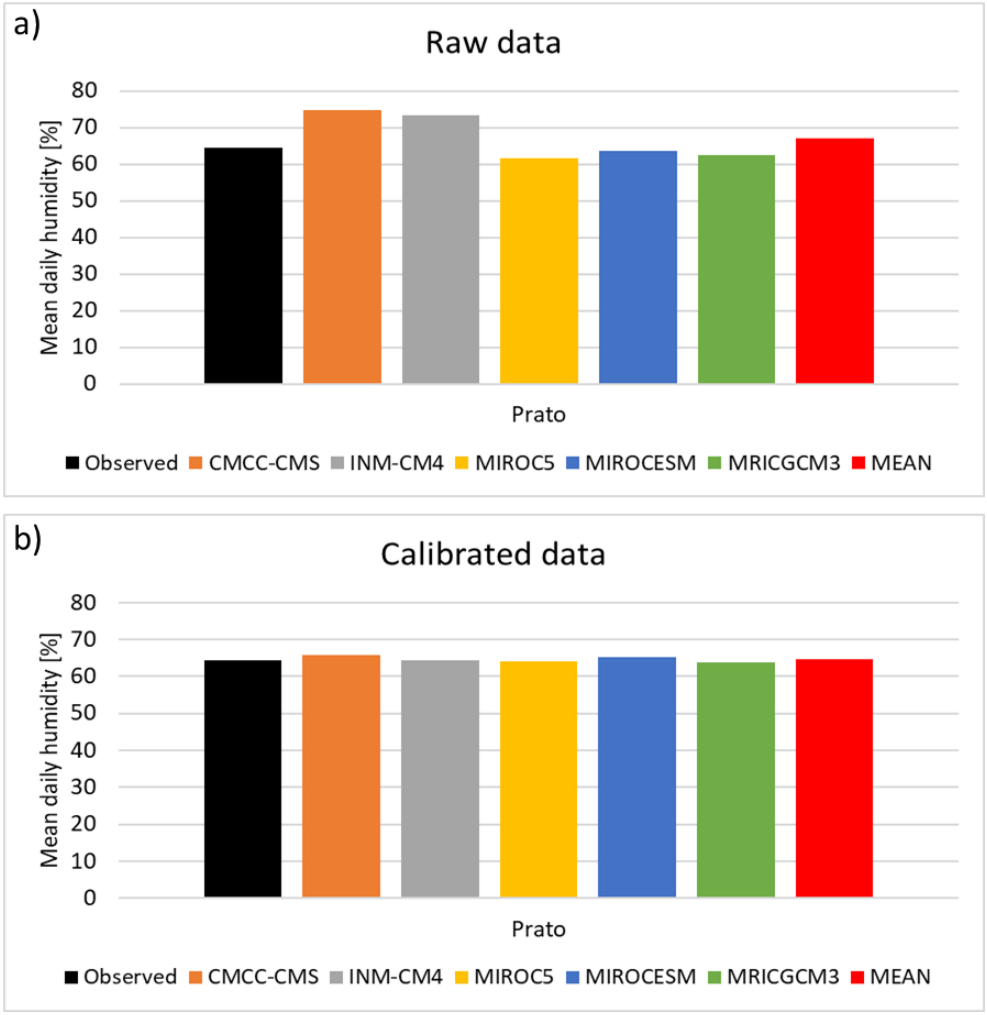

Figure 100 - Mean daily humidity for a) Raw RCMs and b) Calibrated RCMs at Prato station over the period 1992-2018.

Concerning standard deviation index, only CMCC-CMS and INM-CM4 calibrated humidity data present values in good agreement with observations. MIROC5, MIROCESM and MRICGCM3 calibrated data still show higher dispersion than measured values, with differences ranging between 20% and 40%, even after RCMs downscaling procedure (Table 18).

Table 18 – Standard deviation values for observed, raw RCMs and downscaled RCMs air humidity values at Prato station over the 1992-2018 period.

	Observed	CMCC-CMS	INM-CM4	MIROC5	MIROCESM	MRICGCM3
Raw	-	11.70	12.06	20.51	21.93	19.81
Prato	15.60	14.42	14.95	18.85	21.83	18.97

Mean monthly downscaled RCMs relative air humidity values are displayed in Figure 101, in order to identify potential discrepancies with seasonal trend of measured values in the control period. Figure 101a shows that RCMs calibrated data exhibit a good attitude in representing seasonal variations of air humidity, with very low discrepancies with observed data. R^2 values, displayed in Figure 101b, confirm the goodness of the downscaling procedure, showing very high values for all selected RCMs and demonstrating their predictive capabilities.

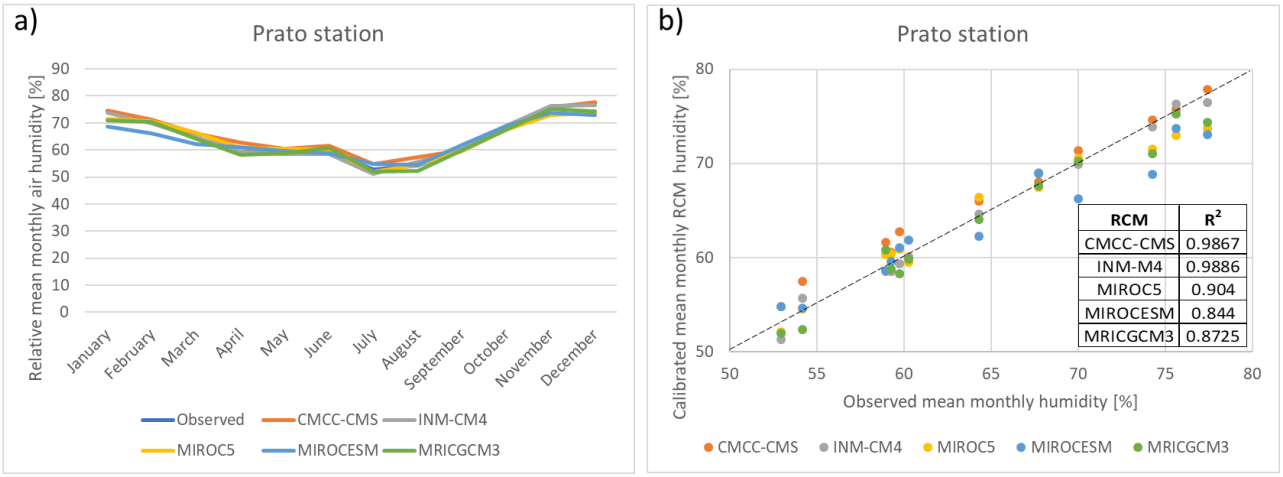

Figure 101 – a) RCMs seasonal variations of mean relative air humidity at Prato station in the 1992-2018 period and b) Comparison between observations and RCMs downscaled output, with relative coefficient of determination.

Historical trend and projected variations in air relative humidity obtained by RCMs calibrated data at Prato station are presented in Figure 102. Starting from 1992-1999 decade, relative humidity is characterized by a descendent trend, that it is expected to stabilize during the 2040-2049 period. In the analyzed period, RCMs simulation provide an average total reduction of about 2% in air relative humidity. Air humidity decrease in 1992-2049 period can be related with the correspondent increase in maximum and minimum temperature identified by all selected RCMs.

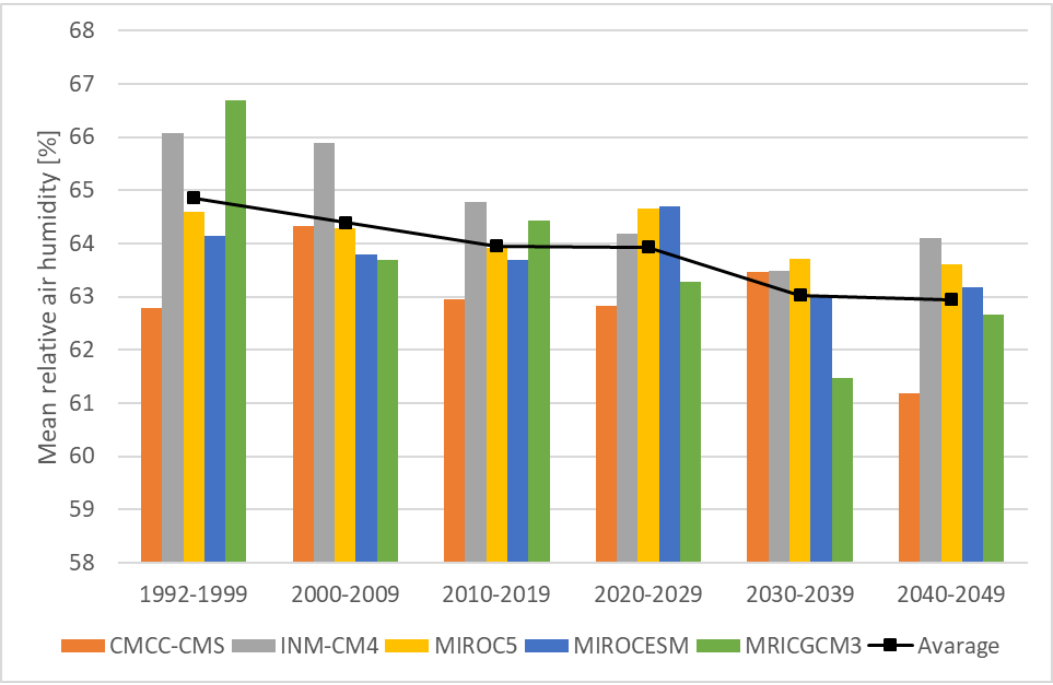

Figure 102 - RCMs mean air humidity for historic and future periods obtained by RCMs calibrated output under RCP4.5 scenario at Prato station.

8.3.6 Wind speed

Average raw RCMs and calibrated RCMs daily wind velocity, and their comparison with wind speed observations at Albano and Pontelungo meteorological stations for the 1992-2018 period, are displayed in Figure 103. For RCMs downscaling, the linear scale method with a multiplicative correction has been applied. Albano and Pontelungo stations provide a mean daily measured wind velocity of about 1.71 m/s and 1.27 m/s respectively, that is largely overestimated by raw RCMs output (Figure 103a). As for all other analyzed meteorological variables, calibrated wind speed data show a very good fit with observation, especially at Albano station. Some minor differences still remain at Pontelungo station, with all RCMs downscaled values that underestimate observation of about 8% (Figure 103b).

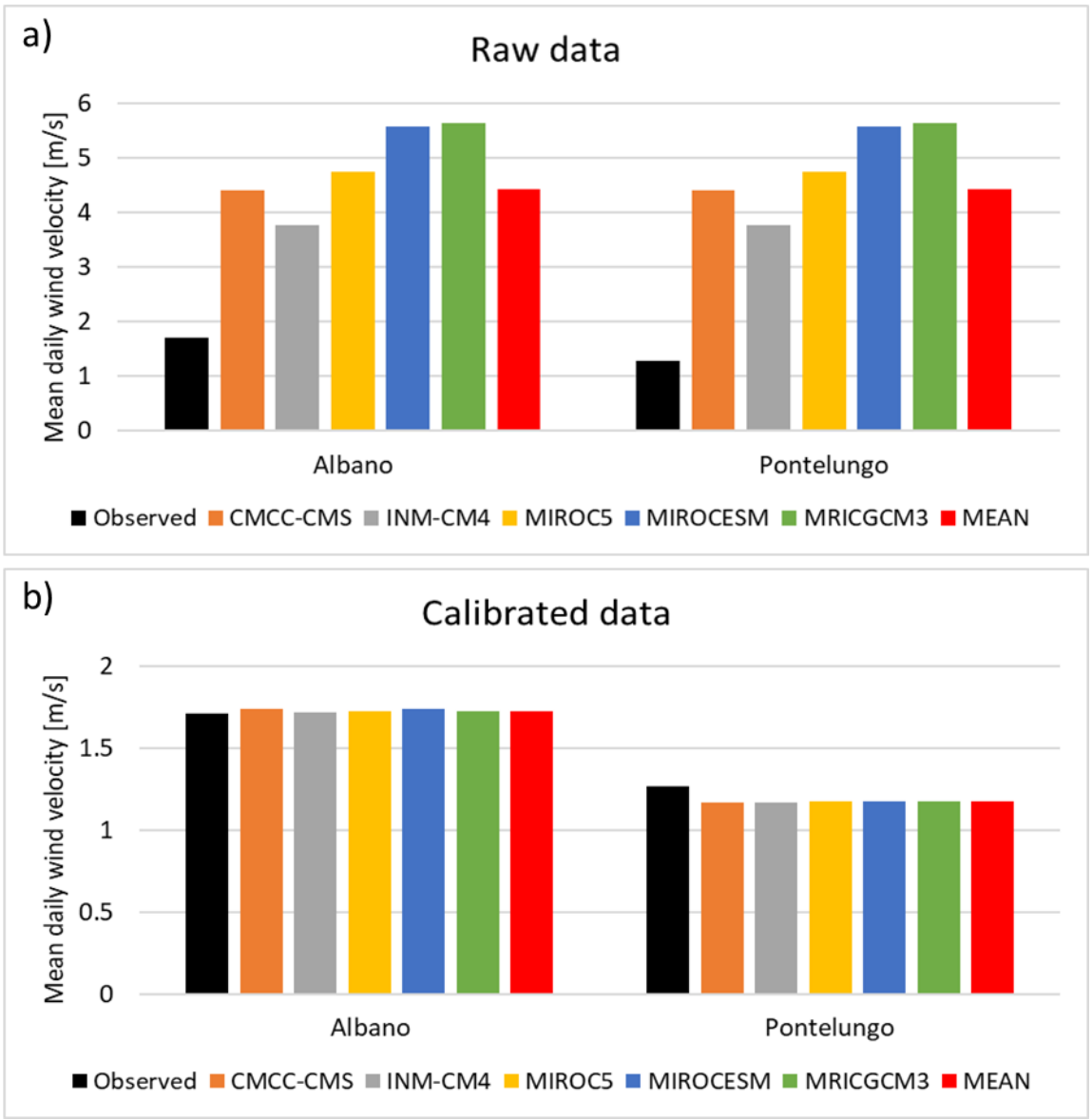

Figure 103 – Observed, raw RCMs and downscaled RCMs mean daily wind velocity at Albano and Pontelungo stations for the 1992-2018 period.

Standard deviation values presented in Table 19 show large discrepancies between observed and both raw and downscaled RCMs output. In particular, raw RCMs output present a higher dispersion than observed values, while calibrated RCMs underestimate the standard deviation of measurements. As for precipitation, such mismatches in standard deviation values can be ascribed to the nature of LS method, that is more accurate in matching the mean of corrected RCM output with that of observed values.

Table 19 – Standard deviation values for observed, raw RCMs and downscaled RCMs wind speed values.

	Observed	CMCC-CMS	INM-CM4	MIROC5	MIROCESM	MRICGCM3
Raw	-	1.92	1.83	2.53	2.63	2.73
Albano	1.42	0.74	0.87	0.81	0.75	0.78
Pontelungo	1.11	0.53	0.60	0.56	0.52	0.56

Seasonal trend of mean wind speed at Albano and Pontelungo station for the analyzed control period are showed in Figure 104. For Albano station, a perfect match between downscaled RCMs output and measured wind speed data can be observed, characterized by high values (very close to 1) of the coefficient of determination for all selected RCMs. Analyzing RCMs calibrated output at Pontelungo station, on the other hand, some differences in monthly pattern of mean daily wind speed are clearly visible, if compared to measured data. The lower accuracy reached at Pontelungo station is further demonstrated by R^2 index, that shows values < 0.9 for each RCM. Worst results are obtained for INM-CM4 and MRICGCM3 models, characterized by R^2 values of 0.7543 and 0.785 respectively.

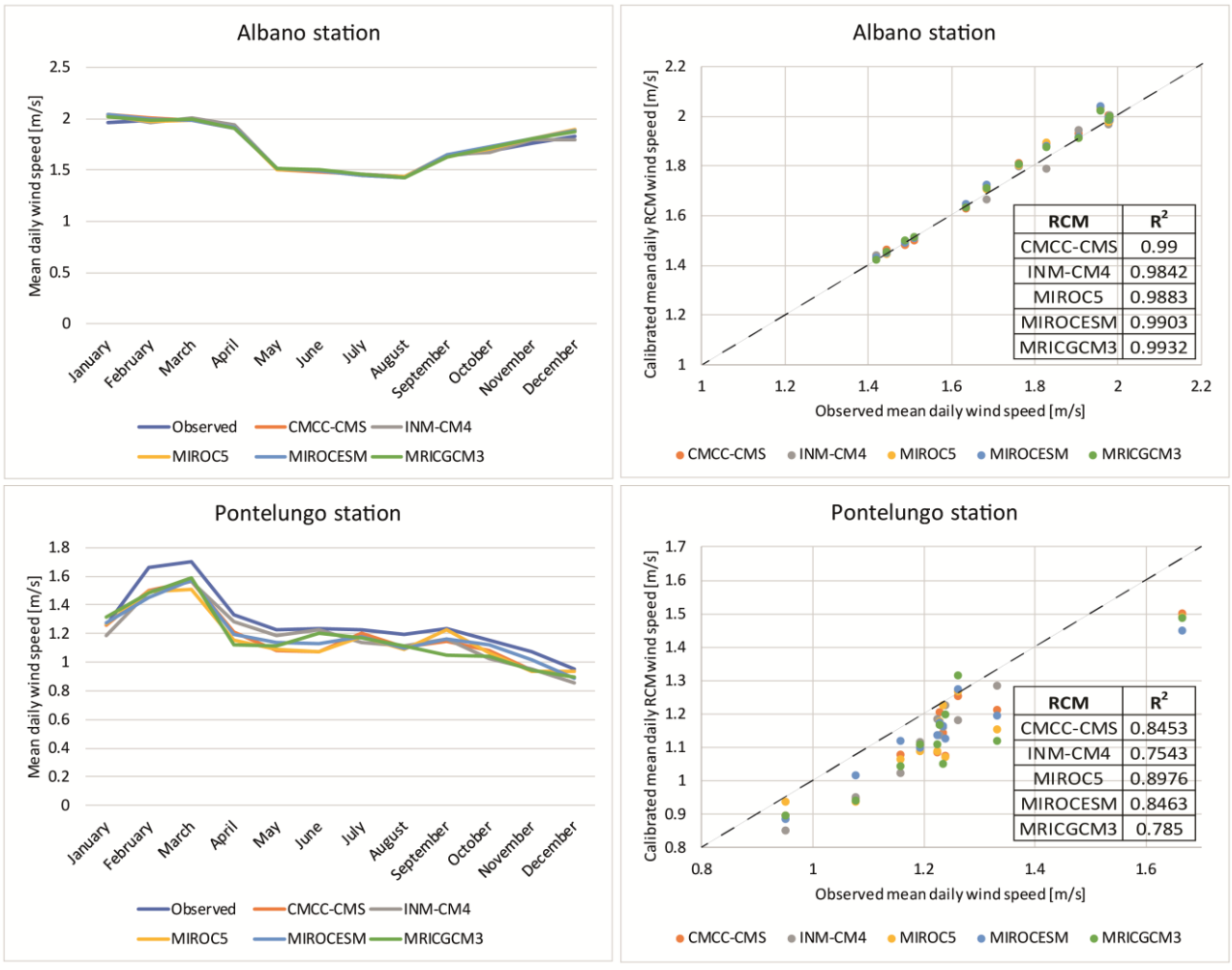

Figure 104 – Comparison between seasonal trends of observed and calibrated RCMs wind speed output with relative values of coefficient of determination.

Mean wind speed values for RCMs downscaled output over 1992-1999, 2000-2009 and 2010-2019 historical periods and 2020-2029, 2030-2039 and 2040-2049 future periods at Albano and Pontelungo meteorological stations are displayed in Figure 105. Accordingly to all RCMs data, no particular pattern in wind velocity can be detected at Albano station for both historical and future periods, with average values that range between

1.69 m/s and 1.79 m/s for the entire analyzed time frame (Figure 105a). A very similar trend can be observed at Pontelungo station, characterized by lower mean wind velocity values ranging between 1.145 m/s and 1.215 m/s (Figure 105b). Small variations detected in the mean wind speed pattern at both stations can be totally ascribed to the range of natural variability.

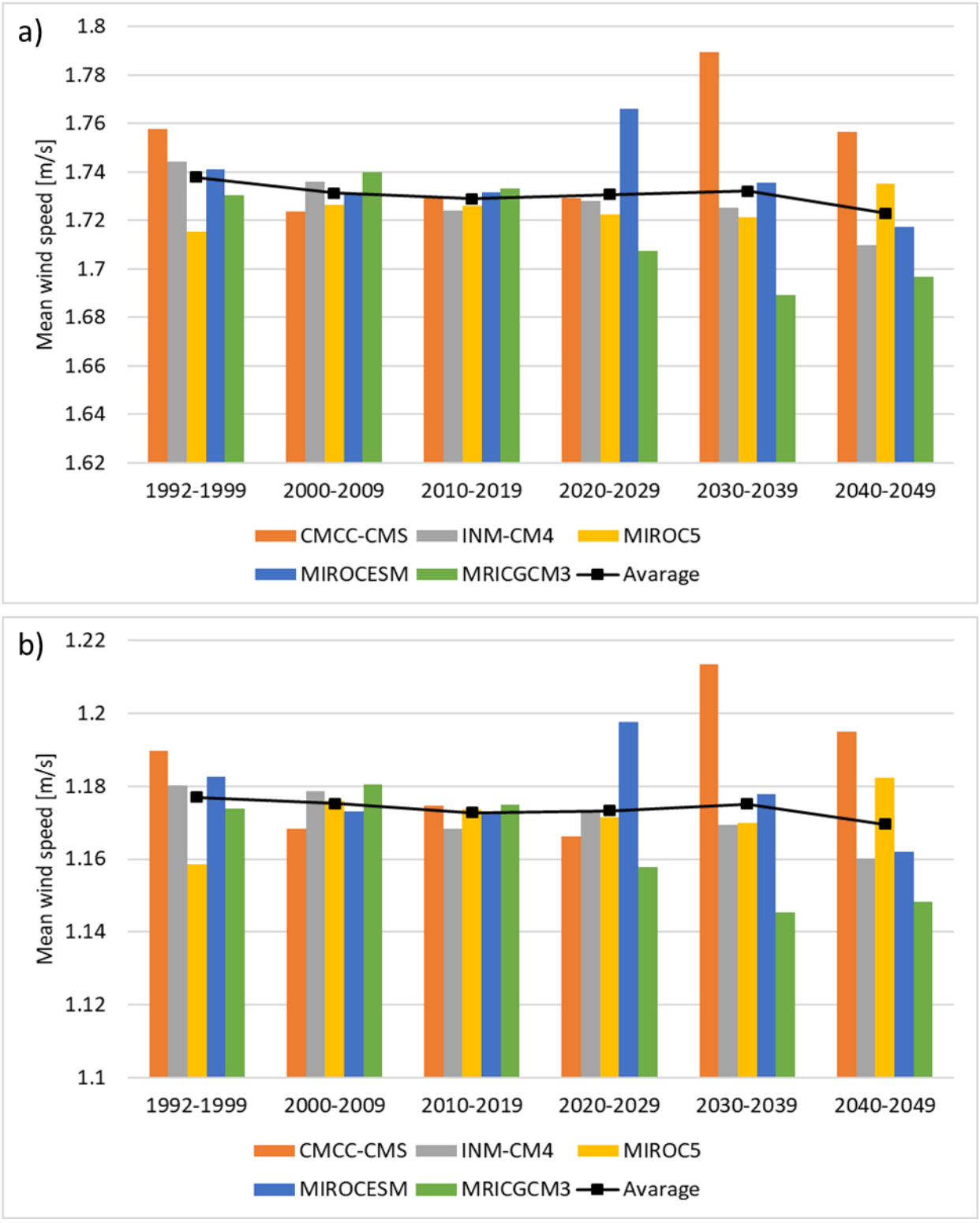

Figure 105 – Downscaled RCMs mean wind speed values for historic and future periods obtained under RCP4.5 scenario at a) Albano and b) Pontelungo stations.

8.3.7 Hydrologic forecasting

The calibrated hydrological model developed by means of MOBIDIC code for Ombrone basin, described in chapter 5, was run for the future climate change scenario using, as input data, the corrected RCMs meteorological data from CMCC-CMS, INM-CM4, MIROC5, MIROCESM and MRICGCM3 models. The analysis has been performed for the 1992 - 2050 period, with a daily time step, using 1992 and 1993 for the model warm-up, considering the 1994-2017 time frame as a control period for the comparison with the original simulation and the 2018-2050 time frame for the hydrological forecasting.

Monthly average discharge values calculated by means of selected RCMs data for the control period at Pontelungo and Poggio a Caiano river gauging stations are displayed in Figure 106 and Figure 107.

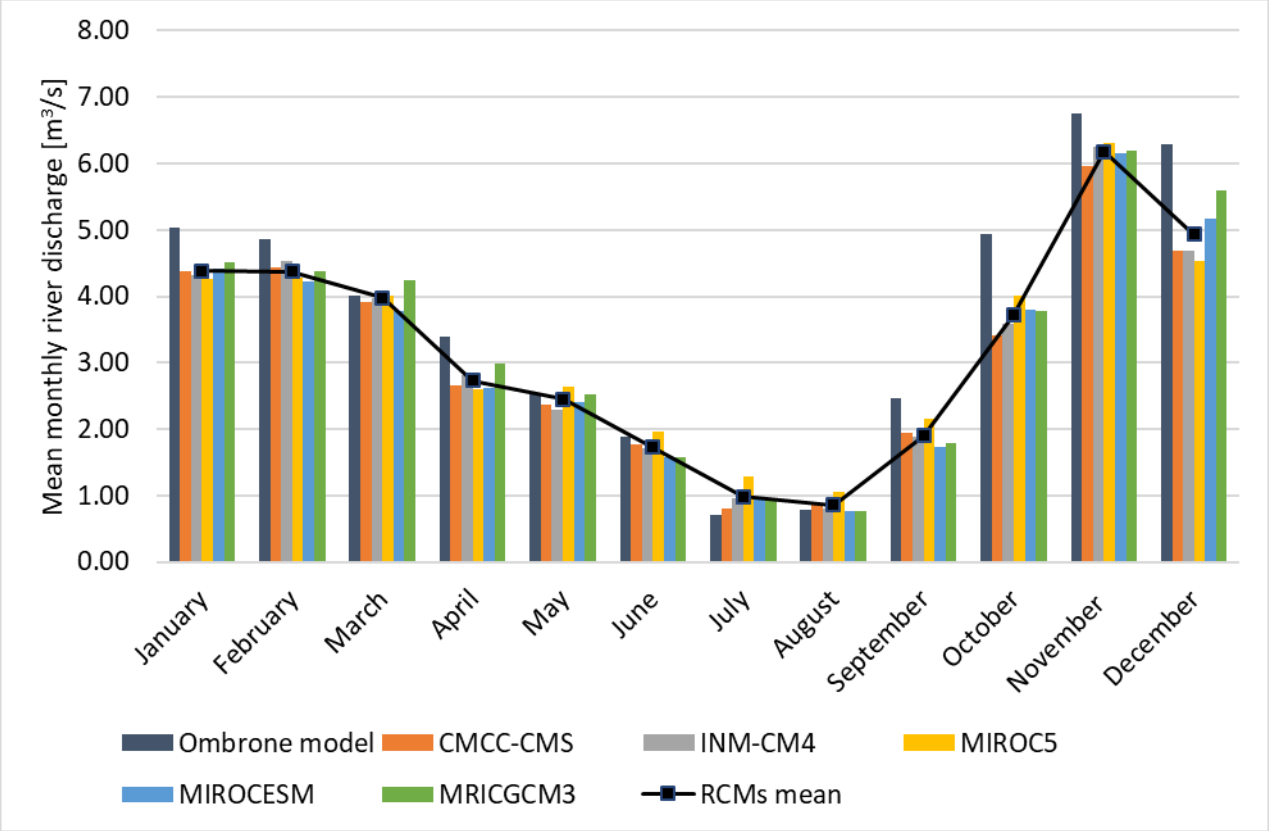

Figure 106 – Mean monthly river discharge values of Ombrone Pistoiese river at Pontelungo monitoring station for the 1994-2017 period.

For both gauging stations, results of the RCM's hydrologic modelling procedure match very well the original simulation output, confirming the goodness of the *bias* correction procedures. In particular, for Pontelungo station, the mean monthly discharge simulated by RCMs slightly underestimates the original simulation for the first part of the year (from January to June) and it slightly overestimates discharge in July and August. Higher discrepancies are identified from September to December, even if all RCMs simulations describe the overall seasonal trend with a good approximation, highlighting a maximum discharge peak in November and a minimum flow in July and August. Comparing RCMs output for each month, a very small variability can be observed in the mean simulated discharge, with all RCMs showing very similar values, in agreement to the results obtained during the calibration of meteorological data.

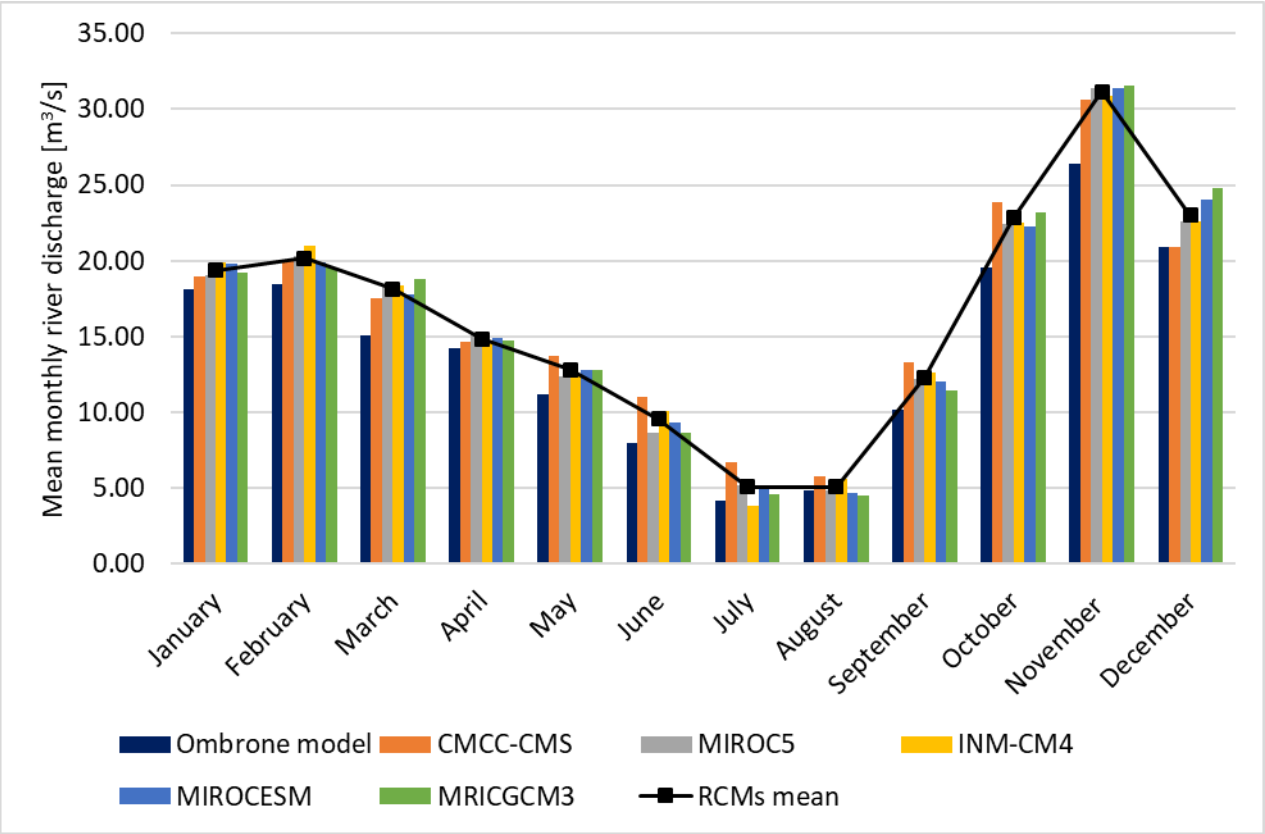

Figure 107 - Mean monthly river discharge values of Ombrone Pistoiese river at Poggio a Caiano monitoring station for the 1994-2017 period.

At Poggio a Caiano station, all hydrologic simulation performed by means of RCMs output overestimate the original simulation, except for INM-CM4 in July and for MIROCESM and MRICGCM3 in August. As for Pontelungo station, each RCMs show a good capability in describe the seasonal variation of river discharge, as a result of the *bias* correction method used to calibrate the RCMs raw output (Linear Scale method), that is capable to perfectly match the monthly mean of corrected RCMs values with observations.

Following the proposed integrated procedure between MOBIDIC hydrologic model and MODFLOW, river network has been discretized withi the groundwater model grid with 11 branches, characterized by a constant width and water level height. In order to evaluate the goodness of the hydrologic simulations performed with RCMs calibrated output, the mean river discharge values, calculated by each RCMs for the control period, are showed in Figure 108, together with the discharge values of the original simulation (named “Ombrone model”).

For each year of simulation, the average, maximum and minimum modelled discharge of all selected RCMs is reported.

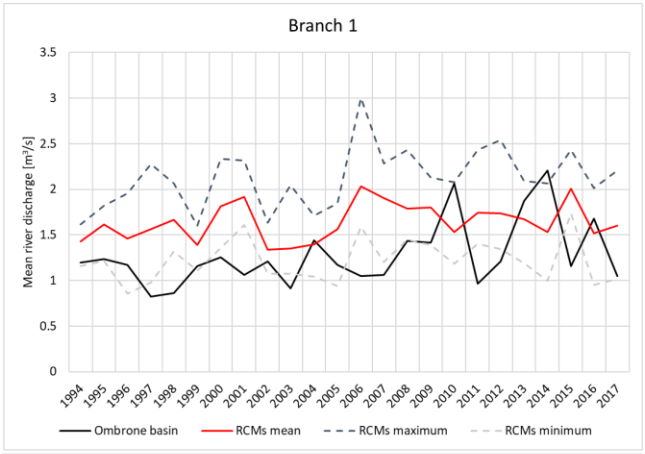
Branch 1
Mean river discharge [m³/s]
Ombrone basin
RCMs mean
RCMs maximum
RCMs minimum

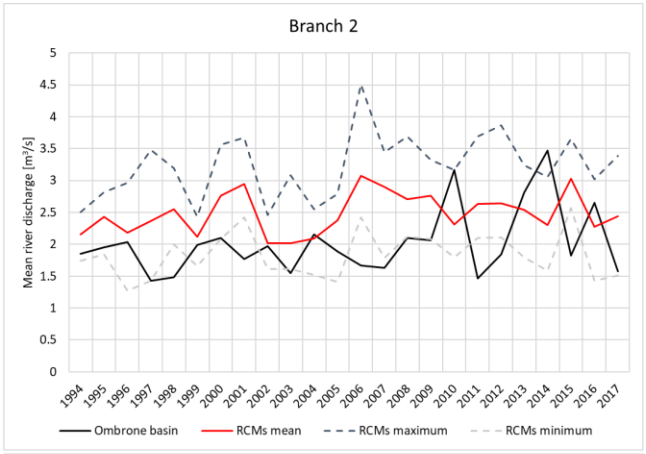
Branch 2
Mean river discharge [m³/s]
Ombrone basin
RCMs mean
RCMs maximum
RCMs minimum

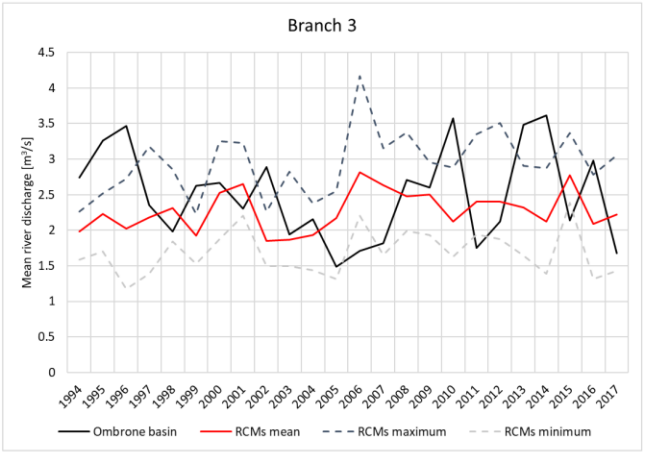
Branch 3
Mean river discharge [m³/s]
Ombrone basin
RCMs mean
RCMs maximum
RCMs minimum

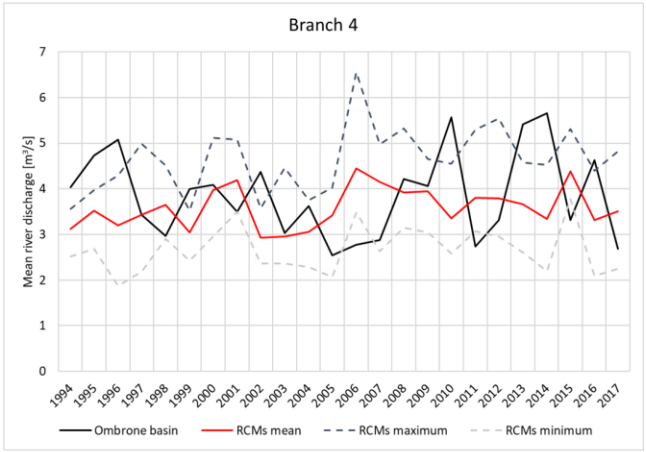
Branch 4
Mean river discharge [m³/s]
Ombrone basin
RCMs mean
RCMs maximum
RCMs minimum

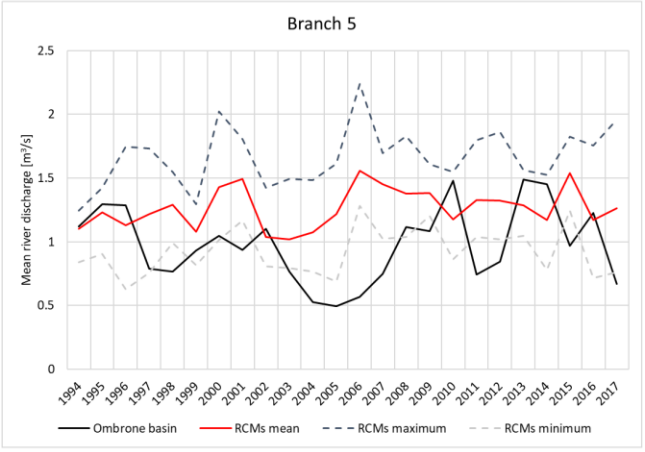
Branch 5
Mean river discharge [m³/s]
Ombrone basin
RCMs mean
RCMs maximum
RCMs minimum

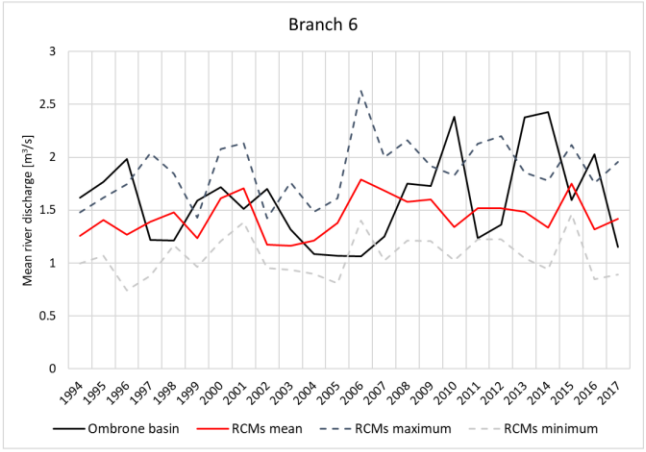
Branch 6
Mean river discharge [m³/s]
Ombrone basin
RCMs mean
RCMs maximum
RCMs minimum

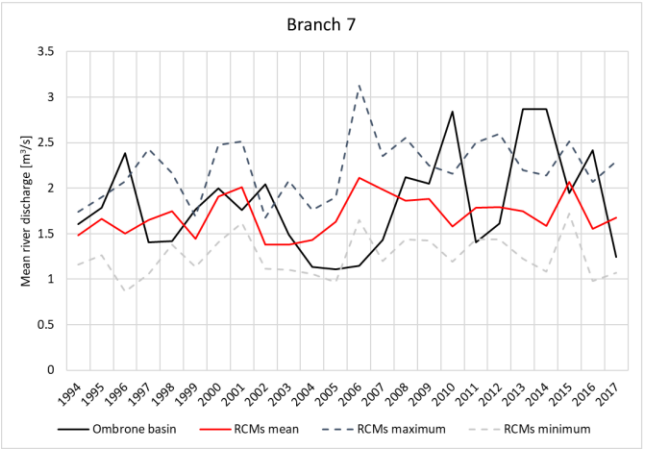
Branch 7
Mean river discharge [m³/s]
Ombrone basin
RCMs mean
RCMs maximum
RCMs minimum

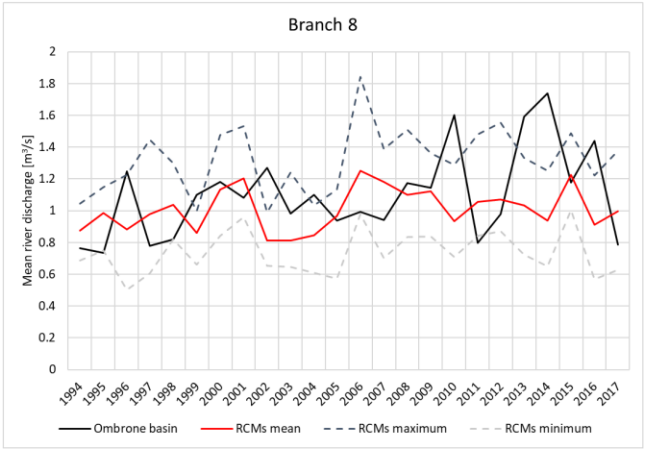
Branch 8
Mean river discharge [m³/s]
Ombrone basin
RCMs mean
RCMs maximum
RCMs minimum

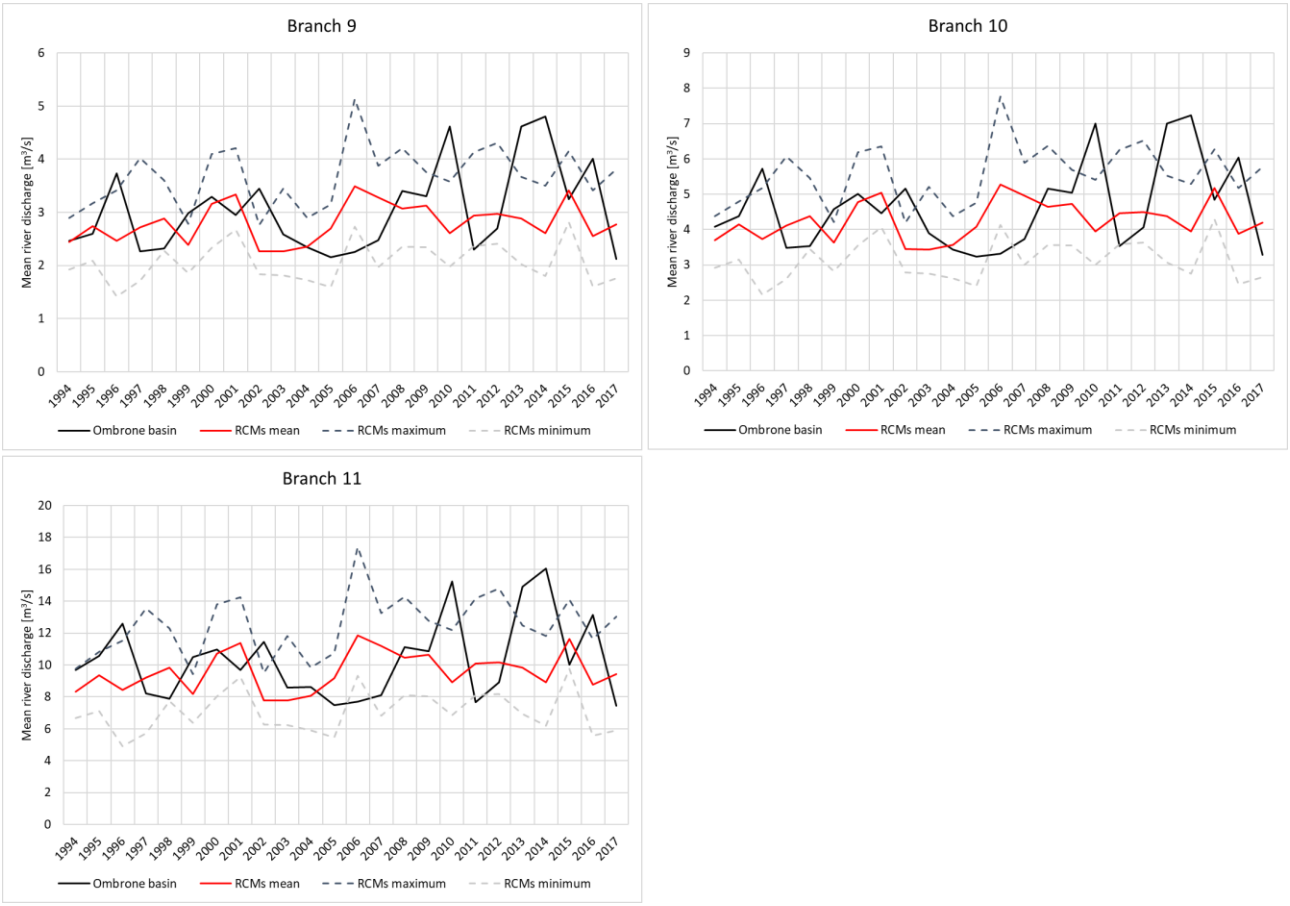

Figure 108 – Mean RCMs and original simulation discharge values for each branch of the river network.

For all river branches, simulated discharge obtained by the hydrologic modelling with RCMs corrected meteorological data is in good agreement with the original Ombrone model simulation, carried out by means of real observed data. Mean RCMs output are very close to the Ombrone model discharge for the simulated temporal domain, even if some differences still remain looking at each single yearly value. This is probably due to the correction method used to calibrate RCMs data, that is based on a constant correction factor given by the differences between GCMs/RCMs output and observation for each month in the whole historical reference period, leading to the loss of information about each single year variability.

Some discrepancies between RCMs and Ombrone model discharge can be observed for branches 1, 2 and 5, with RCMs mean discharge that underestimate the original simulation. However, such lower flow volume is recovered by the other river branches, with a very good agreement between RCMs and Ombrone model discharge observed in correspondence of branch 11 (the closing section of the basin), not compromising the total hydrologic water budget.

Since it was not possible to identify the RCM model that better approximate the original Ombrone simulation, for the subsidence forecasting analysis with MODFLOW, the mean RCMs discharge has been considered, in order to keep into account the uncertainty of each RCM and to obtain more reliable information about future hydrologic variability.

To evaluate the suitability of the RCMs *bias* correction procedure on all the hydrologic variables that directly affect the groundwater system, the mean monthly values of RCMs percolation through the aquifer in the 1994-2017 reference period is showed in Figure 109, together with the percolation values estimated by the original Ombrone model simulation.

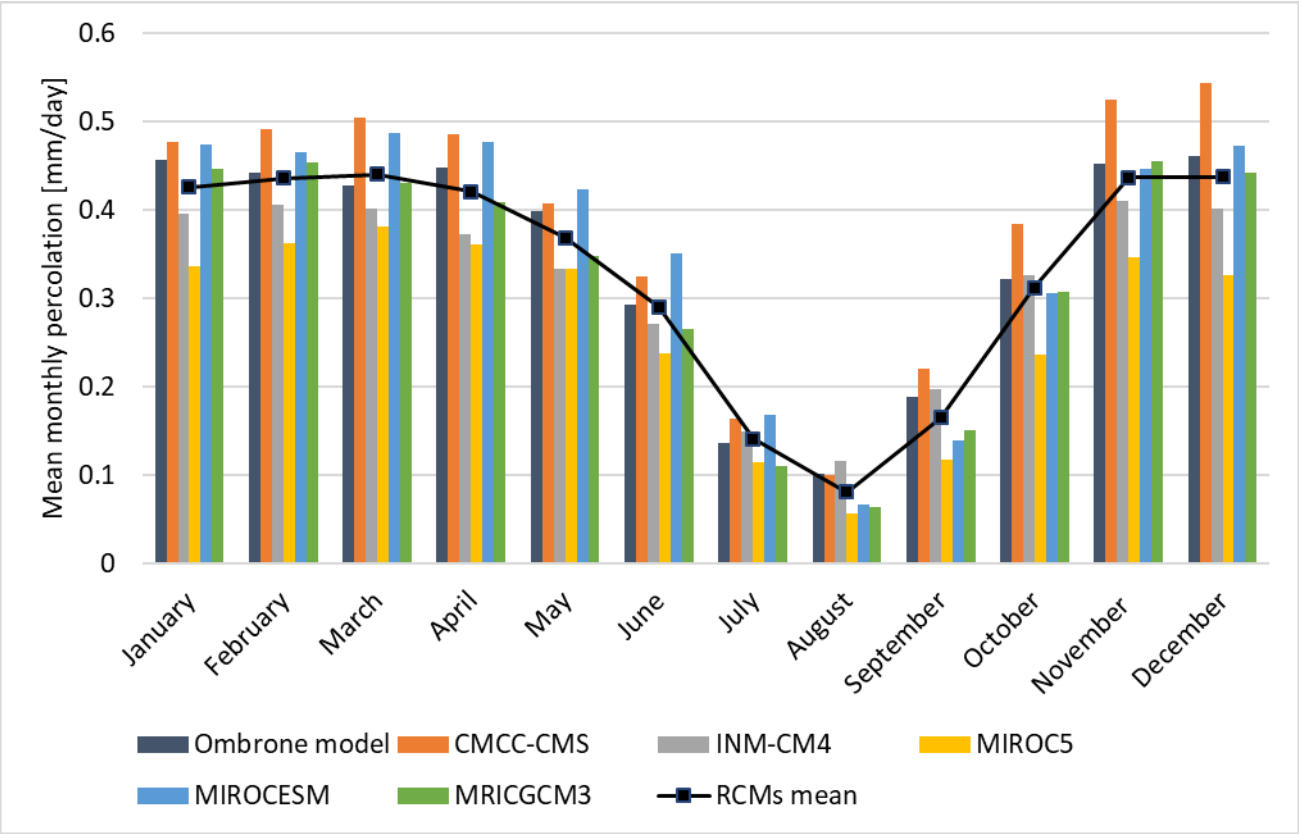

Figure 109 – Mean monthly percolation values in the Ombrone basin for the 1994-2017 period.

CMCC-CMS model overestimates Ombrone model percolation value on each month, while MIROC5 model always underestimates it. INM-CM4, MIROCESM and MRICGCM3 are characterized by a different behavior, with mean monthly values that oscillate around the original modelled percolation. However, all selected RCMs describe the seasonal trend with a very good approximation, following faithfully the Ombrone model percolation pattern.

Figure 110 describes the mean annual percolation trend on the Ombrone basin for the 1994-2017 period, as simulated by the selected RCMs, and its comparison with percolation values simulated by the Ombrone model. For each simulated year, the average, maximum and minimum modelled percolation of selected RCMs is displayed.

RCMs simulated percolation is in good agreement with the original simulation values obtained by Ombrone model, showing an average value for the analyzed period of 0.34 mm/day (0.345 mm/day for the Ombrone model). As for river discharge, nature of the Linear Scale bias correction method does not allow RCMs percolation to perfectly describe the Ombrone model percolation pattern, that is characterized by a higher variability during the 1994-2017 period.

Once again, it was not possible to identify the best RCM, among the selected, that better represent the original simulation and, in order to reduce their uncertainty, RCMs mean simulated percolation seemed to be the more suitable to describe the future infiltration pattern in Ombrone aquifer and to approximate the aquifer recharge value in the forecasting groundwater model.

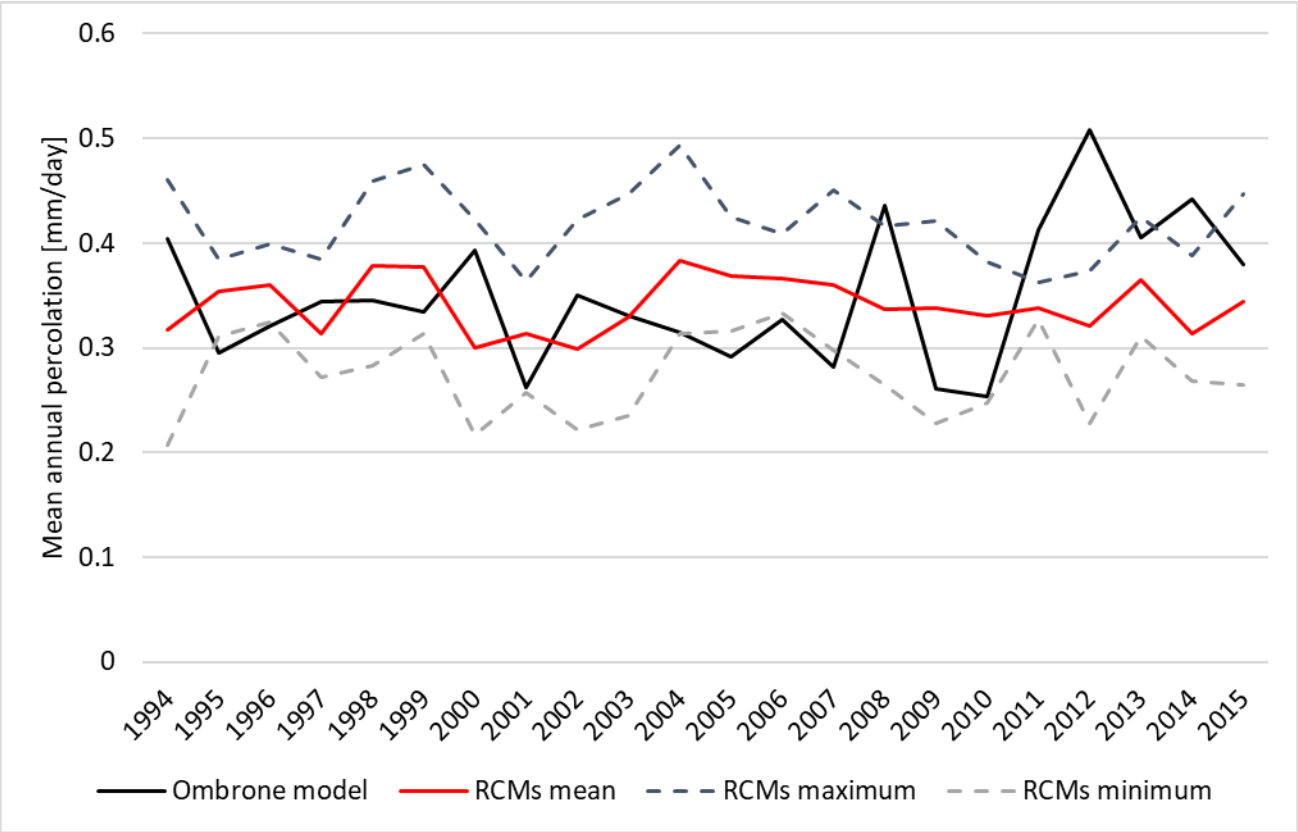

Figure 110 – Mean annual RCMs and Ombrone model percolation values.

8.3.8 Climate change impact on hydrology

The calibrated RCMs hydrological models were run for the future climate change scenarios, under RCP4.5, until the year 2050. In order to identify the potential variation of Ombrone basin hydrology in the future, river discharge, percolation and evapotranspiration parameters have been compared to a baseline period, defined as the average condition of the hydrologic system between 1994 to 2017. Figure 111 shows the percentage change of stream flow, as predicted by the different regional climate models, expressed as an average discharge in a quinquennial time frame from 2019 to 2050.

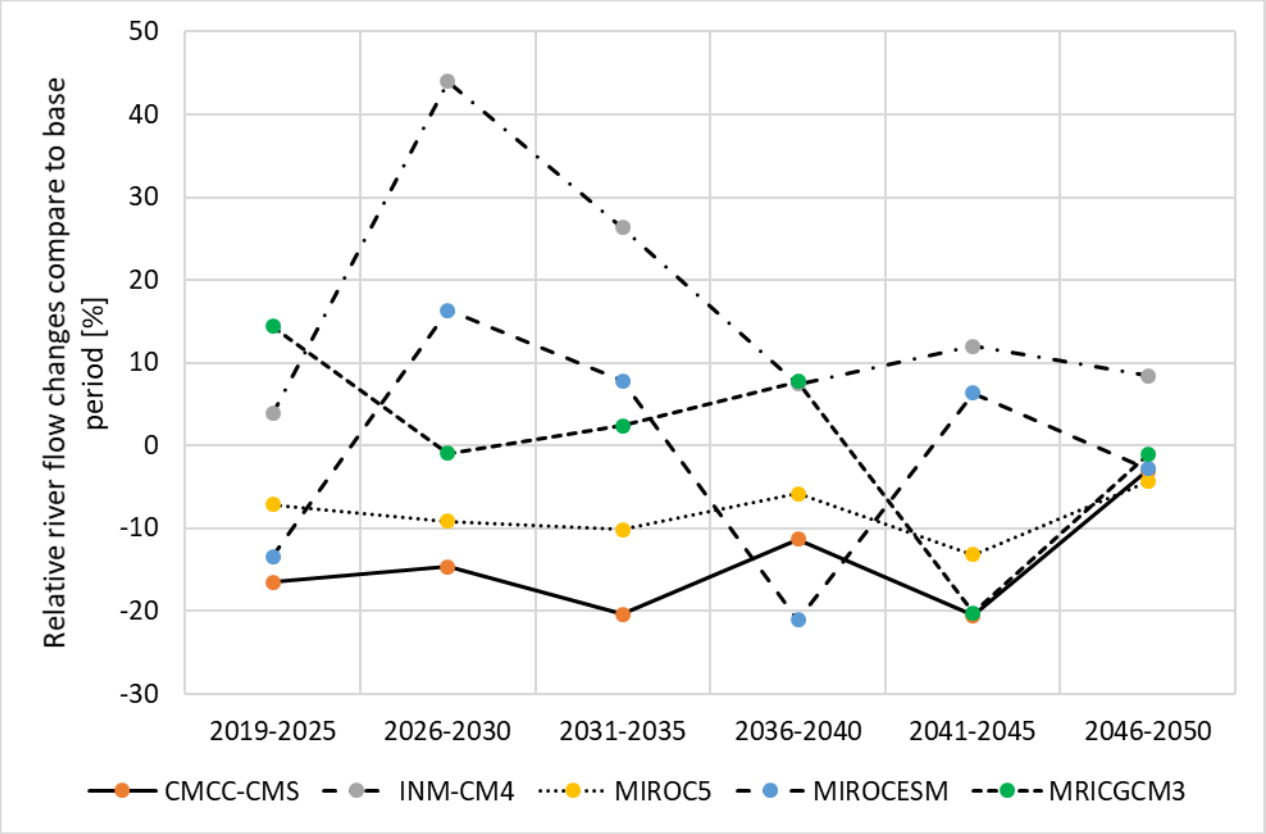

Figure 111 – Projected changes in discharge for Ombrone river under RCP4.5 scenario.

All climate models, except for INM-CM4, show a decrease in discharge for Ombrone river network under RCP 4.5 scenario at the end of 2050. Discharge is expected to increase of about 8.5% for INM-CM4 model, while an overall decrease of 1.09%, 2.8%, 4.3% and 3.03% are estimated by MRICGCM3, MIROCESM, MIROC5 and CMCC-CMS, respectively.

Changes in river discharge of such entity can be also identified in the original Ombrone model output and in measured discharge values at Poggio a Caiano and Pontelungo gauging stations for the 1992-2017 historic period, indicating variations that can be related to the range of the natural variability.

A maximum peak in river discharge is described by INM-CM4 (-44%) and MIROCESM (-16%) models for the 2026-2030 period, only partially decreased during the following 2031-2035 period. However, MIROC5, MIROCESM and MRICGCM3 models do not confirm this positive peak, showing a quite stable or slightly decreasing trend during the same period.

The percentage variation of percolation variable in Ombrone basin, simulated by selected RCMs under RCP 4.5 scenario for the period 2019-2050, is represented in Figure 112.

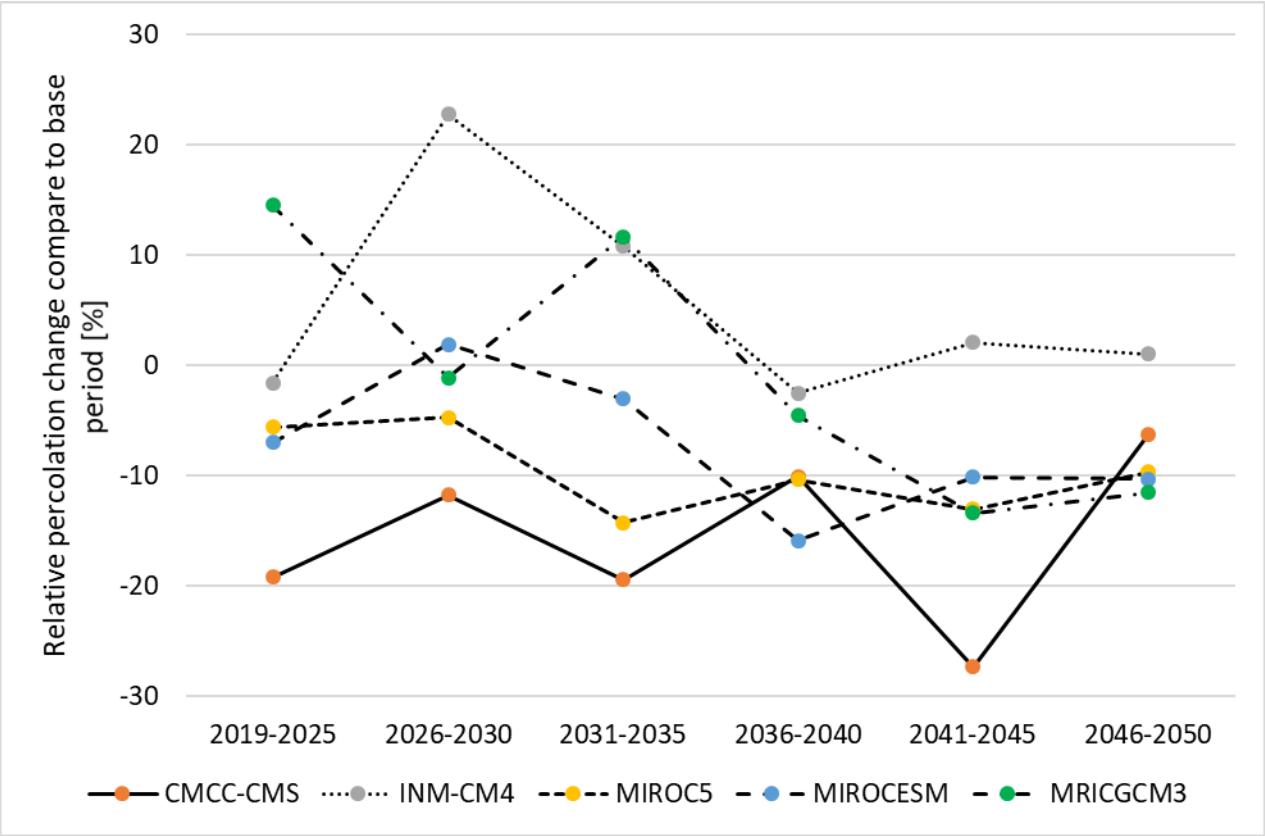

Figure 112 – Projected changes in percolation for Ombrone basin under RCP4.5 scenario.

Following MIROC5, MIROCESM and MRICGCM3 simulation, water percolation in Ombrone basin is expected to decrease of about 10% in 2050, while a lower decrease of about 6% has been estimated by CMCC-CMS model. A small percolation increment in the area has been estimated by INM-CM4 regional climate model (+1%), but such value can be ascribed to the field of natural variation.

Figure 113 displays the potential evapotranspiration pattern over Ombrone basin for he 2020-2050 period, as simulated by MOBIDIC hydrologic model for the different RCMs. As discussed before, evapotranspiration evidence a trend mainly driven by temperature. Since all RCMs forecast an increasing of temperature in future years, evapotranspiration is expected to increase as well, with an increment that ranges between +1% to +12%. MIROC5 model, according to INM-CM4 and MRICGCM3, estimates an overall increase in evapotranspiration of about 5% at the end of 2050, while MIROCESM simulates the maximum increment, with a total increase of about 12% in 2050. The lower increment (+1%) is estimated by CMCC-CMS model and fall in the range of natural variability.

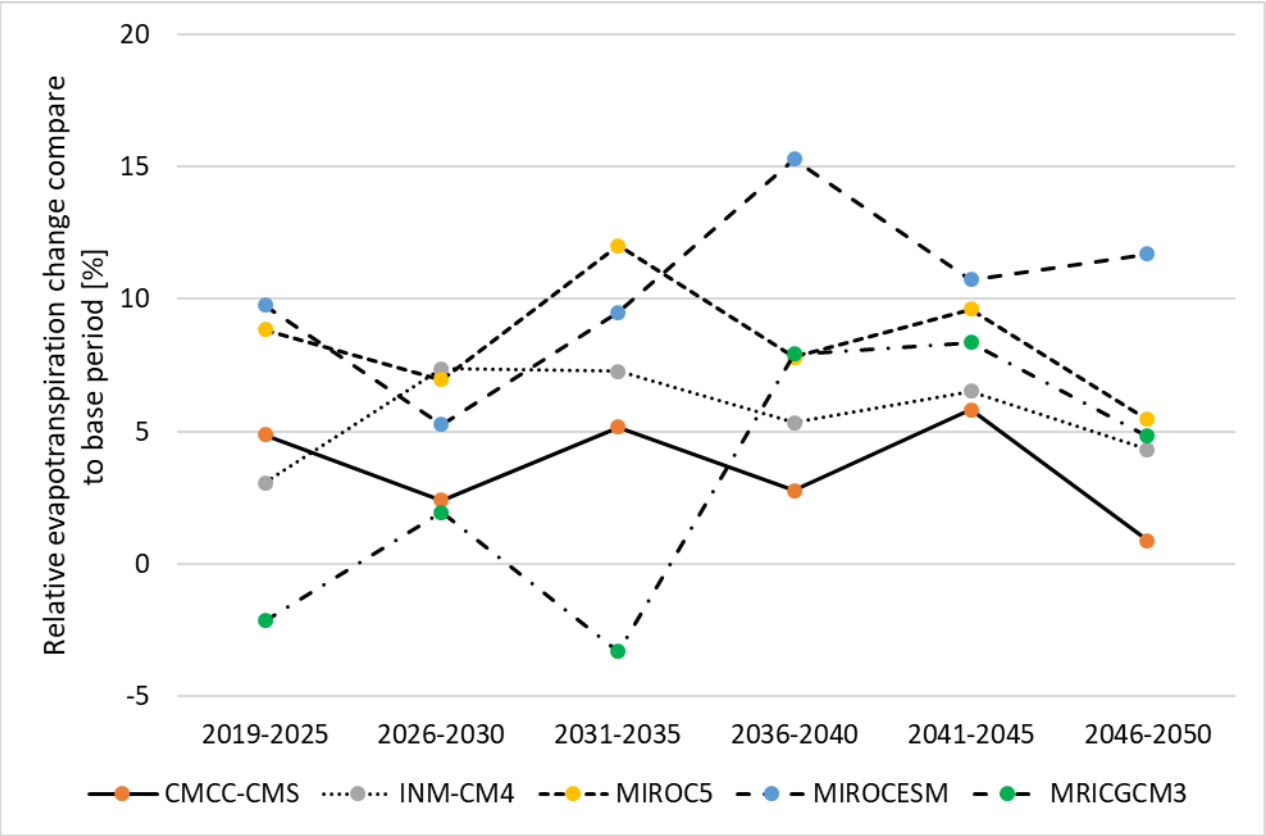

Figure 113 - Projected changes in evapotranspiration for Ombrone basin under RCP4.5 scenario.

8.4 Subsidence Forecasting

Climate change is becoming one of the main one of the main issue that is affecting the entire planet in last decades, since it affects all anthropic and natural systems on the Earth, included hydrological and hydrogeological variables like river discharge, seasonal and local water availability, and groundwater states.

In this situation of rapid evolving climate, one of the consequences caused by potential changes that could occur in groundwater systems in the future, is the variation of aquifers response to external stresses, like groundwater exploitation. This, especially in areas susceptible to sediments compaction, can lead to the development of land subsidence or to the modification of existing ground displacement patterns.

In Ombrone basin, subsidence is a well-known phenomenon since the early 1990's, with ground displacement that affected the area until present and that probably will continue to occur in Pistoia surroundings in the years to come. Here, the characterization of the potential subsidence pattern and ground displacement rate has a primary importance, in order to assess the hazard that can affect buildings and human activities in the most anthropized parts of the basin.

Integrating results obtained from the analysis of the hydrological modelling, carried out by means of Regional Climate Models meteorological data until 2050, with the calibrated MODFLOW subsidence model of the Pistoia aquifer, it was possible to identify the potential evolution of land subsidence affecting Pistoia area, in order to characterize the risk associated with the phenomenon.

Using mean RCMs hydrological simulations output, a 58 stress periods groundwater model has been set up, including a 25 years historical period (1992-2017) for model validation and a 33 years ahead forecast (2019-2050). The groundwater simulations are based on the calibrated MODFLOW model of Pistoia aquifer, using the proposed integrated procedure to link RCMs estimated river discharge and percolation with MODFLOW boundary conditions (involving RIV, WEL and RCH packages). Three different pumping scenarios have been investigated:

- considering the current pumping rates and water dynamics;

- considering an average increase in pumping rate of +1%/year, starting from 2020 (+10% at the end of 2030, +20% at the end of 2040 and +30% at the end of 2050);

- considering an average decrease in pumping rate of -1%/year, starting from 2020 (-10% at the end of 2030, -20% at the end of 2040 and -30% at the end of 2050).

In order to evaluate the goodness of the groundwater simulation developed with RCMs boundary conditions, a comparison between the modelled ground displacement rate and the Sentinel-1 PS-InSAR data has been carried out, considering the average land surface lowering velocity identified during the 2015 – 2017 period (Figure 114). The RCMs groundwater model reproduces the general shape of the subsidence bowls with quite good accuracy, both in Pistoia historical center and in plant nursery area. Here, the model slightly underestimates the observations value, identifying a maximum ground displacement rate of about 15.5 mm/year (against 20 mm/year of PS data) and interesting a smaller area. The third subsidence bowl identified by the PS-InSAR analysis and located 1km South of the San Jacopo hospital, in correspondence of the main pumping center of the region, is well described by the RCMs groundwater model in terms of magnitude, but its maximum peak is located about 1.5 km North-West of its real position. Major discrepancies are encountered East of the plant nursery area, where the RCMs model identify no subsidence occurring in the 2015-2017 period (lower than 2.5 mm/year), while up to 15.5 mm/year ground displacement rate has been monitored by Sentinel-1 sensors.

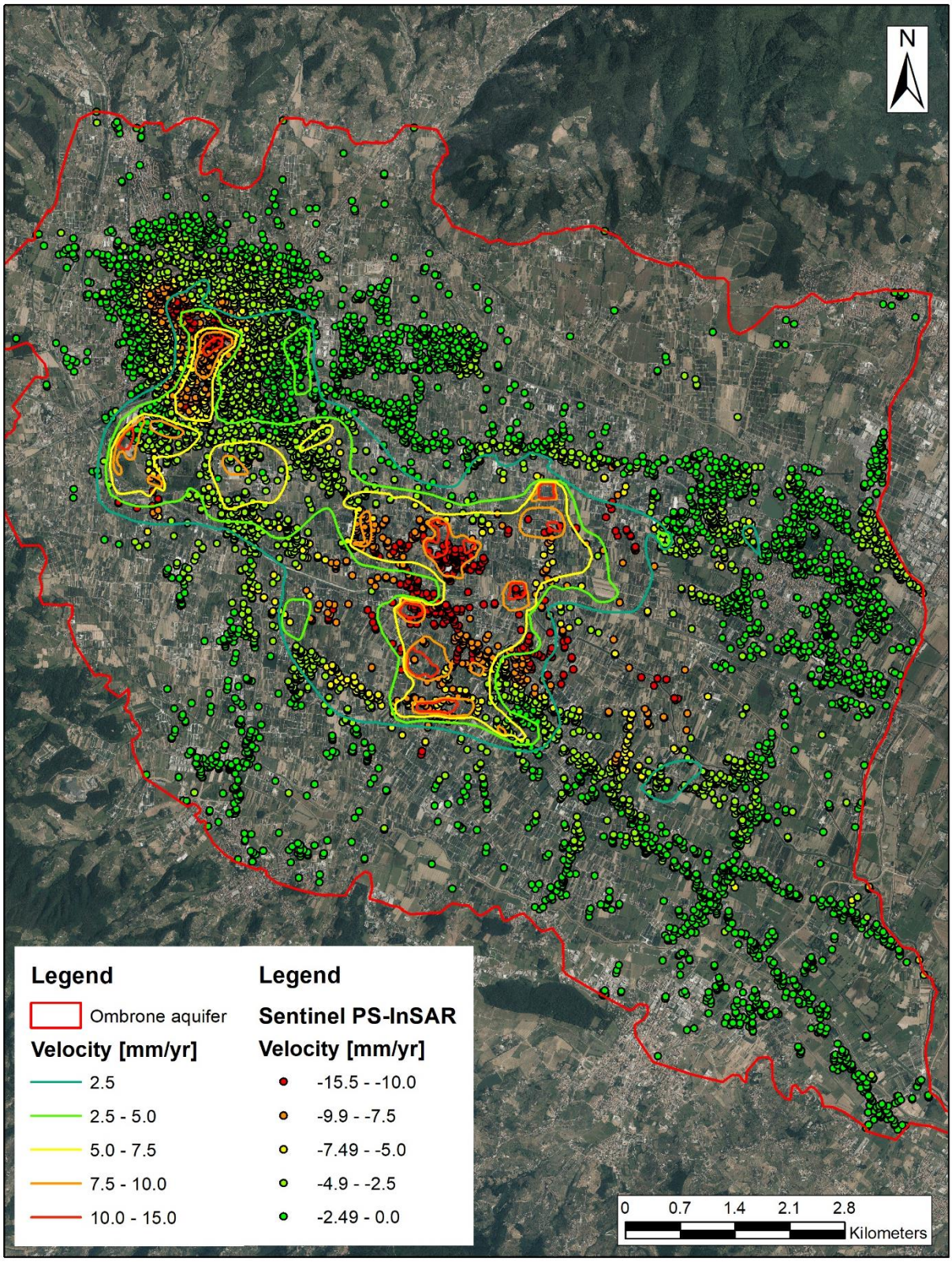

Figure 114 – Pistoia aquifer ground displacement velocity comparison between Sentinel-1 PS-InSAR data (points features) and RCMs groundwater model estimation (isolines) for the 2015-2017 period.

Figure 116 displays time series of modelled ground displacement for historical center and plant nursery area modelled by the calibrated ground water model ("Original model") and by the RCMs groundwater model ("RCMs model") for the 2003-2017 period, together with the PS-InSAR data available in the same period.

In order to analytically evaluate the forecasting model reliability, a direct comparison between Sentinel-1 PS-InSAR and simulated ground displacement velocity is presented in Figure 115. The two datasets show an acceptable degree of correlation, certified by a coefficient of determination R^2 value of 0.5747. Observed discrepancies between model output and observation are quite limited, considering that PS-InSAR measurement are data referred to a single point in the space, while model values are based on a discretization grid of 50mx50m of resolution, with one ground displacement value assigned in correspondence of each cell of the model.

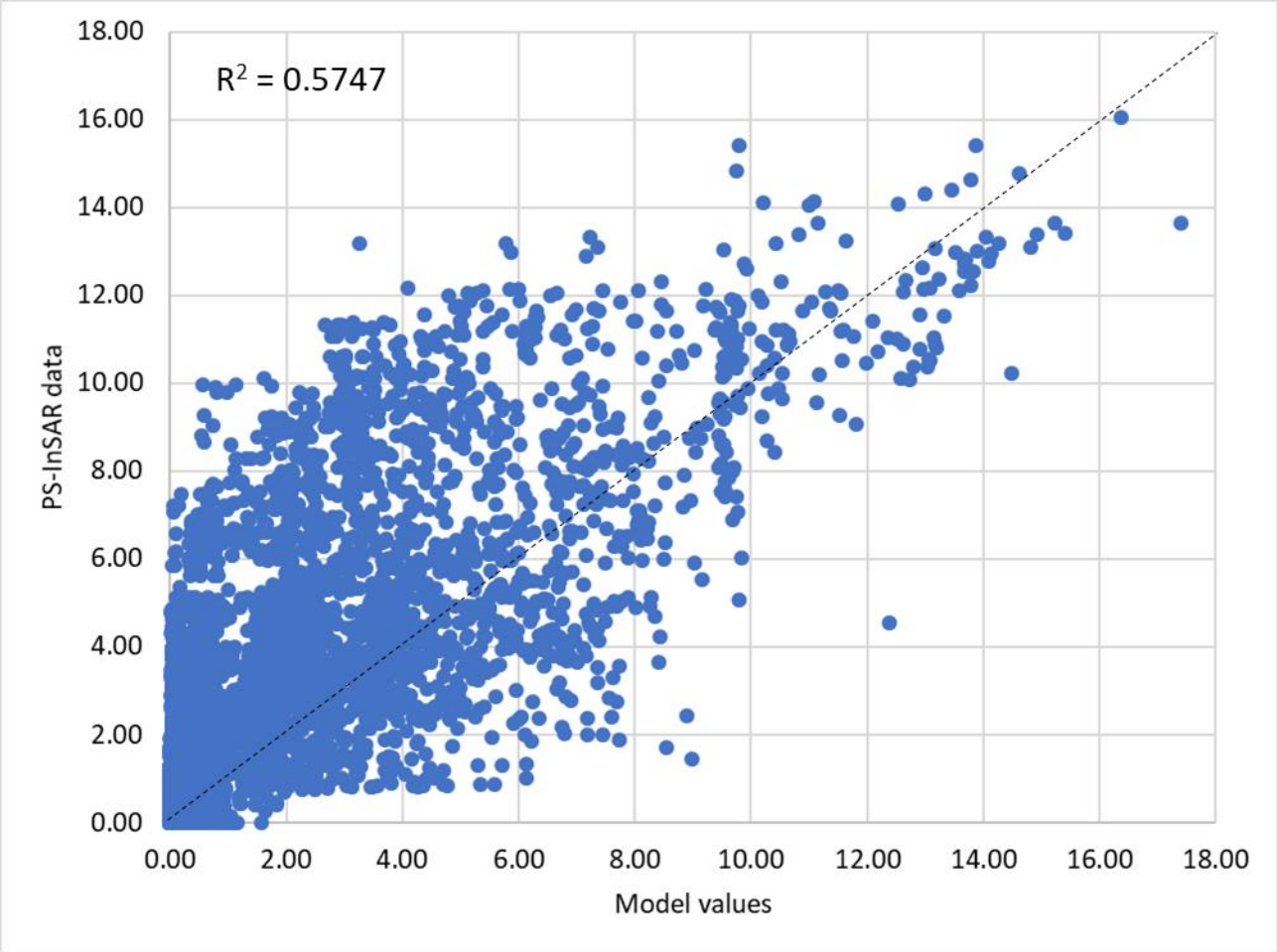

Figure 115 – Comparison between PS-InSAR data and forecasting model ground displacement rate for the 2015-2017 period.

Figure 116 displays time series of modelled ground displacement for historical center and plant nursery area modelled by the calibrated ground water model ("Original model") and by the RCMs groundwater model ("RCMs model") for the 2003-2017 period, together with the PS-InSAR data available in the same period.

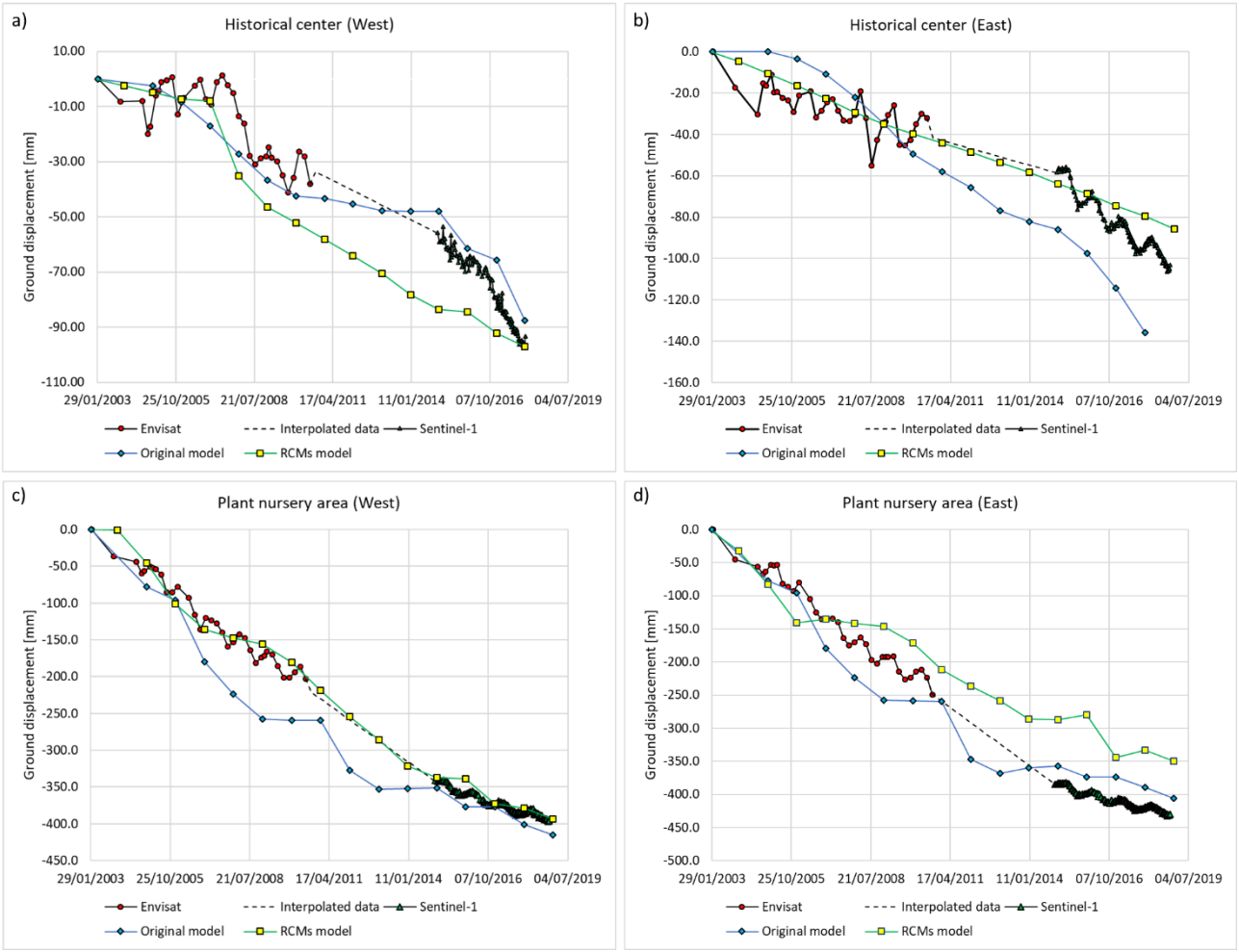

Figure 116 – Time series of ground displacement in Pistoia area as measured by PS-InSAR data and modelled by the calibrated groundwater model and by RCMs forecast model for the 2003-2018 period.

The RCMs model time series are in good agreement with observations, resulting able to describe the total amount of subsidence observed at the end of 2003-2017 period with a satisfying degree of approximation in all considered zones. A perfect match between modelled subsidence and InSAR data has been achieved for the West side of the plant nursery area, with RCMs groundwater model describing in a very good way the monitored ground displacement of both ENVISAT and Sentinel-1 constellations (Figure 116c). Differences of 17% and 18% are observed for the East side of historical center and plant nursery area respectively, with RCMs model that underestimates observed subsidence in both cases (Figure 116b and d). Part of such mismatches can be due to the constant trend of deformation used to connect ERS/ENVISAT and Sentinel-1 time series between July 2010 and December 2015, when no satellite data were available. Concerning the West part of the historical center, RCMs ground displacement pattern does not accurately match the observations, showing a rapid increase between 2006 and 2007 that is delayed of about one year in satellite data (Figure 116a). However, at the end of the analyzed period, the total amount of estimated subsidence perfectly matches the cumulated measured ground displacement.

The analysis of the potential ground displacement velocity that could affect Pistoia aquifer in the future has been performed in a decennial time frame, considering the average subsidence rate of the 2020-2030 (Figure 117), 2031-2040 (Figure 118) and 2041-2050 periods (Figure 119).

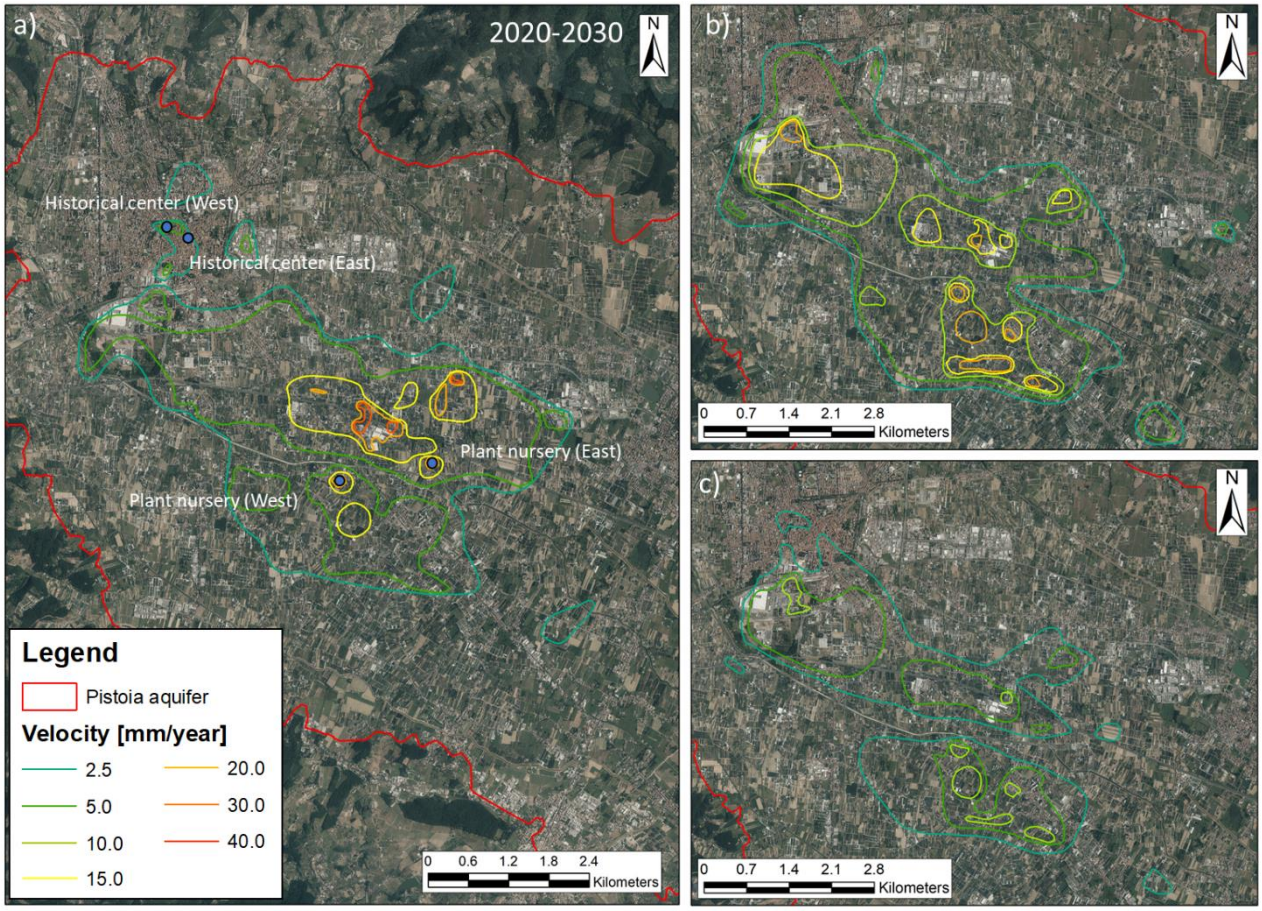

Figure 117 – Potential subsidence rate of Pistoia area in 2020-2030 period, as calculated by the developed groundwater model, considering a) The present pumping rate, b) An increase in pumping rate of 1%/year and c) A decrease in pumping rate of 1%/year. Blue points represent the location of ground displacement time series used for the different subsidence pattern comparison.

In the 2020-2030 period, assuming the current water extraction rate from the aquifer, the evolution of subsidence phenomena in Pistoia area show different trends, depending on the location within the basin (Figure 117a). In Pistoia historical center, ground surface is characterized by an average displacement velocity of 5-10 mm/year, exhibiting a decrease from current subsidence rate (15-20 mm/year at the end of 2017). Plant nursery area keep showing an average subsidence rate of about 15 mm/year, with limited peaks of 20-30 mm/year, in accordance with current displacement velocities.

Considering an increase of +1%/year in pumping rate, starting from January 2020 (for an overall +10% at the end of 2030), model results indicate that current subsidence bowls in Pistoia city and its surroundings will expand, and the land surface in these areas will subside more rapidly, especially in correspondence of the inhabited area (Figure 117b).

Figure 117c displays results of groundwater modelling assuming a decrease in extraction patterns (-1%/year). Model output show a reduction in subsidence spreading and intensity all over the study area, with ground displacement velocities that remain below 5 mm/year in most part of the region and only few zones characterized by up to 10 mm/year.

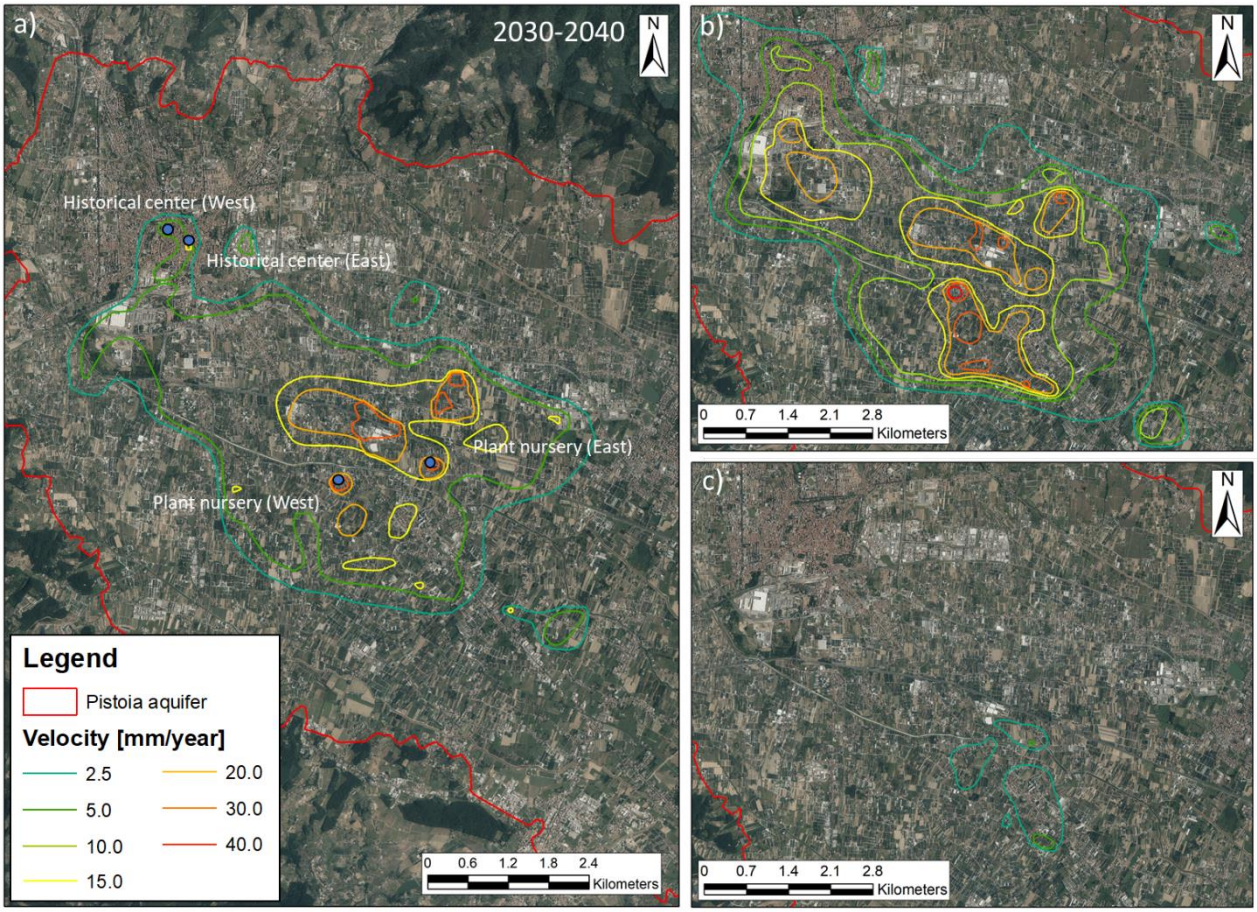

Figure 118 - Potential subsidence rate of Pistoia area in 2030-2040 period, as calculated by the developed groundwater model, considering a) The present pumping rate, b) An increase in pumping rate of 1%/year and c) A decrease in pumping rate of 1%/year. Blue points represent the location of ground displacement time series used for the different subsidence pattern comparison.

Forecasts for 2030-2040 indicate a slight increase in subsidence rate, especially in plant nursery area, where ground displacement is characterized by average values of 15-20 mm/year, with peaks of 30 mm/year. Similar velocities were already detected in the area by ERS and ENVISAT sensors in 1992-2000 and 2003-2010 periods (Figure 118a). Pistoia historical center keeps showing the same subsidence rate of the previous 2020-2030 decade.

In the pumping increasing scenario (Figure 118b), subsidence bowls keep expanding in all directions, involving the North – Western part of Pistoia city and the South-Eastern part of plant nursery area. Land surface keeps subside rapidly, with higher velocity than the previous decade. Plant nursery area show an average displacement velocity of 15-20 mm/year, reaching 20-30 mm/year in some parts of it and a maximum peak of about 40 mm/year in its center while, in Pistoia downtown, subsidence rate of more than 10 mm/year are expected.

The decreasing scenario displayed in Figure 118c, characterized by a -20% in pumping rate at the end of 2040, indicates a total absence (lower than 2.5 mm/year) of ground displacement related to groundwater exploitation for the entire basin. Small subsidence bowls are still visible in the central part of plant nursery area, limited in terms of spreading and intensity.

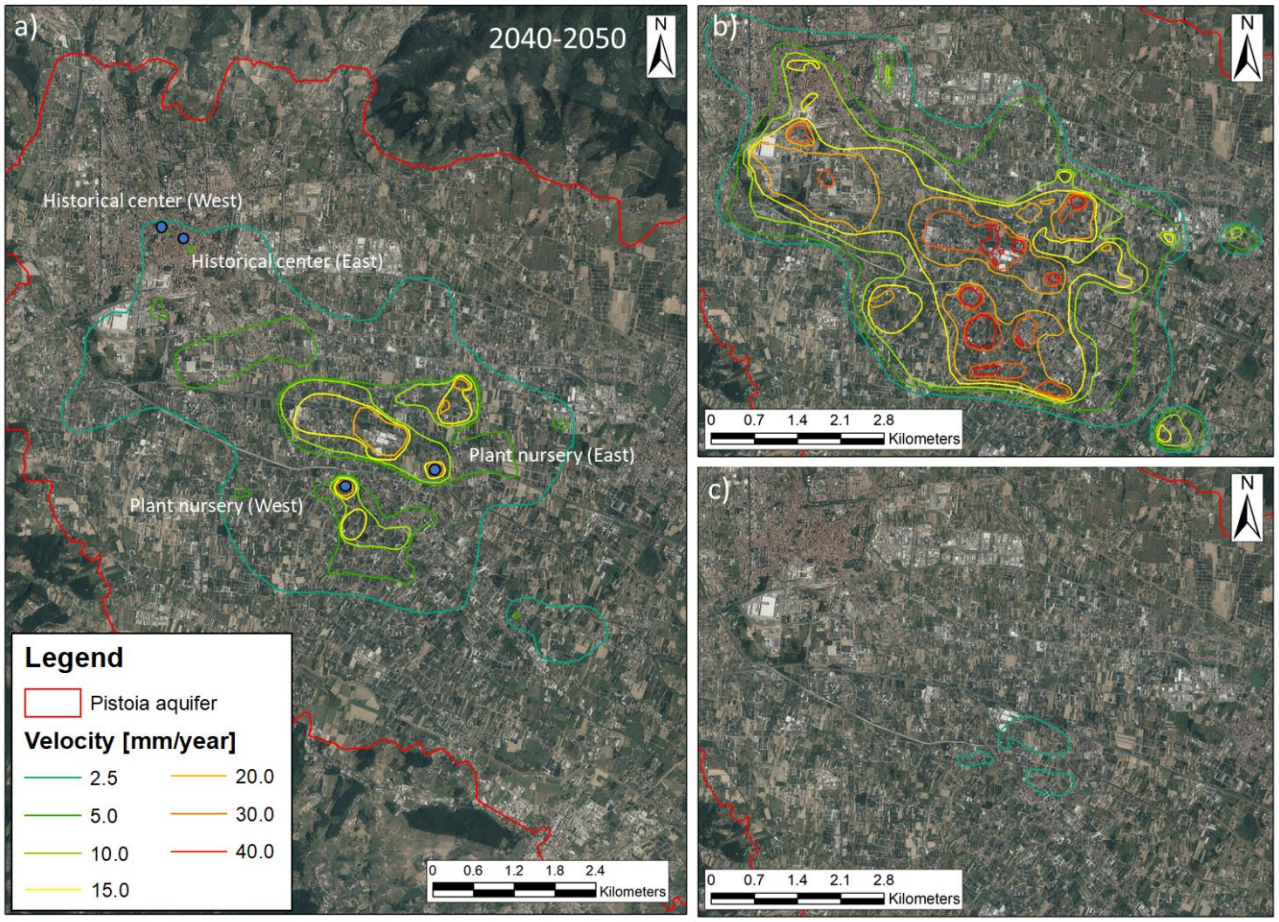

Figure 119 - Potential subsidence rate of Pistoia area in 2040-2050 period, as calculated by the developed groundwater model, considering a) The present pumping rate, b) An increase in pumping rate of 1%/year and c) A decrease in pumping rate of 1%/year. Blue points represent the location of ground displacement time series used for the different subsidence pattern comparison.

Considering constant pumping rates, subsidence in 2040-2050 period is rapidly slowing down all over the basin, especially in terms of magnitude. In Pistoia city, ground displacement rate reaches very low values, ranging between 2.5 to 5 mm/year. An important subsidence rate is still affecting the plant nursery area, but of lower intensity than the previous period, characterized by average velocities of about 10-15 mm/year and spatially limited peaks of up to 20 mm/year (Figure 119a).

Figure 119b displays results of subsidence modelling considering an increase in pumping rate that reached, at the end of 2050, a +30% with respect of current values. All the investigated area is subsiding rapidly, assuming very high velocities in both historical center (ranging between 20 and 30 mm/year) and plant nursery area (30-40 mm/year). Except for a small area North – East of Pistoia city, the area affected by subsidence phenomena remains constant, if compared to the previous decade.

Compared to the 2030-2040 decade, a further decreasing in water extraction rate (-30% in 2050) does not strongly affect the residual subsidence pattern still occurring in plant nursery area (Figure 119c). Here, subsidence bowls are very limited and characterized by velocity values of about 2.5 mm/year, according to the subsidence trend identified in the previous period.

Figure 120 displays time series of forecasted ground displacement in Pistoia area under the three simulated pumping scenarios for the 2020-2050 period, together with the subsidence pattern identified between 2003 and 2018.

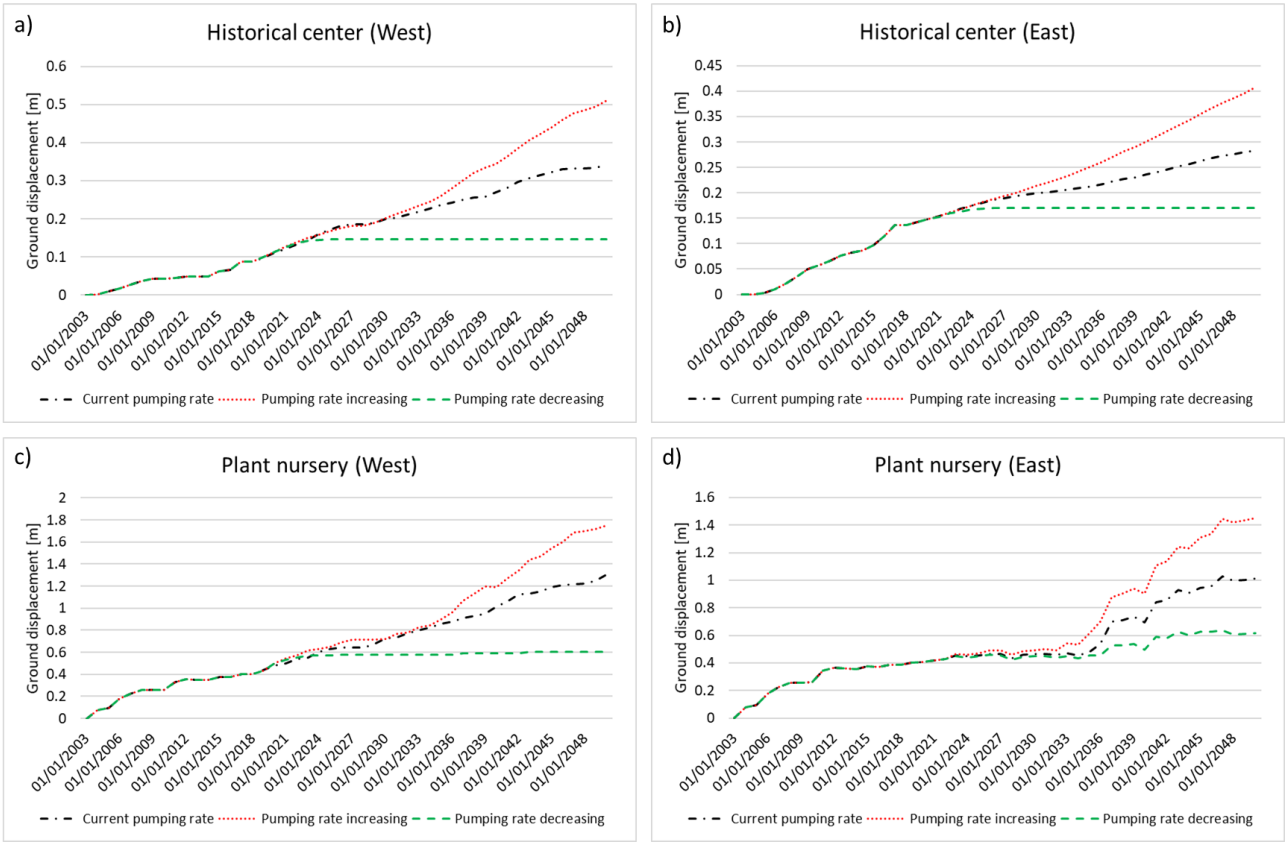

Figure 120 – Time series of potential ground displacement for Pistoia city and plant nursery area, considering different pumping rate patterns.

Ground displacement patterns show similar subsiding trend in correspondence of all the investigated locations. Following the expectations, the maximum subsidence values are forecasted by the increasing pumping rate scenario, while the lower values are obtained decreasing the water extraction rate. Extending the current pumping rate to the future, subsidence patterns are influenced only by variations in aquifer recharge, driven by expected changes of future climate. Climate variation effects does not show a strong influence on subsidence control, with ground displacement rate that remains quite stable during the 2020-2050 period, following the previous 2003-2018 trend in all parts of Pistoia area. Only in the East side of plant nursery zone (Figure 120d), an increasing of subsidence rate is observed, starting from 2035 and characterized by an average velocity of about 35 mm/year.

In MODFLOW SUB package, skeletal specific storage values, S_{ske} and S_{skv}, are stress-dependent (equations 19 and 20. As head declines and effective stress increases, these values should become smaller. As a direct consequence, calculated compaction and storage change are smaller for equivalent changes in effective stress. Unfortunately, SUB package does not consider reductions in skeletal specific storage for subsequent stress periods and projections of future subsidence might be overestimated.

However, the analysis confirms the role of groundwater pumping on driving subsidence patterns in Pistoia area, showing a higher influence than changing climate effects on controlling ground displacement rate. Subsidence risk mitigation actions should include a correct management of the groundwater resource and the development of new environmental policies. Increasing human activities linked with groundwater withdrawal could lead to severe groundwater stress if it continues uncontrolled.

8.5 Fragility curves and vulnerability maps

In literature, procedures to quantitatively evaluate the risk associated with subsidence phenomena are still not well established and they are far from being commonly used by the scientific and technical community. A better understanding on the type and extent of damage to buildings and infrastructures produced by subsidence is essential to reduce the high uncertainty associated with instability phenomena modelling. The probabilistic treatment of these uncertainties may be achieved through the use of fragility (or vulnerability) curves.

A fragility curve is a statistical tool representing the probability of reaching or exceeding a given damage state severity level (Di) as a function of an engineering demand parameter, which usually defines the ground displacement rate (Mohamed, 2018).

In this work, fragility curves are empirically built combining InSAR data and field data to evaluate the potential damage on buildings affected by land subsidence. The main advantage of this method is that represents a realistic image of the real vulnerability of buildings (Billah and Alam, 2014) since they are based on actual recorded damage and measured ground displacement.

Once the fragility curves have been calibrated using empirical data, they provide the probability of occurrence of some level of damage for certain building displacement. Consequently, since InSAR data cover the whole city of Pistoia and provides information about the vertical displacement of all buildings, assuming a homogeneous structural typology, the probability of damage (i.e. the vulnerability) within the whole city of Pistoia can be calculated. Vulnerability curves can be very useful to evaluate the extent of the city in which damage caused by land subsidence are expected.

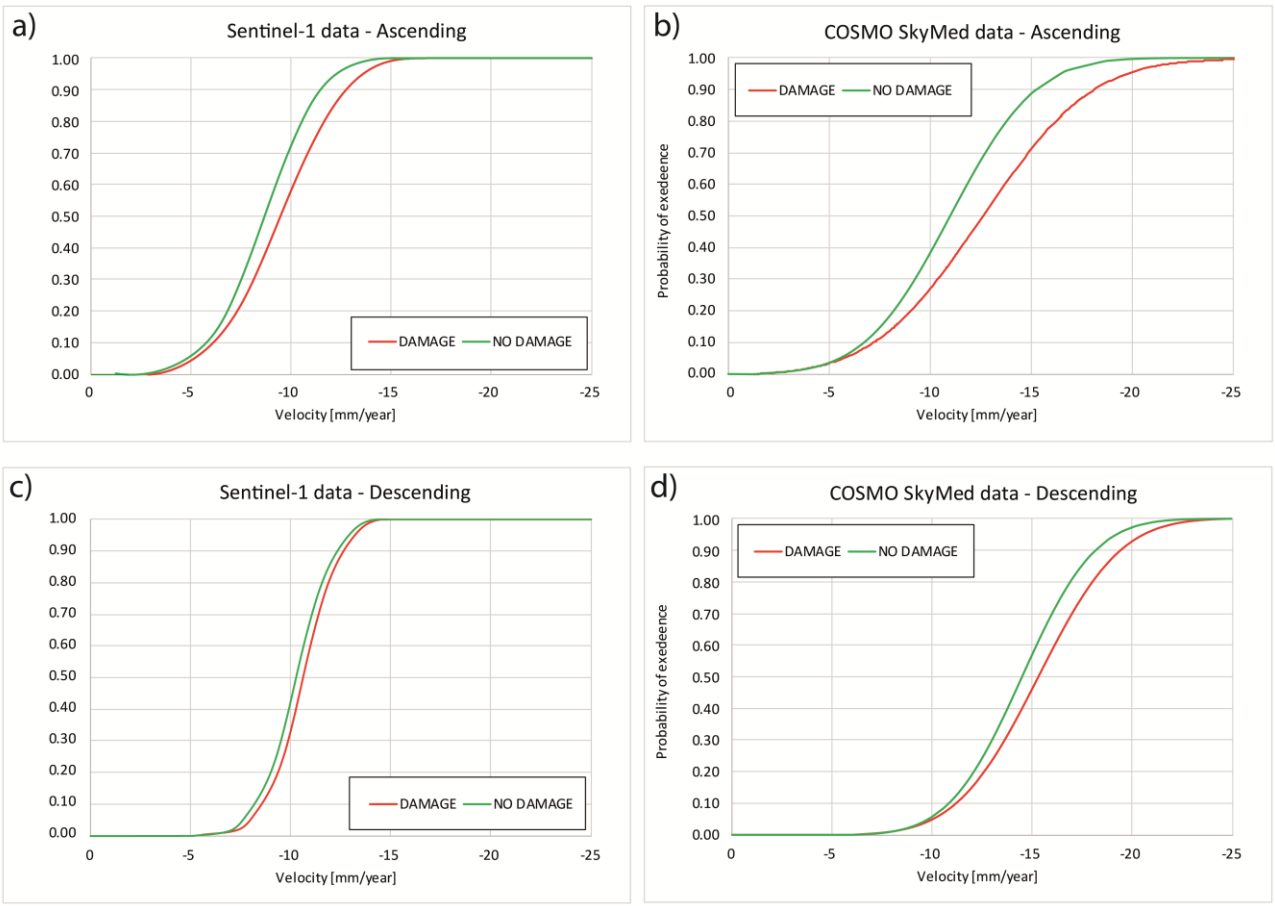

Figure 121 – Fragility curves of inspected buildings for a) Sentinel-1 ascending, b) COSMO SkyMed Ascending, c) Sentinel-1 descending and d) COSMO SkyMed Descending.

In order to assess the level of damage that affect buildings in Pistoia city because of subsidence phenomena, two damage detection field campaigns were carried out. Field surveys resulted in the sampling of 227 buildings (39 in the first campaign and 188 in the second one). Inspection methodology and low damage level detected led to classify the buildings as damaged or non-damaged. 47% of the buildings didn't show any level of damage meanwhile 53% of them presented different type of cracks and damages that could be ascribed to subsidence effects.

By means of the four available datasets (Sentinel-1 and COSMO SkyMed satellites with ascending and descending orbits) and damage information, eight fragility curves have been calculated (Figure 121). All curves were constructed in agreement to the PS-InSAR detected ground displacement, ranging between 2.5 and 25 mm/year. Observing the difference between damage and no damage curves, higher variability is detected by ascending geometry for both sensors, establishing it as the most sensible to the spatial distribution of displacements and damages. Taking into account the amplitude of the displacement range, CSK ascending curve cover the maximum range, resulting the most sensible to subsidence magnitude changes (Figure 121b).

8.5.1 Vulnerability maps

Damage fragility curves were used to classify the PS-InSAR observed velocities into five probability classes, using their cumulated distribution (0-20%, 20-40%, 40-60%, 60-80% and 80-100%). InSAR displacement rates were interpolated into a refined 5 m grid using Inverse Distance Weighting interpolation technique and reclassified using the previously calculated classes to generate the vulnerability maps (Figure 122).

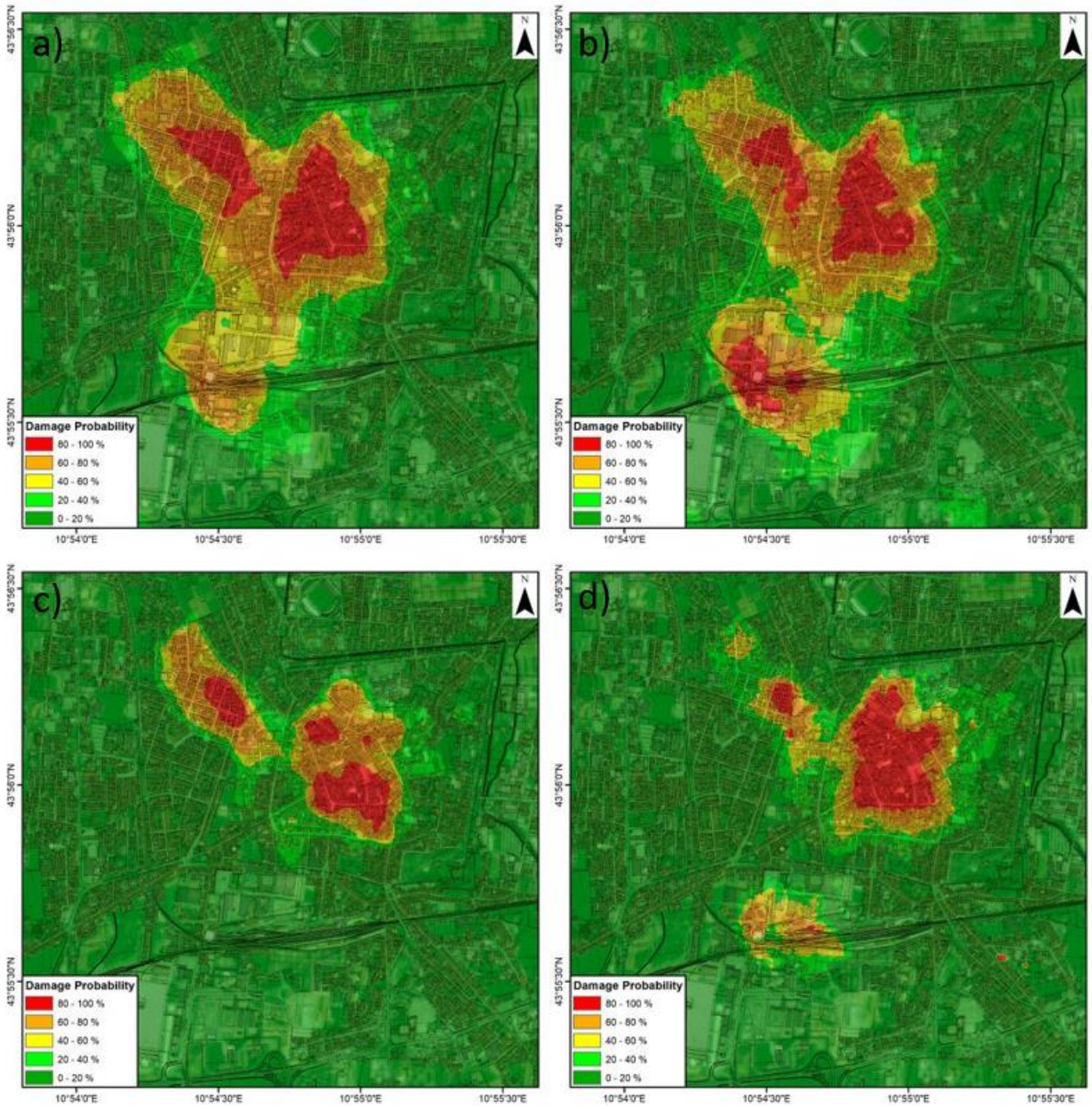

Figure 122 – Damage probability distribution calculated using the developed fragility curves for a) Sentinel-1 ascending, b) COSMO SkyMed Ascending, c) Sentinel-1 descending and d) COSMO SkyMed Descending.

Vulnerability maps of Sentinel-1 and COSMO-SkyMed constellation are very similar to each other, while major differences are observed between ascending and descending acquisition geometries. Worse distribution of data in descending datasets reflect the steep shape of their fragility curves, that generate fast changes from low to high probability. Lower inclination of CSK ascending fragility curves resulted in a smoother vulnerability map that better covered all the displacement velocities range. This solution is also the

most conservative result because identifies the largest vulnerable area (1 km^2 above 40% of damage probability).

Using the cadastral information of Pistoia city, the probability of each building to suffer damage due to the relative detected subsidence has been calculated. Mean ground displacement velocity of each cadastral plot was identified, and probability of damage calculated (Figure 123). 5% of the buildings are in the 80-100% damage probability class while 15% has 0% probability of damage and 81% below the 40% of probability.

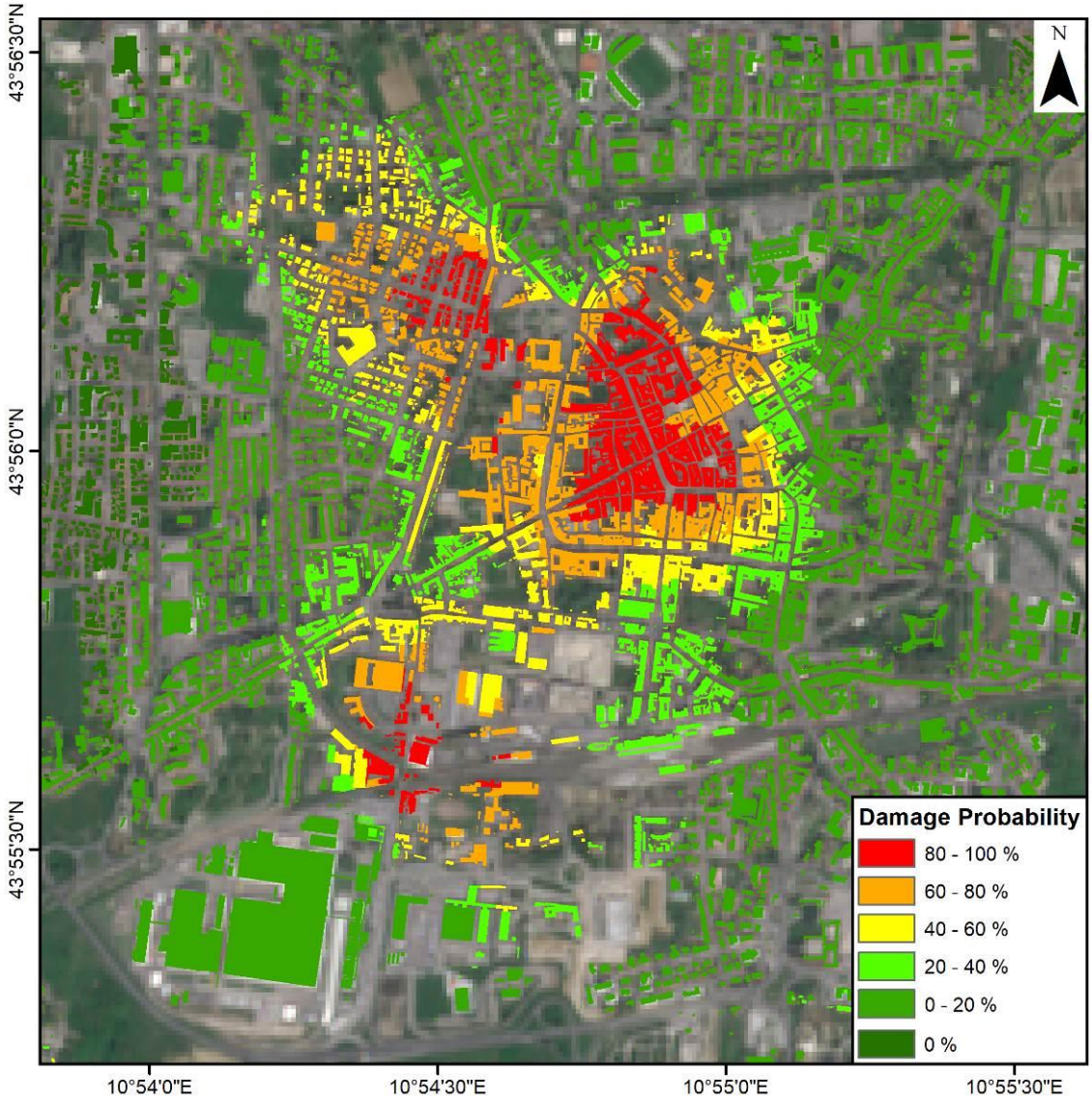

Figure 123 – Damage probability distribution of each cadastral plot.

Anomalous subsidence detected in Pistoia city began only in 2015 and, for some old buildings, type of foundations and other structural characteristics can have a major influence on damage occurrence than cumulated ground displacement. However, vulnerability maps may represent a valuable tool for urban planners to identify the areas most susceptible to subsidence and to reduce the risk associated with it.

8.5.2 Forecasted vulnerability maps

Forecasted ground displacement rate for 2020-2030, 2030-2040 and 2040-2050 decades were used, together with the developed fragility curves, to define the potential damage probability distribution in Pistoia historical center in the years to come (Figure 124).

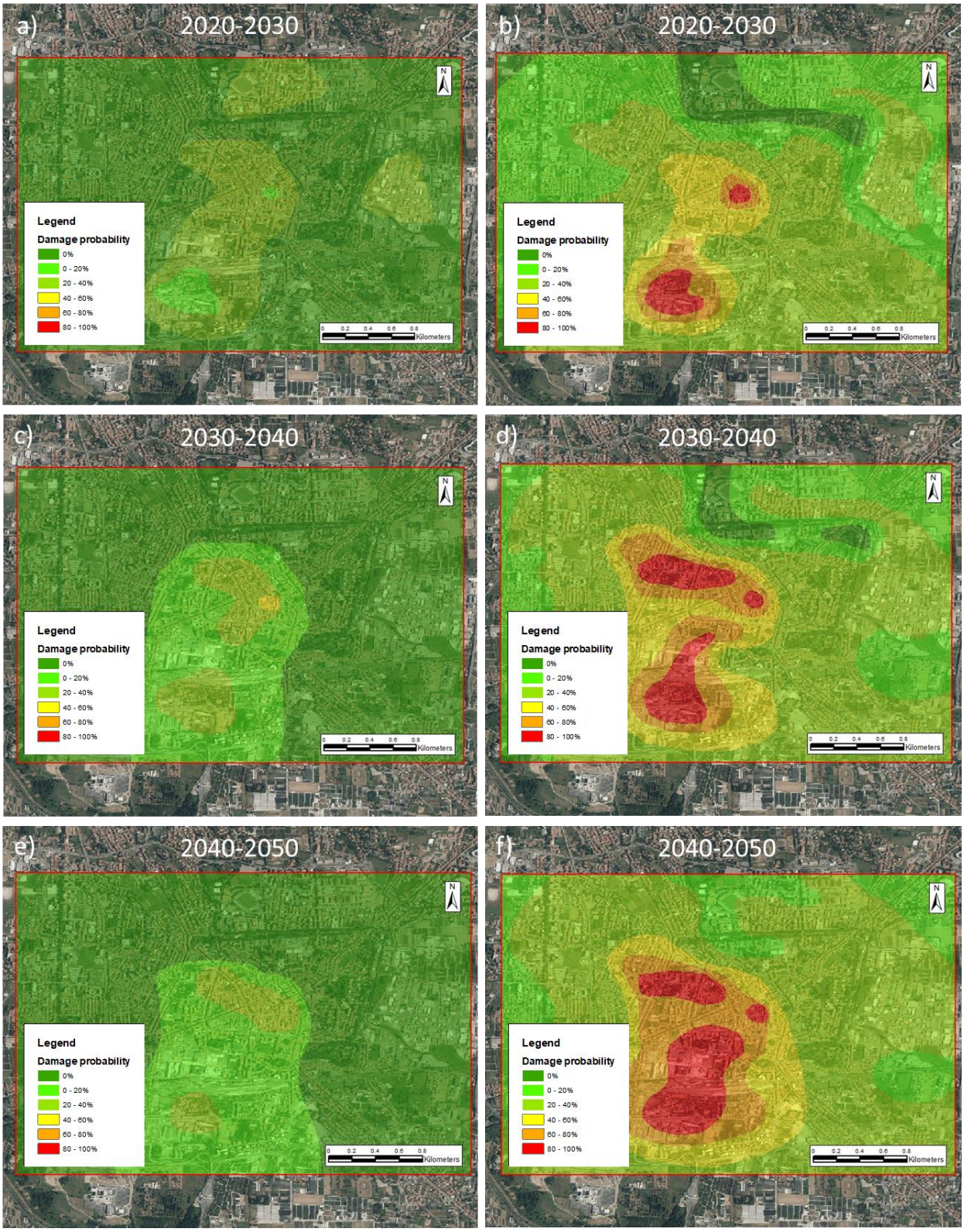

Figure 124 – Forecasted damage probability distribution of Pistoia historical center under a), c) and e) constant pumping rate and b), d) and f) Increasing pumping rate scenarios.

In the vulnerability map developing procedure, pumping rate decreasing scenario was not considered. Starting from the first forecasted decade (2020-2030), in fact, subsidence rate estimated under the lowest pumping scenario in Pistoia city decreased to a very low value, below 2.5 mm/year, that would have led to the development of a complete 0% damage probability distribution for the entire area.

Forecasted vulnerability maps have been developed considering the COSMO SkyMed ascending fragility curves, since it represents the most conservative solution and it describes in a very good way all the detected ground displacement velocities ranges.

For the constant pumping rate scenario, vulnerability maps follow the subsidence patterns simulated by the forecasting model in Pistoia city (Figure 124a, c and e). Here, a ground displacement rate lower than 10 mm/year is expected for the considered period (2020-2050), resulting in a damage probability distribution mainly ranging between 0 and 40% in all three reference decades.

Considering the maximum pumping rate scenario (Figure 124b, d and f), the probability of damage occurrence in Pistoia historical center is very high and it increases with time (as the simulated water extraction rate from aquifers increases of 1% each year). As for the 2015-2017 vulnerability maps, the higher damage probability distribution interests the mid-Western/South-Wester part of the city, where the maximum ground displacement rate is estimated. In the first 2020-2030 decade, considering only the area with more than 0% of damage probability occurrence (7.2 km^2), about 2% of buildings fall in the 80-100% damage probability class, while 87% are characterized by a probability of damage between 0 and 40% and 11% are affected by a damage probability distribution between 40% and 80% (Figure 124b). In the following 2030-2040 period, the percentage of buildings in the maximum damage probability class rise up to 4.5%, while 75% of buildings have a 0-40% probability and 21% have between 40 and 80% (Figure 124d). In the last forecasted decade, buildings characterized by an 80-100% of damage probability occurrence increase to 7%, for a total area of about 0.5 km^2. 21% have between 40 and 80% probability of damage and only 72% are below the 40% of probability (Figure 124f). Moreover, considering the 2040-2050 period, there are no buildings with a 0% probability of damage.

9 Conclusions

The main goal of the present research work was the development of an analysis procedure to identify the causes of anthropic induced subsidence and to characterize its consequences on environment, structures and human activities.

Pistoia city and surroundings (located within the Firenze-Prato-Pistoia basin, Central Italy) have been chosen as study area, since it is characterized by a long and well-known subsidence history since the early 1990', when the first InSAR data of ground displacement became available. Groundwater represents the main source of freshwater in Pistoia area, and its over exploitation for drinkable and agricultural uses led to the development of subsidence phenomena.

During the 1992-2000 period, ERS data identified a 10 mm/year ground displacement rate South-East of Pistoia city, in correspondence of the plant nursery area that represent one of the main economic activity of the region. ENVISAT data available for the 2002-2010 period show similar subsidence rate (15-20 mm/year), confirming the land surface lowering trend. Many studies ascribe subsidence phenomena that characterize the area of Pistoia to the overexploitation of groundwater from aquifers, that caused a reduction in groundwater levels with the consequent compaction of the sedimentary deposits.

Starting from the end of 2014, Sentinel-1 data identified the presence of two distinct subsidence bowl in Pistoia area. The first one, in plant nursery area, keeps subsiding with a mean ground displacement velocity of about 10-15 mm/year, while the second one, located in the historical center of the city, is characterized by an anomalous rate of 15-20 mm/year. Such trend has been confirmed by COSMO SkyMed data, acquired to validate Sentinel-1 ground displacement data in Pistoia city.

In order to assess the level of damage that is affecting buildings in Pistoia city, caused by the effects of subsidence, two field campaigns have been carried out, recording information on building characteristics as well as level and extent of damage. The combination of the level of damage identified for the surveyed buildings and their associated vertical displacements, obtained from available PS-InSAR data, allowed to build the structures fragility curves, providing the probability of occurrence of some level of damage for certain building displacement. Damage fragility curves were used to classify the measured velocities into five probability classes. Then, since InSAR data cover the whole city of Pistoia and provides information about the vertical displacement of all buildings, assuming a homogeneous structural typology, the probability of damage within the whole city of Pistoia has been calculated and the subsidence vulnerability map of the city has been generated.

To characterize the causes of Pistoia instability phenomena and their relation with groundwater states, an integrated modelling approach combining MOBIDIC hydrologic model and MODFLOW groundwater model has been presented. The methodology was firstly tested in Pesa river basin (Central Italy), to quantifying the interactions between river network and aquifer system in a small basin with a simple aquifer geometry. A surficial hydrologic model was implemented with MOBIDIC code and connected with MODFLOW, in order to evaluate the river network discharge of Pesa river and the net recharge rate of the aquifer, to use them as input parameters for the groundwater model. This was done, for the recharge parameter, by directly transfer the percolation value as obtained from MOBIDIC output to MODFLOW code and, for the water stage in the surficial network, by converting the discharge values calculated by MOBIDIC.

Calibration and validation phases of the hydrological model showed good predictive ability for annual large-scale flow rates, make it suitable for water management purposes. In contrary, the model showed some estimation errors in maximum daily flow simulations, not qualifying it for flood risk analysis uses.

Results of groundwater model simulation evidence a good degree of accuracy if compared with observed data, indicating the goodness of the developed model and the high reliability of the proposed integrated procedure. With the results obtained from the MOBIDIC-MODFLOW simulations, the global water budget estimation of Pesa river basin has been carried out, combining the information of both surficial and groundwater main variables.

The developed MOBIDIC - MODFLOW modelling approach showed very good results in Pasa basin case study and it could represent a tool of significant importance for use in planning and operating water resource strategies. This integrated tool can be very useful to simulate impacts of human activities on groundwater systems and to predict the variation of hydrologic and hydrogeologic variables under different stress conditions and climate scenarios.

Once the methodology was developed and its reliability was tested, a MOBIDIC-MODFLOW combined model was implemented for Pistoia area. Two MOBIDIC hydrologic models has been set, considering a small-scale approach for Ombrone basin and a large-scale approach of the entire Arno river basin, upstream of the Gonfolina closing section. Both models were run for a 25 years period, between 1992 and 2017. Moreover, for the 2009-2017 period, an additional hydrologic simulation by means of SWAT model has been carried out. Evaluation of calibration and validation accuracy rate showed that the small-scale model developed with MOBIDIC was the most suitable to represent the hydrologic conditions of Pistoia area.

Applying the proposed combined methodology, the hydrological model output has been converted as input data for the groundwater model, implemented by using the available information on Pistoia aquifer. MODFLOW groundwater model was calibrated and validated by means of the available hydraulic head data of the region and with the numerous ground displacement measurements obtained from Sentinel-1 and ENVISAT PS-InSAR data for the 2015-2017 and for the 2003-2010 period, respectively. Subsidence has been modelled using MODFLOW Subsidence Package (SUB), able to simulate aquifers compaction as a response of the increasing of the effective stress caused by groundwater over exploitation.

Calibration and validation of the groundwater model, focused on hydraulic conductivity and skeletal storage coefficients of the aquifer, showed a very good agreement with observations, both for hydraulic head and ground displacement data, demonstrating the benefits of using detailed subsidence data in the characterization of aquifer properties values when detailed and complete hydraulic head measurements are not available. Calibrated values of storage coefficients may suggest that the combined effect of groundwater extraction and the presence of compressible fine sediments may represent the driving force of subsidence detected in Pistoia area. Moreover, the statistical analysis of model results further demonstrates the high reliability of the developed MOBIDIC-MODFLOW approach and the good predictive capabilities of MODFLOW SUB package.

Combining results of the hydrological and hydrogeological models and analyzing the global water balance of Ombrone basin, a mean annual deficit in groundwater storage of about 1.1 Mcm has been detected. In the long term, such deficit can represent one of the causes of groundwater levels decreasing that led to the development of land subsidence.

In order to identify the potential subsidence pattern that could affect Pistoia area in the future, a subsidence forecasting model has been developed, considering the climate variability and its influence on the hydrologic cycle. Meteorological data for the 1992-2050 period have been obtained from to the freely available Global and Regional Climate Models (GCMs and RCMs) output (RCP 4.5), representing two of the most powerful tools for simulating future climate scenarios. CMCC-CMS, INM-CM4, MIROC5, MIROCESM and MRICGCM3 were selected as climate forecasting models. Due to their rough resolution and to the several assumptions made during their development, raw GCMs/RCMs output should not be used directly in hydrologic

simulations, and they must be firstly calibrated with real observations at some control stations (*bias* correction procedure). Using the available observed meteorological data of Pistoia area, and by means of the Linear Scale correction method, raw GCMs/RCMs output has been calibrated on the 1992-2018 historical period. Statistical analysis and direct comparison of climate models calibrated data demonstrated the goodness of the *bias* correction procedure, with GCMs/RCMs corrected output resulted to be in very good agreement with observations. The goodness of the calibration procedure was further demonstrated by the values of R^2, mean and standard deviation statistical indexes. Moreover, for each considered variable, the potential pattern variation induced by the effects of climate changes has been evaluated. Rainfall and wind speed showed a stable trend in the analyzed period, while a slight decreasing is occurring in forecasted air relative humidity. An opposite trend characterizes maximum and minimum temperature, showing a constant rising pattern since 1992, and radiation, that is expected to slightly increase as well.

After their calibration, GCMs/RCMs output were used as input data for the calibrated hydrological model of Ombrone basin, in order to evaluate the potential evolution of surficial processes until 2050. To evaluate the goodness of the provisional hydrologic model, its output for the 1992-2017 control period were compared with the original Ombrone model. Models output showed a good agreement with each other, both in term of mean monthly discharge and annual discharge values. All selected RCMs, except for INM-CM4, forecast a slightly increasing in river discharge and percolation through the aquifer in Pistoia area, but such value can be ascribed to the range of natural variations.

Following the MOBIDIC-MODFLOW coupling procedure, forecasting GCMs/RCMs hydrological model output parameters have been used, together with the calibrated groundwater model of Pistoia aquifer, to simulate the potential subsidence pattern that could affect Pistoia area in future years. For the development of the groundwater model, three different pumping rate scenarios have been investigated, assuming (1) the current withdrawals patterns (2) a 1%/year increasing in groundwater withdrawals and (3) a 1%/year decreasing in groundwater withdrawals, considering a 58 years time frame (from 1992 to 2050). In order to evaluate the goodness of the forecasting model results, a comparison between the modelled ground displacement rate and the Sentinel-1 PS-InSAR data of the 2015-2017 period has been carried out. Groundwater forecasting model present a high reliability, reproducing very well the general subsidence pattern occurring in Pistoia area between 2015 and 2017, both in terms of magnitude and areal extension.

The analysis of forecasted ground displacement potentially interesting Pistoia city has been performed in a decadal time frame for the 2020-2030, 2031-2040 and 2041-2050 periods. Starting from 2020-2030 decade, the decreasing pumping rate scenario evidence an important reduction of the subsiding area and of the ground displacement intensity, that become negligible after the 2031-2040 period. This represent a clear indicator of the influence of groundwater levels variation in controlling aquifers compaction in alluvial environment characterized by the presence of fine compressible sediments, enhancing the importance of the correct management of groundwater resource. A further decreasing in groundwater extraction rate, as simulated in the 2040-2050 period, does not strongly affect the residual subsidence pattern still occurring in plant nursery area. Here, subsidence bowls are very limited in extension and they are characterized by velocity values lower than 2.5 mm/year. This is probably linked to the stabilization of water levels within the aquifer that started during the previous analyzed decade, as a direct consequence of the reduction of water extraction from the groundwater system. Considering an extension of the current pumping rate for the next 30 years, in plant nursery area the subsidence rate remains constant for all the forecasted period (10-20 mm/year), while a reduction in ground displacement is expected to occur in the historical center, with values that oscillate around 5 mm/year. Assuming an increasing of groundwater extraction rate, the model evidences an important acceleration of land surface lowering in all Pistoia area, with the extension of the

affected area and a ground displacement rate that rise up to more than 40 mm/year in some parts of the plant nursery area. However, MODFLOW SUB package does not keep into account reductions in skeletal specific coefficients as a consequence of effective stress increasing and subsidence rate identified for future years might be overestimated.

Finally, combining the ground displacement rate obtained from the subsidence forecasting model with the fragility curves built for Pistoia historical center, the potential subsidence vulnerability maps for the different pumping rate scenarios have been generated. The low subsidence rate described by the model assuming a decreasing of groundwater extraction led to the definition of a 0% damage probability distribution for the entire area of interest. Considering the current pumping rate scenario, with future groundwater states influenced only by the effects of climate variations, a damage probability distribution ranging between 0 and 40% has been identified in Pistoia city for all three reference decades. Increasing the groundwater extraction rate of 1%/year from 2020 to 2050 result in a very high damage probability distribution, with respectively 13%, 25.5% and 28% of the total considered area (7.2 km^2) that will be affected by a certain degree of damage in more than 40% of cases.

The proposed integrated MOBIDIC-MODFLOW procedure showed good predictive capabilities, allowing the development of high-resolution numerical models for the analysis of hydrologic and hydrogeologic systems at basin scale. Thanks to its fully adaptive structure, the methodology allows the combination of many different types of dataset and information, improving the research potential in the hydrologic and hydrogeologic field.

In this investigation we use newly acquired basin-wide temporal PS-InSAR as main observations to inversely estimate aquifer parameters and geomechanical properties to obtain a finely discretized groundwater flow model. The results of this research demonstrated that high resolution temporal and spatial ground displacement observations from PS-InSAR can be extremely useful to identify the complex distribution of aquifers properties, providing important information for groundwater models calibration when water levels data are sparse or not detailed.

Furthermore, the damage assessment analysis and the definition of future subsidence scenario can represent a valuable tool for planners and policy makers to improve the management of the groundwater resource, providing important information urban planning strategies.

The developed groundwater models, applied in the subsiding area of Pistoia city and surroundings, confirms the presence of a direct relation between subsidence pattern and groundwater levels variation because of the effects of over pumping. This phenomenon, coupled by the presence of fine compressible sediments, can be identified as one of the primary driving force of subsidence patterns in Pistoia area, showing a higher influence than low-term climate changes on controlling ground displacement. In addition, forecasting analysis showed that if the pumping rate from the aquifer will continue uncontrolled, anomalous subsidence rate affecting Pistoia city are expected to persist, leading to severe consequences for buildings, engineering structures and human activities. As a first step, given the high compressibility nature of alluvial sediments in the study area, subsidence phenomena mitigation actions should include a correct and sustainable use of the groundwater resource. New and updated water levels measurements could provide useful information to assess current groundwater states in Pistoia aquifer, allowing the development of a finer and better calibrated numerical model with improved reliability. Considering the anomalous ground surface displacement velocity observed by PSI in last 30 years in Pistoia surroundings related to high withdrawals rate, an adapted and forward-looking groundwater management in the area is of vital importance, in order to guarantee groundwater quality and quantity, and its renewability.

10 References

Albano M, Polcari M, Bignami C, et al (2016) An innovative procedure for monitoring the change in soil seismic response by InSAR data: application to the Mexico City subsidence. Int J Appl Earth Obs Geoinf 53:146–158.

Anderson Jr., W. P., Storniolo, R. E., and Rice, J. S. (2011): Bank thermal storage as a sink of temperature surges in urbanized streams, J. Hydrol., 409, 525–537.

Aristeidis G, Koutroulis AG, Tsanis IN, Daliakopoulos IN, Jacob D (2012) Impact of climate change on water resources status: a case study for Crete Island, Greece. J Hydrol 479:146–158.

Arjomandi, M., Saremi, A., Sarraf, A., Sedghi, H., Roustaei, M. (2018). 'Predicting land subsidence rate due to groundwater exploitation in the district 19 of Tehran using MODFLOW and InSAR', *Journal of Geoscience*, 27(106), pp. 75-82.

Arnell NW (2003) Effects of IPCC SRES emissions scenarios on river runoff: a global perspective. Hydrol Earth Syst Sci 7:619–641.

Arnold JG, Srinivasan R, Muttiah RS, Williams JR (1998) Large area hydrologic modeling and assessment – Part 1: Model development. J American Water Resour Assoc 34(1):73–89.

Aslan, G.; Cakir, Z.; Lasserre, C.; Renard, F. (2019) Investigating Subsidence in the Bursa Plain, Turkey, Using Ascending and Descending Sentinel-1 Satellite Data. *Remote Sens. 11*, 85.

Babel MS, Bhusal SP, Wahid SM, Agarwal A (2013) Climate change and water resources in the Bagmati River Basin, Nepal. Theoret Appl Climatol 112:3–4.

Bailey R.T., Wible T.C., Arabi M., Records R.M., Ditty J. (2016) Assessing regional-scale spatio-temporal patterns of groundwater–surface water interactions using a coupled SWAT-MODFLOW model J. Hydrol. Process., 30, pp. 4420-4433.

Batini, F., Brogi, A., Lazzarotto, A., Liotta, D., Pandeli, E., (2006). Geological features of Larderello-Travale and Mt. Amiata geothermal areas (southern Tuscany, Italy). Episodes 3, 239–244.

Bell, J. W., Amelung, F., Ferretti, A., Bianchi, M., and Novali, F. (2008), Permanent scatterer InSAR reveals seasonal and long-term aquifer-system response to groundwater pumping and artificial recharge, Water Resour. Res.

Bergstrom, S., Carlsson, B., Gardelin, M., Lindstrom, G., Pettersson, A., and Rummukainen, M. (2011): Climate change impacts on runoff in Sweden-assessments by global climate models, dynamical downscaling and hydrological modelling, Clim. Res., 16, 101–112.

Berti, M., Corsini, A., Franceschini, S., and Iannacone, J. P. (2013): Automated classification of Persistent Scatterers Interferometry time series, Nat. Hazards Earth Syst. Sci., 13, 1945–1958, https://doi.org/10.5194/nhess-13-1945-2013.

Bianchini S, Cigna F, Righini G, Proietti C and Casagli N (2012) Landslide hotspot mapping by means of persistent scatterer interferometry. Environmental Earth Sciences 67: 1155-1172.

Billah, A.H.M.M., & Alam, M.S. (2013). Seismic vulnerability assessment of a typical multi-span continuous concrete highway bridge in British Columbia. Canadian Journal of Civil Engineering, Manuscript ID: CJCE-2013-0049R2.

Bitelli G.; Bonsignore F.; Carbognin L.; Ferretti A.; Strozzi T.; Teatini P.; Tosi L.; Vittuari L. (2012), Radar interferometry-based mapping of the present land subsidence along the low-lying northern Adriatic coast of Italy, in: Land Subsidence, Associated Hazards and the Role of Natural Resources Development, WALLINGFORD, IAHS Press, pp. 279 – 286.

Blanco-Sánchez, J., Mallorquí, J., Duque, S., Monells, D., (2008). The Coherent Pixels Technique (CPT): An Advanced DInSAR Technique for Nonlinear Deformation Monitoring. Pure Appl. Geophys. 165, 1167– 1193.

Boccaletti, M., Corti, G., Gasperini, P. et al. (2001) Active tectonics and seismic zonation of the urban area of Florence, Italy Pure appl. geophys. 158: 2313. https://doi.org/10.1007/PL00001172.

Boccaletti, M., Guazzone, G., (1974) Remnant arcs and marginal basins in the Cainozoic development of the Mediterranean, Nature 252 (5478), 18.

Bozzano F., Esposito C., Franchi S. et al. (2015), "Understanding the subsidence process of a quaternary plain by combining geological and hydrogeological modelling with satellite InSAR data: The Acque Albule Plain case study," Remote Sensing of Environment, vol. 168, pp. 219–238.

Burbey, Thomas J. and Meijing Zhang. (2015) "Inverse modeling using PS-InSAR for improved calibration of hydraulic parameters and prediction of future subsidence for Las Vegas Valley, USA.".

Campo, L., Caparrini, F. & Castelli, F. (2006) Use of multi-platform, multi-temporal, remote sensing data for calibration of a distributed hydrological model: an application in the Arno basin, Italy. Hydrol. Processes 20(13), 2693–2712.

Canuti, P., Casagli, N., Farina, P., Ferretti, A., Marks, F., Menduni, G., (2006). Analisi dei fenomeni di subsidenza nel bacino del fiume Arno mediante interferometria radar. G.G.A 4, 131–136.

Cao, G., Han, D. & Moser, J. (2013). Groundwater exploitation management under land subsidence constraint: empirical evidence from the Hangzhou-Jiaxing-Huzhou Plain, China. Environ. Manage. 51, 1109–1125.

Capecchi, F.; Guazzone, G.; Pranzini, G. (1975) Il bacino lacustre di firenze-prato-pistoia; geologia del sottosuolo e ricostruzione evolutiva. Boll. Soc. Geol. Italiana, 94, 637–660.

Carpenter T. M., Georgakakos K. P. (2006) Intercomparison of lumped versus distributed hydrologic model ensemble simulations on operational forecast scales[J]. Journal of Hydrology, 329(1-2): 174- 185.

Carrera-Hernández, J.J., Gaskin, S.J., (2007). The Basin of Mexico aquifer system: regional groundwater level dynamics and database development. Hydrogeology Journal 15 (8), 1577–1590.

Casagrande, Arthur (1936). "The determination of the pre-consolidation load and its practical significance". Proceedings of the international conference on soil mechanics and foundation engineering. 3. Harvard University Cambridge. pp. 60–64.

Castelli, F., Menduni, G. and Mazzanti, B. (2009). A distributed package for sustainable water management: A case study in the Arno basin. In: H. J. Liebscher, R. Clarke, J. Rodda, G. Schultz, A. Schumann, L. Ubertini, G. Young. The Role of Hydrology in Water Resources Management, pp. 52 - 61.

Chen, M., R. Tomás, Z. Li, M. Motagh, T. Li, L. Hu, H. Gong, X. Li, Y. Jun, and X. Gong. (2016). "Imaging Land Subsidence Induced by Groundwater Extraction in Beijing (China) Using Satellite Radar Interferometry." Remote Sensing 8 (6): 468.

Chung IM, Kim NW, Lee J, Sophocleous M (2010) Assessing distributed groundwater recharge rate using integrated surface water-groundwater modeling: application to Mihocheon watershed, South Korea. Hydrogeol J 18:1253–1264.

Cigna, F., Del Ventisette, C., Gigli, G., Menna, F., Agili, F., Liguori, V., and Casagli, N. (2012): Ground instability in the old town of Agrigento (Italy) depicted by on-site investigations and Persistent Scatterers data, Nat. Hazards Earth Syst. Sci., 12, 3589–3603, https://doi.org/10.5194/nhess-12-3589-2012.

Ciulli, B., Dini, I., Palmieri, F., Rossi, A., (2005). Interpreting ground deformation and microgravity changes in the travale-radicondoli geothermal field (Italy). In: Proceedings World Geothermal Congress, Antalya, Turkey, 24–29 April, 2005, pp. 1–7.

Colesanti C, Ferretti A, Prati C and Rocca F (2003) Monitoring landslides and tectonic motions with the permanent scatterers technique. Engineering Geology 68: 3-14.

Coli M., Rubellini P., (2007) "Note di geologia fiorentina". Comune di Firenze SELCA Firenze Winter T.C., Harvey J.W., Franke O.L. and Alley W.M. (1998). Ground water and surface water; a single resource. USGS Circular 1139. US Geological Survey, Denver, Colorado.

Confuorto, P., Di Martire, D., Centolanza, G., Iglesias, R., Mallorqui, J.J., Novellino, A., Plank, S., Ramondini, M., Thuro, K., Calcaterra, D., (2017). Post-failure evolution analysis of a rainfall-triggered landslide by multi-temporal interferometry SAR approaches integrated with geotechnical analysis. Remote Sens. Environ.

Covello, F., F. Battazza, A. Coletta, E. Lopinto, C. Fiorentino, L. Pietranera, G. Valentini, S. Zoffoli, (2010). COSMO-SkyMed an existing opportunity for observing the Earth. Journal of Geodynamics, Vol 49, 3–4, pp 171-180, https://doi.org/10.1016/j.jog.2010.01.001.

Del Soldato M.; Bianchini S.; Calcaterra D.; De Vita P.; Di Martire D.; Tomãs R.; Casagli N. (2017). A new approach for landslide-induced damage assessment. Geomatics, Natural Hazards & Risk, vol. 8, pp. 1524-1537.

Del Soldato, M.; Farolfi, G.; Rosi, A.; Raspini, F.; Casagli, N. (2018) Subsidence evolution of the Firenze–Prato–Pistoia plain (Central Italy) combining PSI and GNSS data. Remote Sens., 10, 1146.

Dlugolecki A. (2004) A Changing Climate for Insurance Association of British Insurers, London, June 2004 24pp.

Doherty, J., (2003). Groundwater model calibration using pilot points and regularisation. Ground Water. 41 (2): 170-177.

Doherty, J., Fienen, M.N., and Hunt, R.J., (2010), Approaches to highly parameterized inversion: Pilot-point theory, guidelines, and research directions: U.S. Geological Survey Scientific Investigations Report 2010-5168, 36 p.

Doherty, J. (2010): PEST: Model-independent Parameter Estimation, User Manual, 5th edn., Watermark Numerical Computing, Brisbane, Queensland, Australia.

Duro J, Inglada J, Closa J, Adam N and Arnaud A (2004) High resolution differential interferometry using time series of ers and envisat sar data. FRINGE 2003 Workshop, pp 72.

Ehtiat, M., Jamshid Mousavi, S. & Srinivasan (2018), Groundwater Modeling Under Variable Operating Conditions Using SWAT, MODFLOW and MT3DMS: A Catchment Scale Approach to Water Resources Management R. Water Resour Manage 32: 1631.

El-Nasr A. A., Arnold J. G. and Feyen J. et al. (2005) Modeling the hydrology of a catchment using a distributed and a semi-distributed model[J]. Hydrological processes, 19(3): 573-587.

Ezquerro P., Guardiola-Albert C., Herrera G., Fernández-Merodo J. A., Béjar-Pizarro M., and Bonì R. (2017) "Groundwater and Subsidence Modeling Combining Geological and Multi-Satellite SAR Data over the Alto Guadalentín Aquifer (SE Spain)," Geofluids.

Fabris, M., Achilli, V. and Menin, A. (2014) Estimation of Subsidence in Po Delta Area (Northern Italy) by Integration of GPS Data, High-Precision Leveling and Archival Orthometric Elevations. International Journal of Geosciences, 5, 571-585.

Fancelli R., Focardi P., Gozzi F., Vannucchi G., (1980) Dissesti statici dei fabbricati nel centro storico di Pistoia (1964-1966) – Associazione Geotecnica Italiana, XIV Convegno Nazionale di Geotecnica.

Ferretti A, Fumagalli A, Novali F, Prati C, Rocca F and Rucci A, (2011) A new algorithm for processing interferometric data-stacks: Squeesar. IEEE Transactions on Geoscience and Remote Sensing 49: 3460-3470.

Ferretti A, Prati C and Rocca F (2001) Permanent scatterers in sar interferometry. Geoscience and Remote Sensing, IEEE Transactions on 39: 8-20.

Ferretti A., Prati C., Rocca F., (2000) Nonlinear subsidence rate estimation using permanent scatters in differential SAR interferometry IEEE T. Geosci. Remote, 38 (5), pp. 2202-2212.

Fondelli M., (1975) - Studio dei movimenti verticali del suolo nell'area urbana della città di Pistoia. «Boll. Geod. Sci. Aff., 1, 1.

Funning GJ, Parsons B and Wright TJ (2007) Fault slip in the 1997 manyi, tibet earthquake from linear elastic modelling of insar displacements. Geophysical Journal International 169: 988-1008.

Furman, A. (2008), Modeling coupled surfacesubsurface flow processes: A review, Vadose Zone J., 7(2), 741–756.

Galloway D., Jones D.R., Ingebritsen (1999). land subsidence in the united states. circular 1182. us geological survey.

Gambolati, G., (1970), A one-dimensional model of the subsoil for computing the surface subsidence: IBM Venice Scientific Center Technical Report CRV002, Venice, Italy, 57 p.

Gardner, M., Morton, C., Huntington, J. L., Niswonger, R. G., and Henson, W. R. (2018): Input Data Processing Tools for Integrated Hydrologic Models, Environmental Modelling and Software.

Guzman, J. A., Moriasi, D. N., Gowda, P. H., Steiner, J. L., Starks, P. J., Arnold, J. G., & Srinivasan, R. (2015). A model integration framework for linking SWAT and MODFLOW. Environmental Modelling & Software, 73, 103–116.

Harbaugh, A.W., Banta, E.R., Hill, M.C., and McDonald, M.G., (2000), MODFLOW-2000, the U.S. Geological Survey modular ground-water model -- User guide to modularization concepts and the Ground-Water Flow Process: U.S. Geological Survey Open-File Report 00-92, 121 p.

Helm, D.C., (1975), One-dimensional simulation of aquifer system compaction near Pixley, California, 1. Constant parameters: Water Resources Research, v. 11, no. 3, p. 465–478.

Hempel S, Frieler L, Schewe J, Piontek F (2013) A trend-preserving bias correction—the ISI-MIP approach. Earth Syst Dyn 4(219–236):2013 Ines VMA, Hansen JW (2006) Bias correction of daily GCM rainfall for crop simulation studies. Agric For Meteorol 138:44–53.

Höffmann, J., Leake, S.A., Galloway, D.L., and Wilson, A.M., (2003), MODFLOW-2000 Ground-Water Model--User Guide to the Subsidence and Aquifer-System Compaction (SUB) Package: U.S. Geological Survey Open-File Report 03-233, 44 p.

Huang G., Yeh G.T. (2009) Comparative study of coupling approaches for surface water and subsurface interactions J. Hydraul. Eng., 14 (5), pp. 453-462.

Ines, A. V. and Hansen, J. W. (2006): Bias correction of daily GCM rainfall for crop simulation studies, 10 Agr. Forest Meteorol., 138, 44–53, doi: 10.1016/j.agrformet.2006.03.009.

Ireland, R.L., Poland, J.F., Riley, F.S. (1984). Land subsidence in the San Joaquin Valley, California. USGS.

Kim N.W., Chung I.M., Won Y.S., Arnold J.G. (2008) Development and application of the integrated SWAT–MODFLOW model J. Hydrol., 356, pp. 1-16.

Langevin, C., Swain, E., and Wolfert, M. (2005). “Simulation of integrated surface-water/ground-water flow and salinity for a coastal wetland and adjacent estuary.” J. Hydrol., 314_1–4_, 212–234.

Leake, S.A., and Prudic, D.E., (1991), Documentation of a computer program to simulate aquifer-system compaction using the modular finite-difference ground-water flow model: U.S. Geological Survey Techniques of Water-Resources Investigations, book 6, chap. A2, 68 p.

Lenderink, G., Buishand, A., and van Deursen, W. (2007): Estimates of future discharges of the river Rhine using two scenario methodologies: direct versus delta approach, Hydrol. Earth Syst. Sci., 11, 1145–1159, doi:10.5194/hess-11-1145-2007.

Manzo M, Ricciardi G, Casu F, Ventura G, Zeni G, Borgstrom S, Berardino P, Del Gaudio C and Lanari R (2006) Surface deformation analysis in the ischia island (italy) based on spaceborne radar interferometry. Journal of Volcanology and Geothermal Research 151: 399-416.

Markstrom, S.L., Niswonger, R.G., Regan, R.S., Prudic, D.E., and Barlow, P.M., (2008), GSFLOW - Coupled Ground-water and Surface-water FLOW model based on the integration of the Precipitation-Runoff Modeling System (PRMS) and the Modular Ground-Water Flow Model (MODFLOW-2005): U.S. Geological Survey Techniques and Methods 6-D1, 240 p.

Massonnet D and Feigl KL (1998) Radar interferometry and its application to changes in the earth's surface. Reviews of geophysics 36: 441-500.

Masui T, Matsumoto K, Hijioka Y, Kinoshita T, Nozawa T, Ishiwatari S, Kato E, Shukla PR, Yamagata Y, Kainuma M (2011) An emission pathway for stabilization at 6 wm−2 radiative forcing. Clim Chang 109(1):59.

Mcdonald, M.G. and Harbaugh, A.W. (1984) A Modular Three-Dimensional Finit-Difference Ground-Water Flow Model, U.S. Geological Survey. Techniques of Water Resources Investigations, Book 6.

Meinshausen, M., S. J. Smith, K. V. Calvin, J. S. Daniel, M. L. T. Kainuma, J.-F. Lamarque, K. Matsumoto, S. A. Montzka, S. C. B. Raper, K. Riahi, A. M. Thomson, G. J. M. Velders and D. van Vuuren (2011). "The RCP Greenhouse Gas Concentrations and their Extension from 1765 to 2300." Climatic Change (Special Issue).

Minville M, Brissette F, Leconte R (2008) Uncertainty of the impact of climate change on the hydrology of a nordic watershed. J Hydrol 358:70–83.

Mohamed Nazri F (2018) Fragility curves. Seismic fragility assessment for buildings due to earthquake excitation, Springer Singapore, Singapore, pp 3-30.

Mora O, Mallorqui JJ and Broquetas A (2003) Linear and nonlinear terrain deformation maps from a reduced set of interferometric sar images. IEEE Transactions on Geoscience and Remote Sensing 41: 2243-2253.

Mugunthan, P., Russell, K. T., Gong, B., Riley, M. J., Chin, A., McDonald, B. G. and Eastcott, L. J. (2017), A Coupled Groundwater–Surface Water Modeling Framework for Simulating Transition Zone Processes. Groundwater, 55: 302-315.

Narasimhan, T.N., and Witherspoon, P.A., (1977), Numerical model for saturated unsaturated flow in deformable porous media, 1. Theory: Water Resources Research, v. 13, p. 657–664.

Negulescu C. and Foerster, E. (2010). Parametric Studies and Quantitative Assessment of The Vulnerability of a Rc Frame Building Exposed to Differential Settlements. Natural Hazards and Earth System Science, 10(9), 1781-1792.

Neuman, S.P., Preller, C., and Narasimhan, T.N., (1982), Adaptive explicit-implicit quasi three-dimensional finite element model of flow and subsidence in multiaquifer systems: Water Resources Research, v. 18, no. 5, p. 1551–1561.

Ng, A. H., L. Ge, X. Li, and K. Zhang (2012) "Monitoring Ground Deformation in Beijing, China with Persistent Scatterer SAR Interferometry." Journal of Geodesy 86 (6): 375–392.

Ng, G.-H. C., Wickert, A. D., Somers, L. D., Saberi, L., Cronkite-Ratcliff, C., Niswonger, R. G., and McKenzie, J. M. (2018): GSFLOW–GRASS v1.0.0: GIS-enabled hydrologic modeling of coupled groundwater–surface-water systems, Geosci. Model Dev., 11, 4755-4777.

Nkomozepi T, Chung S (2014) The effect of climate change on the water resources of the Geumho River Basin, Republic of Korea. J Hydro-environ Resources.

Notti D, Herrera G, Bianchini S, Meisina C, Garcia-Davalillo JC and Zucca F (2014) A methodology for improving landslide psi data analysis. International Journal of Remote Sensing 35: 2186-2214. doi: 10.1080/01431161.2014.889864.

Olmstead SM (2013) Climate change adaptation and water resource management: a review of the literature. Energy Economics 46 (2014) 500–509.

Ouchi K (2013) Recent trend and advance of synthetic aperture radar with selected topics. Remote Sensing 5: 716.

Panday, S. and Huyakorn, P.S. (2004) A Fully Coupled Physically-Based Spatially Distributed Model for Evaluating Surface/Subsurface Flow. Advances in Water Resources, 27, 361-382.

Peduto, D., Ferlisi, S., Nicodemo, G., Reale, D., Pisciotta, G., & Gullà, G. (2017). Empirical fragility and vulnerability curves for buildings exposed to slow-moving landslides at medium and large scales. Landslides, 14(6), 1993–2007. doi:10.1007/s10346-017-0826-7 persistent scatterer interferometry (psi) technique. Remote Sensing 6: 10510-10522.

Pieri, L., Russo, P. (1984). The survey of soil vertical movements in the region of Bologna. Proceedings of the Third International Symposium on Land Subsidence. Venezia (Italy).

Poeter, E. P., and M. C. Hill, (1997), Inverse, models: A necessary next step in groundwater modeling: Ground Water, v. 35, p. 250-260.

Poland, J.F., and Davis, G.H., (1969), Land subsidence due to withdrawals of fluids, in Varnes, D.J., and Kiersch, G., eds.: Geological Society of America Reviews in Engineering Geology, v. 2, p. 187−269.

Poland, J.F., Lofgren, B.E., Ireland, R.L., and Pugh, R.G., (1975), Land subsidence in the San Joaquin Valley, California, as of 1972: U.S. Geological Survey Professional Paper 437-H, 78 p.

Pulido-Velazquez M, Pena-Haro S, Garcia-Prats A, Mocholi-Almudever AF, Henriquez-Dole L, Macian-Sorribes H, Lopez-Nicolas A (2015) Integrated assessment of the impact of climate and land-use changes on groundwater quantity and quality in Mancha Oriental (Spain). Hydrol Earth Syst Sci 19:1677–1693.

Ramirez-Villegas, J., Challinor, A.J., Thornton, P.K., & Jarvis, A. (2013). Implications of regional improvement in global climate models for agricultural impact research. Environ Res Lett 8:24018.

Reed S., Koren V. and Smith M. et al. (2004) Overall distributed model intercomparison project results[J]. Journal of Hydrology, 298(1-4): 27-60.

Refsgaard J. C., Knudsen J. (1996) Operational validation and intercomparison of different types of hydrological models[J]. Water Resources Research, 32(7): 2189-2202.

Riahi K, Rao S, Krey V, at al. (2011) RCP 8.5—a scenario of comparatively high greenhouse gas emissions. Clim Chang 109:33–57.

Riley F.S. (1986) Developments in borehole extensometry. In Land Subsidence, Johnson A.I., Carbognin L., Ubertini L. (Eds.), IAHS Publication No. 151: pp. 169–186.

Riley, F.S., (1969), Analysis of borehole extensometer data from central California: International Association of Scientific Hydrology Publication 89, p. 423–431.

Rizzoli P and Brautigam B (2014) Radar backscatter modeling based on global tandem-x mission data. IEEE Transactions on Geoscience and Remote Sensing 52: 5974-5988.

Rosi A, Agostini A, Tofani V and Casagli N (2014) A procedure to map subsidence at the regional scale using the Persistent Scatterer Interferometry (PSI) Technique. Remote Sensing 6(11):10510-10522.

Rosi, A., Tofani, V., Agostini, A., Tanteri, L., Stefanelli, C.T., Catani, F., & Casagli, N. (2016). Subsidence mapping at regional scale using persistent scatters interferometry (PSI): The case of Tuscany region (Italy). Int. J. Applied Earth Observation and Geoinformation, 52, 328-337.

Rossetto T., Elnashai A. (2003) Derivation of Vulnerability Functions for European-Type Rc Structures Based on Observational Data. Engineering Structures 25 (2003) 1241–1263.

Rota M. Penna A. And Strobbia C. (2006). Typological Fragility Curves from Italian Earthquake Damage Data. Proceedings 1st European Conference on Earthquake Engineering and Seismology, Geneva, Paper (No. 386).

Rumbaugh, J., and D. Rumbaugh. (2004). Groundwater Vistas Version 4 User's Guide. Environmental Simulations Inc.

Sabetta F., Goretti A. And A. Lucantoni (1998). Empirical Fragility Curves from Damage Surveys and Estimated Strong Ground Motion. 11th European Conference on Earthquake Engineering, Paris, Cd-Rom, Isbn 90 5410 982 3, Balkema.

Saeidi A., Deck O. And Verdel, T. (2009). Development of Building Vulnerability Functions in Subsidence Regions from Empirical Methods. Engng Struct. 31, No. 10, 2275–2286.

Santoyo, E., Ovando-Shelley, E., Mooser, F., y León, E., (2005). Síntesis Geotécnica de la Cuenca del Valle de México, Editorial TGC, Mexico.

Schmidt DA and Burgmann R (2003) Time-dependent land uplift and subsidence in the santa clara valley, california, from a large interferometric synthetic aperture radar data set. Journal of Geophysical Research: Solid Earth 108.

Seager, R. and Vecchi, G. A. (2010): Greenhouse warming and the 21st century hydroclimate of southwestern North America, Proc. Natl. Acad. Sci. USA, 107, 21277–21282.

Shrestha S., Shrestha M., Babel M. S. (2016) Modelling the potential impacts of climate change on hydrology and water resources in the Indrawati River Basin, Nepal Environmental Earth Sciences, Volume 75, Number 4, Page 1.

Sophocleous, M. and Perkins, S.P. (2000) Methodology and Application of Combined Watershed and Ground-Water Models in Kansas. Journal of Hydrology, 236, 185-201.

Sridhar, V., M.M. Billah, and J.W. Hildreth. (2017) Coupled surface and groundwater hydrological modeling in a changing climate. Groundwater 56: 618–635.

Stramondo S.; Saroli M.; Tolomei C.; Moro M.; Doumaz F.; Pesci A.; Loddo F.; Baldi P.; Boschi E. (2006), The subsidence in Bologna city (Italy) and the Po Plain detected by InSAR SBAS technique, in: Geophysical Research Abstract, VIENNA, European Gephysical Union.

Swain, E.D., and Wexler, E.J., (1996), A coupled surface-water and ground-water flow model (MODBRANCH) for simulation of stream-aquifer Interaction: U.S. Geological Survey Techniques of Water-Resources Investigations Report, book 6, chapter A6, 125 p.

T. J. Burbey and M. Zhang (2015) “Inverse modeling using PS-InSAR for improved calibration of hydraulic parameters and prediction of future subsidence for Las Vegas Valley, USA,” Proceedings of the International Association of Hydrological Sciences (IAHS '15), vol. 372, pp. 411–416.

Tahiri, A., Ladeveze, D., Chiron, P. et al. (2018) Reservoir Management Using a Network Flow Optimization Model Considering Quadratic Convex Cost Functions on Arcs. Water Resour Manage 32: 3505.

Taylor, K. E., Stouffer, R. J. & Meehl, G. A. (2012) *An overview of CMIP5 and the experiment design*. Bull. Am. Meteorol. Soc. 93, 485–498.

Terzaghi, K., (1925), Erdbaumechanik auf bodenphysikalisher Grundlage: Wien, Austria, Deuticke, 399 p.

Teutschbein C, Seibert J (2012) Bias correction of regional climate model simulation for hydrological climate-change impact studies: review and evaluation of different methods. J Hydrol 456:12–29.

Thomson AM, Calvin KV, Smith JS, Kyle PG, Volke A, Patel P, Delgado-Arias S, Bond-Lamberty B, Wise MA, Clarke LE, Edmonds JA (2011) RCP4.5: a pathway for stabilization of radiative forcing. Clim Chang 109:77–94.

Tomas R, Romero R, Mulas J, Marturia JJ, Mallorqui JJ, Lopez-Sanchez JM, Herrera G, Gutierrez F, Gonzalez PJ and Fernandez J (2014) Radar interferometry techniques for the study of ground subsidence phenomena: A review of practical issues through cases in spain. Environmental earth sciences 71: 163-181.

Tortajada, C., (2006). Water management in Mexico City metropolitan area. Water Resources Development 22 (2), 353–376.

Van den Hurk, B. J. J. M. & Holtslag, A. A. M. (1997) On the bulk parameterization of surface fluxes for various conditions and parameter ranges. Boun. Layer Met. 82, 119–134.

van Vuuren DP, Edmonds J, Kainuma M, Riahi K, Thomson A, Hibbard K, Hurtt GC, Krey V, Lamarque JF, Masui T, Meinshausen M, Nakicenovic N, Smith SJ, Rose SK (2011a) The representative concentration pathways: an overview. Clim Change 109:5–31.

van Vuuren DP, Stehfest E, den Elzen MGJ, Kram T, van Vliet J, Deetman S, Isaac M, Klein Goldewijk K, Hof A, Mendoza Beltran A, Oostenrijk R, van Ruijven B (2011b) RCP2.6: exploring the possibility to keep global mean temperature increase below 2°C. Clim Chang 109:95–116.

Werner C, Wegmuller U, Strozzi T and Wiesmann A (2003) Interferometric point target analysis for deformation mapping. Geoscience and Remote Sensing Symposium, 2003 IGARSS'03 Proceedings 2003 IEEE International, IEEE, pp 4362-4364.

Wilson, M.F., and A. Henderson-Sellers, (1985): A global archive of land cover and soils data for use in general-circulation climate models. J. Climatol., 5, 119–143.

Winter T.C., Harvey J.W., Franke O.L., and Alley W.M. (1998) Ground Water and Surface Water A Single Resource, USGS Circular 1139.

Xu YP, Zhang X, Ran Q, Tian Y (2013) Impact of climate change on hydrology of upper reaches of Qiantang River Basin, East China. J Hydrol 483:51–60.

Yan, Tingting. (2007) “Effects of delayed drainage on subsidence modeling and parameter estimation.”.

Yang, J., Castelli, F., and Chen, Y. (2014): Multiobjective sensitivity analysis and optimization of distributed hydrologic model MOBIDIC, Hydrol. Earth Syst. Sci., 18, 4101-4112.

Yuanyuan, M., Xuegang, Z., and Zhijia, L. (2013). “Coupled simulation of Xinanjiang model with MODFLOW.” J. Hydrol. Eng., 10.1061/(ASCE)HE.1943-5584.0000706, 1443–1449.

Zeevaert, L. (1983). Foundation Engineering for difficult subsoil conditions. Van Nostrand Reinhold Company Inc. (USA).